

The Causes of Regional Sea-level Change since 1993

Machado Lima de Camargo, C.

DOI

[10.4233/uuid:ea31fff1-bd06-40de-8071-582331e0da9e](https://doi.org/10.4233/uuid:ea31fff1-bd06-40de-8071-582331e0da9e)

Publication date

2023

Document Version

Final published version

Citation (APA)

Machado Lima de Camargo, C. (2023). *The Causes of Regional Sea-level Change: since 1993*. [Dissertation (TU Delft), Delft University of Technology]. <https://doi.org/10.4233/uuid:ea31fff1-bd06-40de-8071-582331e0da9e>

Important note

To cite this publication, please use the final published version (if applicable).
Please check the document version above.

Copyright

Other than for strictly personal use, it is not permitted to download, forward or distribute the text or part of it, without the consent of the author(s) and/or copyright holder(s), unless the work is under an open content license such as Creative Commons.

Takedown policy

Please contact us and provide details if you believe this document breaches copyrights.
We will remove access to the work immediately and investigate your claim.

THE CAUSES OF REGIONAL SEA-LEVEL CHANGE

SINCE 1993

THE CAUSES OF REGIONAL SEA-LEVEL CHANGE

SINCE 1993

Dissertation

for the purpose of obtaining the degree of doctor

at Delft University of Technology

by the authority of the Rector Magnificus prof.dr.ir. TH.J.J. van der Hagen,

chair of the Board of Doctorates,

to be defended publicly on [Thursday 15 June 2023 at 15:00 o'clock]

by

Carolina MACHADO LIMA DE CAMARGO

Master of Science in Marine and Lacustrine Science and Management,

Universiteit Gent, België

born in São Paulo, Brazil.

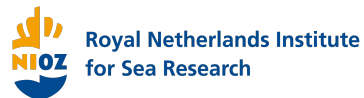
This dissertation has been approved by the promotor.

Composition of the doctoral committee:

Rector Magnificus,	chairperson
Prof. dr. L.L.A. Vermeersen	Delft University of Technology & NIOZ, promotor
Dr. R.E.M. Riva	Delft University of Technology, promotor
Dr. ir. A.B.A. Slangen	NIOZ, copromotor

Independent members:

Dr. A. Meleter	Mercator Ocean Int.
Prof. dr. S.S. Drijfhout	University of Utrecht & KNMI
Prof. dr. -ing. habil R. Klees	Delft University of Technology
Prof. dr. B.J.J.M van den Hurk	VU Amsterdam
Prof. dr. ir. S.G.J. Aarninkhof	Delft University of Technology, reserve member



This research was funded by the Netherlands Space Office User Support program (grant no. ALGWO.2017.002).

Keywords: sea-level change, sea-level variability, sea-level budget, observations

Printed by: Gildeprint

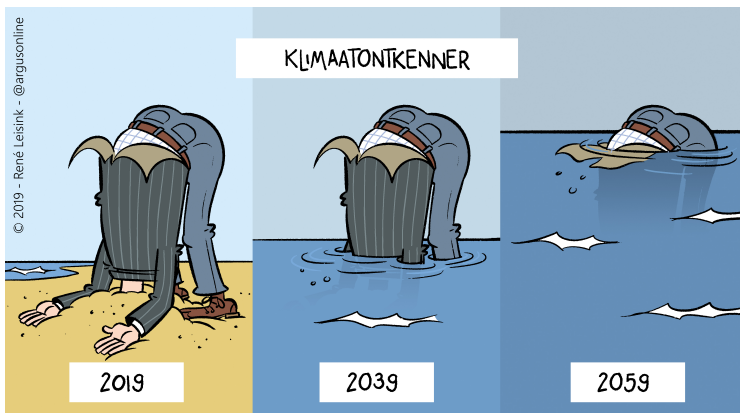
Front & Back: Cover art by Carolina Camargo.

This thesis is printed on recycled paper

Copyright © 2023 by C.M.L. Camargo

ISBN 978-94-6419-821-8

An electronic version of this dissertation is available at
<http://repository.tudelft.nl/>.



Reproduced with permission from René Leisink ©

It's better to know some of the questions, than all of the answers.

R. J. Palacio, Wonder

CONTENTS

Summary	xi
Samenvatting	xv
Resumo	xix
1 Introduction	1
1.1 Total sea-level change	3
1.2 The drivers of sea-level change	7
1.3 The sea-level budget	11
1.4 Uncertainties in sea-level studies	20
1.5 This thesis	22
2 Steric Sea-level Change	25
2.1 Introduction	26
2.2 Methods and Data	28
2.3 Global mean steric sea-level change	32
2.4 Regional steric sea-level change.	38
2.5 Discussion	44
2.6 Conclusion	48
2.7 Supplementary information	50
2.8 Appendix: The deep ocean steric contribution	60
3 Mass-driven Sea-level Change	65
3.1 Introduction	66
3.2 Data and Methodology	68
3.3 Results	77
3.4 Discussion	88
3.5 Supplementary Information	91
4 Regional Sea-level Budget	103
4.1 Introduction: The sea-level budget	104

4.2	Data and methods	105
4.3	Identifying Domains of Sea-Level Variability	114
4.4	The Regional Sea-Level Budget on Different Spatial Scales	117
4.5	Discussion & Conclusions.	125
4.6	Supplementary Information	128
5	Conclusions & perspectives	139
5.1	Main Findings.	139
5.2	Potential Applications.	144
5.3	Societal Implications	153
5.4	Communicating uncertainties, a reflection	155
5.5	New satellites, new possibilities.	156
	Bibliography	159
	Data Statements	183
	Acknowledgements	185
	List of Publications	187
	Outreach Videos	189
	Curriculum Vitæ	191

SUMMARY

As a result of climate change, sea level is changing all over the world at unprecedented rates. Sea-level change can have significant impacts on coastal communities, infrastructure and global economy, as most of the major cities are located near to or at the coast. Rising sea levels can lead to, for instance, more severe and more frequent flooding, increasing coastal erosion and salt water intrusion. In addition, sea-level change can also influence coastal ecosystems, by altering the habitats of many plant and animals species. Therefore, it is crucial that we understand what is causing sea-level change and at what rate sea levels are changing.

Global mean sea level has been rising at a rate of about 3.4 millimetres per year over the last 30 years. Regionally, however, sea level can be changing at a much higher or lower rate. That is because local processes, such as ocean dynamics and gravitational effects associated with continental ice mass changes, cause regional deviations from the global average. But what is causing sea level to change at a specific location? Is sea level changing because the oceans are warming, and thus expanding? Or because the ice from glaciers and ice sheets are melting? The attribution of sea-level change to these and other drivers can be done using a sea-level budget approach. Sea-level budget studies can be used to constrain missing or poorly known contributions and to validate climate models. While the global mean sea-level budget is considered closed within uncertainties, closing the budget on a regional to local scale is still challenging.

In this thesis, I focused on the question: **Can we close the regional sea-level budget in the satellite altimetry era on a sub-basin scale consistently for the entire world?** For this, we need not only high quality observations of sea-level change and each component, but also of the uncertainties within each process. Therefore, in Chapter 2 and 3, I explored the main drivers of regional sea-level change, focusing on the uncertainty characterization of each component. I then looked at which spatial scale is optimal for analysing the regional sea-level budget, and compared the sum of the drivers with the total observed change in these regions in Chapter 4.

Density-driven sea-level change

Variations in the temperature and salinity of the oceans lead to density-driven changes in sea level, known as steric sea-level change. Steric variations are therefore a reflection of the oceans response to global warming. Several recent studies have quantified the steric contribution to global mean and regional sea-level change. However, the reported rates differ significantly between studies. In **Chapter 2**, I looked at how the value of steric sea-level change varies depending on the different temperature and salinity used. I also investigated how different methods (noise models) used to describe the uncertainties and obtain the rate of change can be another source of differences. I found that the rate of change for the global mean varied up to 2 millimetres per year as a result of different datasets and methods used. Regionally, differences reached up to several tens of millimetres per year. I then presented a method for choosing the best noise model for each region, showing that that the noise models should always be carefully chosen, so that the rate of regional change is accurately estimated.

Mass-driven sea-level change

The mass loss from Antarctica, Greenland and glaciers, and other variations in land water storage cause mass-driven sea-level changes, and is one of the main drivers of present-day sea-level change. While many studies have quantified the mass-driven contribution to global mean sea-level change, fewer works have looked into regional changes. In **Chapter 3**, I analysed the regional patterns of mass-driven sea-level change since 1993, the beginning of the satellite altimetry era, considering a range of datasets of the individual freshwater sources. Combining all the contributions leads to negative sea-level trends close to the ice sheets, and positive and increasing trends towards lower latitudes. This pattern is a reflection of the Gravitational-Rotational-Deformational (GRD) effect, which is marked by a sea-level rise in the far-field and by a sea-level fall close to the source of mass change. I determine the uncertainties of these sea-level changes in detail, considering different types of errors: intrinsic (the uncertainty from the data/model itself); temporal (related to the temporal variability in the time series); and spatial-structural (related to the spatial distribution of the mass change sources). I found that the main sources of uncertainty were the temporal correlation of the land water storage observations, and the datasets used for Antarctica and land water storage components. Our findings revealed the importance of clearly quantifying the uncertainties to obtain significant mass-driven sea-level change trends.

The regional sea-level budget

Sea-level change is mainly caused by variations in the ocean's temperature and salinity (Chapter 2) and mass changes (Chapter 3). After having computed estimates of these contributions and their uncertainties to regional sea-level change, I performed a budget assessment in **Chapter 4**. First, I identified the ideal spatial resolution at which we can close the sea-level budget, considering the uncertainties and limitations of the observations. To do so, I applied two machine learning approaches, namely Self-Organizing Maps and δ -Maps, to extract regions of coherent sea-level variability. These regions reduced the observational uncertainty which limited the regional sea-level budget so far, and highlighted how large-scale ocean circulation controls regional sea-level change. Using these regions I was able to close the sub-basin sea-level budget during the satellite altimetry era for almost the entire ocean. In this chapter I showed that the use of the budget approach in combination with machine learning techniques leads to new insights into regional sea-level variability and its drivers. I found that the steric variations dominated the temporal sea-level variability and determined a significant part of the total regional change. Sea-level change due to mass transport between ocean and land had a relatively homogeneous contribution to all regions, when compared with the other components. The ocean dynamic component was significant in highly energetic ocean regions, such as the Gulf Stream region. Regions where the budget could not be closed highlight processes that are affecting sea level but are not well captured by the observations, such as the influence of western boundary currents.

This thesis focused on understanding the regional processes driving present-day sea-level change, that is, assessing the regional sea-level budget since 1993. Specifically, I investigated if the sum of the processes can explain the spatio-temporal rate of sea-level change observed from satellite altimetry. I performed this assessment on a sub-basin scale consistently for the entire world. Focusing on uncertainty characterization, I showed the importance of considering autocorrelations and more than one dataset when estimating the sea-level trends. I could close the regional sub-basin sea-level budget on almost all ocean regions, which was an improvement from previous regional sea-level budget studies. As discussed in **Chapter 5**, the budget analysis has the potential to inform on more uncertain contributions to sea-level change, evaluate sea-level projections and be used as a first step towards more local budget assessments.

SAMENVATTING

Als gevolg van klimaatverandering verandert de zeespiegel over de hele wereld in een ongekend tempo. Veranderingen in de zeespiegel kunnen aanzienlijke gevolgen hebben voor kustgemeenschappen, infrastructuur en de wereldeconomie, aangezien de meeste grote steden dicht bij of aan de kust liggen. Een stijgende zeespiegel kan bijvoorbeeld leiden tot ernstigere en frequentere overstromingen, toenemende kusterosie en verzilting. Bovendien kan verandering van de zeespiegel ook kustecosystemen beïnvloeden, doordat het leefgebied van veel plant- en diersoorten zal veranderen. Daarom is het van groot belang dat we begrijpen waardoor de zeespiegel verandert en in welk tempo dat gebeurt.

De wereldgemiddelde zeespiegel is de afgelopen 30 jaar met ongeveer 3,4 millimeter per jaar gestegen. Regionaal kan de zeespiegel echter veel meer of minder veranderen. Dat komt doordat lokale processen, zoals oceaandynamiek en zwaartekrachteffecten die samenhangen met veranderingen in ijsmassa op de continenten, regionale afwijkingen van het wereldgemiddelde veroorzaken. Maar waardoor verandert de zeespiegel op een specifieke locatie? Verandert de zeespiegel doordat de oceanen opwarmen en dus uitzetten? Of doordat gletsjers en ijskappen aan het smelten zijn? Het toeschrijven van bepaalde veranderingen in het zeeniveau aan de verschillende oorzaken kan worden gedaan met behulp van een zogenaamde budgetbenadering van de zeespiegelverandering. Budgetstudies van de zeespiegel kunnen worden gebruikt om ontbrekende of slecht bekende bijdragen aan zeespiegelverandering nauwkeuriger te schatten en om klimaatmodellen te valideren. Hoewel het budget van de wereldgemiddelde zeespiegel binnen de onzekerheidsmarges als gesloten kan worden beschouwd, is het sluiten van het budget op regionale tot lokale schaal nog steeds een uitdaging.

In dit proefschrift heb ik me gericht op de vraag: **Kunnen we het zeeniveaubudget in het tijdperk van satellietmetingen consistent sluiten op regionale schaal, voor de hele wereld?** Hiervoor hebben we niet alleen observaties van hoge kwaliteit nodig van de verandering in zeespiegel en elk onderdeel van die verandering, maar ook van de onzekerheden binnen elk proces. Daarom heb ik in Hoofdstuk 2 en 3 de belangrijkste oorzaken van regionale zeespiegelveranderingen onderzocht, en daarbij de nadruk gelegd

op het zorgvuldig beschrijven van de onzekerheid in elke component. Vervolgens heb ik gekeken welke ruimtelijke schaal optimaal is voor het analyseren van het regionale zeespiegelbudget, en heb ik in Hoofdstuk 4 de som van de componenten vergeleken met de totale waargenomen zeespiegelverandering in deze regio's.

Zeespiegelverandering veroorzaakt door veranderingen in de dichtheid

Variaties in de temperatuur en het zoutgehalte van de oceanen leiden tot veranderingen in de dichtheid van het zeewater, waardoor het water krimpt of uitzet en de zeespiegel daalt of stijgt. Dit wordt ook wel sterische zeespiegelverandering genoemd. Sterische veranderingen zijn daarom een weerspiegeling van de reactie van de oceanen op de opwarming van de aarde. Verschillende recente studies hebben de sterische bijdrage aan de verandering van het wereldgemiddelde en de regionale zeespiegel gekwantificeerd. De gerapporteerde percentages verschillen echter aanzienlijk tussen studies. In **Hoofdstuk 2** heb ik gekeken naar hoe de mate van sterische zeespiegelverandering varieert, afhankelijk van de verschillende gebruikte temperaturen en zoutgehalten. Ik heb ook onderzocht hoe verschillende methoden (ruismodellen) die worden gebruikt om de onzekerheden te beschrijven en de snelheid van zeespiegelverandering te berekenen, een andere bron van verschillen kunnen zijn. Ik heb gevonden dat de snelheid van de wereldgemiddelde zeespiegelverandering tot wel 2 millimeter per jaar kan verschillen als gevolg van het gebruiken van verschillende datasets en methoden. Regionaal liepen de verschillen op tot enkele tientallen millimeters per jaar. Vervolgens heb ik een methode gepresenteerd voor het kiezen van het beste ruismodel voor elke regio, waarbij ik heb aangetoond dat het belangrijk is om de ruismodellen altijd zorgvuldig te kiezen, zodat de snelheid van regionale verandering nauwkeurig wordt geschat.

Zeespiegelverandering door massaverlies

Het smelten van Antarctica, Groenland en gletsjers, en andere variaties in de hoeveelheid water die op het land wordt vastgehouden, veroorzaken massa-gedreven zeespiegelveranderingen en behoren tot de belangrijkste oorzaken van de recente zeespiegelverandering. Hoewel veel studies de massa-gedreven bijdrage aan de wereldwijd gemiddelde verandering van de zeespiegel hebben gekwantificeerd, hebben minder studies gekeken naar regionale veranderingen. Daarom heb ik in **Hoofdstuk 3** de regionale patronen geanalyseerd van de door massaveranderingen veroorzaakte zeespiegelveranderingen sinds 1993, d.w.z., vanaf het begin van satellietmetingen, rekening houdend met een reeks datasets van de individuele zoetwaterbronnen. Door alle bijdragen te combineren, werden dicht bij de ijskappen dalende zeespiegeltrends gevonden, en steeds sterker stijgende trends in de richting van lagere breedtegraden. Dit patroon is een weerspiegeling

van het zwaartekracht-rotatie-deformatie-effect (GRD), dat wordt gekenmerkt door een zeespiegelstijging ver weg van, en een zeespiegeldaling dichtbij de bron van massaverlies. Ik bepaal de onzekerheden van deze zeespiegelveranderingen in detail, rekening houdend met verschillende soorten onzekerheid: intrinsiek (de onzekerheid in de data/het model zelf); temporeel (gerelateerd aan de temporele variabiliteit in de tijdreeks); en ruimtelijk-structureel (gerelateerd aan de ruimtelijke verdeling van de bronnen van massaverandering). Ik heb ontdekt dat de belangrijkste bronnen van onzekerheid de temporele correlatie waren van waarnemingen van de hoeveelheid water opgeslagen op het land, en de datasets die worden gebruikt voor het schatten van de bijdrage van Antarctica en de opslag van water op land. Onze bevindingen onthullen het belang van het duidelijk kwantificeren van de onzekerheden om significante massa-gedreven trends in zeespiegelveranderingen te bepalen.

Het regionale zeespiegelbudget

Veranderingen in de zeespiegel worden voornamelijk veroorzaakt door variaties in de temperatuur en het zoutgehalte van de oceaan (Hoofdstuk 2) en massaveranderingen (Hoofdstuk 3). Na het maken van schattingen van deze bijdragen en hun onzekerheden voor regionale zeespiegelveranderingen, heb ik in **Hoofdstuk 4** het zeespiegelbudget geanalyseerd. Eerst heb ik de ideale ruimtelijke resolutie geïdentificeerd waarop we het zeeniveaubudget kunnen sluiten, rekening houdend met de onzekerheden in en beperkingen van de waarnemingen. Om dit te doen, heb ik twee machine learning methodes toegepast, namelijk Self-Organizing Maps en δ -Maps, om regio's met coherente temporele variabiliteit in zeespiegel te identificeren. Door de zeespiegelverandering in deze regio's te middelen neemt de waarnemingsonzekerheid af, die tot nu toe het regionale zeeniveaubudget bemoeilijkte, en wordt benadrukt hoe de grootschalige oceaancirculatie de regionale zeespiegelveranderingen bepaalt. Met behulp van deze regio's waren we in staat om het zeespiegelbudget te sluiten op ruimtelijke schalen kleiner dan oceaانبekkens sinds 1993 in bijna alle delen van de oceaan. In dit hoofdstuk heb ik laten zien dat het gebruik van de budgetbenadering in combinatie met machine learning-technieken leidt tot nieuwe inzichten in regionale zeespiegelvariabiliteit en de oorzaken daarvan. Ik heb ontdekt dat de sterische variaties de temporele variabiliteit in zeeniveau domineerden en een aanzienlijk deel van de totale regionale verandering bepaalden. Veranderingen in de zeespiegel als gevolg van het verschuiven van massa tussen oceaan en land hadden een ruimtelijk relatief homogene bijdrage aan alle regio's in vergelijking met de andere componenten. De dynamische component was significant in hoogenergetische oceaangebieden, zoals het Golfstroomgebied. Regio's waar het budget niet kon worden gesloten, wijzen op processen die van invloed zijn op de zeespiegel, maar die niet goed worden weergegeven

door de waarnemingen, zoals de invloed van westelijke grensstromingen.

Dit proefschrift was gericht op het begrijpen van de regionale processen die de huidige veranderingen in de zeespiegel veroorzaken, dat wil zeggen, het beoordelen van het regionale zeespiegelbudget sinds 1993. Ik heb met name onderzocht of de som van de individuele bijdrages van verschillende processen die met satelliethoogtemetingen waargenomen ruimtelijk-temporele snelheid van zeespiegelverandering kan verklaren. Ik heb deze beoordeling consistent uitgevoerd op een schaal kleiner dan oceanbekkens, voor de hele wereld. Door me te richten op de karakterisering van onzekerheid, heb ik laten zien hoe belangrijk het is om autocorrelaties en meer dan één dataset in overweging te nemen bij het schatten van de zeespiegeltrends. Ik heb het regionale zeeniveaubudget op schalen kleiner dan oceanbekkens kunnen sluiten voor bijna alle oceanregio's, wat een verbetering is ten opzichte van eerdere regionale zeeniveaubudgetonderzoeken. Zoals besproken in **Hoofdstuk 5**, heeft de budgetanalyse potentie om informatie te verschaffen over meer onzekere bijdragen aan de verandering van de zeespiegel, om zeespiegelprojecties te evalueren en om gebruikt te worden als een eerste stap richting lokalere budgetbeoordelingen.

RESUMO

Devido às mudanças climáticas, o nível do mar está mudando em todo o mundo com taxas nunca vistas antes. A mudança do nível do mar pode ter impactos significativos nas comunidades costeiras, na infraestrutura e na economia global, já que a maioria das grandes cidades está localizada perto ou na costa. O aumento do nível do mar pode causar, por exemplo, inundações mais severas e frequentes, aumentando a erosão costeira e a intrusão de água salgada. Além disso, a mudança do nível do mar também pode influenciar os ecossistemas costeiros, alterando os habitats de muitas espécies de plantas e animais. Portanto, é crucial entendermos o que está causando a mudança no nível do mar e a que taxa o nível do mar está mudando.

A média global do nível do mar tem subido a uma taxa de cerca de 3,4 milímetros por ano nos últimos 30 anos. Regionalmente, entretanto, o nível do mar pode estar mudando a uma taxa muito maior ou menor. Isso porque processos locais, como a dinâmica dos oceanos e efeitos gravitacionais associados ao derretimento gelo continental, causam desvios regionais da média global. Mas qual fator causa a mudança do nível do mar em um local específico? Seria por que a temperatura dos oceanos está subindo, e conseqüentemente o oceano expande? Ou por que o gelo das calotas polares está derretendo? A atribuição da mudança do nível do mar a esses e outros fatores pode ser feita usando uma abordagem de balanço do nível do mar. Os estudos de balanços do nível do mar podem ser usados para informar quais processos estão faltando ou mal descritos, e para validar os modelos climáticos. Apesar de sabermos quais são os fatores alterando a média global do nível do mar, explicar estes fatores em escala regional e local ainda é um desafio.

Nesta tese, eu foquei na questão: **É possível explicar o balanço do nível do mar nos últimos 30 anos em uma escala regional consistente para todo o mundo?** Para isso, é necessário não apenas observações de alta qualidade da mudança e dos fatores causando a mudança do nível do mar, mas também das incertezas de cada processo. Nos Capítulos 2 e 3, eu explorei os principais fatores que causam a mudança regional do nível do mar, com foco na caracterização da incerteza de cada componente. Em seguida, eu analisei qual é a escala espacial ideal para explicar o balanço regional do nível do mar, e comparei a mudança total com cada fator que causa mudanças regionais no Capítulo 4.

Mudança do nível do mar causada por variações de densidade

As variações na temperatura e na salinidade dos oceanos levam a mudanças no nível do mar causadas por variações na densidade dos oceanos, conhecidas como mudanças estéricas do nível do mar. As variações estéricas são, portanto, um reflexo da resposta dos oceanos ao aquecimento global. Vários estudos quantificaram a contribuição estérica para a mudança média global e regional do nível do mar. No entanto, as taxas relatadas diferem significativamente entre os estudos. No **Capítulo 2**, eu analisei como o valor da variação estérica do nível do mar pode variar dependendo de qual dado de temperatura e salinidade é usado. Eu também investiguei como diferentes métodos usados para descrever as incertezas e obter a taxa de variação podem ser outra fonte de diferenças. Eu descobri que a taxa de variação da média global pode variar até 2 milímetros por ano como resultado de diferentes conjuntos de dados e métodos usados. Regionalmente, as diferenças podem chegar a várias dezenas de milímetros por ano. Finalmente, eu apresentei então um método para escolha do melhor modelo para cada região, mostrando que estes devem sempre ser escolhidos com cuidado, para que a taxa de variação regional seja estimada com precisão.

Mudança do nível do mar causada por variações de massa

O derretimento de gelo da Antártica, da Groenlândia e das geleiras, e outras variações no armazenamento de água terrestre causam mudanças no nível do mar impulsionadas por variações na massa dos oceanos. Estas variações um dos principais fatores causando elevação do nível do mar. Embora muitos estudos tenham quantificado a contribuição de variações de massa para a mudança do nível médio global do mar, poucos trabalhos analisaram as mudanças regionais. No **Capítulo 3**, eu analisei as mudanças regionais do nível do mar causada por variações de massa desde 1993, o início da era da altimetria por satélite, considerando uma variedade de fontes individuais de água continental. A combinação de todas as contribuições leva a tendências negativas do nível do mar próximas aos mantos de gelo (Antártica e Groenlândia), e tendências crescentemente positivas em direção a latitudes mais baixas. Este padrão é um reflexo do efeito Gravitacional-Rotacional-Deformacional (GRD) da Terra, que é marcado por um aumento do nível do mar longe das fontes de variações de massa, e por uma queda do nível do mar perto da fonte de mudança de massa. Neste capítulo, eu determinei detalhadamente as incertezas dessas variações do nível do mar, considerando diferentes tipos de erros: intrínsecos (a incerteza do próprio dado/modelo); temporal (relacionado à variabilidade temporal na série de dados); e espacial-estrutural (relacionado à distribuição espacial das fontes de mudança de massa). Eu descobri que as principais fontes de incerteza são devido a correlação temporal das observações de armazenamento de água no continente, e

em segundo lugar dos conjuntos de dados usados para a Antártica e as águas terrestres. Nossos resultados mostram a importância de quantificar claramente as incertezas para obter tendências significativas de mudança do nível do mar impulsionadas por variações de massa.

O balanço regional do nível do mar

As mudanças do nível do mar são causadas principalmente por variações na temperatura e salinidade do oceano (Capítulo 2) e mudanças na massa dos oceanos (Capítulo 3). Depois de calcular as estimativas dessas contribuições e suas incertezas, eu avaliei o balanço regional do nível do mar no **Capítulo 4**. Primeiro, eu identifiquei a resolução espacial ideal na qual podemos explicar o balanço do nível do mar, considerando as incertezas e limitações das observações. Para fazer isso, eu apliquei duas abordagens de inteligência artificial, nominalmente, as técnicas "Self-organizing Maps" e " δ -Maps", para extrair regiões coerentes de variabilidade do nível do mar. O uso dessas regiões reduz a incerteza observacional que limitava o balanço regional do nível do mar até então, além de destacar como a circulação oceânica em grande escala controla a mudança regional do nível do mar. Usando essas regiões, eu pude fechar o balanço do nível do mar desde 1993 (período da altimetria por satélite) numa escala de sub-bacias para quase todo o oceano. Neste capítulo, eu mostrei que o uso da abordagem de balanço do nível do mar em combinação com técnicas inteligência artificial traz novos insights sobre a variabilidade regional do nível do mar e suas causas. Eu descobri que as variações estéricas dominaram a variabilidade temporal do nível do mar e determinaram uma parte significativa da mudança regional total. A variação do nível do mar devido ao transporte de massa entre oceano e terra teve uma contribuição relativamente homogênea para todas as regiões, quando comparada com os outros componentes. A contribuição da dinâmica dos oceanos foi significativa em regiões oceânicas altamente energéticas, como a região da Corrente do Golfo. As regiões onde o balanço não pôde ser fechado destacam processos que afetam o nível do mar que não são bem captados pelas observações, como a influência de fortes correntes oceânicas.

Esta tese centrou-se na compreensão dos processos regionais que impulsionam a mudança do nível do mar nos dias de hoje, ou seja, na avaliação do balanço regional do nível do mar desde 1993. Especificamente, eu investiguei se a soma dos processos pode explicar a taxa de mudanças do nível do mar observada por satélite. Eu realizei esta avaliação em uma escala de sub-bacia consistentemente para todo o mundo. Com foco nas incertezas das observações, eu mostrei a importância de considerar autocorrelações e mais de um conjunto de dados ao estimar as tendências do nível do mar. Eu pude fechar

o balanço regional do nível do mar, numa escala de sub-bacia, em quase todas as regiões oceânicas, o que foi uma melhoria em relação aos estudos anteriores. Conforme discutido no **Capítulo 5**, este tipo de análise regional tem o potencial de trazer informações sobre os processos mais incertos que contribuem para a mudança do nível do mar, além de poder avaliar as projeções do nível do mar e ser usada como um primeiro passo para estudos locais.

1

INTRODUCTION



Oceans and Climate

The Earth's climate and oceans are complex and intrinsically coupled systems. Both are continuously varying on different timescales and affecting each other. On one hand, the oceans can be leading the dance, controlling the climate system (Siedler et al., 2013). For example, the circulation of the Atlantic Ocean is responsible for carrying heat from low latitude to the poles, which during the winter is the main source of heat in Northern Europe, compensating for the lack of solar radiation and making the region more hospitable (Broecker, 1997). There is also strong evidence that the thermohaline circulation was the primary trigger of the last ice age (Broecker, 2003; Stewart, 2008). On the other hand, climate variations can lead to changes in the oceans. For example, climate fluctuations can affect the strength and position of ocean currents, as well as changes in ocean stratification and heat budget (Talley et al., 2011). Additionally, climate variations can trigger changes in the volume of the oceans, as sea level rises and falls in response to changes in global temperature.

Sea-level change

Sea-level rise, one of the main consequence of global warming, has been identified a major threat of the upcoming century and beyond (Fox-Kemper et al., 2021). Most of the major cities worldwide are located at or close to the coast (Neumann et al., 2015). About 2.8 billion people, more than 1/3 of the world population, live within 100km from the coast (Maul and Duedall, 2019), and about 600 million people currently live in low elevation coastal zones (McGranahan et al., 2007; Nicholls et al., 2021), that is about one in every ten people on Earth. As sea level rises, these low-elevation areas will become permanently and irreversibly inundated, becoming uninhabitable and instigating human migration (Hauer et al., 2019). Even considering a future low carbon emissions scenario, about 190 million people currently live in areas that will be below high tide in 2100 (Kulp and Strauss, 2019). Sea-level rise also threatens coastal agriculture and aquaculture, drinking water supplies, fisheries and other ecosystem services (Hauer et al., 2019). It is therefore imperative to have a good understanding of sea-level change and its contributing processes.

Global mean sea level has been rising at a rate of $1.7 \pm 0.4 \text{ mm yr}^{-1}$ in the 20th century mainly due to ocean warming, which results in thermal expansion, and due to the melt of continental ice (Fox-Kemper et al., 2021). However, sea level does not change at the same rate all over the world, and regions can experience a smaller or larger sea-level change than the global average due to local processes. For example, while some locations have experienced less than 2 mm yr^{-1} over the last two decades, other coastal cities, like Jakarta, experienced a sea-level rise above 10 mm yr^{-1} (Nicholls et al., 2021). Understanding the

regional variability of the processes driving sea-level change is critical for identifying missing or misrepresented contributions, constraining sea-level projections, and to better prepare for the impacts of climate change.

But how much do the different processes (e.g., ocean warming and land ice melt) contribute to regional and local sea-level change? The attribution of sea-level change to its drivers can be studied by setting up a sea-level budget. Sea-level budgets can also be used to constrain missing or poorly known contributions and to validate climate models (Cazenave et al., 2018). While the global mean sea-level budget is considered closed within uncertainties (e.g., Cazenave et al., 2018; Frederikse et al., 2020), closing the budget on a regional, sub-basin scale, is still challenging. **In this thesis, this gap is filled by exploring the regional (sub-basin) sea-level budget in the satellite altimetry era (1993-present).**

In this chapter, I first introduce total sea-level change (Section 1.1) and its driving processes (Section 1.2). I then give an overview of the state-of-art of the sea-level budget (Section 1.3). I finalize this chapter introducing uncertainties in sea-level observations (Section 1.4), and with the outline of this thesis (Section 1.5).

1.1. TOTAL SEA-LEVEL CHANGE

Total sea-level change can be measured either by tide gauges or satellite altimetry, and both methods can be combined to reconstruct total global mean sea-level change (Bradshaw et al., 2015). The long records of tide gauges, some dating back to the 19th century, allow for century-long sea-level reconstructions. However, tide gauges provide local observations at the coast and have an uneven spatial distribution, with most stations historically located in the Northern Hemisphere (Woodworth et al., 2011). Consequently, they provide limited information of the spatial variability of sea-level change. Complementary to tide gauges is satellite radar altimetry, which has been registering sea surface height almost continuously with a virtually global coverage since 1992 (Ablain et al., 2017). While altimetry observations cannot be used for century-long sea-level reconstructions, they provide vital information on regional patterns of sea-level variations (Woodworth et al., 2011). In this thesis, the sea-level budget analysis uses satellite altimetry observations.

MEASURING TOTAL SEA-LEVEL CHANGE

Satellite altimetry missions measure the distance between the satellite and the ocean surface (Figure 1.1), known as the altimeter range (R). In order for those observations to be useful for sea level studies, they need to be converted into sea surface height (η), and referred to a well-defined reference surface. Usually, this reference surface is represented by an ellipsoid, a three-dimensional figure that approximates the Earth's shape, centred at the centre of mass of the Earth (Gregory et al., 2019; Angermann et al., 2022). Precise tracking systems, such as GPS, DORIS and satellite laser ranging, are employed to reference the altitude of the satellite orbit (H) to a fixed coordinate system.

The satellite carries a radar altimeter which emits a short pulse of microwave radiation. When the pulse reaches the sea surface, part of the radiation is reflected back to the altimeter. The travel time between the satellite and the sea surface determines the altimeter range (R), which is a relative measure of the distance between the satellite orbit and the sea surface topography. A set of corrections needs to be applied to R to compensate for biases from the interaction of the pulse with the atmosphere and the sea surface (e.g., sea-state bias and dry atmosphere correction, Andersen and Scharroo, 2011; Passaro et al., 2018). Once the altitude of the satellite above the reference ellipsoid (H) and the altimeter range (R) are known, it is possible to compute the geocentric, or absolute, sea surface height ($\eta_{geo(satellite)}$):

$$\eta_{geo(satellite)} = H - R. \quad (1.1)$$

Satellite altimeters, however, do not measure the height of the water column with respect to a terrestrial landmark. This quantity, known as relative sea surface height (h), is obtained from tide gauges or ocean models outputs. Relative sea-level depends on the height of the Earth's surface in relation to the ellipsoid (F), which is affected by vertical land motion (VLM) changes, such as land subsidence and tectonics (Wöppelmann and Marcos, 2015). On the other hand, geocentric sea-level measurements can not differentiate if the change is either from the solid Earth or the ocean. The relationship between geocentric and relative sea-level change, illustrated in Figure 1.1, is:

$$\eta_{geo(satellite)} = h + F. \quad (1.2)$$

The comparison between the sea surface height from satellite and tide gauge records is used to calibrate and correct the satellite measurements (Mitchum, 2000). For example, a significant drift error on the calibration of TOPEX A altimeter was discovered by compar-

ing the altimeter observations with tide gauge records (Watson et al., 2015). Applying an improved drift correction caused a reduction of 0.26 mm yr^{-1} to the global mean sea level trend from 1993 to 2018 (Ablain et al., 2019). Incorporating corrections to these systematic errors, among others, is necessary to obtain a correct sea-level estimate.

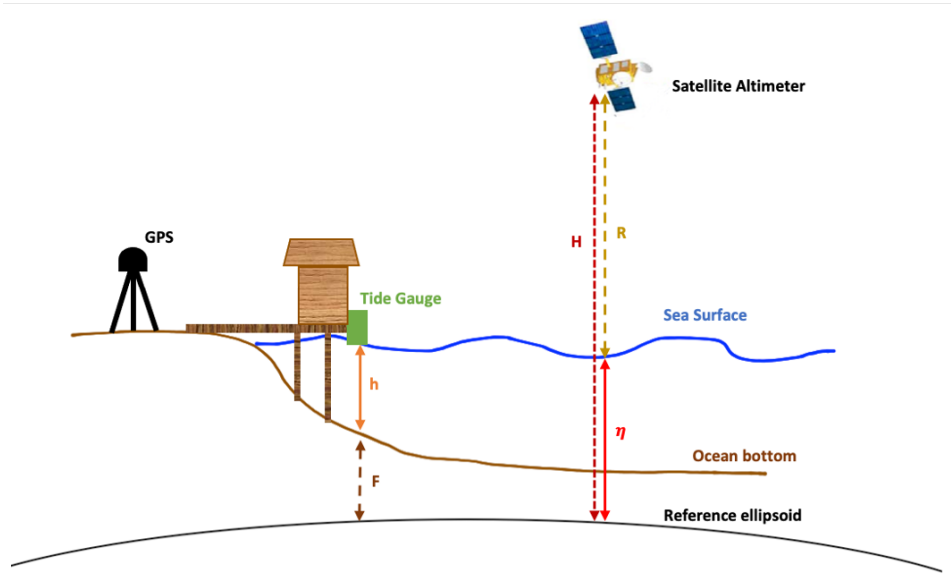


Figure 1.1: Sketch of the different sea-level observations and instruments. H is the vertical distance between the satellite and the reference ellipsoid; R is the range between the satellite and the sea surface. η is the geocentric sea level, given by the difference between the satellite altitude H and satellite range R , as shown in equation 1.1; F is the position of the solid earth surface with reference to the ellipsoid; and h is the relative sea level, obtained from tide gauges. Ideally, the tide gauge station has a collocated GPS antenna, to provide an accurate benchmark of VLM (Ponte et al., 2019).

THE SATELLITE ALTIMETRY ERA

The satellite altimetry era (Figure 1.2), from 1992 until present, is characterized by high-precision and high spatial and temporal resolution sea-level measurements, provided mainly by satellite radar altimeters (Ablain et al., 2017). The first high-precision satellite-based sea surface height measurements were obtained with the radar altimeter TOPEX/-Poseidon (T/P), launched in August of 1992 and marked the beginning of the satellite era of sea-level studies. Covering the Earth's surface from 66°N to 66°S , with a 10-day repeat orbit, groundtrack spacing of approximately 300 km at the Equator and with high-accuracy orbit determination, the T/P satellite provided 1 Hz altimetry measurements for almost 13 years (Woodworth et al., 2011). Following the same orbit as the T/P mission (i.e., same spatial coverage and repeat period), the Jason satellite series (Jason-1, 2, 3)

continued to provide high-resolution measurements, with increasing precision (Abdalla et al., 2021). Each mission had an overlap period with the previous one, guaranteeing calibration and stability of these so-called reference missions (Figure 1.2a, green bars). The recently launched Sentinel-6 mission has inherited the T/P orbit, assuring the continuity of the reference record (Abdalla et al., 2021; Donlon et al., 2021). These reference missions provide the most accurate and stable altimetry record (Cazenave et al., 2018), with a global mean sea-level change rate of $3.4 \pm 0.4 \text{ mm yr}^{-1}$ for 1993 until 2022 (Figure 1.2b).

Other satellite radar altimeters with different orbits (Figure 1.2a, light brown bars) have provided complementary observations to the reference missions, increasing the spatial coverage and resolution of the altimetry record (Cazenave et al., 2018). For example, CryoSat-2 has an inclination of 92° , providing invaluable measurements of ice sheets and polar regions (Scharroo et al., 2012). The satellite altimetry products used in this thesis (Chapter 4) are multi-mission products, which include both the reference and complementary altimetry missions.

In addition to radar altimetry data, other technologies have also provided cardinal observations during the satellite era, such as laser altimeters and gravimeters (indicated in pink and blue Figure 1.2a, respectively) and Argo floats. For example, the Gravity Recovery and Climate Experiment (GRACE) satellite gravimeter mission (2002-2017) made independent observations of the mass changes over the Earth for the first time, significantly increasing the accuracy of the ocean mass contribution to sea-level change (discussed in Chapter 3 of this thesis). In the early 2000s, the Argo float network was developed (Roemmich et al., 2009). Argo floats autonomously measure ocean temperature and salinity down to 2000m depth, which can be used to estimate the steric contribution to sea-level change (Chapter 2). All of these observations are essential for assessing the sea-level budget on a sub-basin scale (Chapter 4).

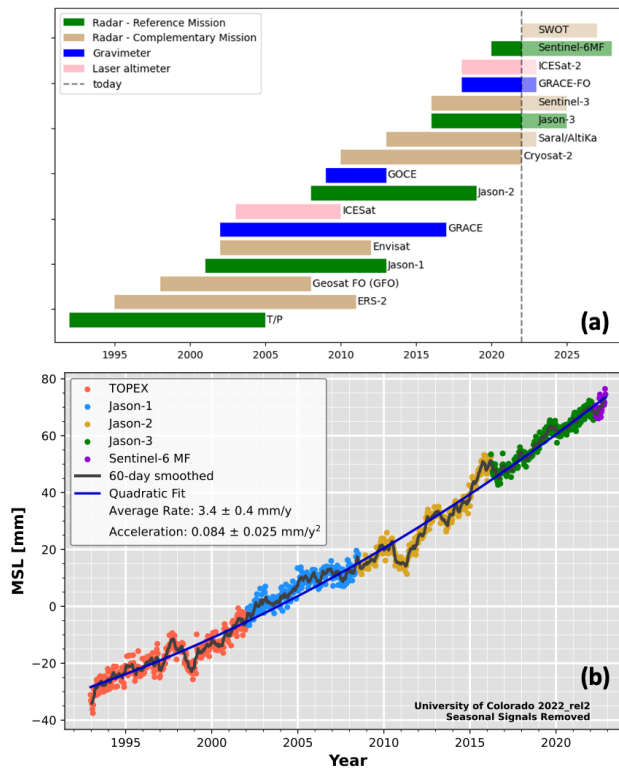


Figure 1.2: (a) Timeline of satellite missions during the satellite altimetry era. Reference radar altimetry missions in green, complementary radar altimetry missions in light brown, laser missions in pink and gravimetry missions in blue. Vertical line indicates the year 2022. After that, the on-going missions are in lighter shade. (b) Global mean sea-level change (mm) based on the reference radar altimetry missions, with seasonal signal removed, corrected for tides and inverted barometer signals. (University of Colorado).

1.2. THE DRIVERS OF SEA-LEVEL CHANGE

Sea-level change is the volumetric expression of variations in ocean's density and/or mass. These variations can be caused by several processes, and depending on the temporal and spatial scale different processes play a role. This is because sea-level change is not equivalent to the water height of a bath tub, which rises all over at the same rate. Local processes cause sea level to change at different rates in different locations around the world (e.g., Stammer et al., 2013). For example, salinity variations are not relevant for the global mean sea-level change, but can have a significant local impact. Another local effect is the loss of gravitational attraction of an ice sheet when it melts, which leads to a sea-level fall in its vicinity. In this section I will explain the main drivers of present-day sea-level change, including the differences between global mean and regional processes.

STERIC SEA-LEVEL CHANGE

One of the main drivers of sea-level change is represented by water density changes. Density-driven sea-level change, known as steric sea-level change, comprises variations in the temperature (thermosteric) and salinity (halosteric) of the oceans, which leads to either expansion (heating/freshening) or contraction (cooling/salinification) of the water (Noerdlinger and Brower, 2007; Talley et al., 2011). Steric sea-level change is expressed by the vertical integration of density changes from a reference depth z_2 to the water surface z_1 :

$$\eta_{steric} = -\frac{1}{\rho_0} \int_{z_2}^{z_1} \rho' dz, \quad (1.3)$$

where ρ_0 is a reference density, and ρ' is the local density anomaly (Gill and Niller, 1973; Tomczak and Godfrey, 2003).

Steric sea-level height can be estimated using different approaches (MacIntosh et al., 2017). First, it can be estimated from in situ observations of temperature and salinity. That includes ship-based hydrographic data, such as conductivity, temperature and depth (CTD) profiles and observations from expendable and mechanical bathythermographs, and observations collected by Argo profiling floats. Additionally, steric sea-level height can also be estimated from ocean reanalyses and models (Storto et al., 2017). Via data assimilation techniques, ocean reanalyses combine the data from ocean models, atmospheric fluxes and ocean observations (MacIntosh et al., 2017).

On a global scale, the steric contribution is dominated by thermal expansion (thermosteric), while salinity variations (halosteric changes) can be neglected (Cazenave et al., 2018). On a regional scale, however, the halosteric component can have a strong impact and even dominate the changes in ocean density. Thus, regional steric sea-level change studies need to account for both salinity and temperature variations (Ponte, 2012).

MASS-DRIVEN SEA-LEVEL CHANGE

Manometric

All sea-level variations not driven by density changes are defined as manometric sea-level change (Gregory et al., 2019). Manometric sea-level change, also referred to as the bottom pressure term (Gregory et al., 2019), comprises changes in sea-level due to the redistribution of ocean mass, both in a passive (η_{GRD}) and dynamic ($\eta_{dynamic}$) ocean:

$$\eta_{manometric} = \eta_{GRD} + \eta_{dynamic}, \quad (1.4)$$

Manometric sea-level change can be obtained from direct measurements of mass movement in the oceans, for instance from the GRACE satellite missions (Chambers et al., 2004). Manometric variations refer to regional sea-level changes. Since dynamic mass redistribution has a negligible global mean, the global mean of $\eta_{manometric}$ equals the global mean of η_{GRD} , which corresponds to the barystatic term.

Barystatic

The integrated response of sea-level change due to the exchange of mass between land and ocean is known as barystatic sea-level change (Gregory et al., 2019):

$$\eta_{barystatic} = \frac{\Delta M}{\rho_f * A}, \quad (1.5)$$

where A is the ocean area, ρ_f is freshwater density and ΔM is the mass variation.

Mass is added into the oceans mainly from continental ice melt from the glaciers and Antarctic and Greenland ice sheets. Variations in water stored in rivers, lakes, wetlands, artificial reservoirs, snow pack, canopy and soil (groundwater), known as land water storage, also cause barystatic sea-level changes. The barystatic term can be obtained from either summing up the observed mass contributions (from Antarctica, Greenland, glaciers and land water storage), or from ocean mass measurements which have been corrected for dynamic effects.

Gravity-Rotation-Deformation (GRD)

When mass is redistributed over the Earth, it causes changes in the Earth's gravity field, Earth's rotation and a viscoelastic deformation of the solid Earth (GRD, Gregory et al., 2019). The GRD component (η_{GRD}) reflects how the mass loss of continental ice stored in glaciers and ice sheets and variations in land water storage results in spatial differences in sea-level change. This spatial pattern that modulates barystatic sea-level change is described by the sea-level equation (Farrell and Clark, 1976; Vermeersen and Sabadini, 1999):

$$\eta_{GRD} = \frac{\rho_i}{g} \phi^G *_{I} I + \frac{\rho_{sw}}{g} \phi^G *_{O} \eta + c, \quad (1.6)$$

where $\rho_{i,sw}$ is the density of ice and ocean, $*_{I,O}$ represents the convolution over the ice and ocean area in both space and time, ϕ^G are the Green's functions, which express how changes of mass over the Earth's surface modify the gravitational potential of the Earth, I represents mass changes over the continents, and η changes in sea level. The results of the sea-level equation are the so-called sea-level fingerprints (Mitrovica et al., 2001). These fingerprints have a characteristic regional pattern: sea-level rise in the far-field and

fall close to the mass source (Mitrovica et al., 2001).

The integrated response of the GRD effect over the oceans, i.e. its global mean, is the barystatic term. Thus, η_{GRD} only plays a role in regional sea-level change. The GRD component can be computed by solving the sea-level equation, using mass changes as an input (as in Chapter 3). The GRD effect can be split between changes due to contemporary mass changes, and due to mass changes since the last ice age, generally known as post-glacial rebound or as glacial isostatic adjustment (GIA).

Glacial Isostatic Adjustment (GIA)

When large amounts of ice accumulate on the continents, the solid Earth underneath is pushed down, due to the weight of the ice. When the ice melts and the weight over the solid Earth is relieved, the crust lifts up again. This deformation has a instantaneous elastic response, and a slow viscous one, on a time scale of millennia and longer (Spada, 2017). This process is known as glacial isostatic adjustment (GIA), and is usually used to refer to the on-going response of the Solid Earth to ice melt after the last ice age.

GIA can trigger changes in sea level and the solid Earth on scales of hundreds of kilometers over tens of thousands of years (Whitehouse, 2018). Locations where extensive ice sheets grew during Last Ice Age, such as Canada, Scandinavia and Antarctica, have a significant present-day land uplift due to GIA. For example, on the east coast of Canada, in the Great lakes region, land is uplifting with a rate of about 8 mm yr^{-1} , and even up to 2 cm yr^{-1} , due to GIA (e.g., Han et al., 2015). Note that, when the ice sheets first melt there is an effect on the total ocean mass. GIA, however, only affects the shape of the ocean surface and of the ocean bathymetry, but not the total ocean mass.

DYNAMIC SEA-LEVEL CHANGE

The dynamic component ($\eta_{dynamic}$) is the sea-level change due to dynamic mass redistribution, caused by ocean circulation, atmospheric pressure and steric expansion and contraction (Landerer et al., 2007). Note that differently than the GRD component, which is the redistribution of added (or removed) ocean mass, $\eta_{dynamic}$ is the redistribution of mass that was already in the oceans. Following Landerer et al. (2007), dynamic sea-level is given by:

$$\eta_{dynamic} = \eta' - \eta'_{steric} + \frac{\overline{p'_a}}{g\rho_0}, \quad (1.7)$$

where η' is the total sea surface height anomaly, η'_{steric} is the steric height anomaly, p_a is the atmospheric pressure, g is the gravitational acceleration on Earth's surface and ρ_0 is the reference density of ocean water. The term $\frac{\overline{p'_a}}{g\rho_0}$ is the barometric term, known as the

inverse barometer effect.

The dynamic sea-level change is part of the ocean dynamic sea-level change ($\Delta\zeta$, Gregory et al., 2019). The latter is the local sea surface height above the geoid (an equipotential surface that approximates the mean sea level of the oceans, Angermann et al., 2022), corrected for the inverse barometer effect (Gregory et al., 2019), and includes the effect of local steric anomalies (η'_{steric}). Thus, the dynamic component can be obtained by removing local steric anomalies from the ocean dynamic component:

$$\eta_{dynamic} = \Delta\zeta - \eta'_{steric}. \quad (1.8)$$

The dynamic component only plays a role on regional to local sea-level change. The dynamic component can be obtained from ocean general circulation models (e.g., Couldrey et al., 2021), coupled climate models (e.g., Levermann et al., 2005), ocean reanalyses (e.g., Dangendorf et al., 2021; Wang et al., 2021b) and estimated with simple redistribution models (e.g., Landerer et al., 2007).

OTHER LOCAL PROCESSES

In addition to the processes discussed above, regional and local sea-level change is also affected by winds and atmospheric pressure (Stammer et al., 2013). For example, on an annual timescale, atmospheric pressure changes can result in 2-3 cm sea-level change at high latitudes. Additionally, sea level in coastal zones is further influenced by sedimentary processes, such as local erosion, deposition and compaction (Stammer et al., 2013). Another relevant local effect is land subsidence, which is mainly induced by human activities such as groundwater, gas and mineral extraction (Nicholls et al., 2021).

1.3. THE SEA-LEVEL BUDGET

The attribution of total observed sea-level change (Section 1.1) to the different drivers of sea-level change (Section 1.2) can be done using a sea-level budget approach. Besides showing the dominating contributions to the observed sea-level change, sea-level budget assessments allow us to identify temporal changes in the total sea-level change and its drivers. For example, while ice melt from glaciers was the predominant cause of sea-level rise over the 20th century as a whole, ocean thermal expansion and ice melt from Greenland have been the main drivers of the accelerated sea-level rise since the 1970s (Frederikse et al., 2020).

Additionally, sea-level budget analyses can be used to constrain and validate climate models, independent data sources and sea-level projections (Wang et al., 2021a). A non-closure of the budget also provides information on, for instance, missing or misrepresented drivers of sea-level change, such as the deep ocean contribution (e.g., Purkey and Johnson, 2010; Llovel et al., 2014; Yang et al., 2021), and on how instrumental problems, such as issues with the Argo salinity sensors and satellite drifts, can influence the components of the sea-level budget (Barnoud et al., 2021).

Depending on the spatial and temporal scale of the study, the sea-level budget will include different components. In this thesis, the sea-level budget is considered as follows:

$$\eta_{total} = \sum \eta_{drivers} = \eta_{steric} + \eta_{GRD} + \eta_{dynamic}, \quad (1.9)$$

where η_{total} is the total sea-level change estimated from satellite altimetry, and the right-hand side of the equation expresses the sum of the drivers of regional sea-level change. That is, sea-level change due to steric effects, due to the exchange of mass between land and ocean, and due to dynamic effects, respectively.

Quantifying the drivers of the observed sea-level change, that is, assessing the sea-level budget, has been the focus of many studies in the recent years, especially on a global scale (e.g. Cazenave et al., 2018; Frederikse et al., 2020; Horwath et al., 2022). In the next sections I discuss the state of the art of the global and regional sea-level budget (Sections 1.3.1 and 1.3.2, respectively), highlighting recent advances and remaining research gaps.

1.3.1. THE GLOBAL MEAN SEA-LEVEL BUDGET

The high-resolution observational network over the satellite era (Cazenave and Moreira, 2022), both of total sea level and of the components, has allowed closure of the global mean sea-level budget from 1993 until present (Church et al., 2011; Gregory et al., 2013; Cazenave et al., 2018; Fox-Kemper et al., 2021; Frederikse et al., 2020). That is, the total rate of sea-level change is the same, within uncertainties, as the sum of its drivers. On average, observed global mean sea level rose about 3.3 mm yr^{-1} from 1993 to 2018, which can be partitioned in 40% due to ocean thermal expansion, 17% from glaciers, 13% from the Greenland Ice Sheet, 8% from the Antarctic Ice Sheet, 10% from land water storage, closing the budget with a 0.4 mm yr^{-1} uncertainty and a remaining unexplained contribution of 12% (Fox-Kemper et al., 2021). Note that these percentages are in relation to the total observed rate of global mean sea level, and not to the sum of the components, which gives a total rate of 2.9 mm yr^{-1} .

Is there an agreement on the closure of the global mean sea-level budget?

The relative contributions of the sea-level components for a given period can vary significantly between studies, showing how dataset and processing choices affects the budget. For example, using at least three sources of data for each sea-level component, Gregory et al. (2013) analysed 576 possible budget combinations, and found that the budget residual varied from -0.5 to 2 mm yr^{-1} depending on the combination. Furthermore, rates of steric sea-level change can differ up to 0.45 mm yr^{-1} depending on the dataset used (Dieng et al., 2015a), and rates of ocean mass sea-level change can differ up to 0.57 mm yr^{-1} depending on the processing choices for the same dataset (Chen et al., 2020). Consequently, depending on the rate used the global mean sea-level budget may not always be closed within 0.4 mm yr^{-1} of uncertainty. **Thus, one may wonder if there is a scientific consensus on the closure of the sea-level budget.**

To answer this question, I made an overview of studies focusing on the global mean sea-level budget in the satellite altimetry era. As a result of different sources of data used, together these 27 studies provide 53 sea-level budget combinations. For example, Church et al. (2011) presents a sea-level budget based on tide gauges, and a second budget based on the combination of tide gauges and satellite altimetry. The 53 budgets can be divided into two different time periods: 15 cover the entire satellite altimetry era (i.e., starting in 1993, Table 1.1) and 38 cover the GRACE/Argo period (i.e., starting after 2002, Table 1.2). Note that, if a study used more than one dataset for the same estimate and provided an ensemble mean, only the ensemble mean was included in the budget table and figure. For example, Dieng et al. (2015a) provided 6 total sea-level change trends: 5 from different satellite altimetry datasets, and one ensemble mean. Only the latter was included in this overview, to avoid few studies from dominating the analysis.

Table 1.1: Global mean sea-level (GMSL) budget from recent studies covering the entire satellite altimetry era (i.e., since 1993). Trends are in mm yr^{-1} . Unless indicated, GMSL is based on satellite altimetry.

Reference	Time period	GMSL	Sum	Steric	Mass
Dieng et al. (2017)	1993-2004	2.7 ± 0.2	2.5 ± 0.3	0.9 ± 0.3^I	1.5 ± 0.1^C
Cazenave and Llovel (2010)	1993-2007	3.3 ± 0.4	2.9 ± 0.3	$1.0 \pm 0.3^{I*}$	1.8 ± 0.3^C
Church et al. (2011)	1993-2008	$3.2 \pm 0.4^{T,S}$	2.5 ± 0.5	$0.9 \pm 0.3^{I*}$	1.7 ± 0.3^C
Church et al. (2011)	1993-2008	2.6 ± 0.6^T	2.5 ± 0.5	$0.9 \pm 0.3^{I*}$	1.7 ± 0.3^C
Church et al. (2013)	1993-2010	3.2 ± 0.4	2.8 ± 0.6	1.1 ± 0.3^I	1.8 ± 0.4^C
Church et al. (2013)	1993-2010	3.2 ± 0.4	2.8 ± 0.7	$1.5 \pm 0.5^{M*}$	0.9 ± 0.4^M
Dieng et al. (2017)	1993-2015	3.0 ± 0.1	3.0 ± 0.2	$1.1 \pm 0.1^{A,I}$	1.9 ± 0.1^C
Chambers et al. (2017)	1993-2015	3.2 ± 0.6	3.0 ± 0.5	$1.2 \pm 0.2^{I*}$	1.8 ± 0.6^C
Oppenheimer et al. (2019)	1993-2015	3.2 ± 0.4	2.9 ± 0.6	$1.4 \pm 0.4^{I*}$	1.4 ± 0.4^C
Oppenheimer et al. (2019)	1993-2015	3.3 ± 0.4	3.1 ± 0.8	$1.5 \pm 0.6^{M*}$	1.6 ± 0.4^M
Cazenave et al. (2018)	1993-2016	3.1 ± 0.4	2.7 ± 0.2	$1.3 \pm 0.4^{I*}$	1.4 ± 0.2^C
Horwath et al. (2022)	1993-2016	3.0 ± 0.2	2.9 ± 0.2	1.1 ± 0.1^I	1.8 ± 0.1^C
Fox-Kemper et al. (2021)	1993-2018	3.2 ± 0.4	2.9 ± 0.4	1.3 ± 0.3^I	1.5 ± 0.3^C
Frederikse et al. (2020)	1993-2018	3.4 ± 0.5^T	3.2 ± 0.4	1.2 ± 0.2^I	$2.0 \pm 0.3^{G,C}$
Frederikse et al. (2020)	1993-2018	3.3 ± 0.5	3.2 ± 0.4	1.2 ± 0.2^I	$2.0 \pm 0.3^{G,C}$

T and T,S indicate GMSL assessments based on tide gauge (T) and tide gauge combine with satellite altimetry (T,S); M indicates estimated from models (M); I , I,A indicate steric estimates based on multiple in-situ sources not including Argo floats (I) and including data from Argo (I,A), and * indicates steric assessments based only on thermosteric estimates; Inv indicates steric estimate obtained via inversion method; C and G,C indicate ocean mass estimates based on combination of sources for the individual components of the mass budget not including GRACE (C), and including GRACE (G,C).

Table 1.2: Global mean sea-level (GMSL) budget from recent studies covering the GRACE/Argo period (i.e., starting from 2002). Trends are in mm yr^{-1} . Unless indicated, GMSL is based on satellite altimetry, steric estimates on Argo floats and Mass on GRACE data.

Reference	Time period	GMSL	Sum	Steric	Mass
Rietbroek et al. (2016)	2002-2014	2.7 ± 0.6	2.7 ± 0.4	1.4 ± 0.2^{Inv}	1.1 ± 0.3^G
Cazenave and Llovel (2010)	2003-2007	2.5 ± 0.4	2.5 ± 0.8	$0.2 \pm 0.8^*$	2.2 ± 0.3^C
Cazenave and Llovel (2010)	2003-2007	2.5 ± 0.4	2.4 ± 0.8	$0.2 \pm 0.8^*$	2.1 ± 0.1^G
Willis et al. (2008)	2003-2007	3.6 ± 0.8	0.3 ± 0.6	-0.5 ± 0.5	0.8 ± 0.8^G
Cazenave et al. (2009)	2003-2008	2.5 ± 0.4	2.3 ± 0.1	0.4 ± 0.1	1.9 ± 0.1^G
Dieng et al. (2015a)	2003-2012	2.8 ± 0.1	2.3 ± 1.2	0.6 ± 0.1^I	1.7 ± 0.1^G
Mu et al. (2022)	2003-2015	3.1 ± 0.4	3.3 ± 0.4	1.1 ± 0.1	2.1 ± 0.3^G
Leuliette and Miller (2009)	2004-2007	2.4 ± 1.1	1.5 ± 1.0	0.8 ± 0.8	0.8 ± 0.5^G
Leuliette and Miller (2009)	2004-2007	2.7 ± 1.5	1.5 ± 1.0	0.8 ± 0.8	0.8 ± 0.5^G
Dieng et al. (2017)	2004-2015	3.5 ± 0.1	3.3 ± 0.2	1.1 ± 0.1	2.1 ± 0.1^C
Dieng et al. (2017)	2004-2015	3.5 ± 0.1	3.4 ± 0.1	1.1 ± 0.1	2.2 ± 0.1^G
Yi et al. (2015)	2005-2009	2.5 ± 0.8	2.4 ± 0.6	1.0 ± 0.4	1.4 ± 0.3^G
Leuliette and Willis (2011)	2005-2010	1.5 ± 0.9	1.6 ± 0.6	0.5 ± 0.5	1.1 ± 0.6^G
Chen et al. (2013)	2005-2011	2.4 ± 0.4	2.4 ± 0.5	0.6 ± 0.3	1.8 ± 0.5^G
Dieng et al. (2015a)	2005-2012	2.8 ± 0.1	2.5 ± 0.2	0.6 ± 0.1	1.9 ± 0.1^G
Leuliette (2015)	2005-2013	3.0 ± 0.4	3.0 ± 0.5	1.0 ± 0.5	2.0 ± 0.2^G
Llovel et al. (2014)	2005-2013	2.8 ± 0.3	2.9 ± 0.2	0.9 ± 0.1	2.0 ± 0.1^G
Leuliette (2014)	2005-2013	3.0 ± 0.4	3.0 ± 0.5	1.0 ± 0.5	2.0 ± 0.2^G
Chambers et al. (2017)	2005-2014	3.2 ± 0.7	3.1 ± 0.4	1.0 ± 0.1^I	2.1 ± 0.4^G
Yi et al. (2015)	2005-2014	3.1 ± 0.4	3.0 ± 0.3	1.0 ± 0.2	2.0 ± 0.2^G
Piecuch and Quinn (2016)	2005-2015	3.4 ± 0.6	3.2 ± 0.4	1.0 ± 0.2	2.2 ± 0.4^G
Vishwakarma et al. (2020)	2005-2015	3.0 ± 0.1	2.9 ± 0.1	$1.2 \pm 0.1^{A,I}$	1.6 ± 0.1^G
Chen et al. (2019)	2005-2015	3.8 ± 0.2	3.8 ± 0.2	1.1 ± 0.1	2.6 ± 0.1^G
Cazenave et al. (2018)	2005-2016	3.5 ± 0.2	3.0 ± 0.2	$1.3 \pm 0.4^{A,I,*}$	1.6 ± 0.2^G
Cazenave et al. (2018)	2005-2016	3.5 ± 0.2	3.6 ± 0.4	$1.3 \pm 0.4^{A,I,*}$	2.3 ± 0.1^G
Horwath et al. (2022)	2005-2016	3.8 ± 0.3	3.9 ± 0.2	1.3 ± 0.2	2.7 ± 0.1^C
Horwath et al. (2022)	2005-2016	3.8 ± 0.3	3.7 ± 0.2	1.3 ± 0.2	$2.5 \pm 0.1^{G,C}$
Horwath et al. (2022)	2005-2016	3.8 ± 0.3	4.1 ± 0.3	1.3 ± 0.2	$2.8 \pm 0.3^{G,C}$
Horwath et al. (2022)	2005-2016	3.6 ± 0.3	3.6 ± 0.2	1.2 ± 0.2	2.4 ± 0.1^C
Horwath et al. (2022)	2005-2016	3.6 ± 0.3	3.4 ± 0.2	1.2 ± 0.2	$2.2 \pm 0.1^{G,C}$
Horwath et al. (2022)	2005-2016	3.6 ± 0.3	3.9 ± 0.3	1.2 ± 0.2	2.7 ± 0.3^G
Barnoud et al. (2021)	2005-2019	4.0 ± 0.2	3.2 ± 0.1	1.1 ± 0.1	2.1 ± 0.0^G
Barnoud et al. (2021)	2005-2019	4.0 ± 0.2	3.5 ± 0.1	$1.3 \pm 0.1^*$	2.1 ± 0.0^G
Chen et al. (2020)	2005-2020	3.9 ± 0.3	3.7 ± 0.5	1.0 ± 0.2	2.7 ± 0.5^G
Oppenheimer et al. (2019)	2006-2015	3.6 ± 0.5	3.0 ± 0.4	$1.4 \pm 0.3^{I,*}$	2.2 ± 0.2^C
Oppenheimer et al. (2019)	2006-2015	3.6 ± 0.5	3.5 ± 0.8	$1.5 \pm 0.6^{M,*}$	2.0 ± 0.5^M
Fox-Kemper et al. (2021)	2006-2018	3.7 ± 0.5	3.6 ± 0.7	1.4 ± 0.7	2.2 ± 0.3^G
Yi et al. (2015)	2010-2014	4.5 ± 0.6	4.3 ± 0.6	1.8 ± 0.2	2.6 ± 0.6^G

T and T,S indicate GMSL assessments based on tide gauge (T) and tide gauge combine with satellite altimetry (T,S); M indicates estimated from models (M); I , I,A indicate steric estimates based on multiple in-situ sources not including Argo floats (I) and including data from Argo (I,A), and * indicates steric assessments based only on thermosteric estimates; C and G,C indicate ocean mass estimates based on combination of sources for the individual components of the mass budget not including GRACE (C), and including GRACE (G,C).

Indeed, there are large differences in the sea-level trends and budget closures between the various studies that focus on the global mean sea-level budget within the satellite altimetry era (Figure 1.3). Comparing the different studies allows us not only to see if the sea-level budget is closed (and what are the dominating drivers to the observed change), but also to see why the rates are diverging and what is causing the non-closure of the budget in some of the studies. Considering an uncertainty of $\pm 0.4 \text{ mm yr}^{-1}$, not all of the studies are able to close the budget (indicated with dashed contours in Figure 1.3). The sea-level budgets over the GRACE/Argo period (i.e., starting after 2002, Figure 1.3c,d) have smaller uncertainties, but a larger spread of trends among studies. The increased accuracy is a result of the use of GRACE to estimate ocean mass changes, and from the almost-global coverage of the Argo floats since 2002 (Cazenave and Moreira, 2022). On the other hand, budgets over shorter time periods show a broader spread of values and larger discrepancies between total sea-level change and the sum of the components. This is related to the interannual variations of sea-level change, as at least 10 years of data is required to obtain more stable rates of sea-level change (Nerem et al., 1999).

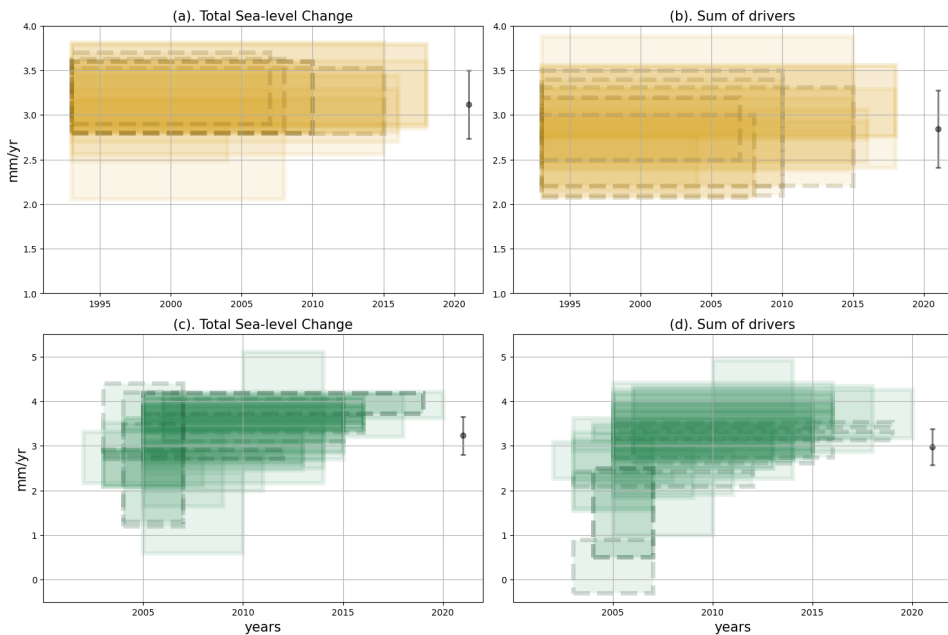


Figure 1.3: Global mean sea-level rates (a, c) and sum of the budget components (b, d) for trends starting in 1993 (a, b) and after 2002 (c, d). Each box represents the trend \pm uncertainty range. Dashed indicates if the budget is closed considering a 0.4 mm yr^{-1} accuracy. The circle with error bars indicates trends for 1993-2018 (a, b) and 2006-2018 (c, d) from Fox-Kemper et al. (2021), for reference. Individual studies and trends used for this plot are listed at the end of the chapter.

In most studies, the sum of components is smaller than the total sea-level change (Figure 1.3), indicating possible missing or misrepresented contributions in the sea-level budget. For example, the contribution of the deep ocean to steric sea-level change is still not well understood, with global mean rates varying from negative (Llovel et al., 2014; Storto et al., 2017) to positive (Purkey and Johnson, 2010; Desbryuyères et al., 2016; Kouketsu et al., 2011; Chang et al., 2019; Yang et al., 2021). Thus, part of the difference between total sea-level change and the sum of the components could be due to misrepresentation of the deep ocean contribution. Another challenge in the sea-level budget lies in estimating the contribution of land water storage, mainly for the pre-GRACE period. Consequently, some studies choose not to include the land water storage in the budget before 2002 (e.g., Cazenave et al., 2018), or use estimates based on hydrological models, which can have a large spread (Scanlon et al., 2018). Finally, most budget studies do not include estimates of ocean bottom deformation, which could explain a missing contribution in the order of 0.1 mm yr^{-1} in the budget (Vishwakarma et al., 2020).

A mismatch between the sum of the components and the total sea-level change might also arise from various processing and correction choices. For example, depending on the GIA correction applied to GRACE data, ocean mass trends can vary up to 1 mm yr^{-1} (Chen et al., 2013; Uebbing et al., 2019). Another example is the effect of instrumental errors in Argo floats: over multidecadal timescales, the concentration of salt in the ocean is more or less constant (Gregory et al., 2019). This means that computing global mean steric changes considering both temperature and salinity or only accounting for temperature should give, virtually, the same rate. However, due to instrumental issues with the salinity profiles of Argo floats, the closure of the global mean sea-level budget improves by excluding the halosteric component from the global budget (Barnoud et al., 2021). A further example are the drift corrections to satellite altimetry data. As illustrated in Figure 1.1, sea surface height from altimetry is computed based on the range between the altimeter and the sea surface height. However, this range can be contaminated if any instrument onboard the satellite, for example the altimeter and radiometer (used for the wet tropospheric correction), suffers drifts or jumps (Ablain et al., 2009). Including drift correction to the TOPEX/Poseidon data resulted in a total sea-level change trend that was 0.7 mm yr^{-1} smaller, improving the closure of the budget (Dieng et al., 2017).

Despite the variations in the published rates, a consensus emerges (indicated by darker colors in Figure 1.3) in the rates of the global mean sea-level change and its drivers over the satellite altimetry era. However, **the spread in the rates will be amplified even further in regional assessments.**

It is also worth noting that most of the studies discussed in this section (and in this thesis) base their budget on linear trends. Budget studies based on a time-varying trend (e.g., Chen et al., 2014, 2017; Cha et al., 2021; Mu et al., 2022) have not been included here. Using a static trend is not always ideal, as it requires an assumption about the type of fit used to describe the change: a first-degree polynomial is used to describe a linear trend over time; while an accelerating trend requires a quadratic function. Although the presence of an acceleration should not change the linear trend (if calculated with a least squares approach), it can affect the uncertainty related to it (Ablain et al., 2019). Budget analyses based on a time-varying trend are a good tool to identify major time-scale components, such as decadal oscillations over the Pacific (Cha et al., 2021), driving sea-level variability.

1.3.2. THE REGIONAL SEA-LEVEL BUDGET

While the global mean sea-level budget over the satellite altimetry era is considered closed (Section 1.3.1), locally attributing the drivers of sea-level change still leads to large differences between the total measured change and the sum of the contributions (e.g., Slangen et al., 2014; Royston et al., 2020). This is partly due to the spatial resolution of the different observational systems, which limits the closure of the sea-level budget on a local spatial scale (Royston et al., 2020). Additionally, the uncertainties of components of the sea-level budget are much larger on a regional scale, hindering the study and closure of the regional budget until recently. Averaging over large regions, such as ocean basins or the entire ocean, reduces the uncertainties and extreme local values and improves the signal-to-noise ratio, allowing the closure of the global mean sea-level budget.

In comparison to the large number of studies focusing on global mean sea-level change, fewer studies have assessed the regional sea-level budget. Most of the regional budget studies focus on a specific region. For example, García et al. (2006) discussed the budget over the Mediterranean Sea, while the budget on the South China Sea and in the Red Sea was investigated by Feng et al. (2012) and Feng et al. (2014), respectively. However, focusing on specific regions might overlook how sea-level variability is interconnected between ocean regions. Over the satellite altimetry era, only five studies hitherto have investigated the sea-level budget regionally for the entire world (Purkey et al., 2014; Rietbroek et al., 2016; Frederikse et al., 2020; Royston et al., 2020; Yang et al., 2022). In addition to these, three other studies have looked into the regional budget globally over a longer period (Slangen et al., 2014; Frederikse et al., 2018; Wang et al., 2021b).

So far, the regional sea-level budget has mainly been analysed on a basin-wide scale (Figure 1.4). These basin scale assessments have brought insights into the dominant processes at a regional scale. For example, basin deviations from the global mean sea-level change could be related to variations in the wind patterns and strength of wind stress and of the Antarctic Circumpolar Current (Purkey et al., 2014). Additionally, although the deep steric contribution to the global mean is of the same magnitude as the uncertainty of the global budget, the basin wide budget can not be closed if the deep ocean contributions are not considered (Purkey et al., 2014).

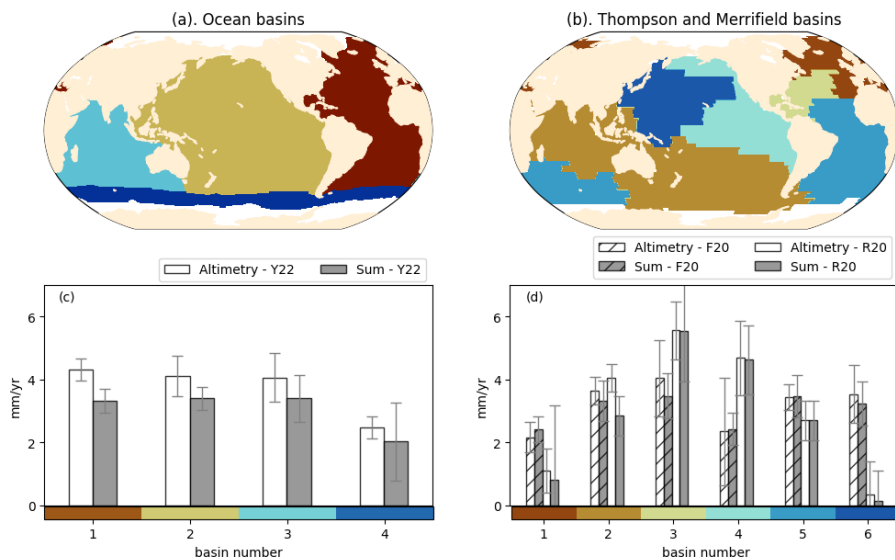


Figure 1.4: Ocean basins (a, b) and sea-level rates (c, d) from previous regional sea-level budget studies. (a) ocean basins and (c) sea-level rates from Yang et al. (2022, Y22); (b) Thompson and Merrifield (2014) ocean basins used for (d) regional sea-level budgets of Frederikse et al. (F20, hashed bars 2020) and Royston et al. (R20, full bars 2020).

However, the closure of the budget and the relative importance of each component are sensitive to the division of the ocean basins. For instance, using the Thompson and Merrifield (2014) basins (Fig 1.4b), Royston et al. (2020) found that the basin scale sea-level budget from 2005-2015 could be closed for all regions, except for the Indian-South Pacific. If ocean basins are used instead (Fig 1.4a), then the sea-level budget for the same period closes in all regions (Yang et al., 2022). At a basin scale, density-driven variations dominate the variability of the budget (Frederikse et al., 2020), while ocean mass is the main contributor to the overall sea-level rise (Yang et al., 2022).

Despite the improvement that basin-wide sea-level budgets have brought to our under-

standing of regional sea-level change, sea level can still vary within an ocean basin. Thus, assessing the sea-level budget on a finer scale can provide insights about local processes. However, the sea-level budget has not yet been closed on sub-basin scales consistently for the entire world. A regional sea-level budget assessment in coastal polygons found that significant percentages of the budget could not be explained by simply adding up the steric and ocean mass sea-level changes (Rietbroek et al., 2016). **Thus, there is still a considerable gap in the understanding and closure of the regional sea-level budget on a sub-basin scale.** With this thesis, I fill this gap and answer the question "*What drives sea-level change on a regional sub-basin scale?*"

1.4. UNCERTAINTIES IN SEA-LEVEL STUDIES

Uncertainty analysis is an integral part of this thesis. Throughout the next chapters, I discuss how to compute and better represent uncertainties within the sea-level budget. Hence, I give a brief introduction to the uncertainties of sea-level observations in this section. Precise uncertainties are necessary to provide significance to the measurements, inform reliability and prevent misinterpretations of the considered observations, evaluate models and validate other observations (Prandi et al., 2021).

In science, uncertainties do not have the same connotation as mistakes. Mistakes can be eliminated from a measurement with careful conduct. Uncertainties, on the other hand, will always be present in any measurement. Hence, one can only work to ensure they are as small as possible and to have a reliable estimate of how large they are (Taylor, 1997). Since uncertainties are unavoidable, understanding the causes of uncertainties and explaining how they are derived is essential for the reliability and interpretation of the results.

In sea-level change studies, uncertainties are present on several levels, from measurements to projections and potential impacts of sea-level change (Figure 1.5, Kettle, 2012; van de Wal et al., 2019). While the uncertainties in sea-level projections have been the main topic of discussion in several recent papers (e.g., Bakker et al., 2017; Hinkel et al., 2019; Kopp et al., 2022), uncertainties in sea-level measurements and how the rate of change is computed (both issues discussed in this thesis), underlie all other sea-level related uncertainties (Figure 1.5). Additionally, uncertainties have a summative effect, that is, they accumulate at each step, magnifying the total uncertainty. When these uncertainties are not clearly defined to stakeholders, the utility of sea-level change assessments is undermined (Kettle, 2012).

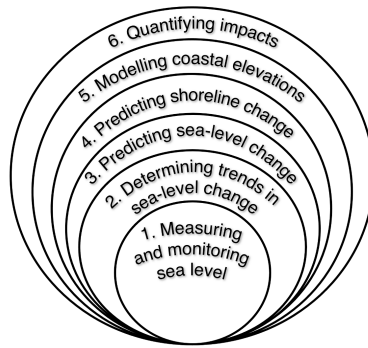


Figure 1.5: Compounding uncertainties in sea-level change assessments. Source: Kettle (2012). Reproduced and modified with permission from the Coastal Education and Research Foundation, Inc.

The uncertainties discussed in this thesis are all related to the data used to compute rates of sea-level change. I now briefly introduce the different types of uncertainties used in this thesis, using sea surface height as an example.

The first type of uncertainty comes from the measurement system, the *intrinsic uncertainty* (Palmer et al., 2021; Thorne, 2021). In satellite altimetry observations, this type of uncertainty arises because we need to apply a set of corrections to account for the interaction of the radar pulse with the atmosphere and the sea surface. These corrections are based on models, and have their own uncertainties, which are then included in the estimated sea surface height.

The second type of uncertainty comes from the use of different datasets and methodologies to describe the same physical system, the *structural uncertainty*. For example, if we compare sea surface height derived from satellite observations to the sea surface height derived from a reanalysis, there will be differences in the two estimates. These differences can be defined as the standard deviation of a central (ensemble) estimate (Thorne et al., 2005; Palmer et al., 2021).

The third type of uncertainty discussed in this thesis comes from the fact that the observations are not independent in time, the *temporal uncertainty*. The sea surface height at one time step is related to the measurement from the previous time step. This temporal relationship, known as autocorrelation, needs to be considered when computing the rate of sea-level change (i.e., the trend). The uncertainty associated with the trend is what we call *temporal uncertainty* (Bos et al., 2013).

The total uncertainty budget of observed sea-level trends is, therefore, a combination of the intrinsic, structural and temporal uncertainties.

1.5. THIS THESIS

This thesis explores the different drivers of regional sea-level change and their uncertainties (Chapter 2 and 3), and how the sum of the drivers compares to the total observed change on a regional level (Chapter 4), over the satellite altimetry era. Potential applications of the results presented in this thesis are discussed in Chapter 5.

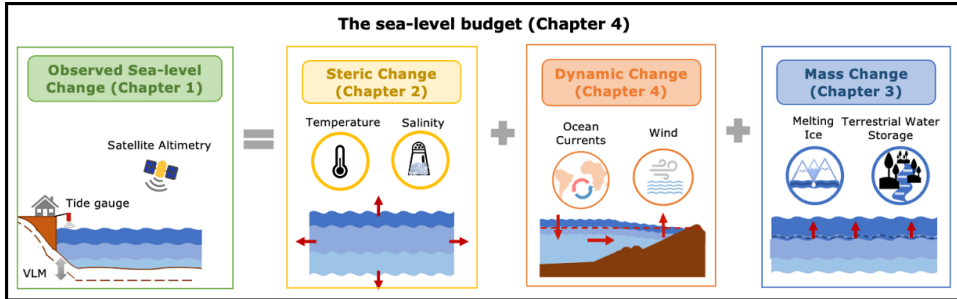


Figure 1.6: Overview of the sea-level budget, indicating in which chapter each component is assessed.

CHAPTER 2

How much have density variations contributed to sea-level change in the satellite altimetry era?

Variations in the density of the oceans, driven by changes in the ocean temperature and salinity, cause steric sea-level change. However, how much density-driven variations have caused sea-level to change since 1993 varies between studies. These differences arise from the use of different temperature and salinity datasets and processing methods. In this chapter I assess the contribution of density-driven (i.e., steric) variations to sea-level change for the periods 1993-2017 and 2005-2015. To answer the research question, I **explore two sources of uncertainty in both global mean and regional steric sea-level trends**. First, I compare a wide range of different temperature and salinity datasets and processing methods (structural uncertainty), and how this translates into different rates of steric sea-level change. Next, I investigate how different noise models used to compute the rate of change (temporal uncertainty) can be another source of differences between rates. I then show how the uncertainties of both datasets and noise models play a role in estimating the steric contribution to sea-level change.

CHAPTER 3

How much have mass variations contributed to sea-level change?

The mass loss from Antarctica, Greenland and glaciers, and variations in land water storage cause sea-level changes. In this chapter, I characterise the regional trends of each

of these sea level contributions, taking into account ice and water mass variations since 1993. **I determine the uncertainties of these sea-level changes, considering different types of errors:** (i) intrinsic, the uncertainty from the data/model itself; (ii) temporal, related to the temporal variability in the time series; and (iii) spatial-structural, related to the spatial distribution of the mass change sources. I first look at the different types of uncertainties separately for each mass contribution, and then analyse how all these uncertainties come together in the estimates of total present-day mass-driven sea-level change.

CHAPTER 4

How to select optimal regions to analyse the sea-level budget? And what are the drivers of sea-level change in these regions?

In this chapter I compare the observed sea-level change to the sum of its drivers on a regional sub-basin level. Building on the results of Chapter 2 and 3, I use satellite altimetry and ocean reanalyses to compute estimates of total and dynamic sea-level change, respectively. To define the sub-basin regions in which the budget is assessed, I use machine learning techniques to identify regions of similar sea-level variability. The use of these regions allows us to reduce the observational uncertainty which has limited regional sub-basin sea-level budget studies up to now. **I then analyse the regional sub-basin sea-level budget consistently for the entire ocean from 1993-2016.** With this budget analysis, I look at what the dominant drivers of sea-level change are in each region.

2

STERIC SEA-LEVEL CHANGE



Published as: Camargo, C. M. L., Riva, R. E. M., Hermans, T. H. J., & Slangen, A. B. A. (2020). *Exploring sources of uncertainty in steric sea-level change estimates*. *Journal of Geophysical Research: Oceans*, 125, doi:10.1029/2020JC016551.

2.1. INTRODUCTION

The oceans are a major reservoir of heat, and have stored about 90% of the human-induced heat in the climate system over the last 50 years (von Schuckmann et al., 2016; MacIntosh et al., 2017). The resulting ocean warming leads to sea-level change (SLC), which is an important reflection of how the oceans respond to global warming (Kopp et al., 2016). This process, known as thermosteric SLC, is the dominant component of the steric contribution to global mean sea-level (GMSL) change.

Steric SLC is also partially driven by salinity variations (i.e., halosteric change). The contribution of salinity to GMSL change is negligible, as the ocean's salt content is considered to be constant over multidecadal timescales (Cazenave et al., 2018). Regionally, however, halosteric SLC can be just as important as thermosteric changes, or even the dominant process of steric sea-level variations, for instance in polar regions (Stammer et al., 2013). Hence, studies of steric contributions to regional SLC should consider both salinity and temperature variations (MacIntosh et al., 2017).

In addition to density-driven variations, present-day SLC is also driven by ocean mass fluctuations (Church et al., 2013). The main processes that change the amount of mass available in the oceans are the melting of glaciers and ice sheets and variations in terrestrial water storage. Together, density and mass variations represent the total budget of SLC (e.g., Cazenave et al., 2018; Gregory et al., 2013). Thus, accurately quantifying steric sea-level variations and their uncertainties constrains the other contributions to the observed SLC.

Comparing published rates of steric GMSL change is complicated, as the period considered differs between studies. For example, while IPCC AR4 (Bindoff et al., 2007) estimated a thermosteric contribution of $1.6 \pm 0.5 \text{ mm yr}^{-1}$ to the GMSL change for 1993-2003, IPCC AR5 (Church et al., 2013) reported a thermosteric contribution of $1.1 \pm 0.3 \text{ mm yr}^{-1}$ for 1993-2010. In addition to the different study periods, part of the difference between steric rates can also be explained by measurement biases, such as depth biases in expandable and mechanical bathythermograph observations (XBTs and MBTs, Ishii and Kimoto, 2009). However, even if one considers the same time period and the same corrections, estimates of steric SLC can still differ for the following three reasons.

First, the deep ocean (>2000 m depth) contribution to steric SLC is uncertain. Given the lack of observational data below 2000 meters depth, different estimates of how much the deep ocean has contributed to SLC have been made in the recent past (e.g., Purkey and Johnson, 2010; Llovel et al., 2014; Dieng et al., 2015a; Desbruyères et al., 2016). For

instance, based on the few high-quality full-depth hydrographic measurements available, Purkey and Johnson (2010) estimated that deep ocean warming contributed 0.1 mm yr^{-1} to the GMSL change from 1980 to 2010. Contrarily, through a budget analysis, Llovel et al. (2014) found a negative ($-0.13 \pm 0.34 \text{ mm yr}^{-1}$) deep ocean contribution to GMSL change from 2005 to 2013. According to an ocean model simulation, repeated hydrographic measurements tend to underestimate the deep ocean warming due to biases induced by temporal and spatial sampling (Garry et al., 2019).

A second source of uncertainty in steric SLC is the use of different temperature and salinity data, and how this data is processed. Dieng et al. (2015a) found that the steric sea-level trend varied from 0.15 to 0.92 mm yr^{-1} , from 2003 to 2012, depending on the dataset analysed. These differences can be explained mainly by the corrections made to individual measurements and by different data processing methodologies, such as gap filling methods (Dieng et al., 2015a). Furthermore, the type of the data used (i.e., in-situ observations, reanalysis or ocean model output) can lead to diverging trends.

Finally, the method used to determine the trend from a time series is another source of uncertainty. Trends are usually obtained by fitting a linear or quadratic model to a time series. The associated error can be described by different stochastic noise models (Bos et al., 2013). (Bos et al., 2014b) showed that uncertainties in SLC can be underestimated when an improper noise model is used. While the effect of using different noise models on estimates of the total SLC from satellite altimetry and tide gauges has already been discussed (Bos et al., 2014b; Hughes and Williams, 2010; Royston et al., 2018), its effect on estimates of steric SLC is still unclear. Given that the choice of the noise model is highly dependent on the nature of the process it describes (Royston et al., 2018), here we investigate the impact of different noise models on steric sea-level trends.

This study explores how steric sea-level trends can vary, based on the datasets and the noise models used. We limit our analysis to the upper ocean (0-2000 m), where most data is available, and leave studying deep ocean uncertainties for future work. We compute and compare steric sea-level trends from 1993 to 2017 (satellite altimetry era) and from 2005 to 2015 (Argo period), considering fifteen different gridded temperature and salinity datasets and eight different noise models. We will show that the uncertainties of both datasets and noise models play an important role in estimating the steric contribution to SLC.

We describe how we calculated steric SLC and the ocean temperature and salinity datasets used in Section 2.2, followed by an explanation of the noise models used to compute the trends and uncertainties. We show the results of the different datasets and noise

models for the global mean and regional steric SLC in Sections 2.3 and 2.4, respectively. We display mainly the results for 2005-2015, when it was inconvenient to display both periods in the same figures. The complementary figures for 1993-2017 can be found in the Supplementary Information 2.7.2.

2

2.2. METHODS AND DATA

2.2.1. CALCULATING STERIC SEA-LEVEL ANOMALIES

Following Gill and Niller (1973) and Tomczak and Godfrey (2003), the steric sea-level anomaly (SLA, η_{SSL}) can be described as follows:

$$\eta_{SSL} = -\frac{1}{\rho_0} \int_{z_2}^{z_1} \rho' dz, \quad (2.1)$$

where ρ_0 is a reference density, and ρ' is the local density anomaly. The expression is vertically integrated from the maximum local depth z_2 to the water surface z_1 . We use the Thermodynamic Equation of Seawater (TEOS-10 McDougall and Barker, 2011) as the equation of state to calculate the steric sea-level anomaly, and consider only the upper ocean (0-2000m) in our computations. The density anomaly ρ' is a function of variations in the ocean temperature, salinity and pressure fields, and is computed using ocean temperature and salinity data from in-situ and reanalysis datasets (Section 2.2.2).

2.2.2. OCEAN TEMPERATURE AND SALINITY DATASETS

We collected and analysed fifteen publicly available gridded datasets of continuously monthly ocean temperature and salinity published by different research groups worldwide (Table 2.1). All datasets were downloaded between January and March 2020, and are currently accessible (last check June 2020). The datasets were selected based on their recurrent use in the literature. Given that we use gridded datasets, we do not consider the uncertainty propagation from a single profile of temperature and salinity to steric height. The concept of uncertainty propagation was reviewed and discussed in detail in MacIntosh et al. (2017).

The datasets were categorized according to their data type: in-situ measurements versus ocean reanalyses. The first category includes ship-based hydrographic data (such as conductivity-temperature-depth (CTD) profiles, XBTs and MBTs) and observations collected by Argo profiling floats (Roemmich et al., 2009). The in-situ observations are generally merged onto a grid using statistical interpolation (Storto et al., 2017). This

category is further divided into two categories: Argo – for datasets that have only data from Argo floats; and Multiple in-situ (MiS) – for products that combine several sources of in-situ observations, in addition to Argo data. The second category, ocean reanalysis (REA), assimilates the observational data into ocean circulation models, extrapolating the information spatially and, sometimes, temporally (MacIntosh et al., 2017).

2.2.3. DATA PROCESSING

First, the steric SLA was computed on the native grid of each dataset following Equation 2.1. We then standardized the varying resolution by remapping all datasets on a 1° by 1° grid, using bilinear interpolation. Next, we selected the grid points within 66°S to 66°N of latitude, and applied a land mask based on ETOPO1 (Amante and Eakins, 2009). The land mask was applied without extrapolating any values, meaning that areas which are not covered by all datasets are still considered, using the available datasets in each location. Figure S2.2 shows the number of datasets available at each grid cell after applying the land mask. Using a more conservative ocean mask, in which only the grid points that all datasets have data are considered, leads to a minor difference of 0.08 mm/year for the global mean trend. Hence, we decided to use the ETOPO1 mask, which has the advantage of a wider spatial coverage. Next, we computed a category mean for each of the three categories (Argo, MiS, and REA) and a total ensemble mean of all individual datasets. Using an area-weighted mean, we computed the global mean steric SLC for each dataset.

2.2.4. ESTIMATING TRENDS AND UNCERTAINTIES

The trends and respective uncertainties were estimated using the Hector software (Bos et al., 2013). Hector uses a weighted least-squares model to estimate the linear trend, while accounting for periodic signals (i.e., seasonal and annual components). The variations not captured by the regression model are defined as noise (Bos et al., 2014b). The software allows the user to choose between a number of stochastic models to describe the noise properties, such as temporal correlation and spectral density behaviour, thus reducing the risk of underestimating the trend (Bos et al., 2013). The uncertainties provided by Hector and shown in this paper represent one standard deviation.

Based on sea-level literature (e.g., Bos et al., 2014b; Royston et al., 2018), we tested eight models to find the best descriptor of the uncertainties in our data: a white noise model (WN); a Generalized Gauss Markov model (GGM); a pure power-law model (PL); a power-law model combined with white noise (PLWN); autoregressive models of order 1, 5 and 9 (AR(1), AR(5), AR(9), respectively); and an autoregressive fractionally-integrated moving

average model of order 1 (ARFIMA, henceforth ARF). The WN is the simplest stochastic model, in which the spectral density of the noise is equal to zero, and no temporal correlation between the residuals is considered. In the PL model, all observations influence one-another, although their correlation decreases with increasing temporal distance. The AR(p) models consider that each observation at time t_i is affected by white noise and the observation at time $t_{(i-1)}$. The time of preceding observations influencing each observation is given by the order p of the autoregressive model. To represent power-law observations at low frequencies, the ARF model combines an AR(1) with a fractional integration and a moving average of the noise. The GGM model is a generalized form of the ARF model. More details about each model can be found in the Hector software manual (Bos and Fernandes, 2013) and in Bos et al. (2013, 2014b,a).

To determine the goodness of fit of the noise models, we use the Akaike Information Criterion (AIC, Akaike, 1974) and the Bayesian Information Criterion (Schwarz, 1978, BIC), together with visual inspection of the power spectrum of the noise model and the fit residual. Both AIC and BIC use the maximum likelihood and the number of parameters to judge the quality of the model. However, BIC penalizes the number of parameters stronger than AIC (Liddle, 2004). AIC and BIC are the most common criteria used to describe the goodness of the fit, yet there is no consensus in the literature about which criterion should be used. Therefore, we used these criteria to select the 'best' noise model for each dataset and then computed an overall ranking of each noise model. Following Royston et al. (2018), we consider the mean scoring of AIC and BIC to decide which noise model is the most suitable. More details about the selection procedure is given in Supplementary Information Text 2.7.1.

We complemented the global mean noise model analysis with the software ARMASA (Broersen, 2022). Given a residual time series, ARMASA identifies the ideal noise model type and order, choosing between different autoregressive, moving average, and autoregressive moving average models (AR(p), MA(q), ARMA(p',p'-1) respectively). More details about ARMASA and the parameters used are given in Supplementary Information Text 2.7.1 and (Klees and Broersen, 2002).

Table 2.1: Temperature and salinity datasets used to compute steric SLA, separated in three categories. The abbreviations are short forms for either the reference paper (e.g., C17 for Cheng et al. (2017)), the responsible institution (e.g., APDRC), or the official name of the dataset (e.g., CORA). Time period in bold indicates the datasets available for the entire satellite altimetry era.

Category	Abbreviation	Version	Institute	References	Time period	Depth Range (m)
Argo	APDRC		IPRC/APDRC	Product Description	2005-2019.06	0 - 2000
	SIO		Scripps Institution of Oceanography	Roemmich & Gilson (2009)	2004-2019.06	10-1975
	BOA		CSIO	Li et al. (2017); Lu et al. (2019)	2004-2018	0 - 1975
	ISAS	15	Ifremer	Gaillard et al. (2016)	2002-2015	0 - 2000
	CORA	v5.2	Ifremer	Cabanes et al. (2013); Szekely et al. (2019)	1940-2017	0 - 2000
Multiple in Situ (MiS)	EN4	v4.2 G10*	UK MetOffice	Good et al. (2013)	1950-2018	5-5350
	IK09	v7	JAMSTEC	Ishii & Kimoto (2009); Ishii et al (2017)	1900-2019.05	5-3000
	C17	v0 (S), v3(T)	IAP/CAS	Cheng et al. (2017)	1940-2019.05	0 - 2000
	ISAS+	15	Ifremer	Gaillard et al.(2016)	2002-2015	0 - 2000
	ARMOR	3D	CSL	Guinehut et al. (2012)	1955-2018	0 - 5500
Reanalysis (REA)	C-GLORS**	5	CMCC	Storto & Masina (2016)	1993-2018	0 - 5902
	GLORYS2**	V4	Mercator Ocean	Garric and Parent (2017)	1993-2017	0 - 5902
	FOAM-GloSea5** (hererin FOAM)	v13	MetOffice	Blockley et al. (2014); Maclachlan et al. (2015)	1993-2017	0 - 5902
	ORAS**	5	ECMWF	Zuo et al. (2019)	1993-2017	0 - 5902
	SODA	3	UMD/ATMOS	Carton et al. (2018)	1980-2017	0 - 5902

*Two versions of the EN4v4.2 are available, depending on the type of correction applied for the XBT and MBT data. Following the description the discussion of (Cheng et al., 2016) about the benefits of each correction, we use the dataset with the (Gouretski and Reseghetti, 2010) correction. ** These products were obtained via the Global Ocean Ensemble Reanalysis Version2 of Mercator Ocean.

2.3. GLOBAL MEAN STERIC SEA-LEVEL CHANGE

2.3.1. STERIC SEA-LEVEL TIME SERIES

From the temperature and salinity datasets (Table 2.1), we computed fifteen global mean steric sea-level time series, three category means (red, blue and green lines for the Argo, MiS and REA) and one ensemble mean (black line) (Figure 2.1). Despite the differences among the time series, all the category means agree within one standard deviation from the ensemble mean. Due to the addition of Argo data, starting in 2002 and reaching a near-global coverage in 2005, the standard deviation of the global mean steric sea level reduces strongly: from about 8 mm yr^{-1} during the first ten years to 4.2 mm yr^{-1} from 2002-2005, and to 3.6 mm yr^{-1} after 2005. This reduction is seen not only for the ensemble mean and Argo datasets, but also for the MiS and REA categories, suggesting that all datasets strongly depend on the Argo float data.

The ensemble means based on the ten and fifteen datasets (for 1993-2017 and 2005-2015, Figure 2.1 solid and dashed black line, respectively) behave very similarly for the overlapping period. This indicates the robustness of the ensemble mean to the number of datasets used. Furthermore, the category means agree well with the ensemble mean for 2005-2015, all within one standard deviation from the ensemble.

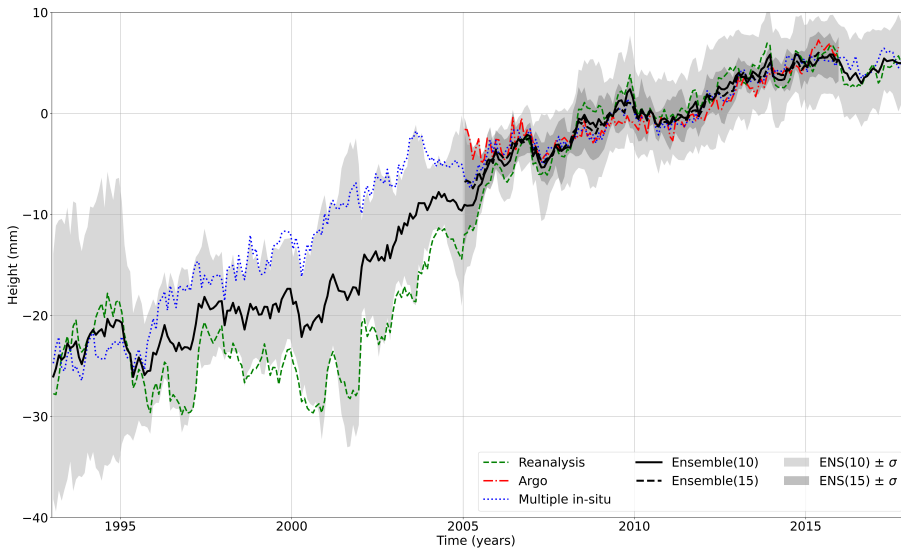


Figure 2.1: Global mean steric sea-level time series of the ensemble (black solid and dashed line) and category means (green for reanalysis, red for only Argo, and blue for multiple in-situ) referenced to the time-mean for 2005-2015. The solid black line and the light grey shaded area represent the ensemble of ten datasets for $1993-2017 \pm 1 - \sigma$, respectively.

2.3.2. INFLUENCE OF DATASETS AND NOISE MODELS ON STERIC ESTIMATES

For each of the time series, category and ensemble means, we computed linear trends using eight different noise models, leading to 104 (13x8) and 152 (19x8) global mean trends for 1993-2017 and 2005-2015, respectively (Figure 2.3 for 2005-2015, Figure S2.3 for 1993-2017). When both the dataset and noise model are varied simultaneously for the 2005-2015 period ($n=15 \times 8=120$), the global mean trend (Figure 2.2a) ranges from 0.56 to 2.33 mm yr^{-1} . Likewise, the uncertainty (Figure 2.2b) ranges from 0.02 to 1.65 mm yr^{-1} .

The situation is similar when a single noise model is chosen and the datasets are varied. For example, in the case of AR(1), the spread of the trend and uncertainty, although reduced, continues to be large, respectively ranging from 0.66 – 1.85 and 0.05 – 0.65 mm yr^{-1} (Figure 2.2c,d, $n=15$). Alternatively, when we choose one dataset and vary only the noise model (Figure 2.2e-h, $n=8$), the spread of the trend becomes significantly smaller. This suggests that varying the dataset has a larger influence on the estimated trend than varying the noise model. In addition, we see that the spread is highly dependent on the chosen dataset (Figure 2.2e, f). While IK09 (grey) has a minimal spread as a result of varying the noise models, GLORYS2 (white) shows a variation of almost 1 mm yr^{-1} depending on the noise model being used. Interestingly, the ensemble mean trend and uncertainty (Figure 2.2g, h) show almost no sensitivity to the choice of noise model. This could be the result of the ensemble mean being smoother than the individual time series, and it indicates that using the ensemble mean reduces the dependency on the noise model choice. The results are similar for the period 1993-2017 (Figure S2.3).

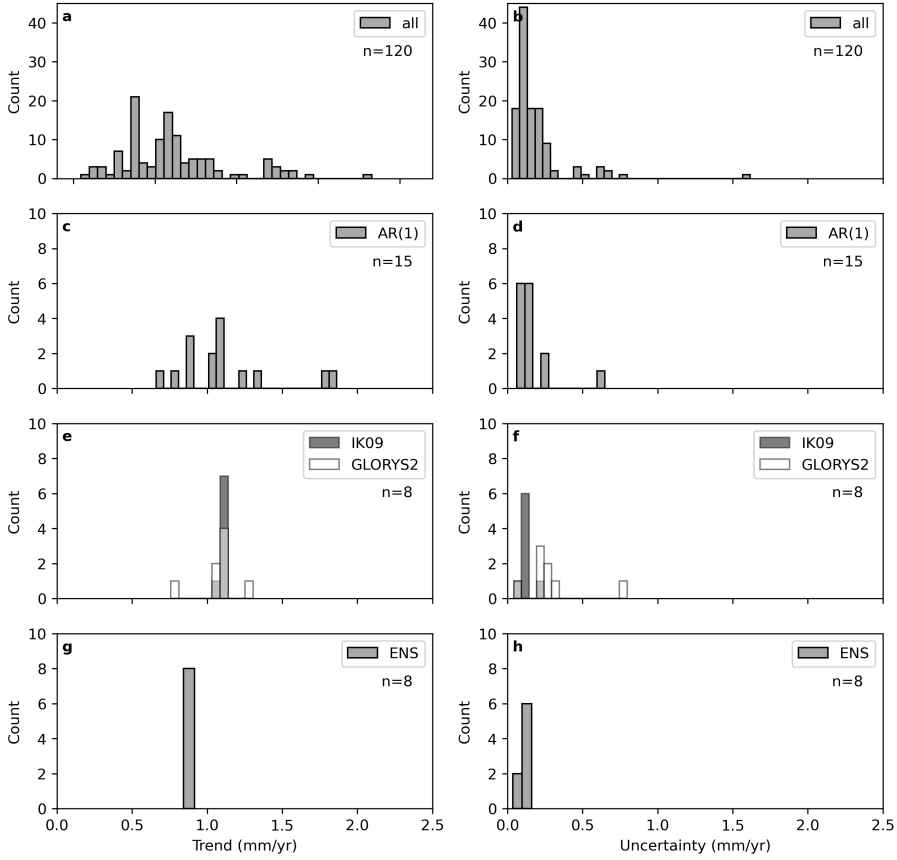


Figure 2.2: Histogram of the trend (left column) and uncertainty (right column) in mm yr^{-1} for 2005-2015 (a,b) varying all datasets and noise models, (c,d) for the AR(1) noise model when varying all the datasets, (e,f) for the IK09 (white) and GLORYS2 (grey) datasets when varying all the noise models, (g,h) for the ensemble mean when varying all the noise models. The count on y-axis is w.r.t to the number of datasets (n) considered in each case.

2.3.3. NOISE MODEL SELECTION (GLOBAL MEAN)

In order to determine which noise model best describes the global mean steric trends and uncertainties, we use the AIC and BIC scores (Section 2.2.4). Our selection criterion is based on a threshold value (see Supplementary Text 2.7.1 for more information), thus multiple noise models can be selected for each dataset if the score passes the threshold, and the final percentage of each score can be larger than 100.

According to AIC, AR(5) is the overall preferred noise model (78% for 2005-2015, Figure 2.3 hashed bars, and 56% for 1993-2017, Figure 2.3 full bars). Contrarily, BIC ranks AR(1) first for 2005-2015 and ARF for 1993-2017. When the category and ensemble means are excluded from the selection (not shown), AR(1) is never chosen as the preferred noise model for 1993-2017. This illustrates how the averaging process in ensemble means reduces the temporal variability of the time series, especially when a longer period is considered. Thus, a simple noise model, such as AR(1), becomes the preferred model for the category and ensemble means. For the mean of AIC and BIC, both AR(5) and ARF are equally preferred for 1993-2017, and AR(1) is ranked first for 2005-2015.

We complement our noise model selection with ARMASA (Section 2.2.4). Between AR(p), MA(q) and ARMA(p',p'-1) models, a simple moving average of order 6 is selected as the preferred noise model for the ensemble mean of 2005-2015. This shows that there is still some short-term periodicity in the residuals, even after the annual and semi-annual signals have been removed. Between AR(p) and ARMA(p',p-1), the AR(1) is selected as the best noise model for both periods. However, for the individual time series, many different AR(p), MA(q) and ARMA(p',p-1) models were chosen (see Table S2.1). For the individual datasets, the most recurrent noise model for both periods was ARMA(2,1). The preferred order of the noise models tends to be higher for the time series for 1993-2017 than for 2005-2015. Interestingly, while AIC and BIC found AR(5) to be one of the best noise models, this order was never preferred by ARMASA. This may be related to the much wider range of orders and model types tested by the ARMASA algorithm in order to select the one model that is statistically representative of the data (Broersen, 2002). We have used the ARMASA results as a qualitative indicator of the ideal noise model and find that, while there are differences with the chosen model in Hector, these differences are small.

Considering the AIC and BIC ranking and the results of ARMASA, we concluded that a first order autoregressive AR(1) is a good descriptor of the trend and uncertainties of the global mean time series, especially for the category and ensemble means. Nevertheless, there is still a periodicity in the residuals. We see that for the Argo period, a signal of

several months (two to six) is still present in the noise, while for the satellite altimetry era, an interannual signal, in the order of three up to twenty months, is seen in the residuals.

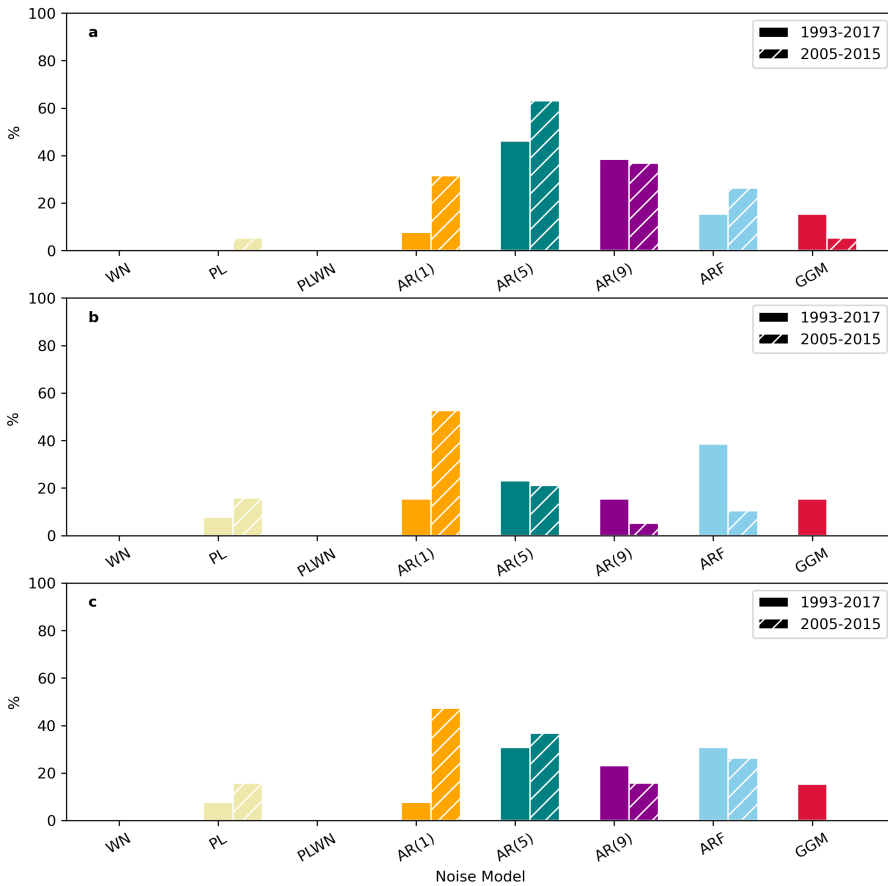


Figure 2.3: Percentage of preferred noise model based on all datasets (including the ensemble and category means) for 2005-2015 (hashed bars) and 1993-2017 (full bars) according to (a) AIC, (b) BIC, and (c) the mean of AIC and BIC.

2.3.4. GLOBAL MEAN STERIC SEA-LEVEL TRENDS

Applying an AR(1) noise model, we find a global mean steric sea-level trend of 1.08 ± 0.07 mm yr^{-1} for the ensemble mean for 2005-2015 (Figure 2.4a) and 1.36 ± 0.10 mm yr^{-1} for 1993-2017 (Figure 2.4b). For most of the datasets, the uncertainties are larger for 1993-2017, mainly as a result of the increased observational quality and coverage in 2005-2015. Overall, there is a better agreement between the observational datasets (i.e., Argo and multiple in-situ, red and blue dots), than between the reanalyses products (green dots).

The Argo category (Figure 2.4, red) shows a good intra-category agreement, with all individual values agreeing within the category uncertainties. The Argo category mean trend of 0.90 ± 0.09 mm yr^{-1} is in the lower uncertainty range of APDRC and SIORG datasets. The multiple in-situ category (Figure 2.4, blue) shows large differences for the two time periods, with a category mean of 1.00 ± 0.07 and 1.24 ± 0.08 mm yr^{-1} for the Argo period and satellite altimetry era, respectively. For 2005-2015, the category mean is within 1-sigma of all individual datasets, except for Armor3D on the lower and EN4 on the upper limit of the category distribution. For the 1993-2017 period, the category mean is only within the uncertainty ranges of CORA and EN4 datasets, with the IK09 on the lower and Armor3D on the upper limit of the category distribution.

The reanalysis category (Figure 2.4, green) shows the largest ranges for both periods, with almost 1 mm yr^{-1} difference between the trends of individual datasets. The category mean for 2005-2015 is 1.40 ± 0.21 mm yr^{-1} , falling within the uncertainty range of C-GLORS, FOAM, and GLORYS2. The category mean for 1993-2017 is 1.47 ± 0.23 mm yr^{-1} , within the uncertainty range of all individual trends. The uncertainties from the reanalyses datasets are much larger than for the other groups, probably related to the higher spatial resolution of such products and the modeled internal variability.

To test if the variance in the ensemble and category means explain the variance of the individual datasets, we computed the R^2 (Table S2.1). All datasets have a relatively high R^2 value ($R^2 > 0.7$) in relation to the ensemble and category means, with exception of the FOAM reanalysis ($R^2 = 0.52$ for 2005-2015, $R^2 = 0.37$ for 1993-2017), IK09 for 1993-2017 ($R^2 = 0.66$) and BOA dataset for 2005-2015 ($R^2 = 0.68$). Thus, the ensemble mean is representative of almost all the individual members. Furthermore, to test the sensitivity of the ensemble mean, we removed up to 2 datasets (one of the largest outliers (FOAM and Armor3D) plus any other dataset), and recomputed ensemble mean. This led to a maximum variation of the trend of 0.12 mm yr^{-1} for 2005-2015 and 0.21 mm yr^{-1} for 1993-2015.

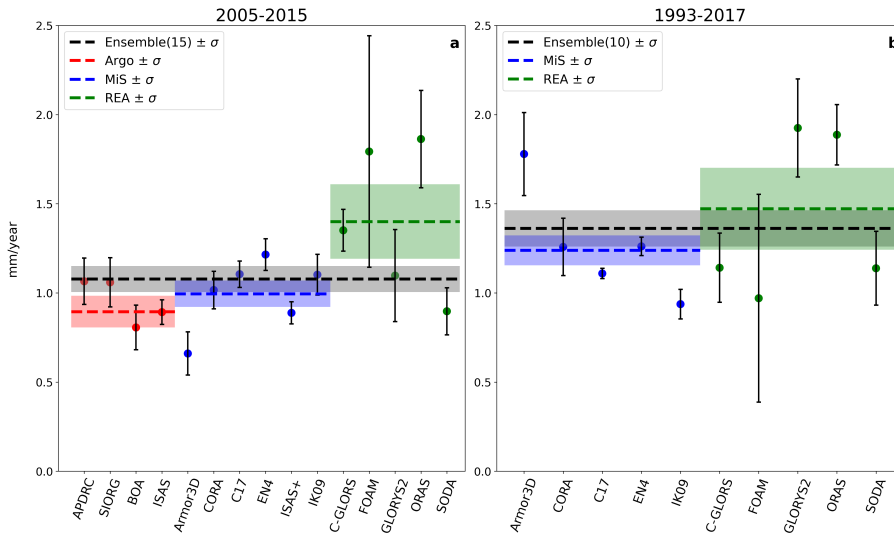


Figure 2.4: Global mean sea-level trends (mm yr^{-1}) and uncertainty (1-sigma) obtained with AR(1) noise model from (a) 2005-2015 and (b) 1993-2017. Dashed lines represent the trends of the ensemble and category means, with the respective uncertainties in the shaded area. Grey, red, blue and green indicate the ensemble mean and the Argo, multiple in-situ and reanalysis category means. The means refer to values obtained from the mean of the individual time series, and not the mean of the trends and uncertainties. The trends and uncertainties are also listed in Table S2.1.

2.4. REGIONAL STERIC SEA-LEVEL CHANGE

Several processes that are important at a regional scale are averaged out in the global mean sea-level analysis, especially when discussing residuals and uncertainties. Thus, in this section we complement the global mean discussion with results about the regional steric sea-level trends. To show how the steric SLC is regionally influenced by the chosen datasets (Section 2.4.1) and the noise models (Section 2.4.2), we selected one latitudinal transect in the center of each ocean basin (Figure 2.5a). We then use the ensemble mean to present the regional selection of noise models (Section 2.4.3) used to obtain the regional steric sea-level trends (Section 2.4.4).

2.4.1. TREND DEPENDENCE ON CHOSEN STERIC DATASETS

We first compare the steric trends of all different datasets for three latitudinal transects, using the AR(1) noise model, based on the noise model selection analysis in Section 3. The ensemble mean (right profile of each transect) represents features of all the other datasets, with smoother transitions. The profiles for 1993-2017 (Figure S2.4) are dominated by positive trends in all transects and lower uncertainties than for 2005-2015, as the effect of

interannual variability is reduced and the positive trend becomes clearer.

The Indian Ocean (Figure 2.5c, d) is dominated by a positive steric trend, which can be related to the increasing atmospheric temperature in the region (Carvalho and Wang, 2019). Around 10°S, the trends in all datasets are not statistically significant and reverse to -2 mm yr^{-1} , accompanied by an increased uncertainty (3 mm yr^{-1}). Going south, the trends reverse back to positive, reaching the highest values of trend and uncertainty around 40°S (up to $30 \pm 10 \text{ mm yr}^{-1}$ for FOAM). Further south (around 55°S) the trend becomes negative again, possibly the effect of negative trends of the Antarctic Circumpolar Current (Frankcombe et al., 2013).

In the Pacific transect (Figure 2.5e, f), the band between 40 – 60°S shows most variation between datasets, with a striping pattern that varies in intensity and width from dataset to dataset. A similar behavior was reported in a climate model study by Slangen et al. (2015), who related these changes to aerosol and greenhouse gas forcing. In the southern South Pacific, all datasets have a negative trend. Similarly to the Indian Ocean, the uncertainties in the Pacific follow the pattern of the trends, and increase where the trends are reversing. There is a band of high uncertainty around the equator, coinciding with the negative trend values. Most of the Atlantic Ocean transect trends and uncertainties (Figure 2.5g, h) agree between the datasets, except for the APDRC results. Most of the datasets have a negative trend in the north, matching the mid-2000s signal of the North Atlantic subpolar gyre (Chafik et al., 2019). However, the length and intensity of this negative band varies significantly between the datasets. Only the CORA dataset shows a positive trend in the north. For most of the datasets, around 20°S the trend becomes positive, with a stripe-pattern of narrow bands until the far south of the transect. Only for the SIORG dataset we see an overall positive trend from 10 – 60°S. The uncertainty values are generally lower in the Atlantic compared to the other transects. Most of the datasets, especially the EN4, show an increase in the uncertainty around 40°S. The atypical negative trend between 40 – 20°N of the APDRC dataset is accompanied by a very high uncertainty value.

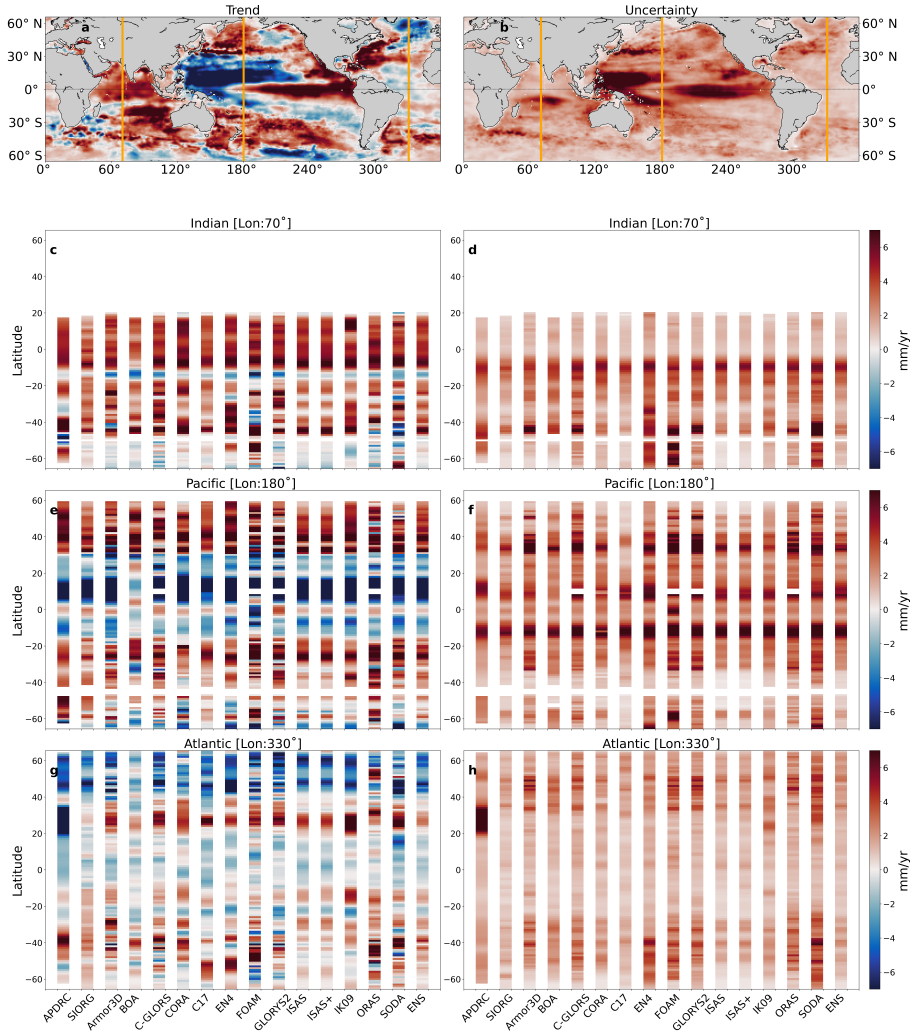


Figure 2.5: (a) Trend and (b) uncertainty for 2005-2015 estimated with the AR(1) noise model, and the latitudinal transects (displayed in orange), as a function of the dataset (x-axis) for the (c,d) Indian, (e,f) Pacific and (g,h) Atlantic Ocean transect.

2.4.2. TREND DEPENDENCE ON CHOSEN NOISE MODELS

In contrast with varying the dataset, there is almost no latitudinal variation in the trend of the ensemble mean when only varying the noise model (Figure 2.6 for 2005-2015, and Figure S2.5 for 1993-2017). However, the effect of the different noise models becomes much clearer in the uncertainty profiles. We see that the WN model is likely underestimating the real uncertainty, because of the low frequency variability in the timeseries. Due to the small impact of WN, PL and PLWN show the same behaviour. The noise models of the autoregressive family are slightly different from each other, with the uncertainties for the AR(1) generally larger than for AR(5), which in turn are larger than the AR(9) uncertainties. The ARF has a more pronounced spatial pattern compared to the simple autoregressive models. The GGM model stands out due to very large uncertainties. For 1993-2017 (Figure S2.5), the latitudinal patterns of the trends and uncertainties are, in general, the same as for 2005-2015.

Figure 2.6 also illustrates the importance of choosing an appropriate noise model to describe the uncertainties present in the data. The mean uncertainty for the WN model, in all transects, is of the order of $\pm 0.7 \text{ mm yr}^{-1}$, while the mean uncertainty for the GGM model is of the order of $\pm 7 \text{ mm yr}^{-1}$. However, a very low or high uncertainty does not mean that a specific noise model cannot be the best descriptor of the data. In the next section, we look at the AIC and BIC criteria to find the preferred noise model for each grid point.

2.4.3. NOISE MODEL SELECTION (REGIONAL)

To find which noise model best describes the regional variations of the ensemble mean, we investigate the noise model performance at each ocean grid point. These results depend on the resolution and ocean mask used. The regional selection of the preferred noise model (Figure 2.7 for the ensemble mean, and Figure S2.6 based on individual datasets), shows that AR(1) and AR(5) are the preferred noise models, agreeing with the global analysis (Section 2.3.3). According to AIC (Figure 2.7a, b), AR(5) is the preferred noise model for 41% of the ocean area for 2005-2015 and 53% of the regions for 1993-2017. In contrast, the preference of BIC (Figure 2.7c, d) for AR(1) is very clear, selecting it as the best noise model for 73% and 54% of the ocean area, for 2005-2015 and 1993-2017 respectively. For the 1993-2017 period, the AR(5) models is preferred in 30% of the ocean area, also according to BIC.

The noise model preference shows some distinctive regional patterns. The AR(5) pattern resembles the ocean gyres, suggesting a link between these dynamic regions and a prefer-

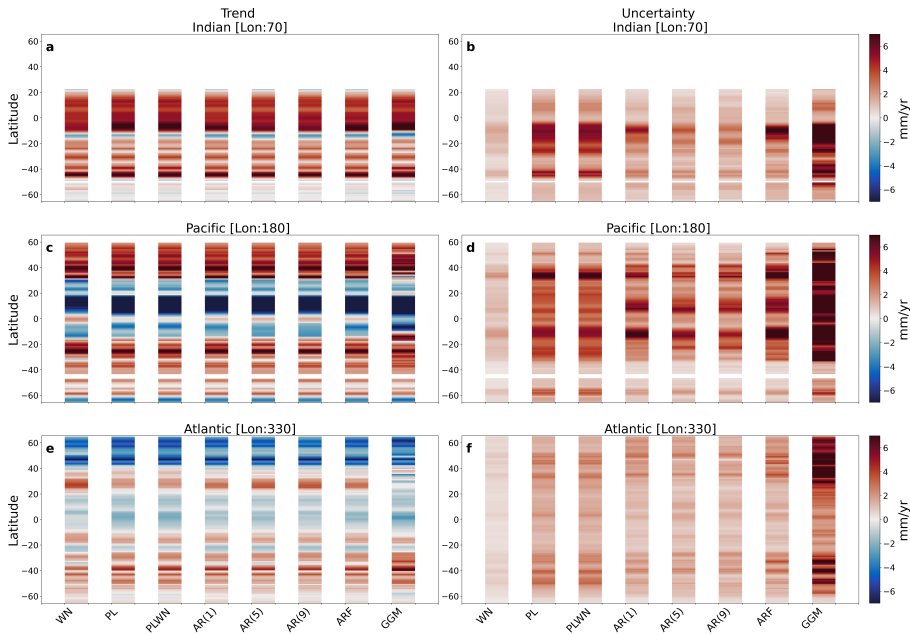


Figure 2.6: Trend (left column) and uncertainty (right column) for the ensemble mean for 2005-2015, as a function of latitude (y-axis) and dataset (x-axis) for the (a,b) Indian, (c,d) Pacific and (e,f) Atlantic Ocean transect.

ence for more complex noise models. The subtropical regions (both north and south), tend to also prefer the AR(5) model, for instance in the AIC for 2005-2015, and BIC for 1993-2017. All scores show a clear ‘boomerang’ shaped pattern in the west equatorial Pacific (from 130°E-180°E of longitude, and 20°S-20°N of latitude), associated with the El Niño Southern Oscillation (ENSO, Wang and Picaut, 2004). However, in this region different orders of autoregressive models score higher for the different criteria: AR(5) for AIC and ARF for BIC. While for some datasets the GGM is selected as the preferred noise model for the global mean time series, regionally this is almost never the case. In contrast, while the WN is never preferred for the global mean, it is selected a few times in the regional patterns. Comparing the two time periods, we see an increase of the preference of higher order of autoregressive noise models with the increasing study period length, as already noted for the case of the global mean.

2.4.4. REGIONAL STERIC SEA-LEVEL TRENDS

In the previous section, the regional noise model selection (Figure 2.7) showed that a combination of different noise models is necessary to best describe the regional ensemble mean trend and uncertainties. While mixing noise models is not standard practice, it

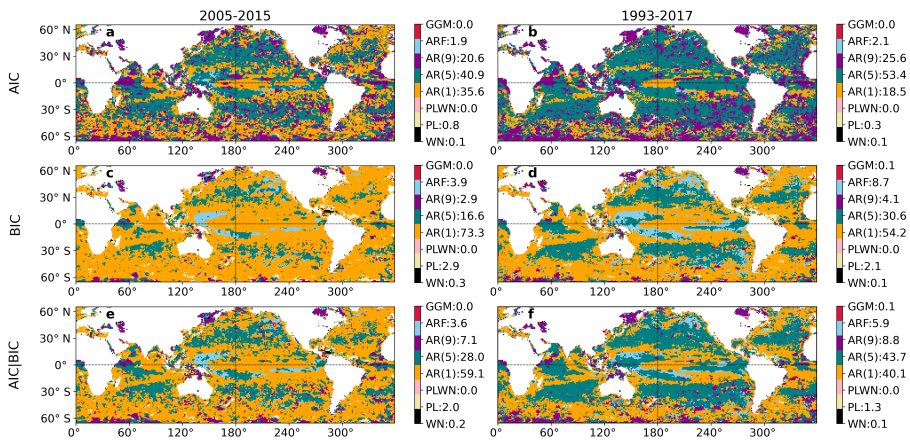


Figure 2.7: Preferred noise model for each grid for the ensemble mean with the respective percentage of the total ocean area selected by each noise model, based on (a,b) AIC, (c,d) BIC and (e,f) the mean of AIC and BIC.

allows local processes to be well represented in the trend and uncertainty estimations. Thus, in this Section we show the regional steric sea-level trend and uncertainty (Figure 2.8) using the preferred noise model for each grid point. As AR(1) was the preferred noise model in more than 50% of the ocean grids, the differences between the trends (Figure 2.8b, e) estimated with AR(1) and with the preferred noise model are only significant in the most dynamic regions. For both time periods, the differences become larger for the estimated uncertainties (Figure 2.8d, g).

Over the shorter time period (2005-2015), the regional trends are dominated by short time-scale dynamics (Figure 2.8a, b). For example, the Equatorial Pacific has a very strong signal of ENSO. The western boundary currents also display strong trend signals. A clear signal of the Gulf Current (west North Atlantic) is marked by a high trend of about 6 to 7 mm yr^{-1} . The same is seen for the Kuroshiro Extension (west North Pacific) and for the Malvinas current (west South Atlantic). The Agulhas current (South Africa) shows well-marked eddies. All these regions are dominated by internal variability rather than a forced trend, with higher uncertainties (Figure 2.8c,d), and consequently they are sometimes not statistically significant.

For the longer period (1993-2017), the trends (Figure 2.8e, f) are reduced in strength and less dominated by interannual oscillations and ocean currents, revealing a predominantly global positive trend. For instance, the strong positive trend in the east Equatorial Pacific from ENSO fades into a weak negative trend, while the negative trend of the west is reversed to a positive, but weaker, trend. The trend also shows a weak reflection of the

western boundary currents. The positive signal of the Gulf Stream is replaced by a negative trend. The negative trend of the North Atlantic Subpolar Gyre in 2005-2015 changes to a positive trend in 1993-2017, as also reported by Chafik et al. (2019). Although the Southern Ocean is outside our domain, we can still see in the lower boundaries of our maps the signal of the Antarctic Circumpolar Current, marked by a negative trend for both periods. As the time series get longer, internal variability has a smaller influence on the long-term trend, resulting in reduced uncertainties in 1993-2017 (Figure 2.8g, h) in comparison to 2005-2015.

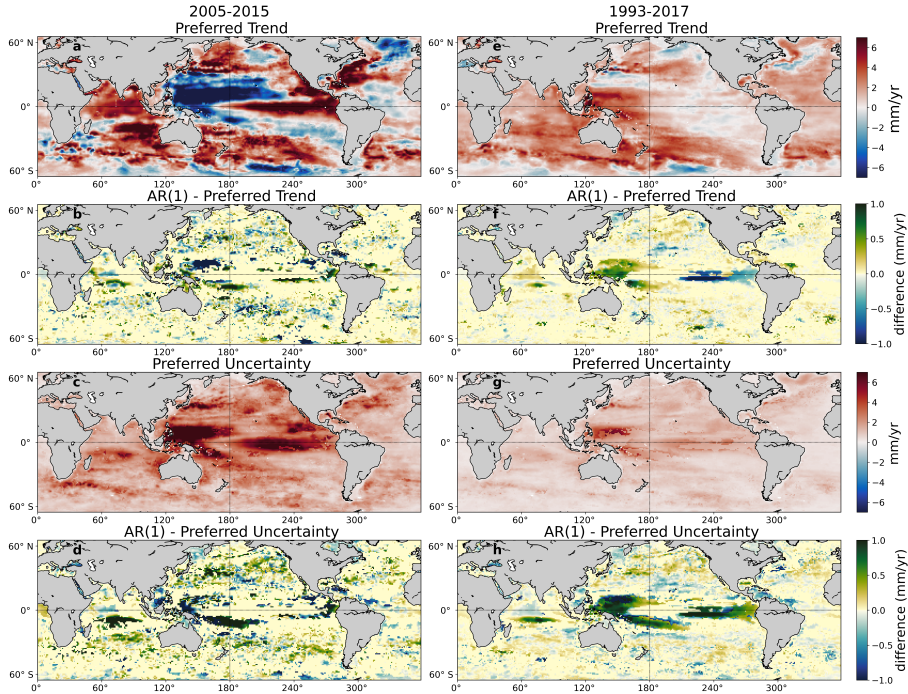


Figure 2.8: Trend and uncertainty (mm yr^{-1}) for the ensemble mean using the preferred noise model for each grid (a,b,c,f) according to the mean of AIC and BIC (Figure 2.7e,f), and the differences between the estimates using AR(1) (Figure 2.5) and the preferred noise model (b,d,e,g), for (a-d) 2005-2015 and (e-g) 1993-2017.

2.5. DISCUSSION

There is no clear consensus in the literature of which criterion should be used to select the best noise model, either AIC or BIC (Burnham and Anderson, 2002) or even another criterion (Klees and Broersen, 2002). While Sonnewald et al. (2018) use only the AIC, Hughes and Williams (2010) advise using BIC, which has less spatial variability and thus would be more reliable than AIC. Figure 2.7 confirms this, since it displays more spatial

differences for AIC selection than for BIC. However, if the aim is to investigate the spatial variability, then using a stricter criterion might not be preferable. Still, the preference of AIC for higher order models and of BIC for simpler models is emphasized in Figures 2.3 and 2.7, as also reported by Sonnewald et al. (2018). To overcome these differences, we have chosen to compare and show both selection criteria, complemented by an ARMASA noise model analysis.

Our global mean analysis indicates that a first-order autoregressive AR(1) is the best descriptor of the residuals of the ensemble mean steric SLC. This contrasts with the findings of Bos et al. (2014b), who investigated the effect of noise models on global mean sea level, focusing on altimetry and tide gauge sea-level data. They found that for altimetry data, ARF and GGM models are equally preferred, followed by an AR(5) model. Although preferable to a white noise model, the GGM model was one of the least preferred models in our global analysis. When considering all datasets in the noise model analysis, our results indicate that AR(5) and ARF are among the best candidates for the global mean time series, partially in line with Bos et al. (2014b).

Regionally, our noise model analysis indicates that most of the oceans are best described by an AR(5) or AR(1) noise model. This agrees with the findings of Hughes and Williams (2010) and Royston et al. (2018), who both looked for the best noise model to describe regional sea level observed with tide gauges and satellite altimetry. While Hughes and Williams (2010) found that AR(5) is the best descriptor of the sea-level uncertainties, Royston et al. (2018) found that most of the regional monthly data (both from tide gauges and altimetry) can be described by the WN or AR(1) noise models. However, the WN model was almost never selected in our analysis. Both studies also highlight that the appropriateness of the noise model is ordered in larger spatial structures. The regional preference of the noise models (Figure 2.7) display spatial coherent patterns based on the temporal and spatial variability of the ocean processes. Our regional results agree to some extent with the spatial patterns described by previous works, particularly the preference of more complex models in the tropics and highly dynamic regions. The latter might be related to multiple baroclinic modes present in these regions (Hughes and Williams, 2010).

The physics of the spatial patterns reported by Hughes and Williams (2010) were also confirmed by Sonnewald et al. (2018), who investigated the linear predictability of sea surface height. Sonnewald et al. (2018) found that up to 50% of the sea surface height variability over 20 years is explained by a seasonal signal. This might explain why the uncertainties for 1993-2017 are smaller than the ones for 2005-2015, as the linear trend

becomes more important than the seasonal signal. The differences between noise model choices of previous studies (Hughes and Williams, 2010; Royston et al., 2018), that focused on tide gauge and altimetry data, and the present study, which focus on steric SLC, illustrate that the best noise model for steric SLC is not necessarily the best for total SLC. Hence, it is important to always analyse which noise model is most appropriate for each type of data, and to consider the effect of different spatial (global vs regional) and temporal (daily, monthly, annual) resolutions.

Several sea-level budget studies use a suite of datasets, where the spread around the ensemble mean is used to describe the uncertainty of the sea-level trends (e.g., Cazenave et al., 2018; Gregory et al., 2013). This can result in misrepresentation of the uncertainty. For example, if we consider the 1-sigma spread of the estimated trends, then we would obtain an uncertainty of 0.71 and 0.36 mm yr^{-1} , whereas with the AR(1) noise model we obtain uncertainties of 0.10 and 0.07 mm yr^{-1} for 1993-2017 and 2005-2015, respectively. In some other cases, the authors do not mention how the uncertainties were obtained or what they represent in detail (e.g., Leuliette, 2015), making it difficult to interpret and compare steric estimates in the literature. As our results show, the noise model has an effect not only on the uncertainty, but also on the derivation of the trend itself. This is expected once the stochastic model is incorporated in the least-squares regression (Bos et al., 2014b). We caution that future studies should carefully describe how uncertainty estimates have been obtained, as this aids physical interpretation.

While we find that the noise model has the strongest effect on the uncertainty, our results show that differences in the trend are mainly a result of the dataset choice, both at a regional scale (Figure S2.9) and for the global mean (Figure 2.2). Most of the differences was seen within the reanalyses products, mainly the FOAM dataset. A possible explanation can be the incorporation of temperature and salinity data from instrumented marine mammals (Carse et al., 2015), which may lead to a high bias in the salinity values. Furthermore, the energy of deep currents (1000m) is highly overestimated in FOAM Desportes et al. (2019). However, in comparison with other ocean reanalyses, FOAM estimates are the closest to tropical mooring observations Desportes et al. (2019), and should not be discarded.

The WRCP sea-level budget report (Cazenave et al., 2018) studied the same Argo period, from January 2005 to December 2015, and found an ensemble mean thermosteric sea-level trend of $1.31 \pm 0.40 \text{ mm yr}^{-1}$ based on eleven in-situ datasets, which is considerably higher than our ensemble mean of $1.08 \pm 0.07 \text{ mm yr}^{-1}$. However, Cazenave et al. (2018) only included thermosteric SLC and their rates are full depth: when excluding a deep

ocean contribution of $0.1 \pm 0.1 \text{ mm yr}^{-1}$, their estimate is within 2-sigma of ours. Amin et al. (2020) considered five datasets (APDRC, SIORG, BOA, EN4 and JAMESTEC) to obtain a global mean steric sea-level trend for 2005-2016. Compared to our trends, both for individual datasets and for the ensemble, all the values agree within the uncertainty ranges, despite the extra year in their analysis.

For 1993-2015, the WCRP report (Cazenave et al., 2018) found a thermosteric trend of $1.32 \pm 0.4 \text{ mm yr}^{-1}$, while Dieng et al. (2017) found a steric sea-level trend of $1.13 \pm 0.12 \text{ mm yr}^{-1}$ for the same period, both based only on in-situ datasets. Keeping in mind that these values are full depth and the period two years shorter than ours, they match our steric trend well for 1993-2017 ($1.33 \pm 0.11 \text{ mm yr}^{-1}$). By merging several reanalyses products, Storto et al. (2019) found a steric sea-level trend of $1.98 \pm 0.3 \text{ mm yr}^{-1}$ for 1993-2016. Their trend agrees, within the uncertainty range, with our reanalysis category mean, corroborating our findings. Although our trends agree within uncertainties with the values found in the literature, our uncertainty values are generally smaller than the previously reported ones, showing the added value of the noise model analysis.

Our results show that the variation of the steric sea-level trends from the use of different datasets can be reduced by using an ensemble of datasets. This is in line with the assumption that the systematic biases of the individual datasets are reduced by the averaging process (Storto et al., 2017). However, Rougier (2016) argues that the offsetting of biases alone is not a good reason to use the ensemble mean, as one should not expect that individual datasets will have such fundamental differences. Rougier (2016) poses that the ensemble mean does not contain all of the variability of the true process, which can result in underestimating the true sea-level trend and uncertainty. Instead of using the ensemble mean, one could use the dataset with the lowest root-mean-squared error in relation to the ensemble mean, which will retain the variability of an individual dataset around the mean of the ensemble (Rougier, 2016; Royston et al., 2018). In our analysis, the ISAS+ and C-GLORS datasets are closest to the ensemble means for 2005-2015 and 1993-2017, respectively. For the global mean, the uncertainty of both datasets is best described by the AR(5) model. The regional pattern of preferred noise models (Figure S2.7) is dominated by AR(9) for 2005-2015 and by AR(5) for 1993-2017. Compared to the ensemble mean, the noise model selection according ISAS+ and C-GLORS displays more spatial variability, especially for the shorter time period. By construction, the final trend and uncertainty patterns for ISAS+ and C-GLORS (Figure S2.8) are similar to the ensemble mean (Figure 2.8), though displaying higher spatial frequency features.

2.6. CONCLUSION

Motivated by the large discrepancies in dealing with uncertainties in the sea-level datasets, and the wide variety in steric sea-level trends published in the literature, this paper explored the variation in present-day steric SLC estimates. Two sources of variation were investigated: the uncertainties caused by the use of different datasets and by the use of different noise models to describe the residuals. We analysed fifteen datasets and eight noise models and showed the different rates and uncertainties of steric SLC for two time periods (2005-2015, the Argo period, and 1993-2017, the satellite altimetry era). By simultaneously varying all the datasets and noise models, the 2005-2015 global mean steric sea-level trend varied from 0.56 to 2.33 mm yr^{-1} and the uncertainty from 0.02 to 1.65 mm yr^{-1} .

Although the noise models are mainly used to describe the uncertainties of time series, we found that they also affect, to a smaller degree, the trend itself. By alternating the eight noise models for the ensemble mean, the 2005-2015 global mean steric sea-level trend varied from 1.07 ± 0.03 mm yr^{-1} to 1.11 ± 0.19 mm yr^{-1} . This illustrates the significant impact of the noise model on the uncertainty, which was even stronger on the regional scale. Our noise model analysis suggests that a first-order autoregressive (AR(1)) is the most appropriate model to describe the residual behaviour of the global mean steric SLC of the ensemble mean, and consequently leads to the most representative uncertainty. Regionally, a combination of different noise models is required to best describe steric SLC and its uncertainty. While AR(1) was the preferred noise model for most of the regions, ultimately the most appropriate noise model depends on the study location. The spatial coherence in the noise model preference shows clusters that have similar dynamics, which can be used to investigate the regional sea-level budget.

Compared to the noise model, the choice of the dataset has a stronger influence on the estimated trend. By alternating the datasets while keeping the AR(1) noise model fixed, the steric SLC varied from 0.66 ± 0.12 mm yr^{-1} to 1.86 ± 0.27 mm yr^{-1} for 2005-2015. Using an ensemble mean of several datasets reduces the effect of uncertainties from a single dataset and gives a more robust estimate of the observed steric change. There are distinct differences in the trends between the three categories of datasets: reanalysis, multiple in-situ and only Argo. While the reanalyses products have clear advantages, such as covering longer periods and depths than in-situ based datasets, there is a large spread of the results within the reanalysis category. Using only one reanalysis product to estimate the steric SLC might lead to a considerable over- or underestimation of the trend.

This study showed that the choice of dataset and noise model results in large differences

in the steric sea-level trend and the associated uncertainty. We therefore recommend that studies on sea-level trends and sea-level budgets perform a noise model analysis and report which noise model was used to determine the trend. A first-order autoregressive (AR(1)) noise model and an ensemble of datasets provide the best estimate of the steric contribution to global mean SLC up to at least 25 years. For the purpose of describing regional variations, more complex noise models are needed, such as higher order autoregressive ones.

2.7. SUPPLEMENTARY INFORMATION

2.7.1. SUPPLEMENTARY TEXT

Selection of noise models in Hector

The noise models obtained with Hector were investigated using the Akaike Information Criterion:

$$AIC = 2k + 2\ln L \quad (2.2)$$

and the Bayesian Information Criterion:

$$BIC = k\ln N + 2\ln L \quad (2.3)$$

where k is the number of parameters included in the model, $\ln L$ is the log-likelihood, and N is the number of observations.

Since AIC and BC are relative values, they cannot be compared between different time series. Thus, we compared the criteria of different noise models for each time series separately. The best noise model is the one which minimizes both AIC and BIC (Liddle, 2007).

For the AIC selection, we computed the relative likelihood of AIC as:

$$RL_{AIC_i} = \exp\left(\frac{AIC_{min} - AIC_i}{2}\right) \quad (2.4)$$

where AIC_{min} is the lower AIC value for a given dataset, and AIC_i is the score of a noise model for a given dataset (Burnham and Anderson, 2002; Burnham et al., 2011). Any noise model with a RL_{AIC} higher than 0.5 was considered suitable.

For the BIC selection, we computed the relative BIC difference as:

$$\Delta BIC_i = BIC_i - BIC_{min} \quad (2.5)$$

where BIC_{min} is the lower BIC value for a given dataset, and BIC_i is the score of a noise model for a given dataset (Burnham and Anderson, 2002). Any ΔBIC_i smaller than 2 was selected as a suitable noise model. The threshold value of 2 is considered as a positive evidence that the noise model performed well (Liddle, 2004).

To find the preferred noise model, we considered AIC, BIC and the mean of both criteria, and selected the noise model that at least two of the criteria selected. If there was no

consensus, then two (or more) noise models were considered suitable for a given time series.

ARMASA Software

ARMASA (Broersen, 2022) was used as a complementary tool to identify the ideal order and model type of a residual time series. A detailed explanation of the software is given in Klees and Broersen (2002). From a residual (noise) time series, we first used the software to compute several autoregressive, moving average, and autoregressive moving average models (AR(p), MA(q) and ARMA(p',p'-1), respectively) models, up to a maximum order. The maximum order of p, q, and p' is defined by the number of observations of the time series, as:

$$p_{max} = \min\left(\frac{N}{2}, 1000\right) \quad (2.6)$$

$$q_{max} = \min\left(\frac{N}{5}, 200\right) \quad (2.7)$$

$$p'_{max} = \min\left(\frac{N}{10}, 100\right) \quad (2.8)$$

where N is the number of observations. Thus, in our case, the maximum orders of p were 150 and 132, of q were 60 and 26 and of p' were 30 and 13, for the time series from 1993-2017 (N=300) and from 2005-2015 (N=132), respectively.

Next, the best-fitting model for each model type is selected in ARMASA, based in the Combined Information Criterion (CIC) for AR(p) models, and the Generalized Information Criterion (GIC) for MA(q) and ARMA(p',p'-1), being:

$$CIC = \ln(\sigma^2 \prod_p^{k=1} (1 - a_{k,k}^2)) + \max\left(\prod_p^{k=1} \left(\frac{1 + 1/(N+1-k)}{1 - 1/(N+1-k)} - 1, 3 \sum_{K=1}^p \frac{1}{N+1-k}\right)\right) \quad (2.9)$$

and

$$GIC = \ln(\sigma^2 \prod_p^{k=1} (1 - a_{k,k}^2)) + 3 \frac{q}{N} \quad (2.10)$$

where K is the number of parameters included in the model, and N is the number of observations (Broersen, 2000)

After the best-fitting AR(p), MA(q) and ARMA(p',p'-1) have been selected, ARMASA uses the minimum prediction error (PE) to select the most suitable model between the three model types. The PE for AR(p) model is defined as:

$$PE(p_{AR}) = RES(p_{AR}) \prod_{k=1}^{p_{AR}} \frac{1 + 1/(N + 1 - k)}{1 - 1/(N + 1 - k)} \quad (2.11)$$

where $RES(p_{AR})$ is the residual variance of the AR model. For the best-fitting MA(q) and ARMA(p',p'-1) models, PE is defined as:

$$PE(m) = RES(m) \cdot \frac{1 + m/N}{1 - m/N} \quad (2.12)$$

where m is the number of estimated parameters, and RES(m) is the residual variance of the model. Finally, the model with the smallest PE is selected as the best model for the residual time series. For each global mean time series, we checked which order of the three model types ARMASA indicated, and then which of the three models was chosen as the best.

In addition, we also visually checked the power spectra of the of the residuals (example in Figure S2.1), used as input for ARMASA against the spectrum of the models chosen by the software.

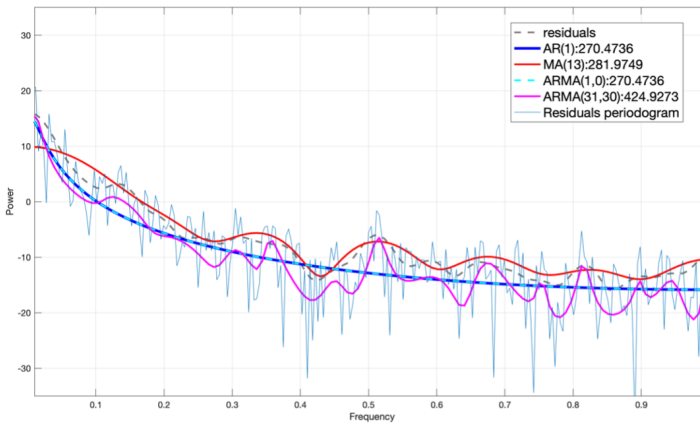


Figure S2.1: Power spectrum of the best-fitting noise models from ARMASA for the ensemble mean of 1993-2017, with the PE for each model given in the legend.

2.7.2. SUPPLEMENTARY FIGURES & TABLES

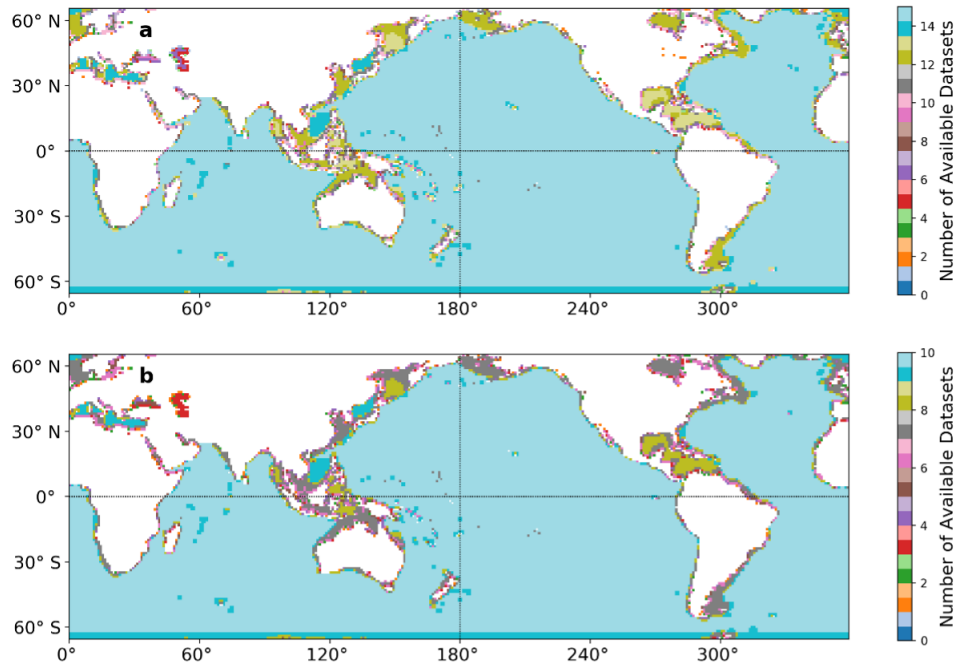


Figure S2.2: Number of datasets available at each grid point after applying the land mask for (a) 2005-2015 and (b) 1993-2017. The maximum number of datasets was 15 for the 2005-2015 period, and 10 for the 1993-2017 period.

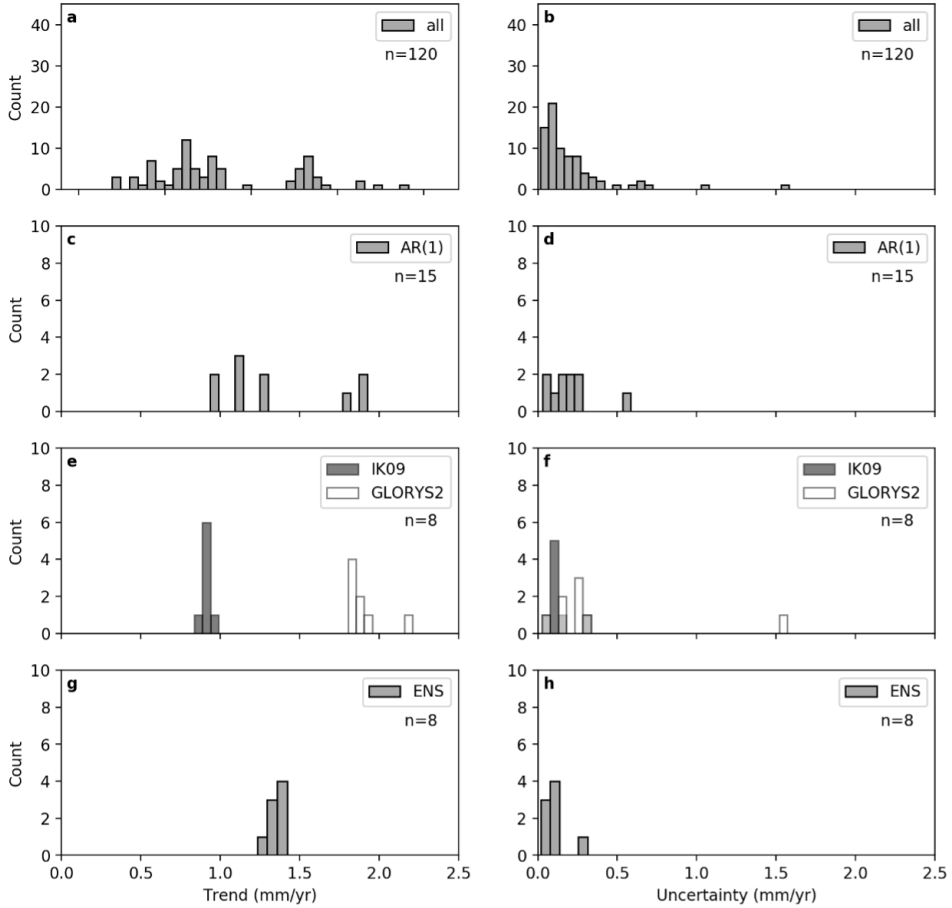


Figure S2.3: Histogram of the trend (left column) and uncertainty (right column) in mm yr^{-1} from 1993-2017 by (a,b) varying all datasets and noise models, (c,d) for the AR(1) noise model when varying all the datasets, (e,f) for the IK09 (white) and Glorys (grey) datasets when varying all the noise models, (g,h) for the ensemble mean when varying all the noise models.

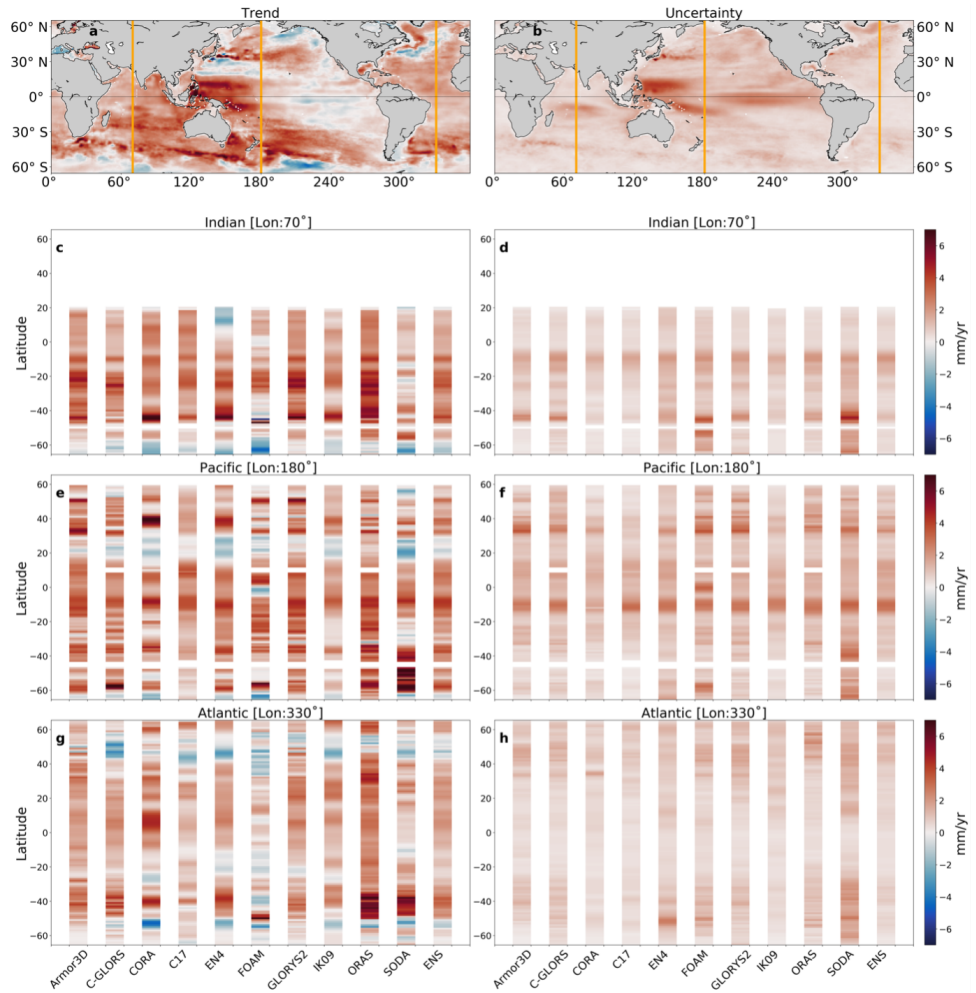


Figure S2.4: (a) Trend and (b) uncertainty from 1993-2017 estimated with the AR(1) noise model, and the latitudinal transects (displayed in orange), as a function of the dataset (x-axis) for (c,d) Indian, (e,f) Pacific and (g,h) Atlantic Ocean transect.

2

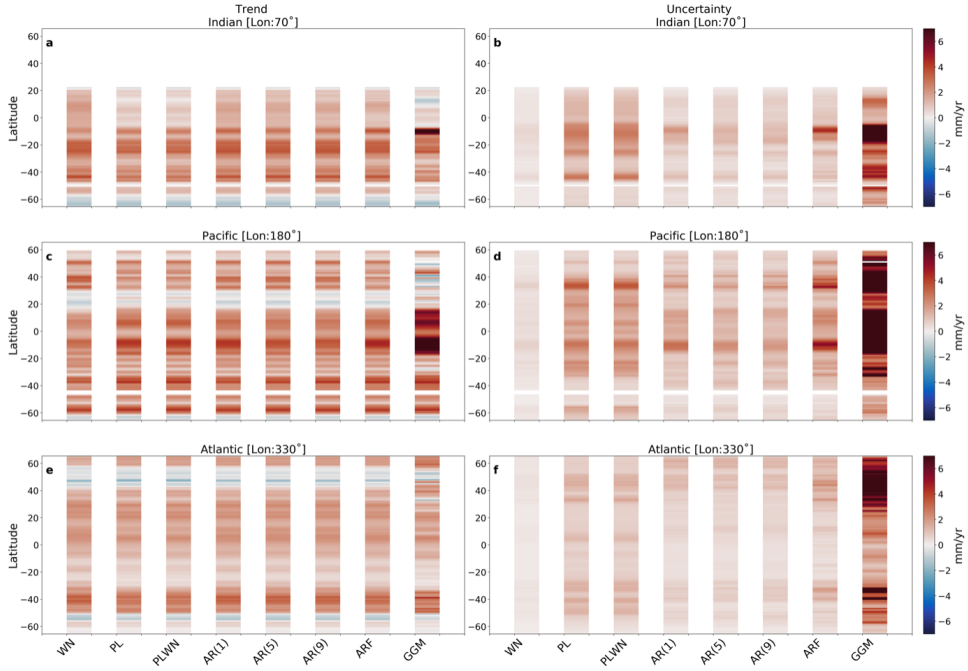


Figure S2.5: Trend (left column) and uncertainty (right column) for the ensemble mean from 1993-2017, as a function of latitude (y-axis) and noise model (x-axis) for (a,b) Indian, (c,d) Pacific and (e,f) Atlantic Ocean transect.

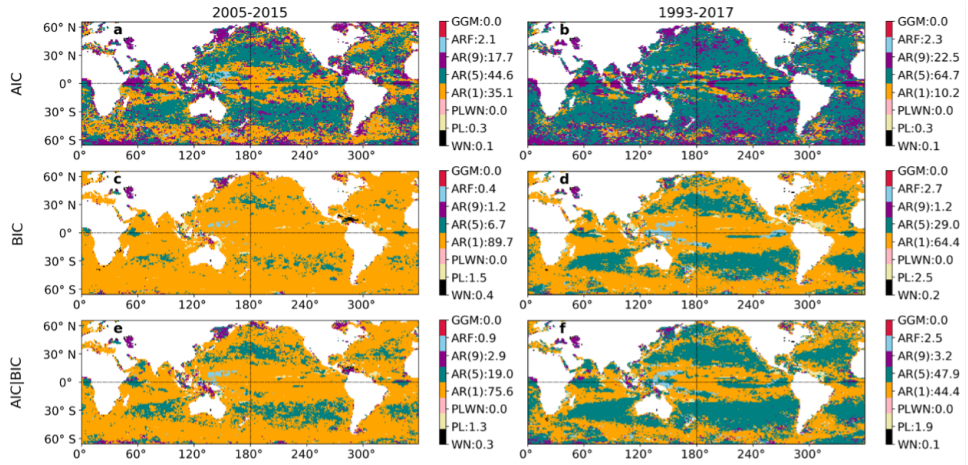


Figure S2.6: Regional noise-model selection for 2005-2015 (left column) and 1993-2017 (right column) for the all the datasets available (15 from 2005-2015, and 10 from 1993-2017), based on (a,b) AIC, (c,d) BIC and (e,f) mean of AIC and BIC.

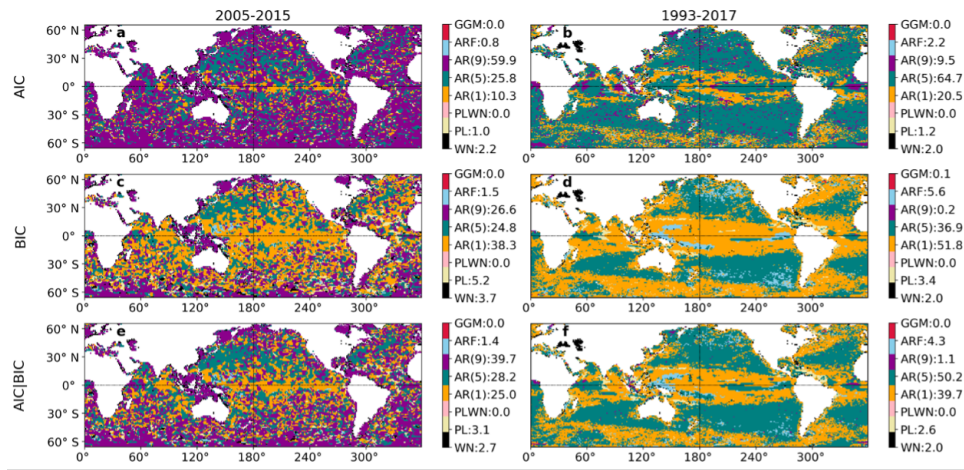


Figure S2.7: Preferred noise model for each gridpoint for the (a,c,e) ISAS+ from 2005-2015, and for (b,d,f) C-Glors for 1993-2017, with the respective percentage of the total ocean area selected by each noise model, based on (a,b) AIC, (c,d) BIC and (e,f) the mean of AIC and BIC.

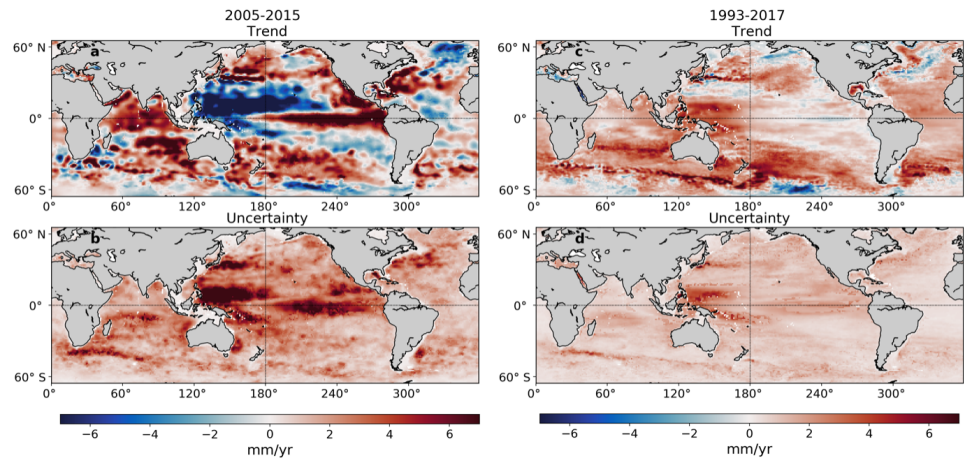


Figure S2.8: Trend and uncertainty for (a,b) ISAS+ from 2005-2015, and for (c,d) C-Glors for 1993-2017 using the preferred noise model according to the mean of AIC and BIC (Figure S2.7).

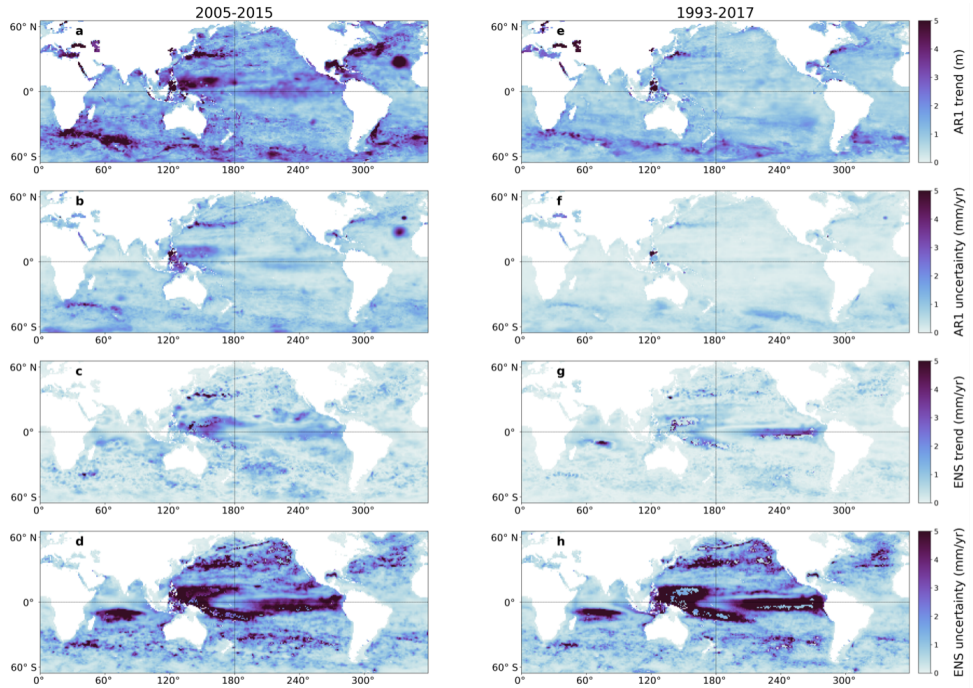


Figure S2.9: Standard deviation of the (a,e,c,g) trend and (b,f,d,h) uncertainty from (a-d) 2005-2015 and (e-g) 1993-2017, for the (a,b,e,f) AR(1) noise model and all datasets, and for the (c,d,g,h) ensemble mean (ENS) and all noise models.

Table S2.1: AR(1) trends ± 1 -sigma for all the datasets (in mm yr^{-1}), and R^2 values in relation to the ensemble mean.

	2005-2015		1993-2017	
	Trend $\pm \sigma$ (mm yr^{-1})	R^2	Trend $\pm \sigma$ (mm yr^{-1})	R^2
APDRC	1.06 ± 0.13	0.81		
SIORG	1.06 ± 0.14	0.84		
BOA	0.81 ± 0.12	0.68		
ISAS	0.89 ± 0.07	0.93		
Argo category mean	0.90 ± 0.09	0.91		
ISAS+	0.89 ± 0.06	0.93		
Armor3D	0.66 ± 0.12	0.76	1.78 ± 0.23	0.84
CORA	1.02 ± 0.10	0.93	1.26 ± 0.16	0.75
C17	1.10 ± 0.07	0.90	1.11 ± 0.03	0.85
EN4	1.22 ± 0.09	0.90	1.26 ± 0.05	0.93
IK09	1.10 ± 0.11	0.93	0.94 ± 0.08	0.67
MiS category mean	1.00 ± 0.07	0.98	1.24 ± 0.08	0.89
C-GLORS	1.35 ± 0.12	0.95	1.14 ± 0.19	0.96
FOAM	1.79 ± 0.65	0.52	0.97 ± 0.58	0.37
GLORYS2	1.10 ± 0.26	0.76	1.92 ± 0.28	0.85
ORAS	1.86 ± 0.27	0.86	1.89 ± 0.17	0.81
SODA	0.90 ± 0.13	0.83	1.14 ± 0.21	0.90
REA category mean	1.40 ± 0.21	0.93	1.47 ± 0.23	0.94
ENS mean	1.08 ± 0.07		1.36 ± 0.10	

2.8. APPENDIX: THE DEEP OCEAN STERIC CONTRIBUTION

Recent studies highlight the importance of the deep ocean (below 2000m depth) in closing the heat and sea-level budgets (e.g., Purkey and Johnson, 2010; Ponte, 2012; Llovel et al., 2014). While the contribution of the deep ocean to the global mean sea level is small, about 0.1 mm yr^{-1} , regionally it can have an important role: in the Southern Ocean, for example, the deep layers contribute up to 1 mm yr^{-1} of sea-level rise (Purkey and Johnson, 2010). Thus, including the deep ocean warming is imperial for sea-level and energy budget studies in both global and regional scales. However, proper detection of the deep ocean signature to the heat budget is still not possible due to large uncertainties in the current observing system (von Schuckmann et al., 2013). Despite the considerable improvement of in-situ observations of temperature and salinity, especially since the Argo project, the deep ocean continues under sampled (Ablain et al., 2017; von Schuckmann et al., 2013). Consequently, there is no clear consensus on how much abyssal waters have contributed to the sea-level and energy budgets.

In this chapter (main text), we investigated how the use of different temperature and salinity datasets can influence the regional and global steric SLC. Upper ocean (down to 2000 m depth) density changes contributed to a global mean steric SLC of $1.36 \pm 0.10 \text{ mm yr}^{-1}$ from 1993-2017. However, depending on the dataset used, this trend can range from 0.69 to 2.40 mm yr^{-1} . Consequently, using an ensemble of several datasets provide a more robust estimate. To keep the large uncertainties of the deep ocean from obfuscating the uncertainties of the upper ocean, we did not include the deep ocean in our analysis. In this appendix, we explore the contribution of the deep ocean to SLC, based on the same datasets used for the upper ocean.

DEEP STERIC ESTIMATES

Some of the temperature and salinity datasets used in this chapter cover the entire water column (see *Depth range* column on Table 2.1): the objective analyses EN4 (Good et al., 2013) and ARMOR3D (Guinehut et al., 2012), and the ocean reanalyses C-GLORS (Storto and Masina, 2016, ,GREPv2), GLORYS (Garric and Parent, 2017), FOAM-GloSea (Blockley et al., 2014; Maclachlan et al., 2015), ORAS5 (Zuo et al., 2019) and SODA3 (Carton et al., 2018). By using all the depth layers provided with these datasets, we can estimate the full depth steric SLC (η_{full}). Then, by removing the upper ocean estimates ($\eta_{0-2000m}$) from each dataset, we can obtain the contribution of the deep layers (η_{deep}):

$$\eta_{deep} = \eta_{full} - \eta_{0-2000m} \quad (2.13)$$

For comparison, we also use the updated deep steric sea-level estimates of Purkey and Johnson (2010); Purkey et al. (2019), hereon referred as 'PJ'. These estimates are based on repeated hydrographic measurements between 1990-2019.

REVISITING THE THE DEEP OCEAN CONTRIBUTION TO SEA-LEVEL CHANGE

The estimates based on ocean reanalyses and objective analyses show diverging trends (Figure A2.1), both regionally and globally. For example, the EN4 dataset has mainly positive contributions and a global average of 0.08 mm yr^{-1} . On the other hand, the GLORYS reanalysis has prevailing negative values and a global average of -0.36 mm yr^{-1} . Another striking difference is the SODA dataset, which has an anomalously warm deep ocean, with a contribution of 1.09 mm yr^{-1} to the global mean SLC. The diverging trends are in line with Storto et al. (2019), who found that steric sea-level trends below 2000 m depth from several ocean reanalyses are less consistent than for the upper ocean and not robust. This is a consequence of the limited in-situ sampling of the deep ocean, which is assimilated by the reanalyses (Storto et al., 2019). The global averages of EN4 and CGLORS are in agreement with the in-situ based trend of Purkey and Johnson (2010), with a mean value of 0.08 mm yr^{-1} . These trends also agree with recent estimates of Chang et al. (2019) and Yang et al. (2021), who estimated a deep ocean contribution of $0.12 \pm 0.03 \text{ mm yr}^{-1}$ and $0.07 \pm 0.18 \text{ mm yr}^{-1}$ to global mean sea-level rise from 2005-2015, respectively. The estimates of Chang et al. (2019) are based on a mathematical model applied to CTDs (hydrographic data) and deep-Argo floats, while Yang et al. (2021) inferred the deep ocean contribution from a sea-level budget analysis (i.e., deep ocean is the residual of altimetry minus Argo measurements from 0-2000m and GRACE ocean mass changes).

Regionally, observational based trends show that the Southern Ocean is the main contributor to deep warming (Purkey and Johnson, 2010; Kouketsu et al., 2011; Desbruyères et al., 2016). In specific, the Subantarctic Front is an important source of deep warming (see for example Figure 3 of Kouketsu et al. (2011)). From the ocean products used here, FOAM is the closer to the regional patterns of PJ, followed by EN4 and CGLORS datasets. The Indian Ocean is, in most cases, marked by a negative trend. However, the Indian Ocean is the one with fewer in-situ observations, hence estimates in this region are less accurate (Purkey and Johnson, 2010; Kouketsu et al., 2011), even in ocean reanalyses. All of our datasets, except for PJ, show positive trends in the North Atlantic Ocean, suggesting that the models do not capture the cooling seen in the observations. It is important to note that in Purkey and Johnson (2010) and Kouketsu et al. (2011) the Northwestern Atlantic does not show any negative trends, only some small warming. Extending the in-situ record of Purkey and Johnson (2010) revealed a warming-to-cooling tendency in

the North Atlantic (Desbruyères et al., 2016). The opposite behaviour, that is, a cooling-to-warming tendency, appears in the Southeastern Atlantic. Thus, we can conclude that the models need a longer record to capture these tendencies.

2

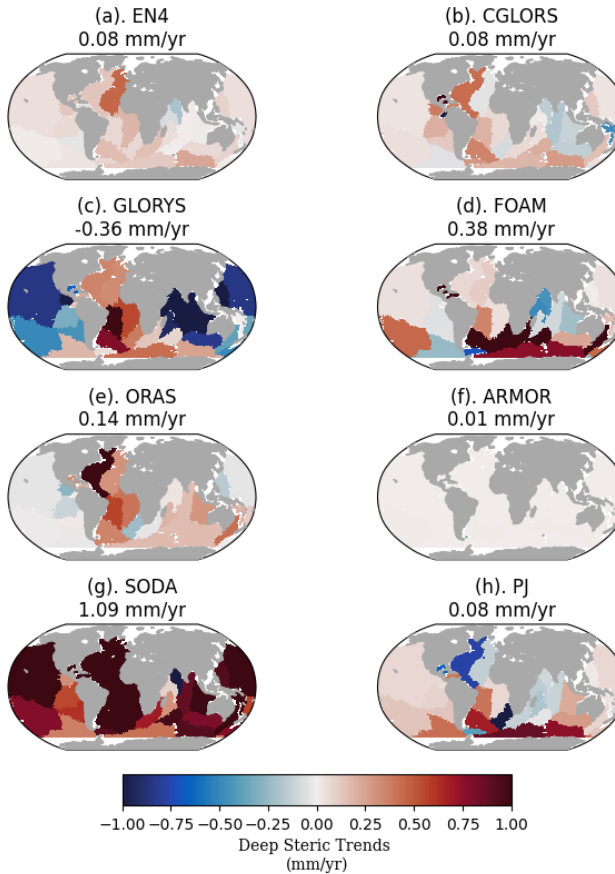


Figure A2.1: Contribution of the deep ocean to regional steric sea-level change for (a) En4, (b) ARMOR, (c) SODA, (d) GLORYS, (e) C-GLORS, (f) FOAM, (g) ORAS.

The ensemble mean of the ocean products (both objective analysis and ocean reanalyses) are shown in Figure A2.2. The deep warming in the Southwestern Atlantic basin, noted by Purkey and Johnson (2010); Storto et al. (2019), is reflected in the ensemble mean. On the other hand, the cooling tendency in the North Atlantic is not represented in the ensemble mean. However, we must reinforce that the quantification of deep ocean processes from reanalyses are not robust (Storto et al., 2019), thus the ensemble mean should be carefully interpreted. In general, the uncertainty of temperature and salinity data in ocean reanalyses is larger than the signal itself, that is, the deep ocean changes in

the reanalyses are not statistically significant (Gasparin et al., 2020). The main divergence of the ocean products can be seen in the Southwestern Atlantic Ocean, in the confluence zone of the Brazil and Malvinas ocean currents, and in and in the Southwestern Indian Ocean, close to Kerguelen Islands. The diverging rates, illustrated by ocean products here (Figure A2.1) and ocean models experiments (Garry et al., 2019), stresses the importance of improving deep ocean sampling.

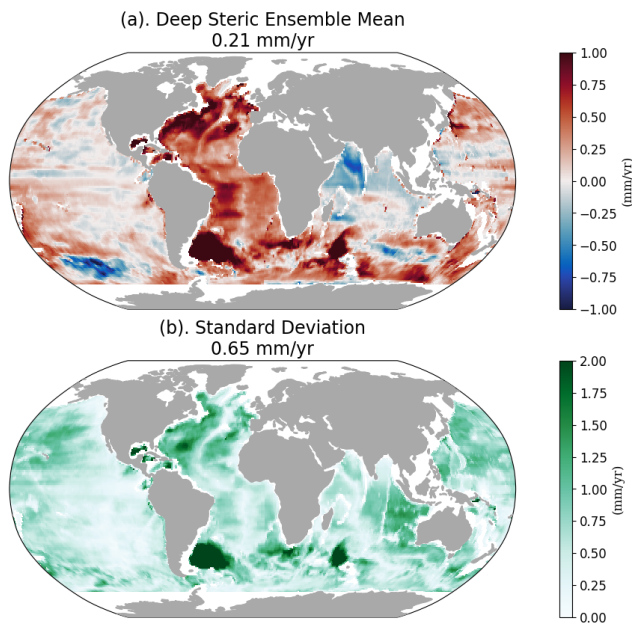


Figure A2.2: (a) Contribution of the deep ocean to regional steric sea-level change from ensemble mean of reanalyses (Figure A2.1). (b) Standard deviation of the ensemble mean.

THE IMPORTANCE OF DEEP OCEAN OBSERVATIONS

As a consequence of the limited data assimilated in such depths, deep steric estimates from ocean reanalyses and objective analysis are not robust. Deep steric estimated based on repeated hydrographic measurements are more consistent (e.g., Purkey and Johnson, 2010; Desbruyères et al., 2016; Chang et al., 2019; Cha et al., 2021), and seems to agree with those obtained by the budget approach (Yang et al., 2021). **We recommend that, up to this point, repeated hydrographic measurement should be used for deep steric estimates.** On the other hand, an ocean model study indicated that sparse ocean observation can lead to an overestimation of the (model) truth (Garry et al., 2019). Current assimilation systems, which ocean reanalyses are based on, have the ability to reproduce observed

deep trends in some regions, but their performance is limited due to the sparsity of the assimilated data (Kouketsu et al., 2011; Gasparin et al., 2020). The only way of overcoming these limitations is by improving the deep ocean observation system.

2

Since the early 2000s, the Argo program has been successfully sampling the upper ocean, with an almost global coverage since 2005 (Roemmich et al., 2009). Consequently, we have currently a very good understanding of large-scale variability in the upper ocean. On the other hand, half of the ocean volume is below 2000m depth, and continues under sampled (Wunsch and Heimbach, 2014). To fill this gap, a "Deep Argo array" is being developed, with plans to continuously measure the deeper waters of the oceans on a global scale (Johnson et al., 2015). To properly detect deep ocean variability, at least 1200 floats are necessary (Johnson et al., 2015), which is about a third of the current number of floats sampling the upper ocean (on October 2022, there were 3880 active argo floats on <https://argo.ucsd.edu/about/>). Gasparin et al. (2020) demonstrated the the current ocean reanalyses system, in specific the GREP products (C-GLORS, GLORYS, FOAM-GloSea and ORAS), would be successfully constrained by deep Argo observations. That is, deep water masses changes and variability can be detected in the reanalyses once the Deep Argo array is included. The development of the Deep Argo array is, therefore, essential to accurately estimate the deep ocean contribution to SLC.

3

MASS-DRIVEN SEA-LEVEL CHANGE

An illustration of three icebergs in a blue ocean. One large iceberg is on the left, a smaller one is in the center foreground, and another is on the right. The rightmost iceberg is partially submerged, with its dark blue underwater portion visible. The background shows a horizon line with a yellow sun or moon.

Published as: Camargo, C. M. L., Riva, R. E. M., Hermans, T. H. J., & Slangen, A. B. A. (2022). *Trends and Uncertainties of Mass-driven Sea-level Change in the Satellite Altimetry Era*, Earth System Dynamics, 13, doi: 10.5194/esd-13-1351-2022

3.1. INTRODUCTION

Even if all countries respect to the Paris Agreement, global mean sea level will continue to rise in the coming decades and beyond (Wigley, 2005; Nicholls et al., 2007; Oppenheimer et al., 2019; Fox-Kemper et al., 2021). The reason for this is the long response time of the ocean and the cryosphere to climate change (Abram et al., 2019). As a consequence, coastal societies all over the world will need to deal with a certain amount of sea-level change (SLC). Therefore, a good understanding of present-day SLC and its drivers is required, as it yields better future sea-level projections, which are necessary for adaption and mitigation planning.

The attribution of SLC to its different drivers is known as the sea-level budget (Cazenave et al., 2018). Alongside density driven (steric) changes (e.g., MacIntosh et al. (2017); Camargo et al. (2020)), present-day SLC is mainly driven by the mass loss of continental ice stored in glaciers and ice sheets, and by variations in land water storage (LWS) (Cazenave et al., 2018; Fox-Kemper et al., 2021). The contribution of ocean mass changes, termed barystatic SLC (Gregory et al., 2019), was responsible for about 60% of the global mean SLC over the 20th century (Frederikse et al., 2020; Fox-Kemper et al., 2021). Barystatic SLC varies significantly from region to region and strongly depends on the location of terrestrial mass loss (Mitrovica et al., 2001). For example, a collapse of the West Antarctic Ice Sheet would cause sea level to rise 1.6 times more in San Francisco (US) than in Santiago (Chile) (Gomez et al., 2010). Thus, for local management and climate planning, it is important to know the barystatic contribution to regional SLC (Larour et al., 2017).

The regional patterns associated with barystatic SLC can be computed by solving the sea-level equation (SLE) (Farrell and Clark, 1976), which results in the so-called sea-level fingerprints (Mitrovica et al., 2001). These patterns reflect the so-called gravitational, rotational and deformation (GRD) response of the Earth to mass redistribution (Gregory et al., 2019). GRD-induced sea-level fingerprints have been the subject of several studies, ranging in scope from paleoclimatic SLC, for example due to the last deglaciation event (Lin et al., 2021), to contemporary SLC (Frederikse et al., 2020) and future sea-level projections (e.g., Slangen et al. (2012, 2014)). Most of the studies including present-day mass contributions have focused either on the GRACE satellite period (since 2002) (Bamber and Riva, 2010; Riva et al., 2010; Hsu and Velicogna, 2017; Adhikari et al., 2019; Frederikse et al., 2019), on the closure of the sea-level budget over a longer period (Slangen et al., 2014; Frederikse et al., 2020) or on their contribution to global mean SLC (Chambers et al., 2007; Horwath et al., 2022). However, an in-depth analysis of the GRD-induced regional patterns associated with barystatic SLC and its uncertainties during the satellite altimetry

era (since 1993) has not yet been done. Insights into the contemporary contributions of ice sheets, glaciers and land water storage to regional SLC and their uncertainties over the last three decades are important to constrain regional sea-level projections and obtain a better closure of the regional sea-level budget.

The importance of quantifying the uncertainties in sea-level studies has increasingly received attention (Bos et al., 2014b; Royston et al., 2018; Ablain et al., 2019; Camargo et al., 2020; Palmer et al., 2021; Prandi et al., 2021; Horwath et al., 2022). One of the approaches to describe the uncertainties of a system is to partition the total uncertainty budget into different kinds of uncertainties. Errors in the measurement system, known as intrinsic uncertainties (Palmer et al., 2021), describe the sensitivities of choices within a methodology (Thorne, 2021). The intrinsic uncertainties, also referred as observational (Ablain et al., 2019; Prandi et al., 2021) or parametric (Thorne, 2021), need to be determined during the low-level data processing and are usually provided with higher level (ready-to-use) products. Another class of uncertainties originates from the use of different methodologies to describe the same physical system, known as structural uncertainty (Thorne et al., 2005; Palmer et al., 2021). This can be defined as the spread around a central (ensemble) estimate. The structural uncertainty is related to the use of different datasets of the same process. Note that, if different datasets use the same product for corrections, calibrations and/or validation, the intrinsic and structural uncertainties could be partially correlated. Regarding the GRD-induced pattern associated with barystatic SLC, the spread in the location of the mass change introduces another source of error, which we call spatial uncertainty. Finally, another type of uncertainty results from the autocorrelation of the observations (Bos et al., 2013), which we refer to as temporal uncertainty. This uncertainty becomes relevant when a functional model, such as a (linear) trend, is used to describe the changes within the system. The temporal uncertainty can be estimated by using noise models while determining the trend. Together, the intrinsic, structural, spatial and temporal uncertainties describe the uncertainties of an observed quantity, in this case the GRD-induced pattern associated with barystatic SLC.

The aim of this work is to provide a comprehensive overview of barystatic SLC and the associated regional GRD-induced patterns with a focus on the global and regional uncertainty budget. Throughout this paper, we use ‘GRD-induced SLC’ when referring to the GRD-induced regional pattern associated with barystatic SLC. We use state-of-the-art datasets of mass contributions from land ice and LWS (Section 3.2.1) to compute regional sea-level fingerprints (Section 3.2.2). In addition, we present a methodological framework to describe the uncertainties of the fingerprints (Section 3.2.2). We follow the noise model

analysis of Camargo et al. (2020) to quantify the *temporal uncertainty* (Section 3.3.1;3.3.2). We combine the effect of ice geometry on sea-level fingerprints (Bamber and Riva, 2010; Mitrovica et al., 2011) with the structural uncertainty definition of Palmer et al. (2021), to compute the *spatial-structural uncertainty* of the fingerprints (Section 3.3.3). Together with the *intrinsic uncertainty* (Section 3.3.4), we present the total GRD-induced SLC trend and uncertainty for 2003-2016 and 1993-2016 (Section 3.3.5).

3

3.2. DATA AND METHODOLOGY

3.2.1. DATASETS

To obtain the GRD-induced SLC patterns we use a range of estimates of mass changes of the Antarctic and Greenland ice sheets (AIS and GIS, respectively), glaciers (GLA), and land water storage (LWS). We define LWS anomalies as water mass changes outside glacierized areas: the sum of water stored in rivers, lakes, wetlands, artificial reservoirs, snow pack, canopy and soil (groundwater) (Cáceres et al., 2020). For each of the contributions we use four different estimates (Table 3.1, Figure 3.1, and discussed in more detail in Supplementary Text 3.5.2). Despite the methodological differences between the datasets, they show a good agreement in reproducing the global mean barystatic sea-level changes (Figure 3.1)

One of the main sources of observations of Earth's mass changes is the satellite mission Gravity Recovery and Climate Experiment (GRACE, Tapley et al. (2004)) and its follow-on mission (GRACE-FO, Landerer et al. (2020)). We use GRACE mass concentrations (mascons) over land as estimates of changes in AIS, GIS, glaciers and LWS. To avoid methodological biases, we use mascon solutions from two different processing centres: RL06 from Center for Spatial Research (CSR) (Save et al., 2016; Save, 2020) and RL06 v02 from Jet Propulsion Laboratory (JPL) (Watkins et al., 2015; Wiese et al., 2019) (Table 3.1). JPL and CSR mascons are provided on a 0.5° and 0.25° lon-lat grid, respectively, but they actually are resampled from the native $3^\circ \times 3^\circ$ and $1^\circ \times 1^\circ$ equal-area grids (Save et al., 2016; Watkins et al., 2015). Considering the native resolution of GRACE observations of about 300km at the equator (Tapley et al., 2004), the JPL mascons should have independent solutions at each mascon centres, with uncorrelated errors, while the CSR mascons are not fully independent of each other and are expected to contain spatially correlated errors.

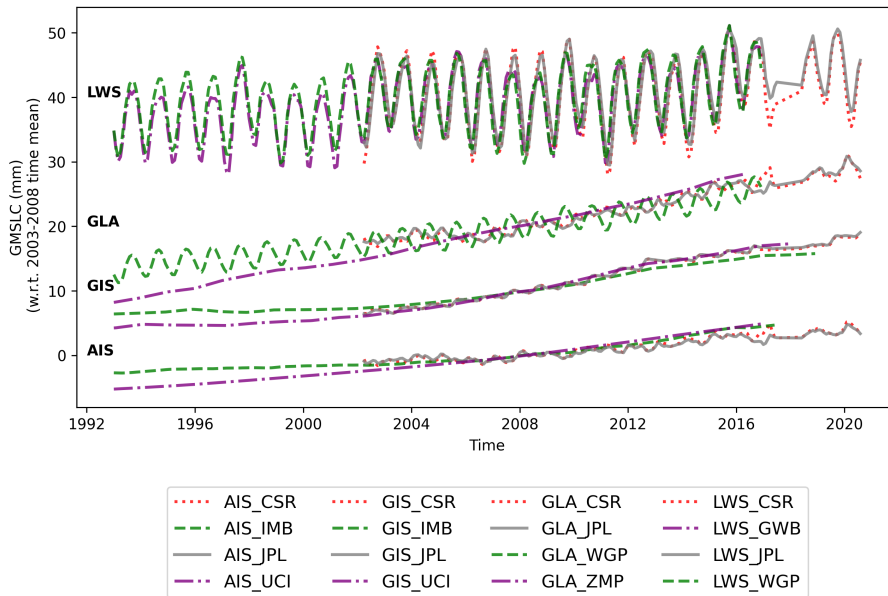


Figure 3.1: Global mean barystatic sea-level change time series. Different components are vertically offset for visualization purposes.

To isolate the individual contributions of AIS, GIS, LWS and GLA in the GRACE mascons, we use an ocean-land-cryosphere mask (Supplementary figure S3.1), which delineates the drainage basins of the ice sheets (based on Mouginot and Rignot (2019), Rignot et al. (2011)), the glaciers (based on the Randolph Glacier Inventory, RGI Consortium (2017)), and the remaining land regions (based on ETOPO1, Amante and Eakins (2009)). Considering the size of glaciers, the resolution of the GRACE signal is not high enough to (i) separate the peripheral glaciers from the ice sheets, and (ii) to separate the signal of glaciers and LWS in regions with small glacier coverage and large LWS contribution. Thus, to isolate the glaciers signals from the mascons we follow the method described in Reager et al. (2016) and Frederikse et al. (2019):

- (1) peripheral glaciers to Greenland and Antarctica are included with the ice sheets mass changes;
- (2) regions where glaciers dominate the mass changes are considered 'full' glaciers, that is, the land signals in those regions are purely denoted as glacier mass change. These include the RGI regions of Alaska, Arctic Canada North, Arctic Canada South, Iceland, Svalbard, Russian Arctic Islands and Southern Andes;

(3) for the remaining glaciated regions, we assume that the mass change is partly due to glacier mass change, and partly due to LWS ('split' glaciers). In these regions the glacier mass changes are known to be small and mass changes are dominated by LWS. We use the glacier estimates of Hugonnet et al. (2021), which are based on satellite and airborne elevation datasets as our glacier estimates in these regions. Unlike gravimetry observations, the estimates of Hugonnet et al. (2021) do not include the hydrological 'contamination'. To isolate the glacier from the LWS signal, we subtract the corrected glacier estimates from the total mass change in the mascons. The remaining signal is then added to the LWS contribution.

Apart from GRACE data, which is only available since late 2002, we use seven other datasets in our analysis, from which five are independent of GRACE and two partly incorporate GRACE information (Table 3.1. For LWS, we use data from two global hydrological models: PCR-GLOBWB (GWB, Sutanudjaja et al. (2018)) and WaterGAP (WGP, Cáceres et al. (2020)). The latter also incorporates a time series of glacier mass variations from the global glacier model of Marzeion et al. (2012). We use the ocean-land-cryosphere mask (Supplementary figure S3.1) to separate the LWS and GLA estimated from WGP. For GLA, in addition to the WGP model simulations, we also use observational estimates from Zemp et al. (2019), which are based on an extrapolation of glaciological and geodetic observations. For the GIS and AIS, we use observation- and model-based data from Mouginot et al. (2019) and Rignot et al. (2019), respectively. We refer to these as UCI datasets, since they were both developed at the University of California at Irvine (UCI). We also use AIS and GIS estimates from the ice sheet mass balance inter-comparison exercise (IMBIE, Shepherd et al. (2018, 2020)), which combines ice sheet mass balance estimates developed from three different techniques (satellite altimetry, satellite gravimetry (GRACE) and the input-output method).

Table 3.1: Overview of datasets used in this manuscript.

Contribution	Dataset	Temporal range	Source	Dependence*	Acronym	Spatial Resolution
All	CSR mascon RL06	2003-2020	observations	GRACE(-FO)	CSR	1°x1° **
	JPL mascon RL06	2003-2020	observations	GRACE(-FO)	JPL	3°x3° **
AIS	IMBIE 2018	1993-2016	ensemble datasets	Hybrid	IMB	Region mean
	Rignot 2019	1979-2017	observations + model	Independent	UCI	Drainage basin mean
GIS	IMBIE 2020	1993-2018	ensemble datasets	Hybrid	IMB	Region mean
	Mouginot 2019	1972-2018	observations + model	Independent	UCI	Drainage basin mean
Glaciers	Zemp 2019	1962-2016	observations + model	Independent	ZMP	Glacier mean
	WaterGAP	1958-2016	glaciers model	Independent	WGP	0.5°
LWS	WaterGAP	1958-2016	hydrological model	Independent	WGP	0.5°
	PCR-GLOBWB	1948-2016	hydrological model	Independent	GWB	5arcmin

*Dataset dependence on GRACE; **Note that while the mascons are provided in 0.25° and 0.5° resolution, the native resolution of the mascons solution are 1°x1° and 3°x3° equal-area grids at the equator for CSR and JPL, respectively (Save et al., 2016; Watkins et al., 2015).

3.2.2. METHODOLOGICAL FRAMEWORK

We characterize GRD-induced SLC by a linear trend and the three types of uncertainties discussed earlier. We use the following time periods for the trend analysis: from 1993-2016 for the non-GRACE datasets, and from 2003-2016 for all datasets. The framework used to compute and combine the uncertainties and associated regional sea-level patterns is schematized in Figure 3.2. The main modules of the framework (bold text in the blue boxes of Figure 3.2a) are further explained in Figure 3.2b and in sections 3.2.2 and 3.2.2.

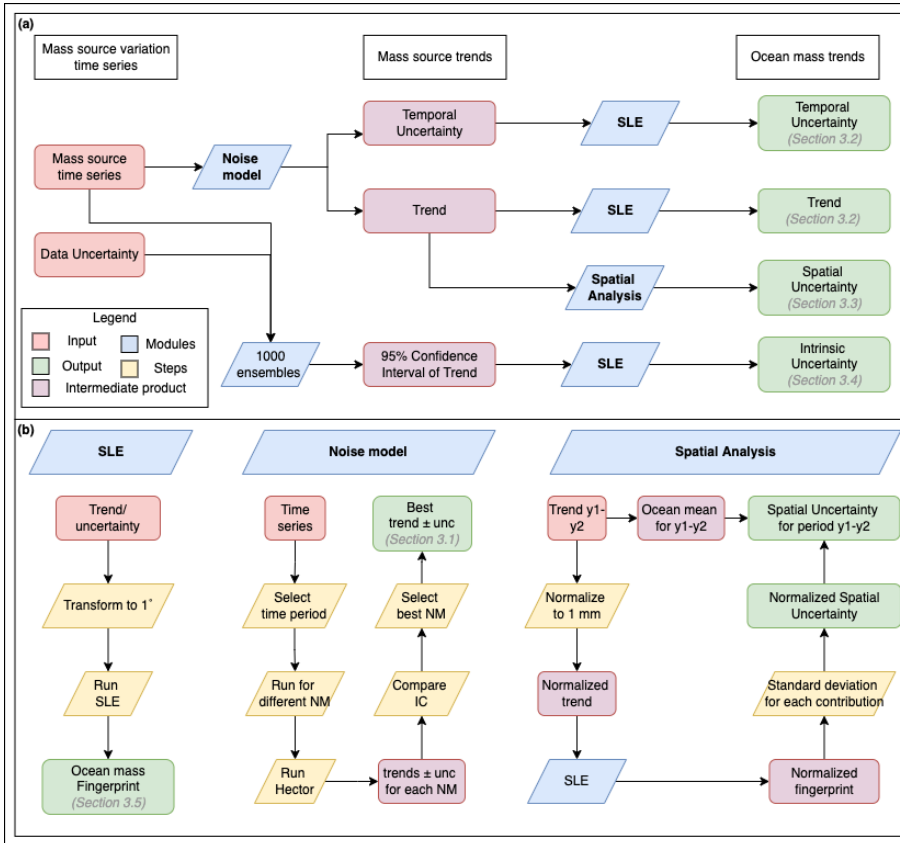


Figure 3.2: Overview of the framework used in this study (a), with detailed modules (b). Red boxes indicate the initial data (Table 1), purple the intermediate products, and green the final products. The yellow boxes indicate steps of the methodology, and the blue the main modules. We use the following acronyms and abbreviations: OLS: ordinary least-squares; SLE; Sea-level equation; IC: Information Criteria; unc: uncertainty; NM: noise model; Hector: software package by Bos et al. (2013).

The trends and associated temporal uncertainties are estimated directly from the mass source time series (Table 3.1) in the *noise model* module (Figure 3.2a). Thus the noise model analysis (Section 3.3.1) describes the physical processes of the mass sources instead of the temporal correlation in the sea-level fingerprint. The mass source change trend and temporal uncertainty are then used as input to the *SLE model* module (Section 3.2.2), which computes how the mass changes on land affect regional ocean mass change (i.e., GRD-induced SLC; Section 3.3.2). The mass source trends are also used as input to the *spatial uncertainty* analysis (Section 3.3.3). The uncertainty of the mass source time series is used as input to the *intrinsic uncertainty* analysis (Section 3.3.4).

THE SEA-LEVEL EQUATION MODEL

The regional GRD-induced SLC patterns resulting from the barystatic contributions can be computed by solving the sea-level equation (SLE) (Farrell and Clark, 1976), using spatial and temporal information of GLA, AIS, GIS and LWS (Mitrovica et al., 2001; Tamisiea, 2011). Before computing the regional SLC fields, all input data (Table 3.1) is converted to equivalent water height, and bilinearly interpolated to a 1° by 1° grid. The SLE model then computes how the source mass change is redistributed over the oceans, taking into account the GRD response of the Earth to these mass changes (Milne and Mitrovica, 1998; Mitrovica et al., 2001; Tamisiea, 2011). The SLE model uses a pseudospectral approach (Mitrovica and Peltier, 1991) up to spherical harmonic degree and order 180 (equivalent to a spatial resolution of one degree). We assume a purely elastic solid-Earth response to the mass redistribution, based on the Preliminary Reference Earth Model (Dziewonski and Anderson, 1981). While we focus here on the fingerprints of relative SLC, that is, the difference in height between the geoid and the solid Earth surface, we also provide the complementary geocentric (absolute) fingerprints (see *Data availability* Section).

TREND AND UNCERTAINTY ASSESSMENT

Our GRD-induced SLC and associated temporal uncertainty (Figure 3.2, centre column) are computed using the software package Hector (Bos et al., 2013), in which the observations are assumed to be the sum of a deterministic model (including annual and semi-annual signals) and stochastic noise. Different noise models can be selected to describe the autocorrelation between the residuals of the regression. The uncertainty of the regression model, representing one standard deviation, is then used as our temporal uncertainty.

Based on previous studies (Bos et al., 2013; Royston et al., 2018; Camargo et al., 2020), we test eight noise models to find the best descriptor of the uncertainties in our data:

- white noise (WN), in which no autocorrelation between the residuals is considered;
- pure power law (PL), where all observations influence one another, although their correlation decreases with increasing temporal distance;
- PL combined with WN (PLWN);
- autoregressive of orders 1, 5, and 9 (AR(1), AR(5), and AR(9), respectively), in which the order represents the number of previous observations influencing the next one;
- autoregressive fractionally integrated moving average of order 1 (ARF), which combines an AR(1) model with a fractional integration and a moving average of the noise;
- generalized Gauss-Markov (GGM), a generalized form of the ARF model.

The goodness of the fit of the models is assessed with the modified Bayesian Information Criterion (BIC_{tp} ; He et al. (2019)), which is an intermediate criterion in relation to the Akaike (AIC; Akaike (1974)) and Bayesian (BIC; Schwarz (1978)) criteria. The best noise model is the one that minimizes these criteria. Since these criteria are relative values, they can not be compared between different datasets. Thus, we compare the criteria of different noise models for each dataset and each grid point separately. To select the best noise model, we compute the relative likelihood of the BIC_{tp} , and select the model with values smaller than 2 (Burnham and Anderson, 2002; Camargo et al., 2020). Note that all noise models reasonably capture the variability of the time series (Figure S3.2), as their scores are always within a similar range.

The second uncertainty we consider is the spatial-structural uncertainty (Figure 1b, right column). Studies that combine a large number of datasets often base the structural uncertainty of an estimate on the standard deviation over the individual datasets in relation to the ensemble mean (Palmer et al., 2021; Cazenave et al., 2018). To isolate the effect that the spatial distribution of the terrestrial mass change has on the fingerprints, we compute the spatial-structural uncertainty by estimating the standard deviation for each contribution based on normalized fingerprints. The latter means that the sum of the regional SLC for each contribution is equal to 1 mm yr^{-1} of SLC. By using normalized fingerprints we remove the weight that the different central estimates (mean) have on the spatial standard deviation. We then take the standard deviation across the four normalized datasets for each mass source contribution, obtaining four normalized spatial-structural uncertainties, which reflects the uncertainty associated with the different spatial resolutions and location of mass change of the datasets. For example, the spatial-

structural uncertainty of the AIS reflects the differences in the fingerprints due to the fact that GRACE datasets provide observations at a 0.25 degrees resolution, while UCI provides mass changes averaged over the 17 main drainage basins of the ice sheet, and IMBIE mass changes averaged over three regions of the ice sheet (west, east and peninsula). While the analysis is based on the 2003-2016 trend, we assume that the normalized fingerprints are time-invariant, and that the resulting uncertainty is also representative of the 1993-2016 period. Lastly, we multiply the normalized uncertainty by the ocean mean (central estimate) of each contribution for 1993-2016 and 2003-2016 to compute the spatial-structural uncertainty for the respective period. We note that all components show some decadal variability in the spatial distribution, and thus assuming that the spatial mass change distributions from 2003-2016 are representative of the period 1993-2016 is an approximation of the study. However, by multiplying the normalized fingerprint by the mean of each period the possible error from this assumption becomes fairly limited. Furthermore, using a shorter spatially dense time series to obtain the variability of a longer period when only limited information is available is a methodology that is often used in sea-level studies (e.g., Church and White (2006); Frederikse et al. (2020)).

The final type of uncertainty considered in our assessment is the intrinsic uncertainty, which represents the formal errors and sensitivities in the measurement system and needs to be provided with the observations/models by the data processor/distribution centre. The intrinsic uncertainty was only provided with the JPL and IMBIE datasets. For all other datasets, our uncertainty budget does not include the intrinsic uncertainty. The uncertainties provided with the JPL Mascons represent the scaling and leakage errors from the mascon approach (Wiese et al., 2016), and, over land, are scaled to roughly match the formal GRACE uncertainty of Wahr et al. (2006). The latter represent errors in monthly GRACE gravity solutions, encompassing measurement, processing and aliasing errors (Wahr et al., 2006). While the mascons have been corrected for mass changes due to glacial isostatic adjustment (GIA) with the ICE6G-D model (Peltier et al., 2018), the intrinsic uncertainties of the JPL mascons do not represent the uncertainties from the GIA correction, which can be large depending on the region (Reager et al., 2016; Wouters et al., 2019). For example, the choice of the GIA model used for the correction could lead to uncertainties representing up to 19% of the signal in Antarctica, but less than 1% in Greenland (Blazquez et al., 2018). Given that estimating GIA uncertainties is in itself an open issue (Caron et al., 2018; Simon and Riva, 2020), we could not propagate full GIA uncertainties into the fingerprints. Since the intrinsic uncertainty represents systematic errors and instrumental noise, which might be serially correlated, we assume that the errors can be approximated by a random walk. We therefore generate an ensemble of

1,000 time series by perturbing the original rate with random normal noise multiplied by the uncertainty time series. We then compute the trend for each ensemble member. We use half of the width of the 95% confidence interval as input in the SLE model to show how the mass associated with the intrinsic uncertainty is distributed over the oceans.

COMBINING TRENDS AND UNCERTAINTIES

To compute total GRD-induced SLC trends and their uncertainties, we sum the individual contributions (AIS, GIS, LWS and GLA) as follows, with a total of six combinations: 1.CSR (all); 2.JPL (all); 3.IMB (AIS/GIS) + WGP (LWS/GLA); 4.UCI (AIS/GIS) + WGP (LWS/GLA); 5.IMB (AIS/GIS) + GWB (LWS) + ZMP (GLA); and 6.UCI (AIS/GIS) + GWB (LWS) + ZMP (GLA).

Whereas the trends are added together linearly, we add the uncertainties in quadrature, assuming they are independent and normally distributed. We acknowledge that this is an important assumption, as it is possible that the intrinsic uncertainty will be reflected in the temporal and structural uncertainties. However, we keep the independence assumption to obtain a more realistic (and smaller) estimate of the final uncertainty (Taylor, 1997). For each contribution, we first combine the different types of uncertainty following Equation (3.1):

$$\sigma_{CONTR} = \sqrt{\sigma_{temporal}^2 + \sigma_{spatial}^2 + \sigma_{intrinsic}^2} \quad (3.1)$$

where σ_{CONTR} is the total uncertainty for each individual contribution (AIS, GIS, GLA, LWS). We then compute the total GRD-induced uncertainty for all contributions (σ_{total}) following Equation (3.2):

$$\sigma_{total} = \sqrt{\sigma_{AIS}^2 + \sigma_{GIS}^2 + \sigma_{LWS}^2 + \sigma_{GLA}^2} \quad (3.2)$$

3.3. RESULTS

In this Section we first present the noise model selection (Section 3.3.1) used to compute the GRD-induced SLC trend and temporal uncertainty (Section 3.3.2). We then present the spatial-structural (Section 3.3.3) and intrinsic uncertainties (Section 3.3.4). Lastly, we show the total GRD-induced SLC trends (i.e., the sum of the different contributions) and uncertainties (i.e., the sum of the different contributions and types of uncertainties) and zoom in on a few coastal examples (Section 3.3.5).

3.3.1. NOISE CHARACTERISTICS OF THE MASS SOURCES

Many geophysical time-series are known to exhibit temporal (auto)correlations, as is the case for sea-level and cryosphere data (Bos et al., 2013). This autocorrelation means that each observation is not completely independent from the previous one (Bos et al., 2013), and it is defined by the shape of the spectrum of the time-series (Hughes and Williams, 2010). Understanding the shape of spectra and determining the best stochastic model to describe these spectra is important to understand the physics of the processes playing a role in the time-series (Hughes and Williams, 2010). In addition, accounting for the autocorrelation of the time-series while estimating a linear trend is important both for the value of the trend itself and for the statistical error of the fit (Bos et al., 2013; Hughes and Williams, 2010). Depending on the nature of the process being studied, different noise models can be used to account for the effects of autocorrelations. Here, we determine the best noise model for each spatial data point of the mass sources of the different barystatic contributions (AIS, GIS, LWS, GLA). Our analysis shows that the optimal noise model depends on both the physical system (AIS, GIS, GLA or LWS) and the dataset (Figure 3.3).

There are clear differences between the GRACE datasets (Figure 3.3a-h), for which the PL and GGM noise models score higher, and the other datasets (Figure 3.3i-p), for which the AR(5) and AR(9) models score higher. The only exception is for the two Greenland datasets (GIS_JPL (f) and GIS_IMB (j)), where the noise model selection is reversed. Over the ice sheets, the higher resolution of GRACE observations (compared to IMBIE and UCI datasets) leads to more heterogeneity in the model selection, which suggests the inclusion/capture of more complex processes. For example, our analysis indicates that only one type of noise model is selected for the entire ice sheet in the IMBIE dataset (Figure 3.3i-j). For LWS changes, where the spatial resolution of GRACE and the hydrological models is relatively high, the noise model selection follows a different pattern. There is a general preference for AR(1) in areas with smaller LWS changes (i.e., not the large

drainage basins). On the other hand, over the large drainage basins, the same model preference mentioned above is maintained (Figure 3.3, right column). This suggests that GRACE observations and the hydrological models might not always be capturing the same processes.

Different noise models are selected as optimal for the two GRACE datasets: CSR datasets (Figure 3.3a-d) are best explained with the PL model, while JPL estimates (Figure 3.3e-h) are best explained with the GGM model. However, the GGM model is fairly similar to a pure power-law model under certain parameters. Furthermore, the noise model selection for the CSR dataset over the ice sheets (Figure 3.3a,b) displays an interesting pattern, which is not seen for the JPL dataset (Figure 3.3e,f). Regions with relatively strong ice melt (i.e., the Antarctica Peninsula, East Antarctica and northwest of Greenland) are better represented by an AR(5) model. Over the extremities of the ice sheets, which are more dynamic regions, the GGM model is the optimal one. On the other hand, internal regions of the ice sheets, where there is little ablation, are better described by the PL model.

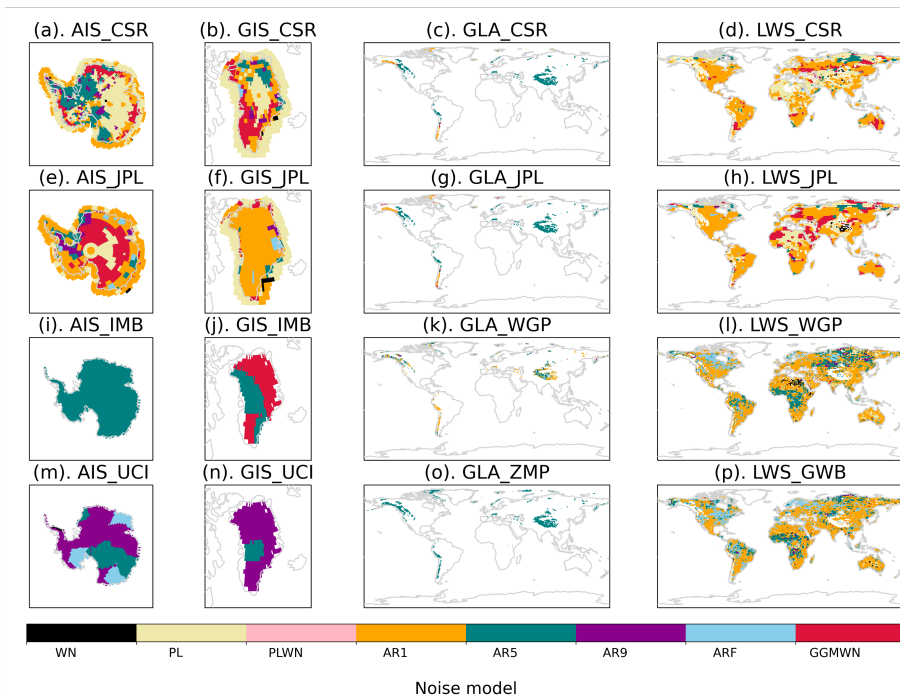


Figure 3.3: Noise model selection based on the time series of the different sources of mass loss for each dataset (rows) and contribution (columns), over the period 2003-2016.

3.3.2. TREND AND TEMPORAL UNCERTAINTY

The mass source trend and uncertainties obtained with the selected noise models (Section 3.3.1) are used to compute the sea-level fingerprints (Figure 3.4). To illustrate the difference between the fingerprints based on GRACE and those based on GRACE-independent datasets, we show the trends and uncertainties for the JPL estimates (Figure 3.4a-d, i-l) and for the UCI estimates for the ice sheets (Figure 3.4e-h) and WaterGAP for glaciers and LWS (Figure 3.4m-p). Trends and temporal uncertainties for the other datasets are provided in Figure S3.3. The typical GRD patterns are visible in all fingerprints: regions closer to a freshwater source experience a negative SLC, due to the mass loss that causes land uplift and reduced gravitational attraction, while in the far-field the sea level rises more than the global average.

While all trends strongly depend on the dataset (Figure 3.4, first and third column), the uncertainty patterns are rather consistent. This suggests that, even though different noise models were used to compute the trend for each dataset, the temporal uncertainty is characteristic of each contribution. We find that for any given contribution, the trends from different datasets are consistent within their respective uncertainties. For glaciers and the ice sheets, the GRACE-independent datasets give a higher trend than the GRACE observations. The temporal uncertainties for ice sheets and glaciers are relatively small, especially for the UCI datasets. This indicates that these contributions do not exhibit strong autocorrelations, and consequently the uncertainty of the trend will be small. On the other hand, the temporal uncertainty for the LWS is larger than the trend itself, and therefore the LWS trend is not statistically significant. This is probably related to the large internal and decadal variability of the time series, in combination with the relatively short period under study.

The largest inter-dataset differences are displayed in the regional patterns of the LWS contribution. Despite the similar global mean LWS trend value for both JPL and WGP, the regional trend patterns and uncertainty values are very different. This may partially be related to the coarse resolution of GRACE (300 km) in comparison to the hydrological models (0.5° by 0.5° grid (55 km by 55 km at the Equator)). This difference can also be related to the difficulty in modelling the complex processes affecting LWS, which relies on parameterisations of physical processes and on sparse observations, while GRACE measures the total mass change.

Another significant inter-dataset difference is in the regional trend pattern as a consequence of AIS mass change (Figure 3.4a,e). This is mainly related to the location of ice mass changes in each dataset. GRACE observes mass accumulation in East Antarctica,

resulting in a positive sea-level trend in the region. This accumulation is not captured by the UCI and IMB datasets. GRACE has a higher spatial resolution, and thus provides more detail of where the mass change is taking place. The UCI dataset provides estimates on a basin scale, so more detailed changes may be averaged out. The effect of the location of mass change at the source of the contribution is further investigated with the spatial-structural uncertainty (next section).

3

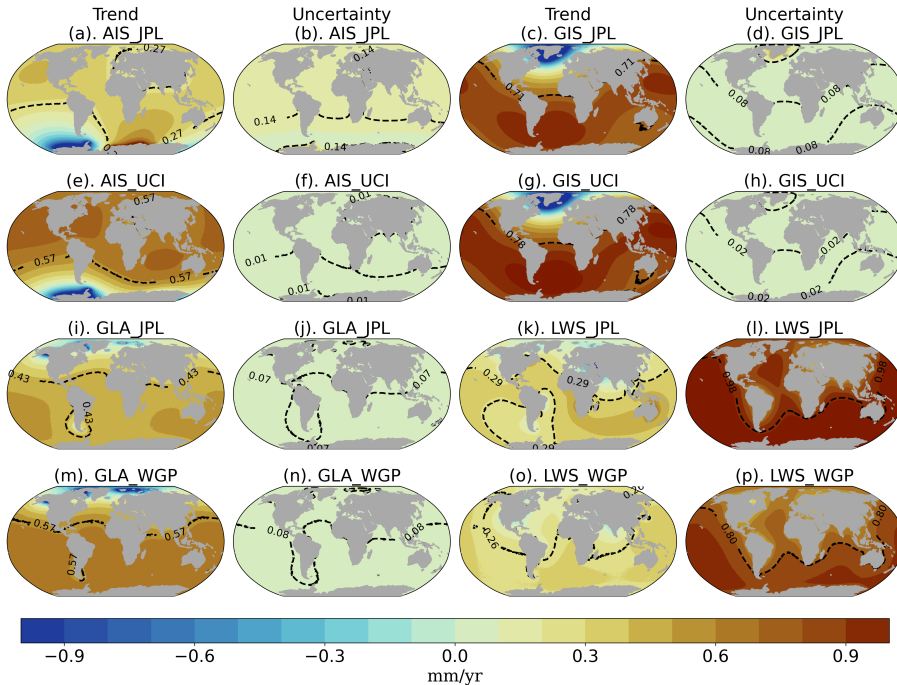


Figure 3.4: GRD-induced sea-level trend and temporal uncertainty (mm yr^{-1}) for GRACE (JPL) and independent combination (UCI + WGP) for 2003-2016. Black dashed contour line and number indicates the spatial average of the regional trend and uncertainty. Trends and uncertainties of CSR, IMB, ZMP and GWB presented in Supplementary Figure S3.3

3.3.3. SPATIAL-STRUCTURAL UNCERTAINTY

The regional SLC fingerprints directly reflect the differences in the spatial distribution of the mass change sources of the datasets (Mitrovica et al., 2011). Over the ice sheets, for instance, IMBIE provides one time series for the entire Greenland Ice Sheet, which is subdivided into dynamic and surface mass balance changes, and the Antarctic Ice Sheet is divided into three drainage basins. GRACE products, on the other hand, have a native resolution of about 300-km at the equator (Tapley et al., 2004). To account for the uncertainties arising from the differences in location of the mass change between

datasets, we first normalize the fingerprints and then combine them into estimates of the spatial-structural uncertainty (Figure 3.5).

For all contributions, the largest spatial uncertainties are concentrated closer to the mass change sources, while the uncertainties are reduced in the far field. The effect of differences resulting from Earth rotational effects (typically leading to four large quadrants) is visible in the far field of the AIS (in the Northern Pacific) and near hotspots of LWS (around the Southern Ocean). As was the case for the trends (Figure 3.4a), the AIS shows the strongest spatial differences, as the underlying datasets strongly differ in their spatial detail. The spatial uncertainties represent the error introduced by using datasets that have insufficient resolution to solve the processes being analysed. In addition, it also shows that different physical processes are captured by the different datasets, as is the case for the LWS estimate. The discrepancies between the processes captured by GRACE and LWS models result in the spatial-structural uncertainty of the LWS component (Figure 3.4d) being the second largest.

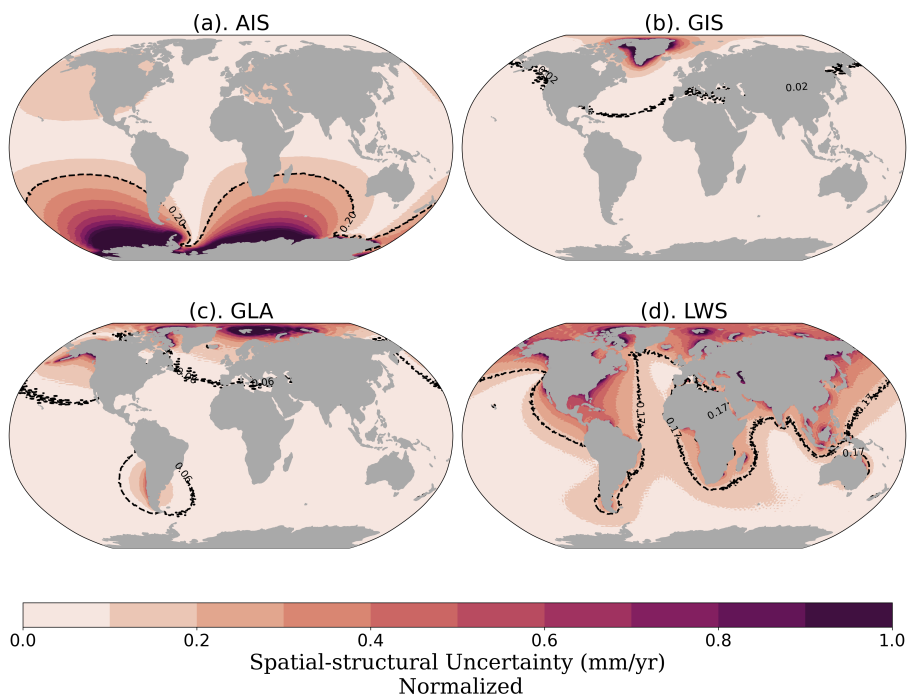


Figure 3.5: Normalised GRD-induced sea-level change fields of the spatial-structural uncertainty ($0-1 \text{ mm yr}^{-1}$), representing the uncertainty arising from the different locations of mass changes for Antarctica (a), Greenland (b), glaciers (c) and land water storage (d). Black dashed contour line and number indicates the spatial average of the regional uncertainty.

3.3.4. INTRINSIC UNCERTAINTY

The final type of uncertainty considered here is the intrinsic uncertainty, which represents noise related to the dataset itself (Figure 3.6). With exception of the LWS, all intrinsic uncertainties are relatively small (spatial averages below 0.1 mm yr^{-1}). The largest intrinsic uncertainty is seen in the LWS contribution (Figure 3.6a), with maximum values of 0.5 mm yr^{-1} . This is expected, as the uncertainty of GRACE is estimated from the standard deviation of the signal anomalies (Wahr et al., 2006), which may lead to an overestimation of the uncertainty in regions where the anomalies represent real hydrological signals (Humphrey and Gudmundsson, 2019). Furthermore, GRACE mass errors are latitude dependent, increasing from the poles to the equator (Wahr et al., 2006), which explains why we see large intrinsic uncertainty for LWS and low values for the ice sheets and glaciers. The IMBIE datasets (Figure 3.6e,f) show larger intrinsic uncertainty than the ice sheet uncertainties from JPL (Figure 3.6c,d), once the IMBIE time series is an ensemble of several datasets and methods. Note that these uncertainties are smaller than those originally reported in the IMBIE studies (Shepherd et al., 2018, 2020), which include not only intrinsic, but also structural and temporal uncertainties. Overall, the intrinsic uncertainty, which depends on the method employed to produce the estimates, is small compared to the spatial-structural and temporal uncertainties, which are related to the physical processes represented.

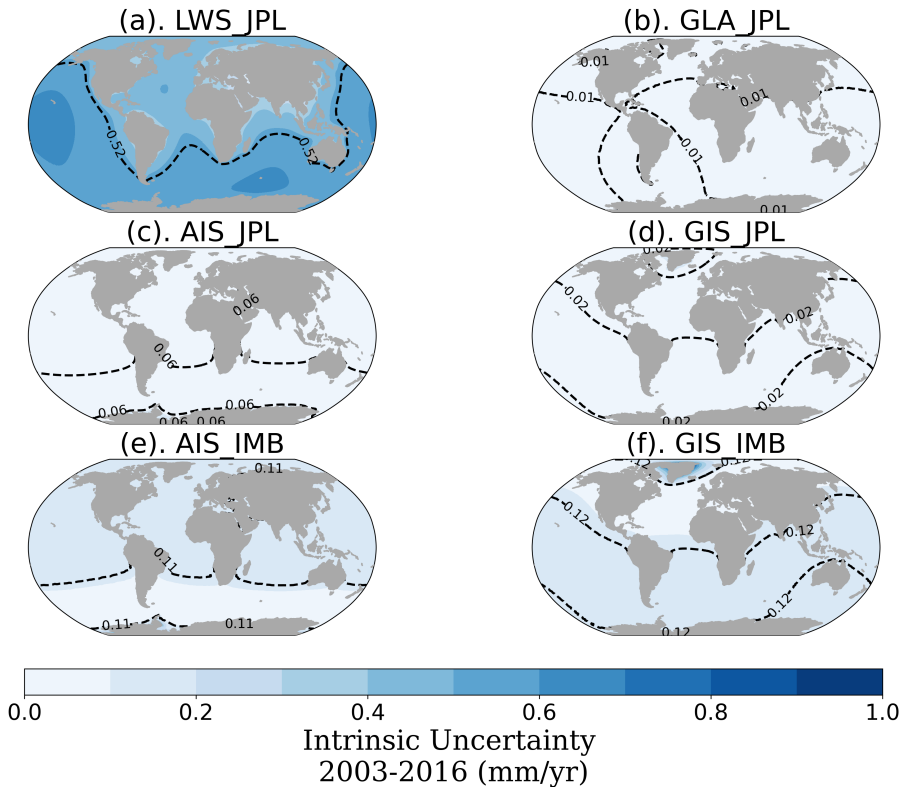


Figure 3.6: GRD-induced sea level fields of the intrinsic uncertainty (mm yr^{-1}) for the land water storage (a), glaciers (b), Antarctica (c) and Greenland (d) contributions of the JPL dataset; and Antarctica (e) and Greenland (f) contributions of the IMBIE dataset. Black dashed contour line indicates the spatial average of the regional uncertainty

3.3.5. TOTAL BARYSTATIC TREND AND UNCERTAINTY

Combining the different contributions, as explained in Section 3.2.2, leads to the total GRD-induced SLC trends and uncertainties shown in Figure 3.7. Although we analysed six dataset combinations, here we show only two (JPL and IMB+WGP) to discuss the patterns and the total uncertainty fields. We show these specific combinations because they present the most complete uncertainty budget (as only JPL and IMB provided intrinsic uncertainties). Additional combinations are presented in Supplementary Figure S3.5, with the global mean barystatic SLC values listed in Supplementary Table S3.1. We recall that the aim of this study is not to provide one final ensemble of GRD-induced SLC, but rather to focus on the uncertainty budget. Figure 3.7 shows the JPL GRACE dataset (panels a-b) and the combination of IMBIE and WaterGAP (c-f), the latter for both the common period of 2003-2016 (a-d) and the longer period of 1993-2016 (e-f). To illustrate the

distribution of the regional trends and uncertainties around the world, we report the 5th to 95th percentile range across all ocean grid cells (Figure 3.7, histograms below the maps), and refer to it as the 90%-range of the field. When all the contributions are combined, we find that the 90%-range of the GRD-induced SLC trends range from -0.43 to 3.31 mm yr^{-1} for 2003-2016, and from -0.32 to 2.56 mm yr^{-1} for 1993-2016, depending on the dataset choice and the location. When all types of uncertainties from all contributions are combined, the 90%-range of GRD-induced total uncertainty ranges from 0.61 to 1.27 mm yr^{-1} for 2003-2016, and from 0.36 to 0.79 mm yr^{-1} for 1993-2016, also depending on the dataset choice and location.

For most regions of the world, we find that the GRD-induced SLC trend is higher than the 1-sigma total uncertainty, with exception of the regions near the polar areas (indicated by stipples in Figure 3.7). Comparing the JPL trend to the IMB+WGP trend, the shape of the pattern is similar, but the global mean (and thereby the regional SLC) is larger for the IMB+WGP combination. Nonetheless, both distributions of the regional SLC have a similar upper bound, with the 90%-range of the ocean grids ranging from -0.26 to 2.24 mm yr^{-1} and from -0.43 to 2.20 mm yr^{-1} , for the JPL and IMB+WGP datasets. The regional histograms also show a skewed distribution of the trend, with mainly positive values. When we compare the two periods of IMB+WGP (Figure 3.7c, e), the regional histogram is slightly narrower for the longer period (i.e., less divergence for the regional values), with the 90%-range of the ocean grids ranging from -0.32 to 1.50 mm yr^{-1} . This is probably because the local effect of internal variability plays a smaller role in the longer period. Nonetheless, the regional pattern is similar for both periods.

The uncertainty patterns (Figure 3.7, right panels) are similar for the different dataset combinations (JPL vs. IMB+WGP) and periods (2003-2016 vs. 1993-2016). However, the regional histograms are slightly different, with the 90%-range of the regional uncertainties ranging from 0.89 to 1.32 mm yr^{-1} and from 0.63 to 0.98 mm yr^{-1} , for respectively JPL and IMB+WGP for the 2003-2016 period. Similar to the trend, the longer period IMB+WGP uncertainties have a similar pattern but with lower values than for the shorter period, with regional values ranging from 0.38 to 0.60 mm yr^{-1} . Although the total uncertainty is dominated by the temporal uncertainty (see Figure 3.8), the similarity of the uncertainty pattern for both periods is influenced by the fact that the spatial-structural errors are based on the 2003-2016 period and extended to 1993-2016. On average, the spatial-structural uncertainty represents 14% (21%) of the total uncertainty, while the temporal represents 77% (75%), for the 2003-2016 (1993-2016) period.

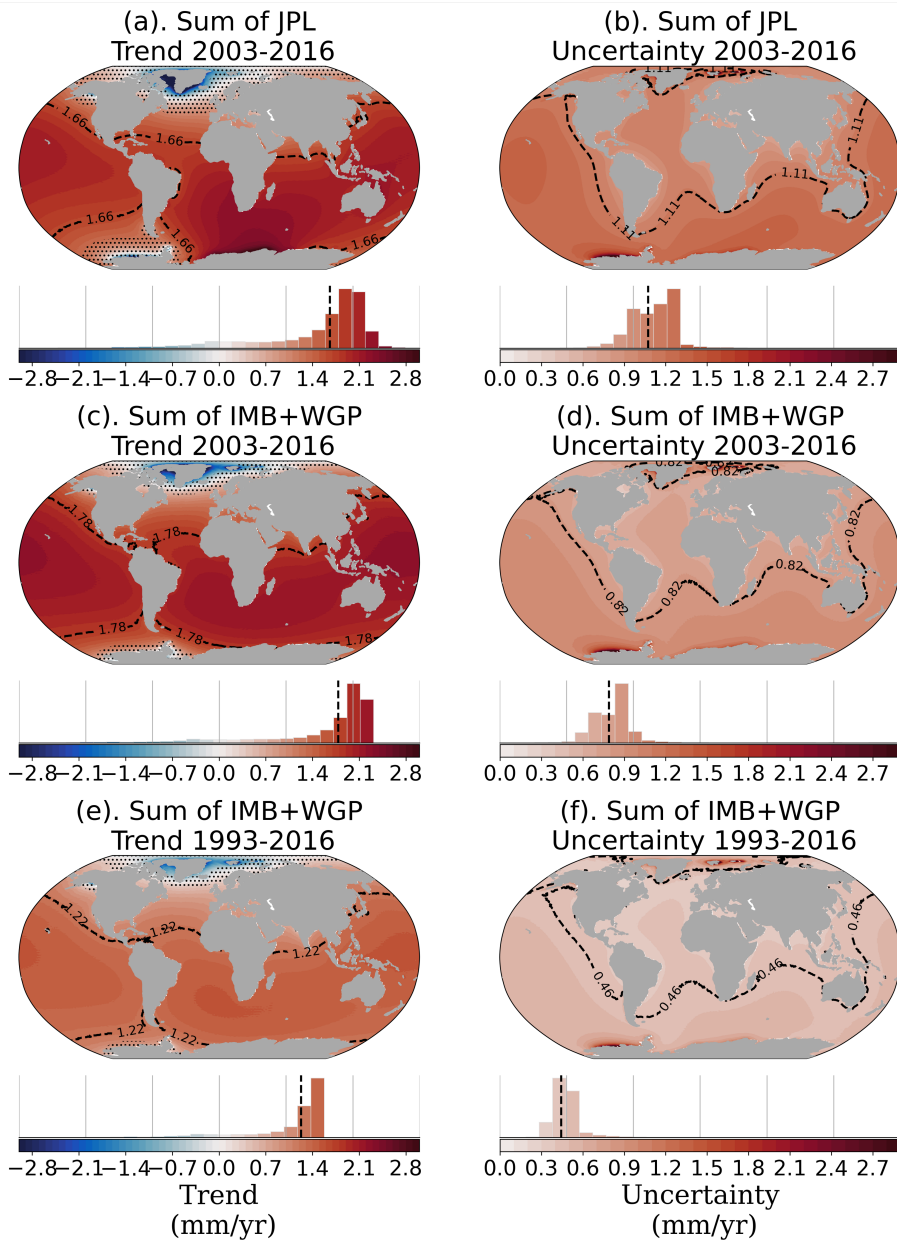


Figure 3.7: Total GRD-induced SLC fields of the trend and uncertainty (mm yr^{-1}) (AIS+GIS+LWS+Glaciers contributions; intrinsic + temporal + spatial uncertainties) for GRACE (a,b) and IMBIE+WaterGAP for 2003-2016 (c,d) and for 1993-2016 (e,f). Histograms underneath each map indicates the distribution of the regional values across the oceans, in which the 5 to 95th percentile range (90%-range) is based on. Spatial average of the regional trend and uncertainty indicated by black dashed lines in the maps and bar charts. Regions with trends smaller than the 1-sigma uncertainty are indicated in the map with stipples.

3.3.6. COASTAL EXAMPLES

To further illustrate how the different contributions and uncertainties contribute to the total uncertainty budget, we selected ten coastal cities around the world in which we break down the total uncertainty of GRD-induced SLC from 1993-2016 into the four contributions (Figure 3.8a), and into the three types of uncertainties (Figure 3.8b). We also show the different types of uncertainties for each of the contributions (Figure 3.8c). As in in Figure 3.7, we show the IMB+WGP combination.

The large contribution of the LWS and temporal uncertainty to the uncertainty budget is highlighted on Figure 3.8. Figure 3.8a shows that the LWS uncertainty plays an important role at all locations, being responsible for at least 50% of the total uncertainty. While the temporal uncertainty is the main contribution of the LWS uncertainty (Figure 3.8c), in some locations, such as Vancouver (Canada, location 1), Washington (US, location 3) and Tokyo (Japan, location 9) the spatial uncertainty is also important. Even without the contribution of LWS to the total uncertainty (Supplementary Figure S3.8b), the temporal uncertainty is still the main contributor. The intrinsic uncertainty (panel b) is fairly small in all locations, with an average contribution of 8% for this dataset combination. However, for the JPL combination (Supplementary Figure S3.7), which has intrinsic uncertainty estimation for all contributions, the intrinsic uncertainty is responsible, on average, for 30% of the total uncertainty, being more important than the spatial-structural one.

The second main contribution to the uncertainty budget comes from the AIS, except for Vancouver (Canada, location 1), for which the glaciers (GLA) contribute about 2 times more than AIS. The AIS uncertainty is mainly dominated by the intrinsic uncertainty, with exception of Cape Town (South Africa, location 6), which is located within the large uncertainty contours of the spatial-structural uncertainty from AIS (see Figure 3.5a). In general, the relative importance of GIS and GLA is fairly similar, with exception of Vancouver (Canada, location 1) and Rotterdam (the Netherlands, location 5). In such locations, the GLA uncertainty is dominated by the spatial-structural contribution, while in all other locations the temporal uncertainty plays the most important role. On average, the GIS uncertainty is dominated by the intrinsic and temporal uncertainties rather than by spatial-structural uncertainty (panel c).

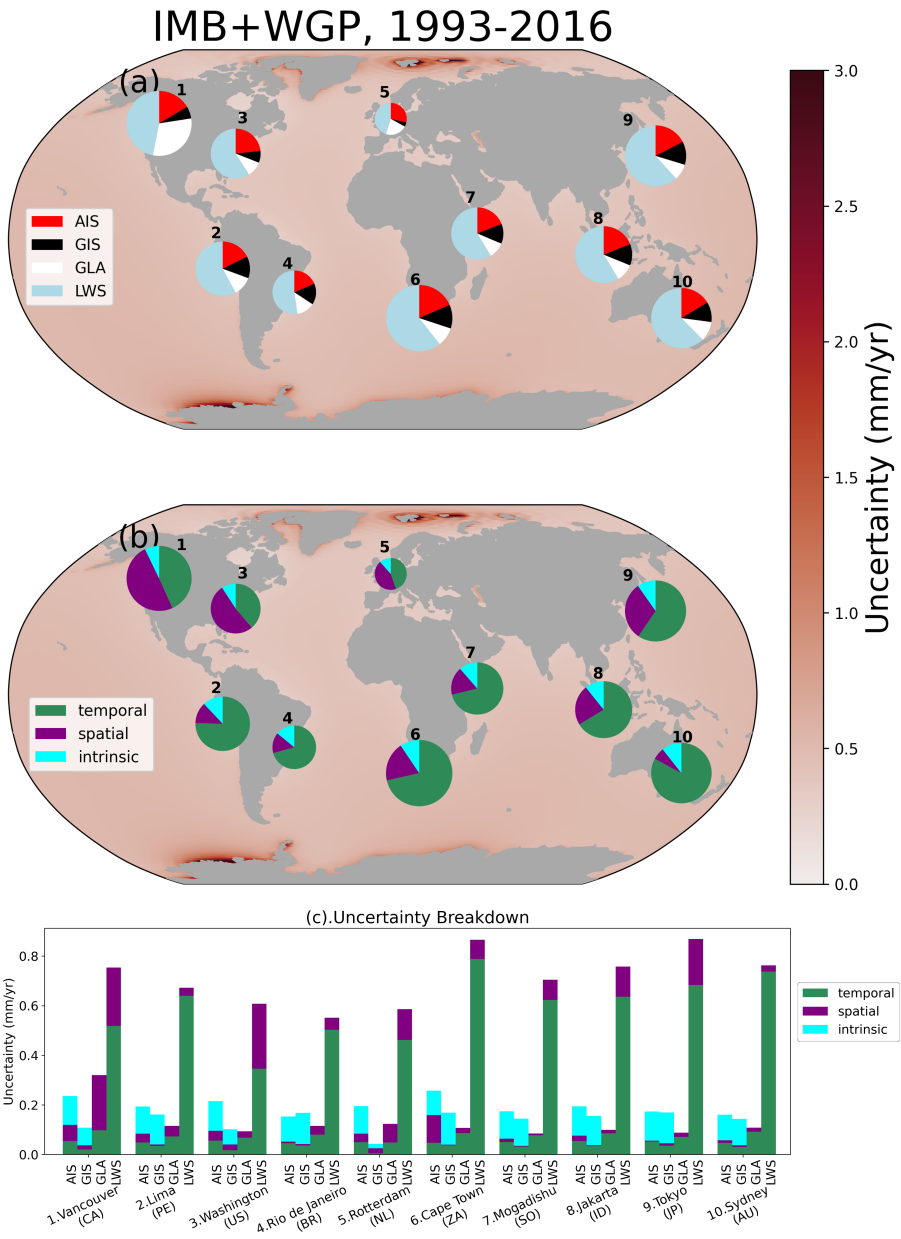


Figure 3.8: Pie charts represent the total uncertainty separated by (a) contribution and (b) type of uncertainty, and the bars the breakdown for each contribution (c). Background maps show the total GRD-induced uncertainty. The size of the pie charts is relative to the magnitude of the total uncertainty. Note that the uncertainties are combined in quadrature, so simply adding up the bars in panel c will not reflect the size of the pie charts on panels a and b.

3.4. DISCUSSION

In this manuscript we investigated the regional GRD-induced SLC patterns associated with barystatic contribution to sea-level trends over 1993-2016 and 2003-2016, focusing on improving the understanding of the uncertainty budget. We showed how mass changes of glaciers, land water storage, and the Greenland and Antarctic ice sheets influence regional SLC by computing sea-level fingerprints. We considered three types of uncertainties in our budget: the determination of a linear trend (temporal); the spread around a central estimate as influenced by the distribution of mass change sources (spatial); and the uncertainty from the data/model itself (intrinsic).

The uncertainty budget is dominated by the temporal uncertainty, responsible on average for 65% of the total uncertainty, while the spatial-structural and intrinsic uncertainties have smaller contributions of similar magnitude, responsible on average for 16% and 18% of the budget, respectively. The temporal uncertainties associated with the trend may represent real climatic signals, and not only measurement errors. For example, the variability due to climatic oscillations, such as El Niño Southern Oscillation (ENSO) and the Pacific Decadal Oscillation (PDO), may be reflected in the residuals of the time series, affecting the trend and its temporal uncertainties (Royston et al., 2018). As such climatic events influence not only mass change, but also other drivers of sea-level change (e.g., thermal expansion), caution must be taken when using and comparing these uncertainties with those from other sea level contributors. Despite the dataset-driven differences, for a given contribution all estimated trends agree within their respective 1-sigma uncertainties, both for regional and global mean values (Figure 3.1), Supplementary table S3.1).

We find that the total GRD-induced sea-level trends range from -0.43 to 2.20 mm yr^{-1} for 2003-2016, and from -0.32 to 1.50 mm yr^{-1} for 1993-2016, depending on location, for the IMB+WGP combination, with spatial averages of 1.78 and 1.22 mm yr^{-1} , respectively. The total uncertainty of the GRD-induced sea-level trend ranges from 0.63 to 0.98 mm yr^{-1} for 2003-2016, and from 0.38 to 0.60 mm yr^{-1} for 1993-2016 for the IMB+WGP combination, with spatial averages of 0.80 and 0.46 mm yr^{-1} , respectively. While these uncertainty values may seem large compared to studies focusing on global changes alone (Horwath et al., 2022; Frederikse et al., 2020), other studies also found that regional uncertainties are higher than the previously published global mean rates (Prandi et al., 2021; Bos et al., 2014b). For example, in a recent satellite altimetry sea-level change assessment, Prandi et al. (2021) found that the local sea-level trend uncertainty due to observational errors (i.e., intrinsic uncertainties) was about two times higher than the global mean sea-level trend uncertainty of Ablain et al. (2019). We note that the spatial average of the

regional uncertainties (indicated by the black dashed line in the figures) is not equal to the uncertainty of the global mean barystatic SLC time series and trend. Consequently, the spatial averages will lead to larger values than the uncertainty of the global mean sea-level time series (see Figure S3.6). Thus, one should not compare the value given here to characterize global mean sea-level changes with other studies focusing on the global mean (e.g. Horwath et al. (2022)).

The GRD-induced sea-level trends clearly show the classical gravitational-rotational-deformational pattern, matching qualitatively with other fingerprints (e.g., Mitrovica et al. (2001); Riva et al. (2010); Hsu and Velicogna (2017); Jeon et al. (2021)). Our spatial-structural uncertainties highlight the effect of using a uniform mass change (i.e., only one value averaged over a region) compared to non-uniform local mass changes (Bamber and Riva, 2010; Mitrovica et al., 2011). For example, we show that different location of mass changes can lead to deviations larger than 20% for AIS (Figure 3.5). As a consequence of the relatively low spatial resolution of the observations, the AIS is the second main contributor to the total GRD-induced uncertainty budget. We show that this effect is important not only for AIS, but for all the GRD-induced SLC contributions.

The main source of uncertainty in the GRD-induced SLC is the temporal uncertainty from the land water storage (LWS) contribution, which is responsible for 35 – 60% of the total uncertainty, depending on the region of interest. This is likely related to the natural variability of LWS (Vishwakarma et al., 2021; Hamlington et al., 2017; Nerem et al., 2018), which is mainly driven by seasonal and interannual cycles (Cáceres et al., 2020). A method to deal with the natural variability of LWS would be to use different metrics than linear trends (Vishwakarma et al., 2021), such as time varying trends based on a state space model (Frederikse et al., 2016; Vishwakarma et al., 2021). However, we choose to use linear trends in this study for the sake of accuracy, reproducibility and discussion. It has also been suggested that a more appropriate way of computing a meaningful linear trend from LWS is to incorporate this variability in the analysis (Vishwakarma et al., 2021), as we did by including the seasonal components in the functional model. Nonetheless, the LWS uncertainties related to the trend are still very high, suggesting that a period of 25 years (1993-2016) might still be too short to solve the low frequency natural variability of LWS, particularly on (multi)-decadal timescales. Indeed, Humphrey et al. (2017) showed that removing the short-term climate-driven variability of the LWS signal yields in a more robust long-term (>10 years) trend, with reduced uncertainties.

Here we assessed the uncertainties related to the regional GRD-induced patterns associated with barystatic sea-level change, in particular their spatial distribution. The true uncertainty of ocean mass contribution to sea-level change is difficult to determine. Our approach of quantifying this uncertainty is to some extent conservative, as it results in larger uncertainties than in previous studies (e.g., Horwath et al. (2022)). Nonetheless, we did assume independence of the different types of uncertainty, and did not propagate GIA uncertainties into our fingerprints, which could lead to even larger uncertainties. Our results highlight that improving the spatial detail of land ice mass loss products, as well as determining more accurate land water storage trends, would lead to better SLC estimates. In addition, our findings can be used to inform projection frameworks. For example, we show that the distribution of ice in the Antarctic Ice Sheet has a significant impact on regional SLC, even in locations far from the ice sheets, such as the Netherlands. This means that, depending on the region of a collapse in the Antarctic Ice Sheet, the sea-level rise projections, which are often based on uniform ice sheet distributions and static fingerprints (e.g., Slangen et al. (2012); Jevrejeva et al. (2019)), may have large regional deviations due to spatial differences in the mass source. Incorporating the insights of uncertainty assessments in sea-level frameworks (as in Larour et al. (2020)) should eventually lead to better sea-level projections.

3.5. SUPPLEMENTARY INFORMATION

3.5.1. SUPPLEMENTARY FIGURES AND TABLES

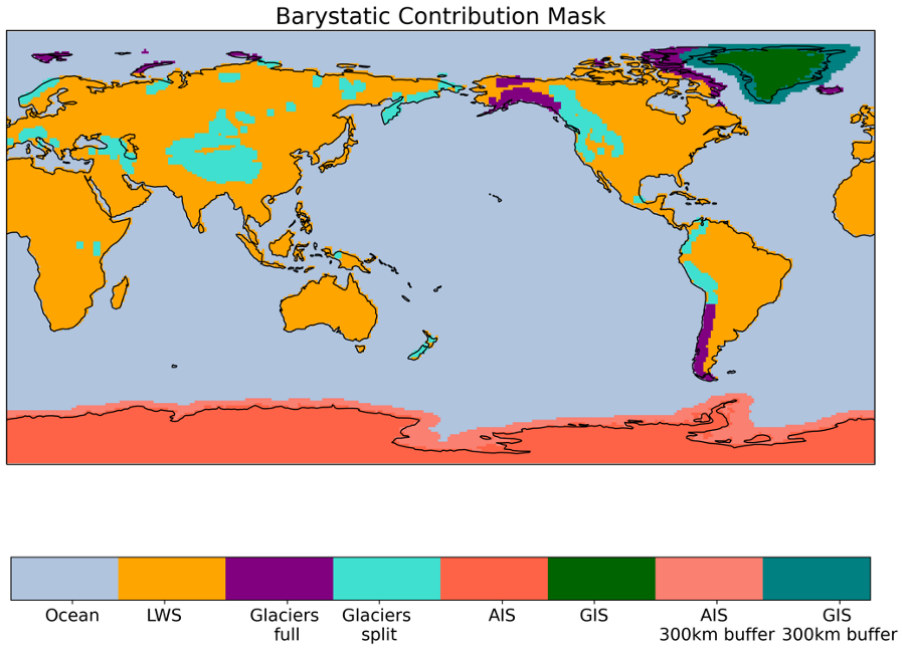


Figure S3.1: Mask of the different contributions to barystatic sea-level change.

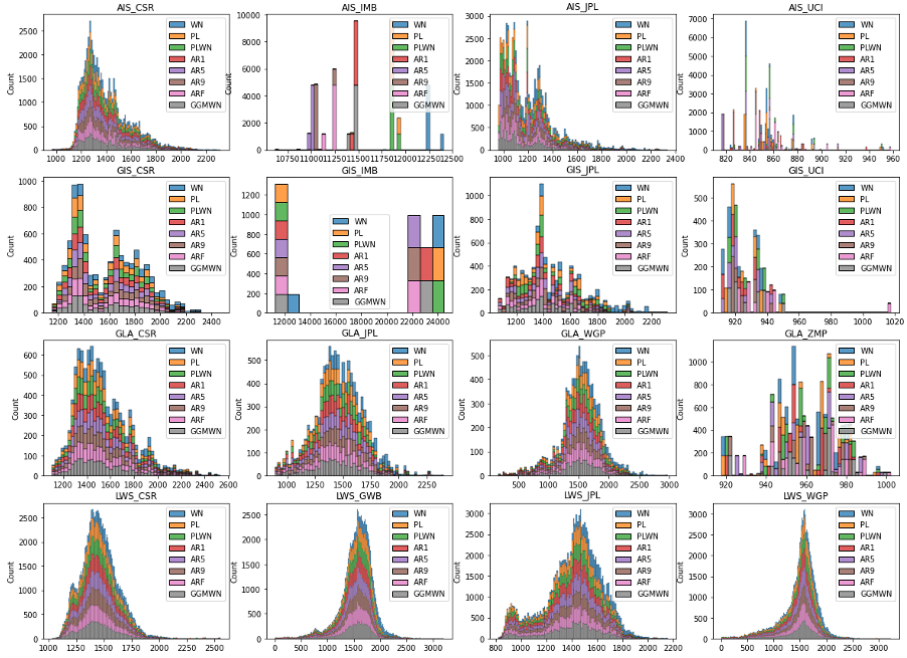


Figure S3.2: Histogram of the modified Bayesian Information Criterion for each dataset, used to select the optimal noise models. The x-axis shows the BIC score, and the y-axis the number of grid points (count). Note that all models have scores within the same range, showing that no model fails in capturing the signal of the observation.

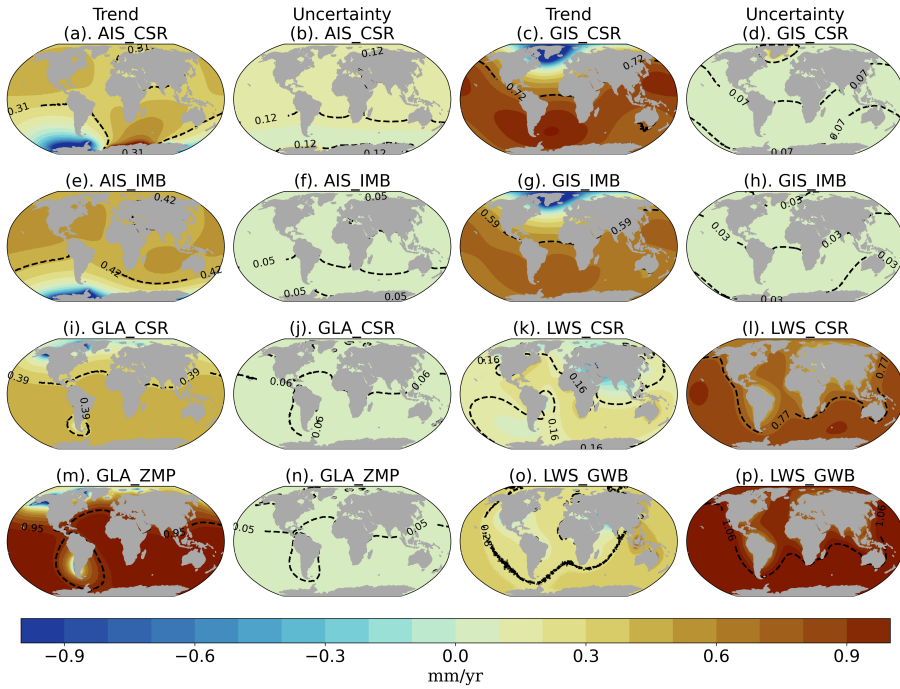


Figure S3.3: GRD-induced sea-level trend and temporal uncertainty (mm yr^{-1}) for GRACE (CSR) and independent combination (IMB + ZMP + GWB) for 2003-2016. Black dashed contour line and number indicates the spatial average of the regional trend and uncertainty. Complementary of trends and uncertainties of Figure 3.4.

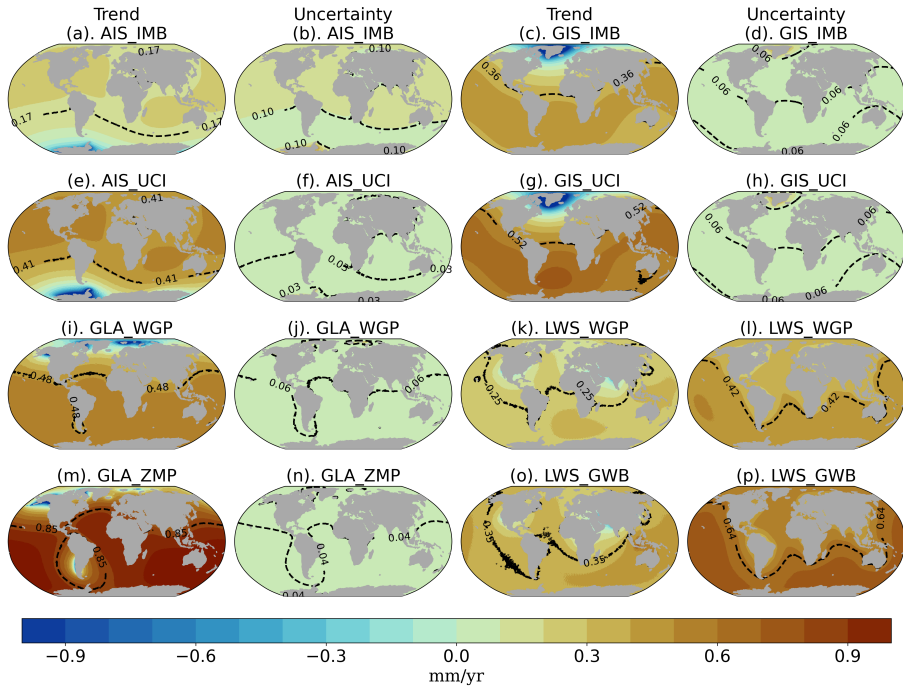


Figure S3.4: GRD-induced sea-level trend and temporal uncertainty (mm yr^{-1}) for (a-d) IMB, (e-h) UCI, (i-l) WGP; (m,n) ZMP and (o,p) GWB datasets for the period 1993-2016. Black dashed contour line and number indicates the spatial average of the regional trend and uncertainty. Complementary of trends and uncertainties of Figure 3.4.

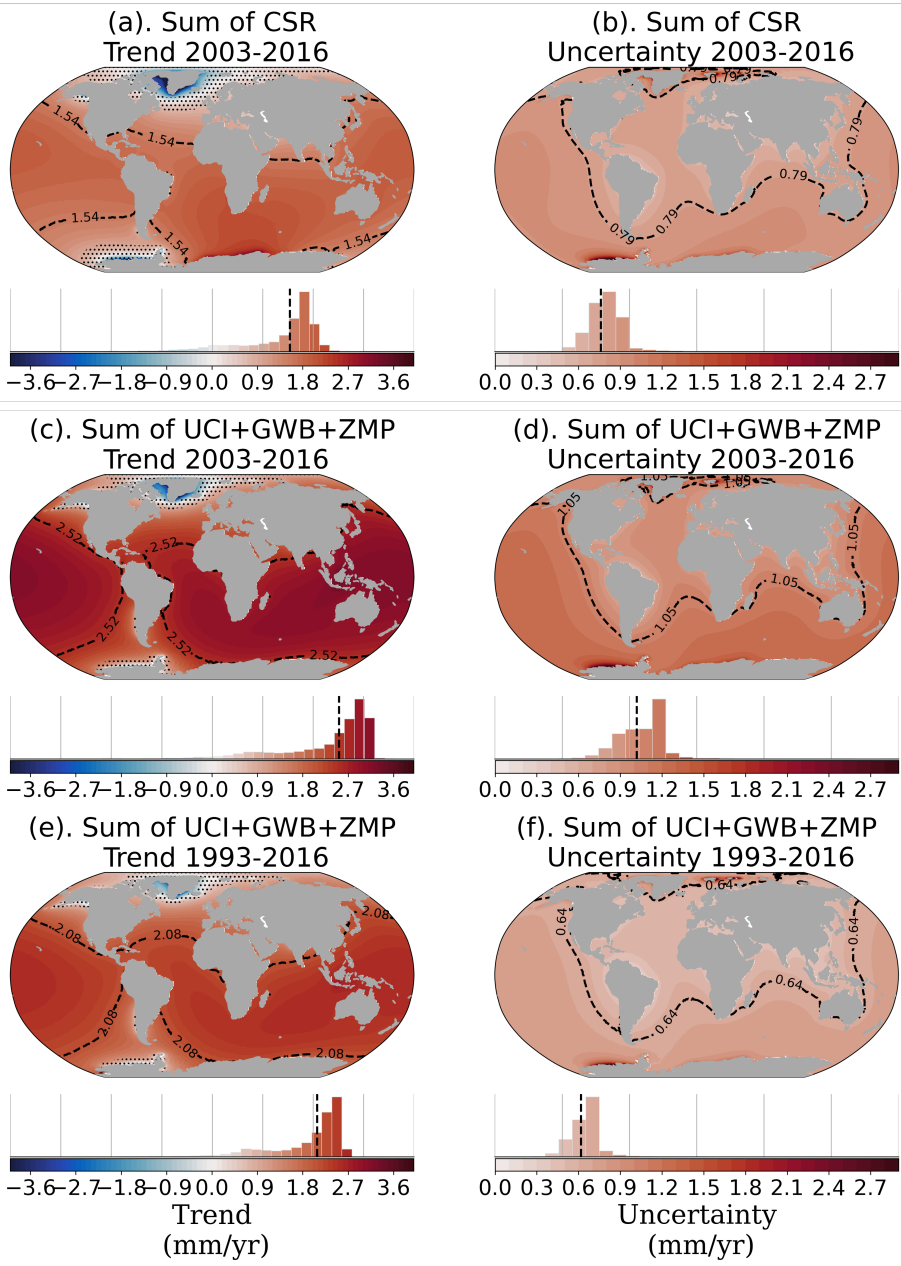


Figure S3.5: Total GRD-induced SLC fields of the trend and uncertainty (mm yr^{-1}) (AIS+GIS+LWS+Glaciers contributions; intrinsic + temporal + spatial uncertainties) for GRACE CRS (a,b) and UCI + GlobWEB + Zemp for 2005-2015 (c,d) and for 1993-2016 (e,f). Histograms underneath each map indicates the distribution of the regional values across the oceans. Spatial average of the regional trend and uncertainty indicated by black dashed lines in the maps and bar charts. Complementary of trends and uncertainties of Figure 3.7.

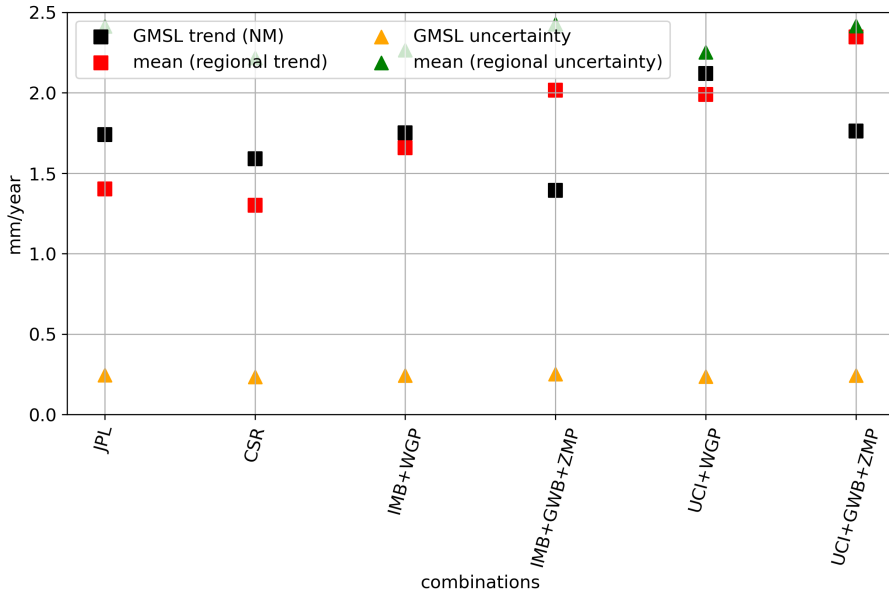


Figure S3.6: Comparison of global mean sea-level trend (black squares) and uncertainty (yellow triangles) with the spatial average of the regional trend (red circles) and uncertainty (green upside down triangles) from 2003-2016. The difference between the GMSL trend and spatial average of the regional trend is due to the use of regionally different noise models (following selection of Figure 3.3)

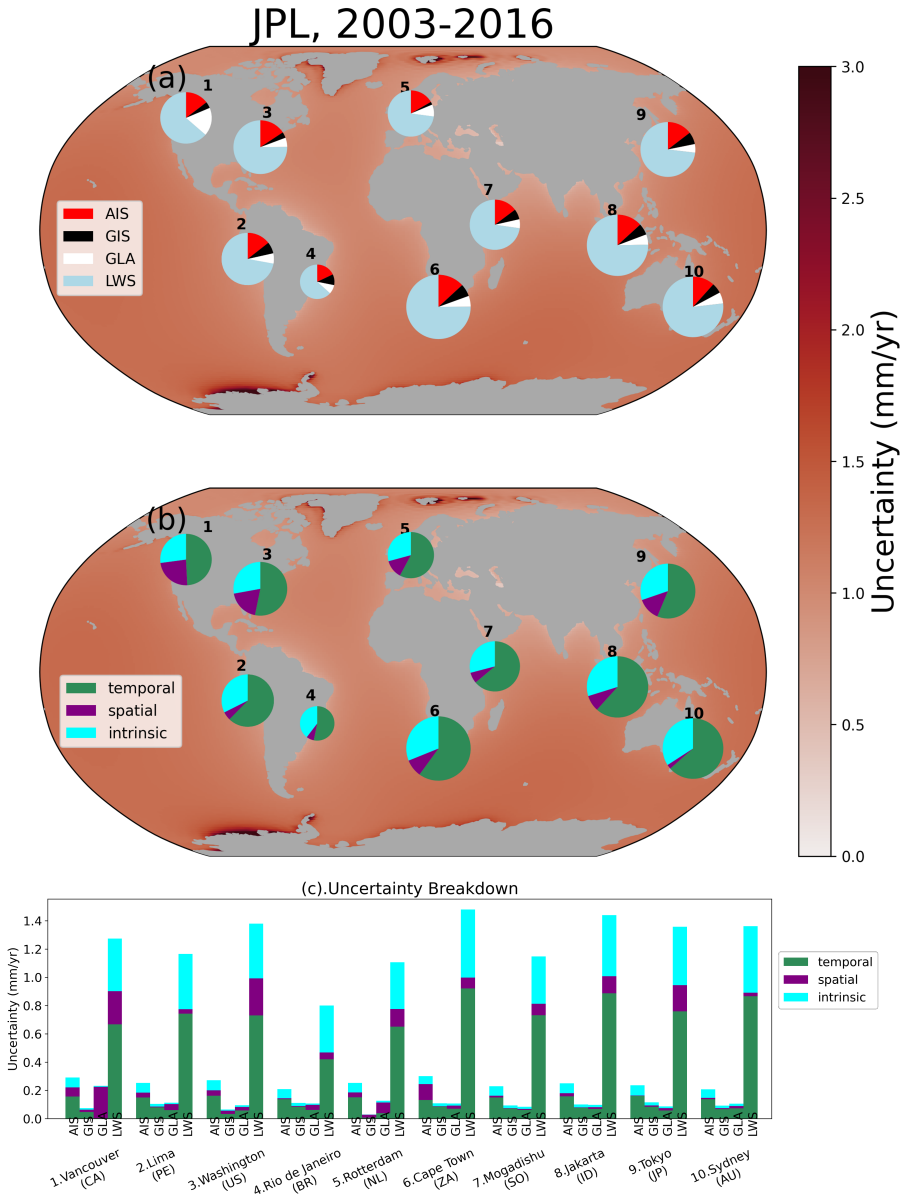


Figure S3.7: Same as Figure 3.8, for JPL dataset, from 2003-2016.

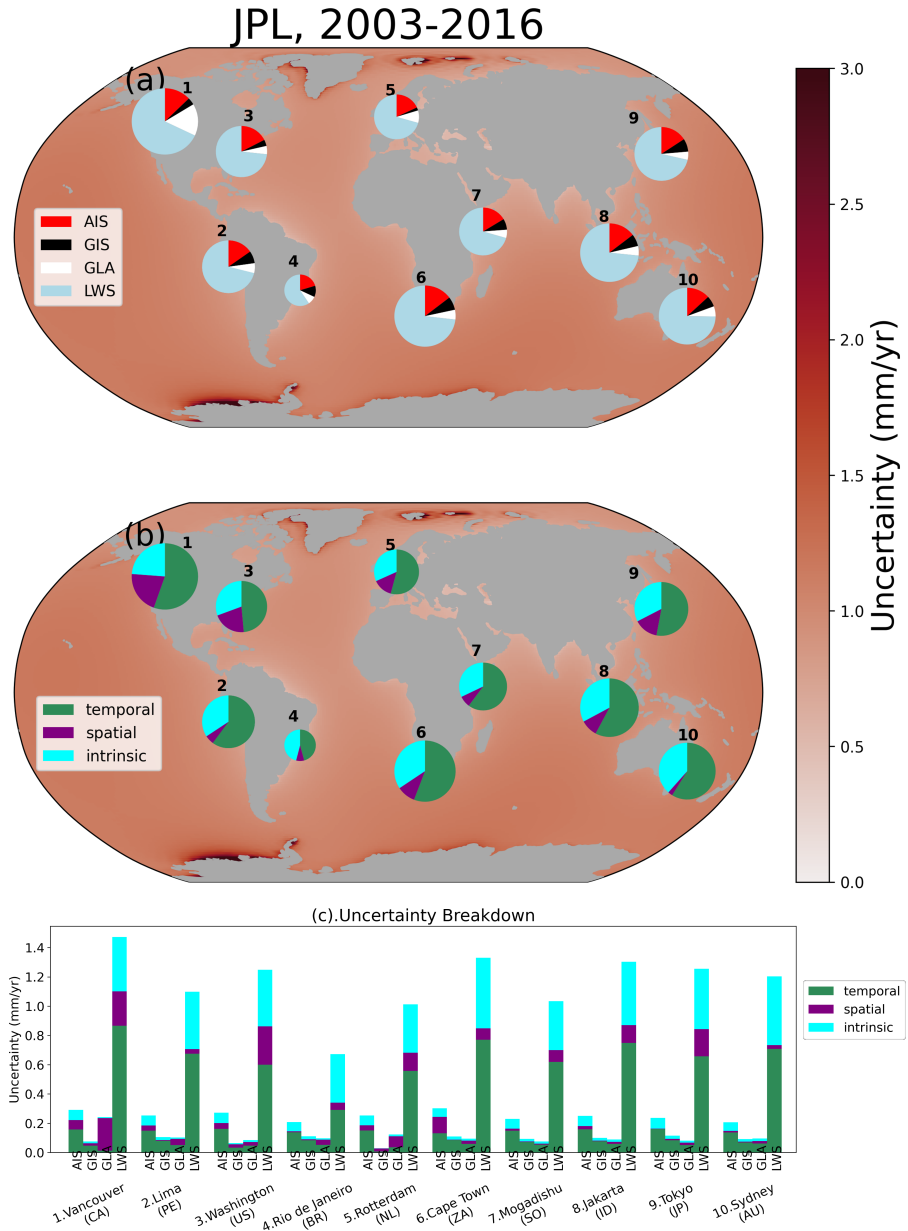


Figure S3.8: Same as Figure 3.8, but without the contribution of land water storage (LWS)

Table S3.1: Global mean barystatic sea-level contributions and uncertainties. Note that these numbers may be different compared to the histograms of Figure 3.7, which represent the spatial average of the regional trend and uncertainty. The difference between the trends is due to the use of noise-models for the regional trend, against an ordinary least-squares fit for the global mean trend. Note that we remove the 'spatial' part of the spatial-structural uncertainty of the regional assessment, and define the structural uncertainty as the standard deviation of the trends for the same contribution.

	2003-2016						1993-2016					
	trend	\pm	σ_{total}	$\sigma_{temporal}$	$\sigma_{structural}$	$\sigma_{intrinsic}$	trend	\pm	σ_{total}	$\sigma_{temporal}$	$\sigma_{structural}$	$\sigma_{intrinsic}$
AIS												
AIS_CSR	0.32	\pm	0.09	0.03	0.09							
AIS_JPL	0.27	\pm	0.1	0.04	0.09	0.04						
AIS_IMB	0.37	\pm	0.13	0.05	0.09	0.07	0.19	\pm	0.15	0.04	0.14	0.03
AIS_UCI	0.48	\pm	0.09	0.01	0.09		0.4	\pm	0.14	0.01	0.14	
GIS												
GIS_CSR	0.72	\pm	0.32	0.03	0.31							
GIS_JPL	0.73	\pm	0.32	0.03	0.31	0.01						
GIS_IMB	0.53	\pm	0.32	0.03	0.31	0.07	0.36	\pm	0.12	0.03	0.11	0.03
GIS_UCI	0.06	\pm	0.32	0.08	0.31		0.52	\pm	0.12	0.03	0.11	
GLA												
GLA_CSR	0.68	\pm	0.16	0.06	0.15							
GLA_JPL	0.64	\pm	0.16	0.07	0.15	0.01						
GLA_WGP	0.58	\pm	0.15	0.03	0.15		0.51	\pm	0.16	0.03	0.16	
GLA_ZMP	0.92	\pm	0.15	0.03	0.15		0.74	\pm	0.17	0.04	0.16	
LWS												
LWS_CSR	0.09	\pm	0.14	0.12	0.06							
LWS_JPL	0.22	\pm	0.33	0.12	0.06	0.3						
LWS_WGP	0.20	\pm	0.12	0.1	0.06		0.21	\pm	0.07	0.04	0.06	
LWS_GWB	0.18	\pm	0.12	0.1	0.06		0.29	\pm	0.07	0.04	0.06	
Combination												
CSR	1.81	\pm	0.39	0.14	0.36							
JPL	1.86	\pm	0.49	0.15	0.36	0.3						
IMB+WGP	1.68	\pm	0.39	0.12	0.36	0.1	1.27	\pm	0.26	0.07	0.25	0.04
IMB+GWB+ZMP	2.00	\pm	0.39	0.12	0.36	0.1	1.58	\pm	0.26	0.08	0.25	0.04
UCI+WGP	1.32	\pm	0.38	0.13	0.36		1.64	\pm	0.25	0.06	0.25	
UCI+GWB+ZMP	1.64	\pm	0.38	0.13	0.36		1.95	\pm	0.26	0.06	0.25	

3.5.2. DATA DESCRIPTION

The datasets used in this manuscript are briefly described below. In-depth description of each dataset can be found in their respective references.

GRACE MASCON ESTIMATES

We use GRACE land mass concentrations (mascons) solutions from two processing centres: RL06 v02 from CSR (Save et al., 2016; Save, 2020) and RL06 v02 from JPL (Watkins et al., 2015; Wiese et al., 2019). We chose to use the mascons solution instead of spherical harmonics to avoid the land-ocean leakage issue (Jeon et al., 2021; Chambers et al., 2007). The mascons include all mass changes in the Earth system, accounting for variations in land hydrology and in the cryosphere, as well as solid Earth motions (Adhikari et al., 2019). We do not, however, use the changes in the ocean, since we focus on land hydrology and cryosphere variations. CSR and JPL mascons are provided on a 0.25 and 0.5 degree grids, respectively, even though the native resolution of the GRACE/GRACE-FO data is roughly 300km (i.e., 3-degree equal-area mascons). The native resolution of CSR mascons are $1^\circ \times 1^\circ$ equal-area grid and $3^\circ \times 3^\circ$ for JPL mascons. Since the native resolution of GRACE observations of about 300 km at the equator (Tapley et al., 2004), the JPL mascons have independent solutions at each mascon centres, with uncorrelated errors, while the CSR mascons are not fully independent and are expected to contain spatially correlated errors. Both mascons have been corrected for glacial isostatic adjustment (GIA) with the ICE6G-D model (Peltier et al., 2018), and for ocean and atmosphere dealiasing (AOD1B 'GAD' fields). In addition, the JPL mascons use a Coastline Resolution Improvement (CRI) filter to separate land/ocean mass within the mascon (Wiese et al., 2016). Only the JPL mascons are provided with intrinsic uncertainty estimates (Wahr et al., 2006; Wiese et al., 2016). Both mascons are given with a monthly frequency, ranging from April-2002 to August-2020.

IMBIE ESTIMATES

For both ice sheets we use the products of IMBIE (Shepherd et al., 2018, 2020), which combines several estimates (26 for GIS and 24 for AIS) of ice sheet mass balance derived from satellite altimetry, satellite gravimetry and the input-output method. The monthly datasets cover the period 1992-2017 and 1993-2018 for AIS and GIS, respectively. In addition to the total ice sheet mass balance, the GIS dataset also distinguishes between surface mass balance (GRE SMB) and dynamic ice discharge (GRE DYN). For the AIS, the data is subdivided in the main 3 drainage regions: West Antarctica, East Antarctica and the Antarctic Peninsula. The IMBIE estimates are provided with intrinsic uncertainty estimates, reflecting the combination of several different datasets.

UCI AIS AND GIS ESTIMATES

Using improved records of ice thickness, surface elevation, ice velocity and a surface mass balance model (RACMOv2.3), Mougnot et al. (2019) and Rignot et al. (2019) present yearly reconstructions of mass changes from the 1970s until 2017 and 2018 for the Greenland and Antarctic ice sheets, respectively. These GRACE-independent reconstructions agree, within uncertainties, with estimates from radar and laser altimetry and GRACE. The reconstructions are provided as the mean for each drainage basin, based on ice velocity data (18 basins for AIS (Rignot et al., 2011) and 6 for GIS (Mougnot and Rignot, 2019)).

WATERGAP HYDROLOGICAL MODEL

We use the integrated version of the WaterGAP global hydrological model (Doll et al., 2003) v2.2d with a global glacier model (Marzeion et al., 2012), presented in Cáceres et al. (2020). The hydrological model uses a homogenized climate forcing from WFDEI (Weedon et al., 2014), with the precipitation correction of GPCC (Schneider et al., 2015). The model is provided on a 0.5 degree grid, covering all continental areas except for Antarctica. In order to consistently treat both ice sheets (GIS and AIS), we remove Greenland from the model. The WaterGAP model simulates human water use, daily water flows and water storage, taking into account dams and reservoirs based on the GRanD database (Lehner et al., 2011) and assuming that consumptive irrigation water use is 70% of the optimal level in groundwater depletion areas. The glacier model computes mass changes for individual glaciers around the world (based on the Randolph Glacier Inventory (Pfeffer et al., 2014), including glaciers surface mass balance, glacier geometry, air temperature and several others glacier-specific parameters and variables (Marzeion et al., 2012). The dataset is provided at a monthly frequency, from 1948-2016.

PCR-GLOBWB HYDROLOGICAL MODEL

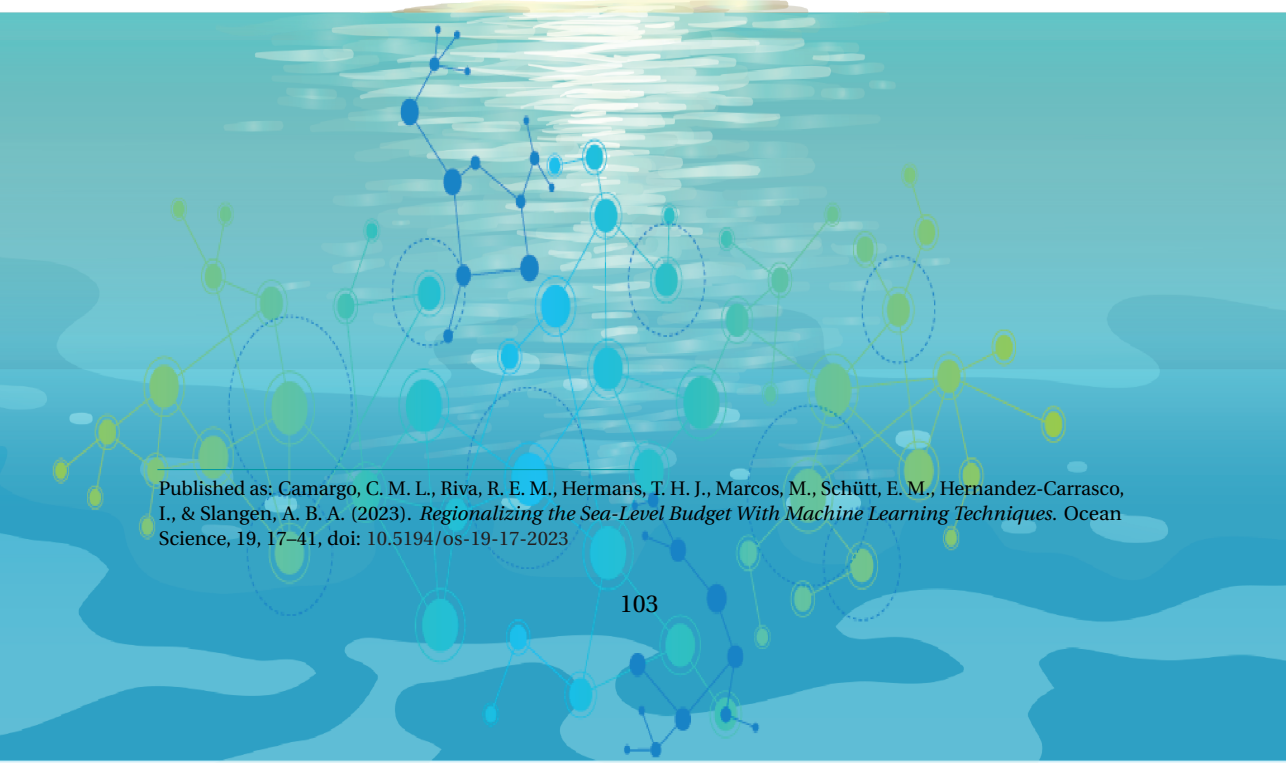
The second global hydrological model included in our analysis is the PCRaster Global Water Balance 2 model (PCR- GLOBW, Sutanudjaja et al. (2018)), which fully integrates different water uses, such as water demand, groundwater and surface water withdrawal, water consumption, with the simulated hydrology. The model is forced with the W5E5 version 1 (Lange, 2019), covering the period 1979-2016. It provides monthly averages of total water storage thickness with a 5 arcmin resolution. Dams and reservoirs from the GRanD database (Lehner et al., 2011) are also included in the model. As this model does not explicitly resolve glaciers nor includes ice sheets, we mask out all the glaciated areas.

ZEMP 2019 GLACIER DATA

We use the yearly glacier mass loss estimates from Zemp et al. (2019) over the period 1961 to 2016. This dataset combines the temporal variability from the glaciological data, computed using a spatio-temporal variance decomposition, with the glacier-specific values of the geodetic observations. Both glaciological and geodetic observations come from the World Glacier Monitoring Service (WGMS, 2022). This combined data is then statistically extrapolated to the full glacier sample to assess regional mass changes, taking into account regional rates of area change. This dataset provides regional mass changes for the 19 regions of the Randolph Glacier Inventory (RGI Consortium, 2017; Pfeffer et al., 2014). As the IMBIE estimates already account for peripheral glaciers to the ice sheets, we remove these from the Zemp dataset.

4

REGIONAL SEA-LEVEL BUDGET



Published as: Camargo, C. M. L., Riva, R. E. M., Hermans, T. H. J., Marcos, M., Schütt, E. M., Hernandez-Carrasco, I., & Slangen, A. B. A. (2023). *Regionalizing the Sea-Level Budget With Machine Learning Techniques*. *Ocean Science*, 19, 17–41, doi: 10.5194/os-19-17-2023

4.1. INTRODUCTION: THE SEA-LEVEL BUDGET

Sea-level change (SLC) is one of the major challenges of the coming centuries for coastal communities worldwide (Fox-Kemper et al., 2021). Global mean SLC has been rising at a rate of 1.6 mm yr^{-1} since 1900, and 3.3 mm yr^{-1} since 1993 (Frederikse et al., 2020). However, sea level does not change uniformly: it displays strong spatial and temporal variations (Hamlington et al., 2020). Ocean dynamics, land ice mass changes and associated gravitational effects, vertical land movement and the inverse barometer effect are some of the processes responsible for these regional differences (e.g., Stammer et al., 2013; Slangen et al., 2017a). Understanding the regional variability of the processes driving SLC is critical for identifying missing or misrepresented contributions, constraining sea-level projections, and to better prepare for the impacts of climate change.

4

The attribution of SLC to its different drivers is typically done using a sea-level budget approach (Chambers et al., 2017; Cazenave et al., 2018). For 1993-2018, about one third of the observed rate of global mean change can be attributed to thermal expansion of the oceans, while the rest is due to the effect of water and ice mass exchanges between land and ocean (Frederikse et al., 2020). Since the observed rate of SLC matches, within uncertainties, with the sum of the contributions of the various sources, the global mean sea-level budget for the period 1993-2018 is considered to be closed (Cazenave et al., 2018; Frederikse et al., 2020; Chen et al., 2020; Barnoud et al., 2021). However, locally attributing the drivers of SLC for this same period still leads to large differences between the total measured change and the sum of the contributions (e.g., Slangen et al., 2014; Royston et al., 2020). This is partly due to the spatial resolution of the current observational systems of the sea-level budget components and of the processes in question, which still limits the closure of the budget on a local spatial scale, for instance on a 1 degree resolution (Royston et al., 2020). Consequently, the regional sea-level budget has mainly been analysed on a basin-wide scale (e.g., Purkey et al., 2014; Frederikse et al., 2018, 2020; Royston et al., 2020) and has not been closed on sub-basin scales consistently for the entire world. The sea-level budget has also been analysed for individual coastline stretches characterized by coherent variability (Rietbroek et al., 2016; Frederikse et al., 2016, 2017b; Dangendorf et al., 2021), and at individual tide gauges (Wang et al., 2021b).

The basin-scale sea-level features extracted by Thompson and Merrifield (2014) have been frequently used in regional sea-level budget studies (Purkey et al., 2014; Frederikse et al., 2018, 2020; Royston et al., 2020). Although these publications have made significant advances in understanding the regional SLC, the basin scale is still too large to really understand the causes of local variations. In this chapter, we argue that understanding

the spatial structure of contemporary SLC is a key point to move towards a budget with finer spatial resolution. By identifying smaller physically coherent regions, some of the effects of small scale variability can be removed, allowing to close the budget at a sub-basin scale. Machine learning techniques, such as complex and neural networks, can be used to identify such spatial structures, determining the ideal resolution and regions of common sea-level variability and change. While machine learning methods have widely been used in oceanography (e.g., Richardson et al., 2003; Liu et al., 2006; Hernández-Carrasco and Orfila, 2018; Sonnewald et al., 2019; Falasca et al., 2019, 2020; Novi et al., 2021), only few examples analyzing sea surface height can be found (e.g., Liu et al., 2016; MA et al., 2016; Sonnewald et al., 2018). Here, we apply two machine learning techniques –self-organizing maps (SOM) and δ -MAPS– to extract coherent spatial features (domains) in SLC observations.

In this study we use the extracted domains to analyse the sea-level budget on a sub-basin scale during the satellite altimetry period (1993-2016), by using state-of-the-art estimates of SLC and its components. We limit our analysis to 2016 because of the temporal span of the hydrological models used to obtain the land water storage contribution to SLC. Additionally, instrumental problems (e.g., in Argo salinity data and satellite drifts) have raised questions about the performance and closure of the global mean sea-level budget after 2016 (Chen et al., 2020; Barnoud et al., 2021; Cazenave and Moreira, 2022). We hypothesize that by investigating the budget in covariant and physically coherent regions, we can resolve the discrepancies (i.e., close the budget) that appear in an increased-resolution sea-level budget (e.g., 1x1 degree).

4.2. DATA AND METHODS

In this section we introduce the datasets used for each of the different components of the SLB (Section 4.2.1). We also describe the trend and budget analysis (Section 4.2.2) and introduce the machine learning techniques used to extract coherent regions (domains) of sea-level variability and change (Section 4.2.3).

4.2.1. THE COMPONENTS OF THE REGIONAL SEA-LEVEL BUDGET

For the budget, we compare the total observed SLC η_{total} to the sum of the drivers of SLC $\eta_{drivers}$:

$$\eta_{total} = \sum \eta_{drivers}, \quad (4.1)$$

where η stands for the rate of SLC.

Total SLC (η_{total}) can be measured by tide gauges and satellite altimeters. Satellite altimeters measure geocentric or absolute change ($\eta_{geo(sat)}$), that is, the sea surface height in relation to the reference ellipsoid (Gregory et al., 2019). On the other hand, tide gauges measure sea surface height in reference to a terrestrial landmark ($\eta_{rel(TG)}$), registering the relative SLC. The latter is affected by vertical land motion (VLM) due to, for instance, land subsidence and tectonics (Wöppelmann and Marcos, 2015), while geocentric sea level can not differentiate if the change is either from the solid Earth or the ocean. The relationship between geocentric and relative SLC is:

$$\eta_{total} = \eta_{geo(sat)} = \eta_{rel(TG)} + VLM. \quad (4.2)$$

4

From hereon, when we use η_{total} , we are referring to the geocentric SLC derived from satellite altimetry (Figure 4.1a). We use multi-mission gridded Level-4 data from 4 distribution centers: CMEMS (CMEMS, 2022), JPL MEaSUREs (Zlotnicki et al., 2019), SLcci (SLcci, 2022) and CSIRO (CSIRO, 2022). All of these products use the same reference ellipsoid model (GRS80/WGS), and have a monthly temporal resolution, except for JPL MEaSUREs time series which provides sea surface height data every 5 days and was averaged into monthly means. All data is regridded to a $1^\circ \times 1^\circ$ map, selected within 66°S to 66°N of latitude, and combined into an ensemble mean, to avoid systematic errors. We apply a glacial isostatic adjustment (GIA) correction to the altimetry data from ICE-6G VM5a (Argus et al., 2014; Peltier et al., 2015), by removing the rate of change of the geoid (i.e., $\text{Drad} + \text{Dsea}$) from the trends.

SLC expresses changes in the volume of the ocean. These can be caused by changes in the ocean density, mass or area. Density-driven changes, known as steric SLC, are caused by variations in the ocean temperature and salinity (Gill and Niller, 1973; MacIntosh et al., 2017). All sea-level variations not driven by density changes are known as manometric SLC (Gregory et al., 2019). Thus, Equation 4.1 can be rewritten to:

$$\eta_{total} = \sum \eta_{drivers} = \eta_{SSL} + \eta_{MAN}, \quad (4.3)$$

where η_{SSL} and η_{MAN} refer to steric and manometric SLC, respectively.

For steric SLC (η_{SSL} , Figure 4.1c), we use the estimates of Camargo et al. (2020), which are based on fifteen different ocean temperature and salinity datasets down to 2000m depth, using Argo floats (Roemmich and Gilson, 2009; Gaillard et al., 2016; Li et al., 2017; Lu et al., 2019), multiple in-situ observations (Ishii and Kimoto, 2009; Guinehut et al., 2012; Cabanes et al., 2013; Good et al., 2013; Gaillard et al., 2016; Ishii et al., 2017; Cheng

et al., 2019; Szekely et al., 2019) and ocean reanalyses (Blockley et al., 2014; Maclachlan et al., 2015; Storto and Masina, 2016; Garric and Parent, 2017; Carton et al., 2018; Zuo et al., 2019). We complement this data with the deep ocean steric estimate of Purkey et al. (2019, updated from Purkey and Johnson (2010)).

Manometric SLC (η_{MAN}), also referred to as the bottom pressure term (Gregory et al., 2019), can be further divided into (i) η_{GRD} , the Gravitational, Rotational and viscoelastic Deformation (GRD) response of the Earth to water and ice mass exchanges between land and ocean, and (ii) η_{DSL} , the dynamic redistribution of ocean mass due to ocean circulation, atmosphere and ocean bottom pressure changes as a result of the steric change of the oceans (Landerer et al., 2007), following:

$$\eta_{MAN} = \eta_{GRD} + \eta_{DSL}. \quad (4.4)$$

The GRD component (η_{GRD} , Figure 4.1d) reflects how the mass loss of continental ice stored in glaciers and ice sheets and variations in land water storage affect sea level. The GRD effect can be split between responses due to contemporary changes, and due to the response of the Earth to the last ice age, known as post-glacial rebound or GIA. The integrated response of the GRD effect over the oceans, i.e. the global mean, is known as barystatic SLC (η_{BSL} , Gregory et al., 2019). For the GRD component, we use the estimates from Camargo et al. (2022), which includes the geocentric sea level response to changes on the Antarctic and Greenland ice sheets, glaciers and terrestrial water storage. These are based on a suite of different estimates of land mass change, and computed solving the sea-level equation following Farrell and Clark (1976) and Slangen et al. (2014).

The dynamic component (η_{DSL} , Figure 4.1e) refers to mass changes driven by bottom pressure changes, that is, the redistribution of mass that was already in the oceans. Note that, by our definition, the dynamic SLC (η_{DSL}) is part of the ocean dynamic change ($\Delta\zeta$, Gregory et al., 2019), the latter also including the effect of local steric anomalies (η'_{SSL}). That is, the dynamic term here is the residual of the sterodynamic SLC with the steric contribution removed (Gregory et al., 2019). η_{DSL} is computed from the sea surface height of five ocean reanalyses (Table 4.1), by first removing the time-varying global mean from the sea surface height, and then by removing the local steric anomaly. This procedure is done in each ocean reanalysis individually, and we then combine the five estimates into an ensemble. We acknowledge that this method introduces some circularity to the budget analysis: the reanalysis, used to obtain η_{DSL} , assimilates satellite sea surface height, and in the budget analysis we compare this estimate with satellite sea surface

height (η_{total}). Compared with the η_{DSL} estimated from Gravity Recovery and Climate Experiment Satellite (GRACE, Tapley et al., 2004), η_{DSL} sea-level trends from 2005-2015 agree on large scale patterns and magnitude of dynamic changes (Figure S4.1). Note that our budget components do not incorporate GRACE mass changes over the oceans, hence it is an independent estimate for validation. More detail on the estimation and validation of η_{DSL} is given in Supplementary Information 4.6.1.

Finally, equation 4.3 can be rewritten as:

$$\eta_{total} = \eta_{SSL} + \eta_{GRD} + \eta_{DSL}, \quad (4.5)$$

4

such that the total observed SLC (Figure 4.1a) can be compared with the sum of the components (Figure 4.1b). The ensemble mean of each term of Equation 4.5, used throughout this manuscript for the sea-level budget analysis, is shown in Figure 4.1, where η_{total} is the geocentric SLC from satellite altimetry, corrected for the inverted barometer and GIA (η_{GIA}) effects; η_{SSL} is the full-depth steric SLC; η_{GRD} is the contemporary ocean mass redistribution due to the land-ocean mass exchange, already corrected for η_{GIA} effects; and η_{DSL} is the mass redistribution due to purely ocean dynamics. A summary of the budget components and datasets sources is given in Table 4.1. Note that all the used datasets have been homogenised to a monthly temporal resolution and a $1^\circ \times 1^\circ$ spatial resolution.

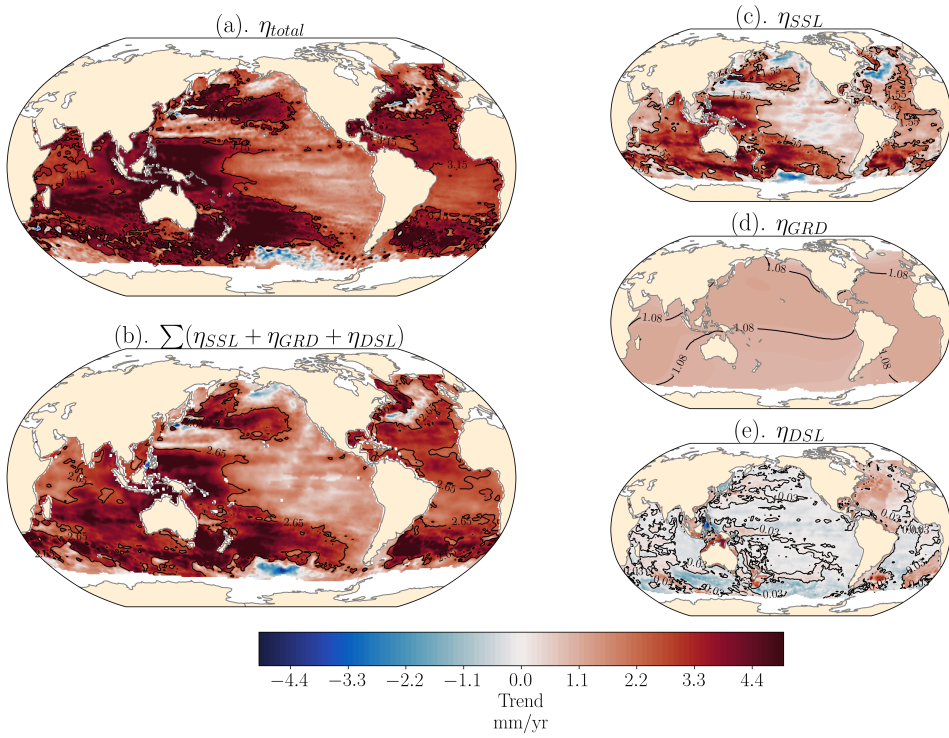


Figure 4.1: Regional sea-level trends for 1993-2016 (mm/yr^{-1}) for (a) altimetry; (b) sum of sea-level components; (c) full-depth steric, (d) GRD effect and (e) dynamic SLC. Black contour line indicates global mean SLC.

Table 4.1: Summary of the sea-level budget components and data sources used in this manuscript.

Symbol	Name	Description	Reference
η_{total}	Observed change	Total sea-level change from satellite altimetry	Ensemble of CMEMS (CMEMS, 2022), JPL MEaSUREs (Zlotnicki et al., 2019), SLcci (SLcci, 2022) and CSIRO (CSIRO, 2022)
η_{SSL}	Steric expansion	Full depth density-driven sea-level change due to ocean temperature and salinity variations	Camargo et al. (2020) and Purkey and Johnson (2010)
η_{GRD}	Mass change	Contemporary ocean mass redistribution due to the land-ocean mass exchange	Camargo et al. (2022)
η_{DSL}	Dynamic change	Mass redistribution due to purely ocean dynamics	Ensemble of SODA (Carton et al., 2018), C-GLORS (Storto and Masina, 2016), GLORYS (Garric and Parent, 2017), FOAM-GloSea (Blockley et al., 2014; Maclachlan et al., 2015) and ORAS (Zuo et al., 2019)

4.2.2. COMPUTING TRENDS AND UNCERTAINTIES

Our sea-level budget includes the comparison of sea-level time series, trends and associated uncertainties. We assume that sea-level trends are the sum of a deterministic model (including annual and semi-annual signals) and stochastic noise (temporal uncertainty). We use the software Hector (Bos et al., 2013) to compute the trends and the associated 1-sigma uncertainty for each of the budget components. Following Bos et al. (2014b); Royston et al. (2018); Camargo et al. (2020, 2022), we test 8 different noise-models to describe the auto-correlation between the residuals of the regression. Using the Akaike and Bayesian information criteria (Akaike, 1974; Schwarz, 1978), we select the best performing noise-model at each grid cell. More information on the noise-model analysis can be found in Camargo et al. (2020, 2022). For the GRD component, in addition to the temporal uncertainties, we also consider the spatial, structural and intrinsic uncertainties (Camargo et al., 2022). Note that, unlike for the identification of the domains (Section 4.2.3), the time series used to estimate trends and uncertainties include seasonality and global mean trends.

We assume independence of the terms, and sum the trends linearly and uncertainties in quadrature. For each sea-level domain we take the area-weighted spatial average of the time series, trend and uncertainties. Performance of the sea-level budget is evaluated by (i) the magnitude of the residual, (ii) the Pearson's correlation coefficient (r) between the altimetry time series and the budget components, and (iii) the normalized root mean squared error (nRMSE, Peck et al., 2008). nRMSE measures the distance between the true value, in this case altimetry, and the modeled value, in this case the sum of the budget components. Contrary to r , nRMSE closer to 0 indicates better performance.

4.2.3. CLUSTERING TECHNIQUES

To answer our research questions, we must first identify regions with similar sea-level variability. To do so, we use two different machine learning pattern detection algorithms, one based on a neural network approach, Self-organizing Maps (SOM), and one based on a deep network detection method, δ -MAPS. The methodological differences in these two techniques lead to different patterns of SLC in terms of geographical location, region size, and ocean coverage. Hence, by using both methods, we can (i) find prevailing sea-level modes, (ii) compare the patterns and sea-level budget for the different methods and (iii) balance out the advantages and disadvantages of using a single method. Both methods are used to reduce the dimensionality of the data, transforming high-dimensional input data into low-dimensional features (Liu et al., 2006; Falasca et al., 2020).

For both clustering techniques we use $1^\circ \times 1^\circ$ monthly satellite altimetry time-series (CMEMS, 2022) from 1993-2019 as input. Note we use a longer time-series than the ones for the budget analysis, as longer time-series can resolve better the temporal variability. However, additional tests (not shown) showed that the clustering is not strongly affected by the extra 3 years of data. We pre-process the input data by removing the global mean trend, seasonality and by applying a spatial Gaussian filter of 300km half-width to remove small scale variability. Note that, after the domains identification, for the budget analysis, global mean trend, seasonality and small scale variability are included in the time series. Smaller seas, such as the Mediterranean, Baltic, Black and Caspian seas have been removed from the data prior to the clustering.

4

SELF-ORGANIZING MAPS (SOM)

SOM (Kohonen, 1982) is a feature extraction and classification method based on an unsupervised neural network (Liu et al., 2006), which was demonstrated to be more powerful than conventional feature extraction methods (e.g., Liu and Weisberg, 2005). The ability of SOM to extract patterns of sea level variability from satellite altimetry data has been shown in previous works (e.g., Hardman-Mountford et al., 2003; Iskandar, 2009; Liu et al., 2016; Weisberg and Liu, 2017; Nickerson et al., 2022). To analyse sea level data, SOM can be applied either in the spatial domain, focusing on the characteristic spatial patterns, or in the time domain, focusing on the characteristic time series (Liu et al., 2016). The latter results in regionalizing the sea-level variability, and is pursued here to analyse global sea level data.

We use the MatLab SOM toolbox (Vesanto et al., 2000), and follow Liu et al. (2006) and Hernández-Carrasco and Orfila (2018) to choose the parameters. We apply the SOM algorithm in the time domain in order to extract the spatial patterns, herein referred to as domains, based on coherent temporal sea-level variability. Before initializing the SOM, the 3D input data (time,lat,lon) is concatenated to 2D (time, latxlon; Richardson et al., 2003; Liu et al., 2016), and normalized to have unit variance. The network is initialized linearly, based on the first two principal components of the time series, and trained in a batch mode, that is, at each step of the training process, all input data vectors are simultaneously used to update the network. Training is performed over 10 iterations, which is necessary to stabilize and converge the network, while avoiding overfitting of the SOM (Liu et al., 2006). We use the 'Epanechnikov function' (Epanechnikov, 1969) as a neighborhood function, which returns the most accurate SOM patterns, a hexagonal lattice, and a neighborhood radius (determining the radius of cells that are updated during the training process) of 2 cells at the beginning, decreasing linearly to 1 during the

training process. We tested different SOM parameters, and verified that this combination gave the smallest quantification errors by computing the averaged Eulerian distance between each data input vector and the best matching unit (BMU).

SOM domains do not need to be geographically contiguous, that is, different non-connected regions can be assigned to a single domain. Initially, the strong sea-level variability of the Equatorial Pacific Ocean dominated the clustering, hindering pattern identification in the Atlantic Ocean (Supplementary Figure S4.8). To overcome this issue we perform the clustering analysis on the Atlantic and Indo-Pacific Ocean basins separately. We select a map size of 3x3 neurons (i.e., neural network nodes) in each basin, leading to a total of 18 domains. Using different map sizes (e.g., Supplementary Figure S4.8) led to more "patchy" results, hence we used map size of 3x3 neurons as a compromise between the amount of detail and the interpretability of the domains.

δ -MAPS

δ -MAPS (Fountalis et al., 2018) is a complex network methodology which reduces the spatiotemporal dimensionality of a field by identifying regions (domains) with similar dynamics and their connectivity (Bracco et al., 2018; Falasca et al., 2020). Here we focus only on the domains identification (dimensionality reduction) function of the δ -MAPS method. δ -MAPS domains are spatially continuous (i.e., grid cells need to be physically connected to be clustered in the same domain) and are potentially overlapping regions that have a highly correlated temporal activity (Falasca et al., 2019).

Formally, each input grid cell is associated with a time series, including the K nearest neighbors, based on the haversine distance (angular distance between two points on a sphere). The local homogeneity, defined as the average Pearson cross-correlation between a grid cell and its K -neighbors, is computed and tested against a threshold value δ . If the local homogeneity is greater than δ , with a statistical significance level of 0.1, then the grid cell is considered a core, which then is expanded to identity domains (Fountalis et al., 2018; Falasca et al., 2019; Novi et al., 2021). Each domain expands to adjacent cells, as long as the local homogeneity continues to be higher than δ . To choose the optimal neighborhood size K , we follow a heuristic approach, testing K values from 4 to 25 following Falasca et al. (2019). As in δ -MAPS not every grid point needs to belong to a domain (in contrast to SOM), we then choose the K -value taking into account the amount of unclustered cells (i.e., the one with most of the ocean belonging to domains). We also use the normalized mutual information (NMI) matrix (Falasca et al., 2019) to identify the K -value with high NMI for it and its neighboring K -values, meaning that the results are less sensitive to the chosen K -value. These parameters led to the use of $K = 5$.

4.3. IDENTIFYING DOMAINS OF SEA-LEVEL VARIABILITY

Both clustering methods successfully reduce the dimensionality of the input data, despite the higher number of domains identified by δ -MAPS (Figure 4.2). SOM identified 18 coherent domains, with a domain area varying from 3.84 to 34.51 million km², and an average and total size of 17.61 and 316.90 million km². δ -MAPS identified 92 coherent domains, with a domain area varying from 0.03 to 24.15 million km², with average and total size of 2.53 and 242.01 million km², respectively. Despite the methodological differences, we find that prominent sea-level features are clustered in a similar way by SOM and δ -MAPS (Figure 4.2). Some of the patterns identified can be linked with known oceanic patterns, as we will discuss below. However, we note that covariability does not imply a common forcing, and that some patterns may be statistically separated or grouped without a clear physical reason. It is also important to note that these clustering methods do not account for auto-correlation in time, that is the time lag in the progression of a signal across the ocean basin. Since we use monthly data, signals that propagate faster than a month (typically barotropic) will be more clearly correlated in our clustering. On the other hand, slower propagating signals, such as the first baroclinic mode, will lose correlation in space and will not be represented in the identified domains.

The central Pacific domain, where the variability is dominated by El Niño Southern Oscillation (ENSO) events, covers a similar region in both methods. The 'ENSO-tongue', starting from the coast of Peru and Ecuador and spreading west until the central Pacific, is identified by both methods (SOM domain 12 (pink), δ -MAPS domain 45 (light green)). The Western Tropical Pacific Ocean (WTPO), influenced by ENSO and the Pacific decadal oscillation (PDO), is also identified as a single domain by both methods (SOM domain 16 (light green), δ -MAPS domain 89 (light brown)). The WTPO domain matches with the region of significant spatial correlation between steric and coastal sea-level found by (Dangendorf et al., 2021) for West Australia. In the SOM clustering, the WTPO domain incorporates the Leeuwin Current (Western Australia, Pattiaratchi and Siji, 2020) in the Indian Ocean, which is affected by waves travelling through the Tropical Australasian Seas (Feng et al., 2004). While this connection is not captured by δ -MAPS, the coherence along the western coast of Australia is featured in a single domain (δ -MAPS domain 92, light pink).

The Kuroshio Extension region is also identified in both methods (SOM domain 10 (brown), δ -MAPS domain 88 (brown)), reflecting how strong boundary currents influence the sea-level variability. Another example is the North Atlantic, which has similar clustering in both methods, especially in the domain south of Greenland (SOM domain 9 (light

purple), δ -MAPS domain 33 (purple)), which is marked by decadal-scale SLC reflecting the strength and shape of the wind-driven Subpolar Gyre and the Atlantic Meridional Overturning Circulation (Chafik et al., 2019). Within these domains, density anomalies are known to flow southward from the Labrador Sea into the Subpolar Gyre through coastally trapped waves (Dangendorf et al., 2021).

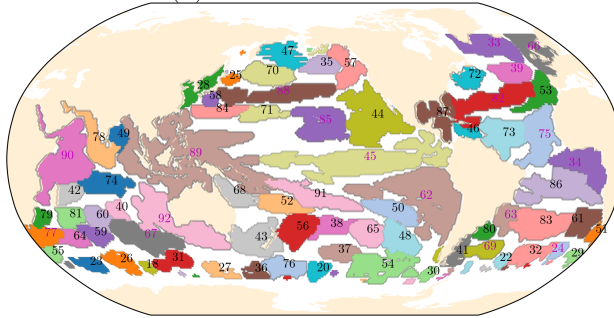
Another region identified in both methods is the Northwestern European Shelf (SOM domain 8 (purple), δ -MAPS domain 66 (grey)), which is part of a domain that extends along the whole western European coast, continuing down to the Canary islands and well into the Atlantic. This connection could be related to the hypothesis that coastally trapped waves and longshore winds cause a coherent region of sea-level variability from around the latitude of the Canary Islands up to the Norwegian Sea (Calafat et al., 2012; Chafik et al., 2019; Hughes et al., 2019; Hermans et al., 2020; Dangendorf et al., 2021). These features are in a separate δ -MAPS domain (53, green) than the Northwestern European Shelf. It is important to note that coherent features smaller than 300km are not captured in the domains because of the spatial filtering applied before the clustering analysis.

As SOM domains do not need to be contiguous, possible pseudo-teleconnections between different ocean regions (within the Atlantic and Indo-Pacific Ocean basins) come out of the analysis. For example, areas adjacent to the 'ENSO-tongue' domain, both north and south, are clustered together in domain 18 (light blue) or in domain 15 (moss green), indicating how the ENSO signal is propagated through the Pacific, possibly through coastally trapped waves (Hughes et al., 2019) in the coastal domains (15), or via atmospheric teleconnections. However, not every region classified into the same SOM domain results from a clear connection. For example, SOM domain 17 (blue) groups the ocean adjacent to South Africa, the region below the Kuroshio Extension (offshore of Taiwan) and a region south of Australia and New Zealand. Another example is SOM domain 7 (salmon-pink), which implies a connection between the Atlantic Caribbean Sea and the west part of the South Atlantic Gyre (capturing parts of the Brazil Current). These regions have been classified together because they have a similar behaviour in terms of sea-level variability, but probably different forcing. Further investigation, with ocean currents, ocean-atmospheric oscillations and ocean waves, is necessary to explore and quantify the physical connection behind these patterns.

Unlike SOM, every δ -MAPS domain is assigned a unique number and not every pixel needs to be clustered (Figure 4.2a, white regions). Consequently, this method yields a larger number of domains with smaller size, while avoiding pseudo-teleconnections. The dominant sea-level modes are clear on δ -MAPS clustering, reflecting the influence, for

example, of ENSO and western boundary currents on sea level. For example, the entire Caribbean (domain 87 (brown)) and Gulf of Mexico (domain 82 (red)) is in a single domain, highlighting the similarity in that region. The same goes for the Equatorial Atlantic (domain 86 (light purple)), the ENSO region (domains 45, 89 and 62 (light green, light brown and light brown, respectively)), and the Kuroshio current (domain 88 (brown)).

(a). δ -MAPS Domains



(b). SOM Domains

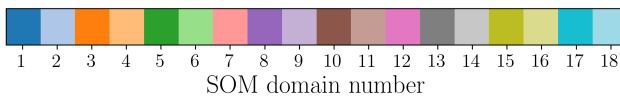
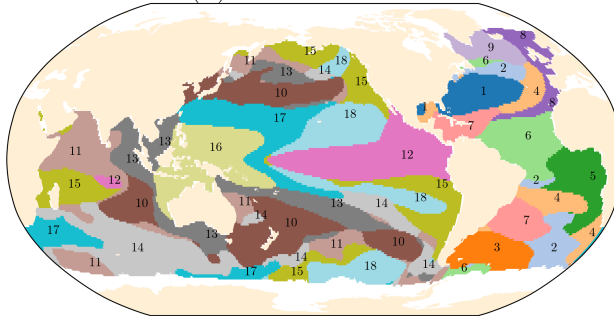


Figure 4.2: Domains of coherent sea-level variability. (a): δ -MAPS method (92 domains); (b): Self-organizing Maps (SOM) method (18 domains). Numbers indicate the domain code, domain names are given through the main text and in Supplementary Table S4.1. δ -MAPS domains with codes in magenta indicate selected domains for Figure 4.4. For visibility, small domains have not been labeled. Given the large number of domains, δ -MAPS has a repeating color pallet, but since δ -MAPS domains need to be continuous, repeated colors do not indicate the same domain. White regions in δ -MAPS indicate incoherent regions, which were not incorporated in any domain.

As shown in Royston et al. (2020), the components of the sea-level budget have a similar spectral power to the total observed sea surface height of altimetry between wavelengths

of approximately 3,000 and 10,000 km. The clustering techniques applied here not only reduce the dimensionality of the data, but also average out sea-level variability in regions of coherent variability, being ideal for a regional budget analysis (next section).

4.4. THE REGIONAL SEA-LEVEL BUDGET ON DIFFERENT SPATIAL SCALES

4.4.1. SEA-LEVEL TREND BUDGET CLOSURE

We investigate the trends of the sea-level budget on different spatial scales, from a finer (1x1 degree) to coarser scale (δ -MAPS and SOM domains; Figure 4.3). The residuals (i.e., the difference between the total SLC and the sum of the components) decrease towards a coarser spatial scale: for 1 degree, they range from -8.2 to 21.1 mm yr^{-1} , while for δ -MAPS they range from -1.2 to 3.8 mm yr^{-1} , and for SOM from 0.1 to 0.7 mm yr^{-1} . This shows an improvement of the budget closure (i.e., total and sum of components agree within uncertainties) by using the pattern detection algorithms: the budget closes in all 18 SOM domains (100% of SOM ocean area), in 70 out of 92 of the δ -MAPS domains (94% of δ -MAPS ocean area (229.9 million km^2)) and in 72% of the grid cells in the 1 degree budget (75% of the ocean area) (Figure 4.3). There is a clear relation between spatial scale of the region considered for the trend, and the residuals of the budget (see also Figure S4.6). The good closure in the 1 degree budget is likely an artefact of the large uncertainties of the observations, which on a local scale can be up to 18.9 mm yr^{-1} (see Supplementary Figure S4.3). This is in line with Royston et al. (2020), who found that local biases of steric estimates together with the resolution limitation of GRACE observations over the oceans hinder the budget closure at 1 degree resolution. When the regional domains based on SOM and δ -MAPS are considered, the uncertainties show a fivefold reduction compared to the 1 degree resolution, reaching up to 3.6 mm yr^{-1} and an average value of 1.6 mm yr^{-1} (Supplementary Figure S4.3), while the budget still closes.

Consequently, there is a better match between the total observed rate of SLC with the sum of the components for the clustered regions (scatter points in Figure 4.3, right column), with a reduction in the spread of the scatter points and moving closer to the 1:1 line (black dashed line) for the coarser resolutions. The dashed pink lines in Figure 4.3 indicate the half-width of the 95% confidence interval of the uncertainty of the residuals, showing a slightly larger width for 1 degree, and a smaller one for SOM and δ -MAPS. Even when the components uncertainties (grey error bars) are considered, the scattered values are mostly within the width of the 95% confidence interval for the SOM domains, confirming the improvement of the budget for this case. There is a strong linear correlation between

the total and the sum of the drivers, with Pearson's r varying from 0.81 for the 1 degree budget and δ -MAPS to 0.98 for SOM. The RMSE also decreases for the coarser scales, from 1.01 mm yr^{-1} for the 1 degree budget to 0.47 mm yr^{-1} for the SOM domains.

The altimetry trends are generally larger than the sum of the SLC drivers, as indicated by the positive residuals and scatter points above the 1:1 line on Figure 4.3. This is true for more than half of the δ -MAPS domains and for all SOM domains except one: SOM domain 9 (South of Greenland) is marked by a negative residual, that is, the sum of the drivers is larger than the observed altimetry trend. Several δ -MAPS domains, such as Southwest of Australia (domains 92 and 67), Southeast Pacific (domains 37 and 54), Gulf Current (domain 82) and Brazil-Malvinas confluence zone (domains 80 and 69), also have a negative residual. This might indicate a larger temporal variability or regime shifts in this region, or might be due to the ocean dynamics contribution, such as the effect of the Subpolar Gyre around the south of Greenland (Chafik et al., 2019), as we will see in the next section (Section 4.4.2).

4

4.4.2. EXPLAINING THE SEA-LEVEL BUDGET CONTRIBUTIONS

In this section, we investigate which components dominate the trend and temporal variability in each of the different domains. For comparison and discussion purposes, we choose 18 δ -MAPS domains (magenta numbers, Figure 4.2b) located close to the 18 SOM domains. Trends for all δ -MAPS domains are available online as an interactive map (see caption Figure 4.4).

As shown previously, we find a good match of total observed SLC and the sum of components (Figure 4.4a,b, green stars and purple triangles, respectively) for all SOM and δ -MAPS domains. The largest budget uncertainties, considering both altimetry and the sum of components, is seen in the WTPO domain (SOM 16, δ -MAPS 89). These uncertainties may be related to: (i) poor performance of standard altimetry products in these shallow regions; (ii) poor Argo float coverage in the region (Kleinherenbrink et al., 2017), influencing both the steric and dynamic components; and (iii) large internal variability due to ENSO events in this region, which may contribute to large temporal uncertainties in the steric and altimetry components (Kleinherenbrink et al., 2017; Wagner and Böning, 2021). This region is also within the Indian-south Pacific basin (Thompson and Merrifield, 2014), which was the only basin in which the regional budget from 2005-2015 could not be closed (Royston et al., 2020).

The GRD component (Figure 4.4, blue) has a relatively comparable contribution to all regions, contributing about 1.5 mm yr^{-1} of sea-level rise. The dynamic and steric com-

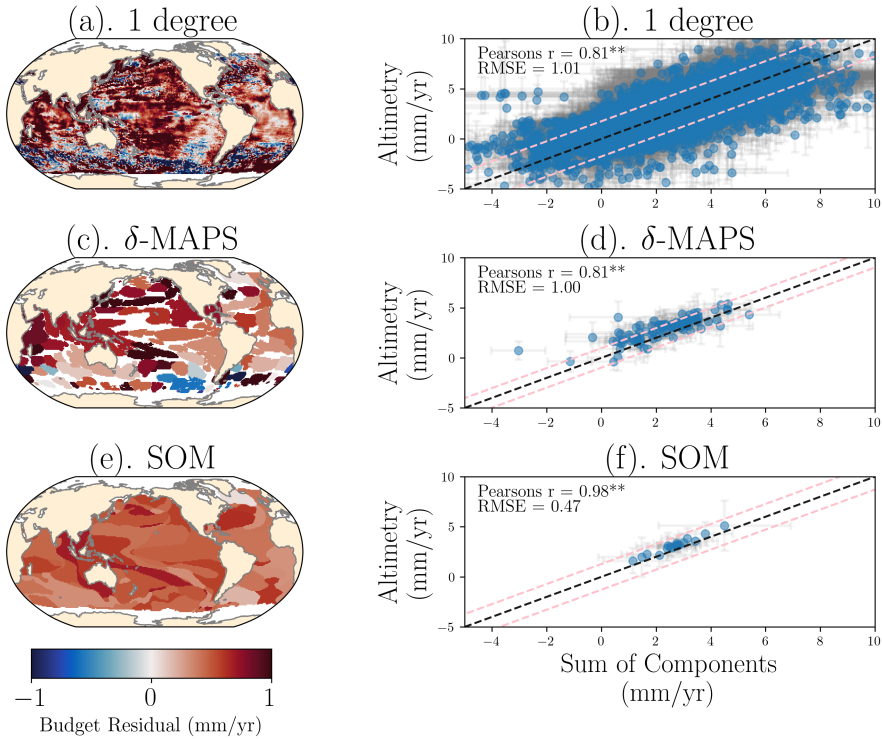


Figure 4.3: Sea-level budget residuals (maps(a,c,e) and comparison between total sea-level change (y-axis) and sum of components (x-axis) (scatter plots (b,d,f)) for 1 degree (a,b), δ -MAPS domains (c,d) and SOM domains (e,f). Gray lines indicate the uncertainties (1-sigma) of the components. In the scatter plots every point indicates one region (grid in case of 1degree), pink dashed lines indicate the half-width of the 95% confidence interval of the residuals uncertainty, grey error bars indicate the component uncertainty. ** indicates that coefficient is statistically significant (p-value <0.01).

ponents, however, show a strong regionally varying contribution (Figure 4.4, red and yellow, respectively). For example, for SOM (δ -MAPS) domains 10 (88), 13 (92), 14 (67) and 16 (89), more than 50% of the total trend is due to steric variations. On the other hand, for SOM domains 1 and 18 and δ -MAPS domains 39, 45 and 62, the steric trend explains less than 20%. The dynamic component shows a small contribution for most of SOM domains, and in some domains even a negative trend (e.g., SOM domain 11, 12 and 14). An exception is the Gulf Stream domain (SOM 1, δ -MAPS 82), where almost half of the total trend is explained by the dynamic component. This dominance of the dynamic component reflects the influence of the strong western boundary current on sea level in this region. The south of Greenland domain (SOM 9, δ -MAPS 33) also includes a relatively large dynamic contribution, with a trend of $0.49 \pm 0.21 \text{ mm yr}^{-1}$, reflecting the influence of the Subpolar Gyre in this region. The dynamic component also has a significant contribution to other δ -MAPS domains, such as domains 24, 69, 39, 66 and 67. Domain 67, located southwest of Australia, shows a large negative dynamic trend, which can be related to the influence of the West Australian Current.

4

Regarding the temporal evolution (Figure 4.4c,d and Supplementary Figure S4.5), both SOM (solid lines) and δ -MAPS (dashed lines) time series show a similar behaviour. The steric component dominates the temporal sea-level variability, with a good match to the altimetry. The time series of 'ENSO-tongue' domain (SOM 12 and δ -MAPS 45, Figure 4.4d) shows the clear response of sea level to ENSO, with peaks coinciding with strong ENSO events, such as the El Niño of 1997 and 2015 (Webb and Magi, 2022). The prominent contribution of the dynamic component to the total trend in the Gulf Stream domain (SOM 1 and δ -MAPS 82) is not reflected in the time series (Figure 4.4c). Hence, while the dynamic component has a significant impact on the overall change, it does not contribute to the seasonal to interannual sea-level variability. This is true for all other domains (Supplementary Figure S4.5), except for SOM (δ -MAPS) domain 2 (24) and 18 (85), where we find a better match between the dynamic and altimetry time series.

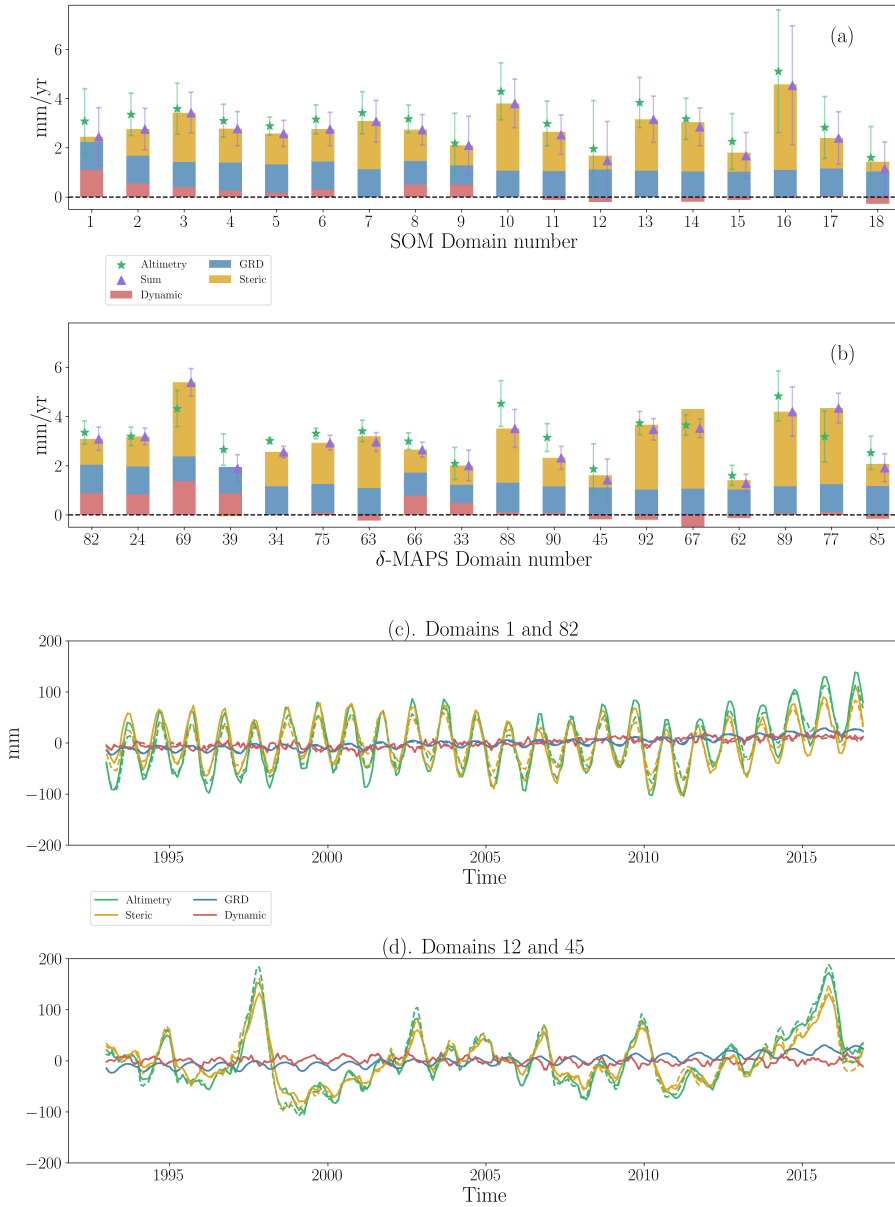


Figure 4.4: Sea-level budget trends (mm yr^{-1}) for (a) SOM and (b) δ -MAPS domains, and (c,d) time series for two example domains, where solid and dashed lines indicate SOM and δ -MAPS time series, respectively. Location of each domain is shown in Figure 4.2 (domain numbers in magenta for δ -MAPS). For comparison δ -MAPS domains are matched to the SOM domains, for example SOM domain 12 to δ -MAPS domain 45. Bar plot for all other δ -MAPS domains can be found in Supplementary Figure S4.4. Error bars indicate the 1-sigma uncertainty of the trend. Time series for all SOM domains and for the 18 δ -MAPS domains in (b) are shown in Supplementary Figure S4.5. An interactive budget map is available at <https://carocamargo.github.io/resources/regional-SLB-domains/> for both SOM and δ -MAPS.

4.4.3. SEA-LEVEL BUDGET PERFORMANCE

Here, we investigate the closure of the budget considering (i) the components included in the budget, (ii) the size of the domains and the clustering method, and (iii) the datasets used for each component. To illustrate the performance of the budget considering the domains used and the components included in the budget, we show how the Pearson's correlation coefficient (r) and the normalized root mean squared error (nRMSE) change when these factors vary (Figure 4.5). This analysis firstly shows that the budget closure improves when more components are included in the budget. While we get a poorer performance when only considering the dynamic or the GRD component, the budget with only steric already performs relatively well. The improved correlation and lower RMSE with the steric component is not surprising; the seasonal cycle is predominantly steric. The budget performance is enhanced by the addition of the dynamic and GRD components, shown by the narrowing of the box-and-whiskers plot.

Figure 4.5 also shows an improvement of the budget closure for δ -MAPS and SOM domains, in relation to the 1 degree resolution, regardless of the budget combination. There are two possible reasons why a coarser spatial resolution leads to decreasing uncertainties and a better budget closure: (i) the spatial scale of the process itself, as changes in long-term sea level typically occur on a coarser resolution than 1 degree; and/or (ii) there is a mismatch in the exact location between the sum of the components and altimetry observations on a finer spatial scale, resulting from the limited resolution of the observations, compared to a coarser scale when such mismatches are partially averaged out. Additionally, the averaging of more samples leads to a smaller standard error. However, the measurement errors between altimetry and the sum of components will only compensate each other if they are uncorrelated in the spatial scale being analysed. The relationship between the spatial scale of the domains and the performance of the budget is further confirmed in Figure S4.6, which shows how the residual of the budget decreases when larger regions are considered. Note however, that simply upscaling the resolution of the observations – i.e, considering 2x2 or 5x5 degrees blocks – does not have the same effect on budget performance as the domains derived by machine learning (Figure S4.7): there is demonstrated added value of considering regions that are physically coherent, rather than artificial blocks, for the budget analysis. That is, spatially averaging over areas of similar variability reduces the unexplained variance of the observations.

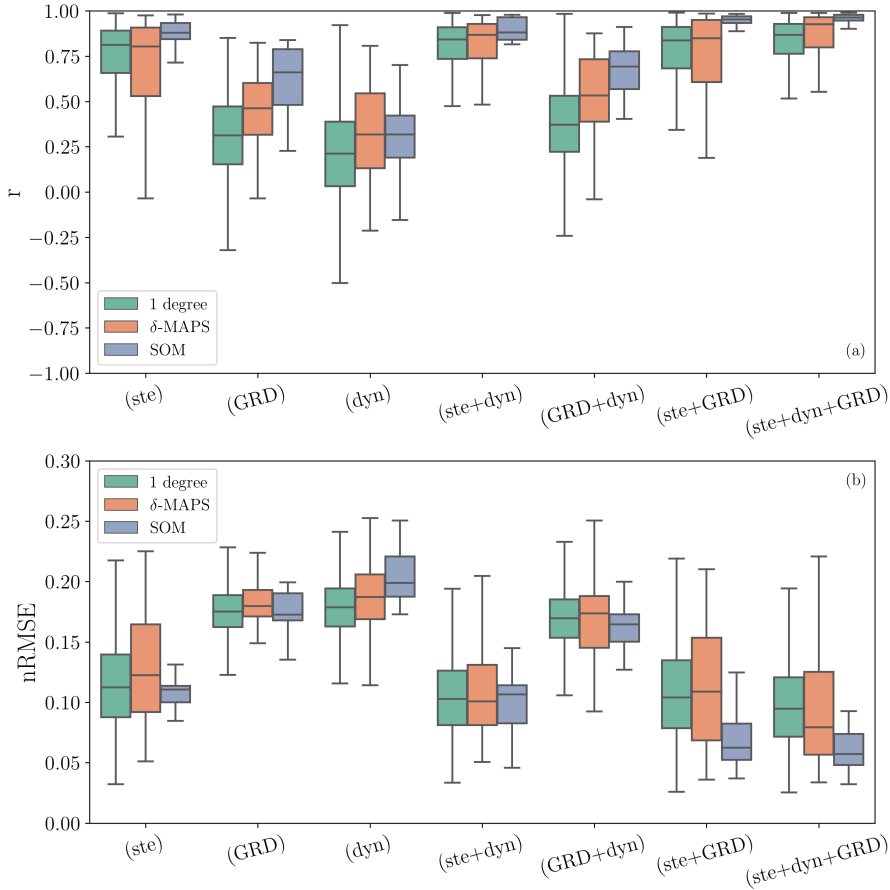


Figure 4.5: The effect on budget closure for different component combinations and spatial resolutions. (a) Pearson's correlation coefficient (r) and (b) normalized root mean squared error (nRMSE), in mm yr^{-1} , between total sea-level (altimetry) and the different components included in the budget (x-axis), for the different spatial resolutions (1 degree in green, δ -MAPS in red and SOM in blue). Boxes represent the quartiles of the distribution, extending from the lower to upper quartile values of the data, with a line at the median, while the whiskers (not error bars) show the full distribution.

When it comes to the datasets of the different SLC drivers, sea-level budget studies often use the ensemble mean of several datasets for each component (e.g., Cazenave et al., 2018), or they compute a range of budget combinations, by varying the dataset for each component, to find the combination that returns the best budget closure (e.g., Gregory et al., 2013). The latter approach can result in a budget closure for the wrong reasons (Royston et al., 2020). On the other hand, while the ensemble mean approach may reduce the systematic biases of using individual datasets (Storto et al., 2017), it may also hinder the real variability of the process being analysed (Rougier, 2016). Alternatively, the budget can be analysed with the datasets closest to the ensemble means, according to the RMSE analysis, which retains the true variability of an individual dataset (Rougier, 2016; Royston et al., 2020).

4

All the results presented so far were computed using the ensemble means for each component, considering 15 steric, 5 dynamic, 4 barystatic and 4 altimetry datasets. Considering all single datasets plus the ensemble of each component we can obtain 2400 possible budget combinations ($16 \times 6 \times 5 \times 5$). To illustrate the dependence of the budget closure on the dataset used, we now also discuss the residuals of each SOM domain considering all 2400 possible dataset combinations (Figure 4.6). The residual value shows a large spread for the different budget combinations, ranging from about -2 to 2 mm yr^{-1} , and 33% of the combinations would result in non-closure of the budget (i.e., the sum of the components does not match with the altimetry values, indicated in red).

The residuals of the ensemble combinations (used throughout this study, and indicated by the blue filled squares in Figure 4.6) are comparable with the residuals of the combinations using the datasets with the smallest RMSE to the ensemble mean (indicated with purple filled triangles in Figure 4.6). With the exception of the domains 14 and 16, we see that the ensemble and the RMSE combination have a similar residual value. This indicates that the closure of the budget is not an artefact of the dataset choice.

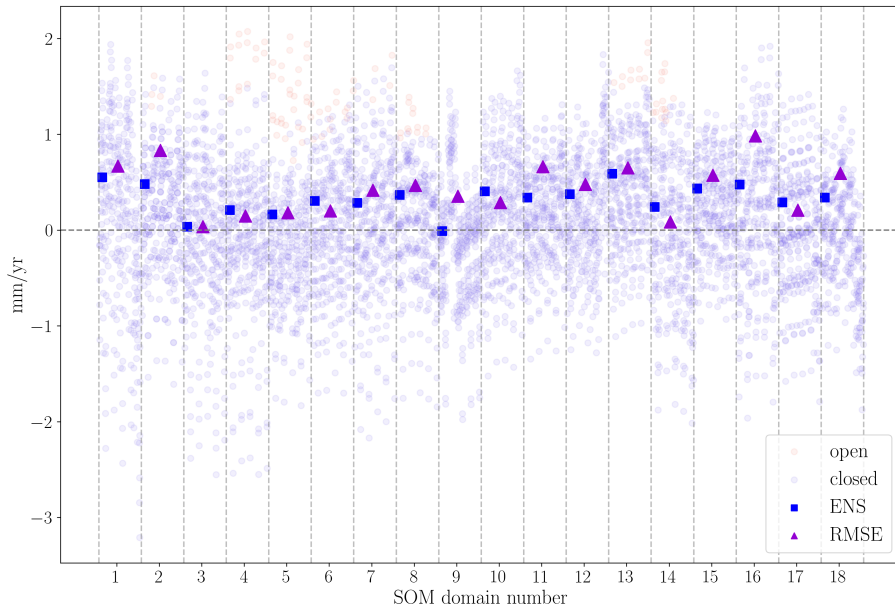


Figure 4.6: Budget residuals (mm yr^{-1}) for all possible datasets combinations for every SOM domain (separated by vertical dashed lines). The ensemble mean combination (used for the main analysis) is indicated with squares. The RMSE combination, that is, the budget combination using for each component the individual dataset with smallest RMSE in relation to the ensemble mean, is indicated with triangles.

4.5. DISCUSSION & CONCLUSIONS

Sea-level budget assessments are important tools for understanding the processes driving SLC, for detecting temporal changes in sea-level and its components, for identifying missing contributions to the budget, and for validating and constraining climate models used in sea-level projections (Cazenave and Moreira, 2022). In particular, understanding the processes on a finer spatial scale is essential for local sea-level projections and coastal management planning. In this study, we investigated the regional sea-level budget for 1993-2016 on a global scale.

Regional sea-level budget closure tends to be difficult due to the complex physical processes acting on different spatial scales. To overcome this spatial resolution issue, we applied a neural network approach, SOM, and a deep-network detection method, δ -MAPS, to identify domains of coherent sea-level variability (Figure 4.2). Note however, that the coherent patterns will depend on whether total sea surface height or the individual components (steric, dynamic, GRD) are considered. Hence, depending on the purpose of the study, it is important to first remove the unwanted components from total

sea surface height and then perform the clustering. The identified patterns reflect, among others, the influence of natural internal climate modes (Han et al., 2017), such as ENSO, PDO and North Atlantic Oscillation (NAO). This indicates the potential of using machine learning and pattern detection algorithms, such as SOM and δ -MAPS, to isolate the effects of natural climate modes from anthropogenic forcing on SLC. The domains also suggest how sea-level variability may be transferred between ocean regions. For example, the Northwestern European Shelf SOM domain extends south down to the Strait of Gibraltar, possibly reflecting how coastally trapped waves propagate sea-level variability into the North Sea (Calafat et al., 2013; Dangendorf et al., 2014; Hughes et al., 2019; Hermans et al., 2020; Dangendorf et al., 2021). Additionally, highly energetic ocean regions, such as the Kuroshio current, the Gulf Stream and the Malvinas confluence zone, are also extracted as single features, matching the spectrum of sea-level variability in those zones (Hughes and Williams, 2010).

4

Compared with the basin regions of Thompson and Merrifield (2014), we have identified more and smaller domains, especially in the Southern Hemisphere. This means our domains can provide an additional level of spatial detail compared to ocean basins, while remaining large enough to provide a consistently closing regional sea-level budget. Using the domains identified with SOM and δ -MAPS, we presented a regional sea-level budget assessment on an average scale of about $5 \cdot 10^6 \text{ km}^2$, with the largest regions about $30 \cdot 10^6 \text{ km}^2$. The performance of the budget improves from finer (1 degree resolution) to coarser scale (SOM domains), with a residual spread of 0.6 mm yr^{-1} for SOM compared to 29.2 mm yr^{-1} for 1 degree resolution. We also showed that the budget closes better when all components (steric, dynamic and GRD) are included, highlighting the importance of including the deep steric and dynamic contributions to regional SLC. Despite the large uncertainties at a regional scale (compared to the global mean) (Royston et al., 2020), we were able to identify dominant drivers in most domains. The δ -MAPS regions where the budget cannot be closed highlight processes that are affecting sea level but are not well captured by the observations, such as the influence of western boundary currents and dynamic processes (e.g., the Malvinas Confluence zone). They may also be related to the quality of global datasets in continental shelves and close to the coast, or to instrumental noise.

The GRD component has a relatively homogeneous contribution, independent of the domain, in agreement with Frederikse et al. (2020). The steric contribution dominates the seasonal and interannual variability, and results in the prevailing sea-level trend in most domains, especially for domains in the southern hemisphere and equatorial regions.

The dynamic component is important in some regions, particularly in the Gulf Stream domain. The domains where the dynamic component plays an important role coincide with the coastal polygons of Rietbroek et al. (2016) where a large part of the budget could not be explained solely by the sum of steric and land-ocean mass exchange. Hence, our analysis sheds light on the unexplained variance of previous sea-level budget studies. Note that the sea-level analysis in coastal regions is more challenging (Dangendorf et al., 2021), since some of the dominant coastal ocean dynamics are not properly represented in the global datasets (Liu and Weisberg, 2007).

Here we showed that pattern detection techniques based on machine learning, such as SOM and δ -MAPS, are powerful approaches for identifying and understanding features of global SLC and variability. The domains identified in this research highlight that different ocean regions are interconnected, revealing how large-scale circulation controls regional sea level. These domains are not only a good starting point for a regional sea-level budget analysis, but also have the potential to separate natural and anthropogenic forcings of SLC in a detection and attribution approach, building on previous work (e.g., Marcos and Amores, 2014; Slangen et al., 2014, 2016). Future work may include multiple linear regressions with climate modes to explore this potential. Additionally, these domains can also be used for coastal sea-level reconstructions (e.g., as Dangendorf et al. (2021)) and for pattern scaling in sea-level projections (Bilbao et al., 2015).

4.6. SUPPLEMENTARY INFORMATION

4.6.1. DYNAMIC SEA-LEVEL CHANGE ESTIMATION AND VALIDATION

The dynamic redistribution of mass due to ocean circulation and atmospheric redistribution effects is known as dynamic SLC (η_{DSL} Landerer et al., 2007; Gregory et al., 2019). η_{DSL} refers to mass changes driven by bottom pressure changes, that is, the redistribution of mass that was already in the oceans, and includes mass exchange at any point by mass redistribution, by wind stress and by non-linear interaction due to density changes. Note that, by our definition, the dynamic SLC (η_{DSL}) is part of the ocean dynamic SLC ($\Delta\zeta$, Gregory et al., 2019), the latter also including the effect of local steric anomalies (η'_{SSL}). When the ocean dynamic component ($\Delta\zeta$) is considered together with the global mean steric SLC ($\overline{\eta_{SSL}}$), then it is known as sterodynamic SLC (η_{SDSL} , Gregory et al., 2019; Dangendorf et al., 2021; Wang et al., 2021b). By decomposing the steric component in a global mean (denoted with the overline bar) and local anomaly component (denoted by the prime symbol), we can write the sterodynamic equation as:

$$\eta_{SDSL} = \Delta\zeta + \overline{\eta_{SSL}} = \eta_{DSL} + \eta'_{SSL} + \overline{\eta_{SSL}} \quad (4.6)$$

To obtain $\Delta\zeta$, we use the sea surface height of 5 ocean reanalysis datasets (SODA (Carton et al., 2018), C-GLORS (Storto and Masina, 2016), GLORYS (Garric and Parent, 2017), FOAM-GloSea (Blockley et al., 2014; Maclachlan et al., 2015) and ORAS (Zuo et al., 2019)). As ocean reanalyses are mass conserving (Griffies and Greatbatch, 2012), the sea surface height of a reanalysis does not include the GRD component, but it does include the steric effect. We acknowledge that this method introduces some circularity to the budget analysis: the reanalysis, used to obtain η_{DSL} , assimilates satellite sea surface height, and in the budget analysis we compare this estimate with satellite sea surface height (η_{total}). Following Wang et al. (2021b) we compute ocean dynamic SLC by removing the time-varying global mean from the reanalysis' sea surface height:

$$\Delta\zeta = \eta_{rea} - \overline{\eta_{rea}}. \quad (4.7)$$

Since we are interested purely in the dynamic part of $\Delta\zeta$, that is, the dynamic SLC (η_{DSL}), we must remove the steric local anomaly (η'_{SSL}) as:

$$\eta_{DSL} = \Delta\zeta - \eta'_{SSL} = \Delta\zeta - (\eta_{SSL} - \overline{\eta_{SSL}}), \quad (4.8)$$

where the steric estimate has been computed with the ocean temperature and salinity

of the respective reanalysis. We then compute the ensemble mean of the 5 dynamic estimates.

To validate our estimate of η_{DSL} , we compare it with η_{DSL} estimated from the Gravity Recovery and Climate Experiment Satellite (GRACE, Tapley et al., 2004). GRACE measures total mass changes, which can be used to derive estimates of manometric SLC over the oceans, that is the change in response to both the dynamic ocean mass redistribution (η_{DSL}) and to mass redistribution due to the land-ocean mass exchange (η_{GRD}) (Chambers et al., 2004; Royston et al., 2020). We use GRACE mass concentrations (mascons) products over the oceans from two different processing centres: RL06 from the Center for Spatial Research (CSR, Save et al., 2016; Save, 2020) and RL06 v02 from the Jet Propulsion Laboratory (JPL, Watkins et al., 2015; Wiese et al., 2019). In order to obtain the η_{DSL} , we then remove the GRD patterns obtained for the same datasets by Camargo et al. (2022). Note that we use GRACE dynamic SLC for validation purposes, but not in our budget analysis, as this dataset only starts in 2002.

Qualitatively, η_{DSL} obtained from GRACE (Figure S4.1a) and from ocean reanalysis (Figure S4.1b) agree on large scale patterns and magnitude of dynamic changes, despite local differences (Figure S4.1c). The main differences are in the region surrounding Indonesia and Japan, related to the signature of the 2004 Sumatra (Indonesia) and 2011 Tokuho (Japan) mega-thrust earthquakes (Chen et al., 2007; Ghobadi-Far et al., 2020) on GRACE observations. To a lesser extent, we also see the effect of the 2010 Maule (Chile) earthquake and tsunami (Ghobadi-Far et al., 2020). Another strong divergence is seen in the South Atlantic, where the positive trends of GRACE are not represented in the reanalysis, possibly suggesting that a source of dynamic SLC is not well parameterized in the reanalysis. Alternatively, this divergence might also be an artefact of the GRACE spherical harmonic solutions and low-degree corrections.

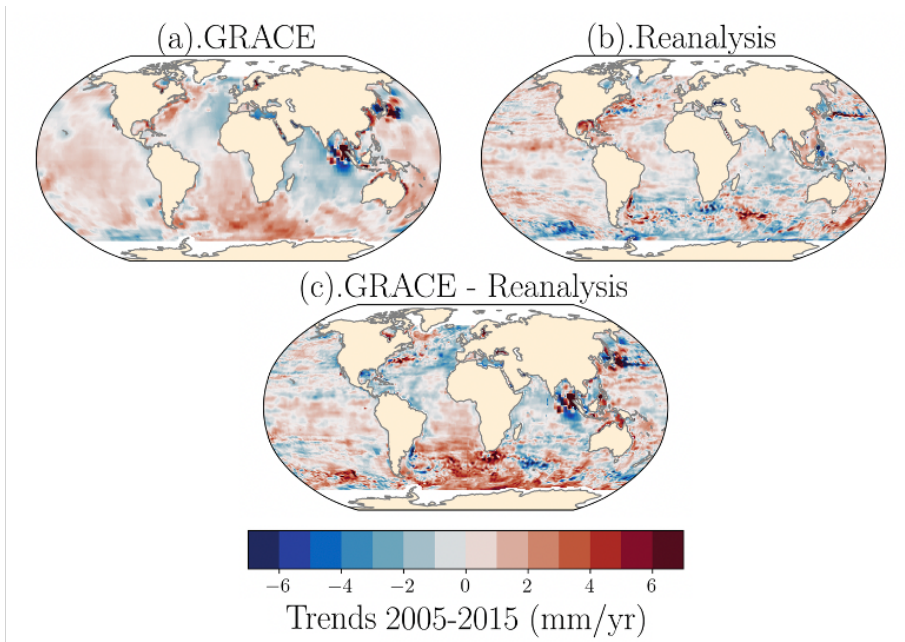


Figure S4.1: Dynamic SLC (η_{DSL}) estimated from (a) GRACE (average of JPL and CSR mascons), (b) ensemble of ocean reanalysis, (c) difference between GRACE and reanalysis.

4.6.2. SUPPLEMENTARY FIGURES AND TABLES

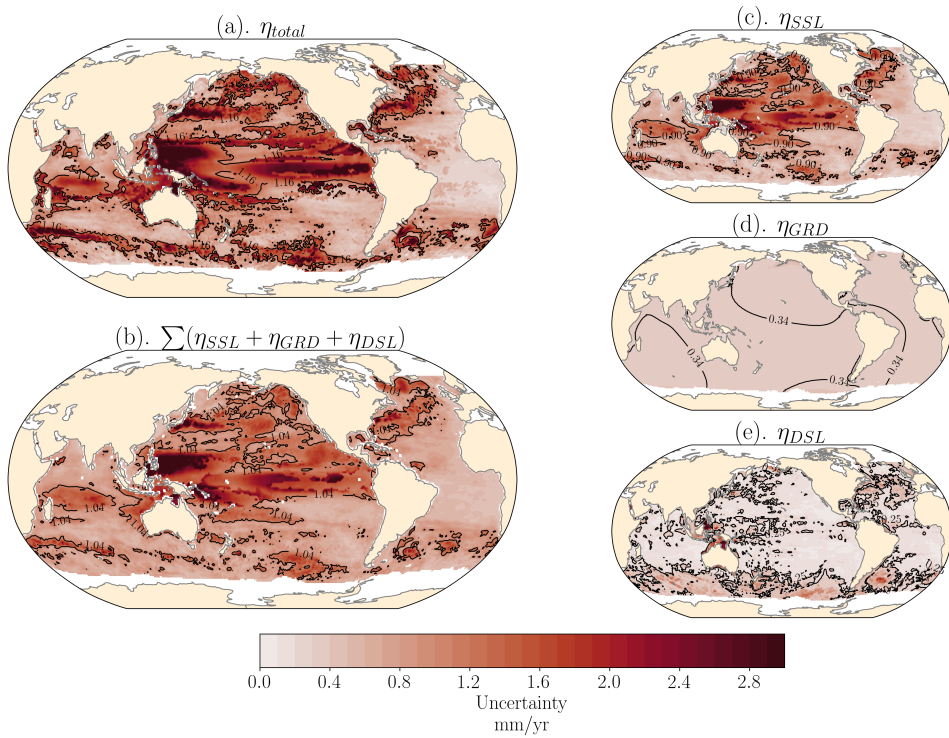


Figure S4.2: Uncertainties of the regional sea-level trends (Figure 1) for 1993-2016 (mm yr^{-1}) for (a) altimetry; (b) sum of sea-level components: (c) full-depth steric, (d) GRD effect and (f) dynamic sea-level change. Black contour line indicates global mean sea-level change.

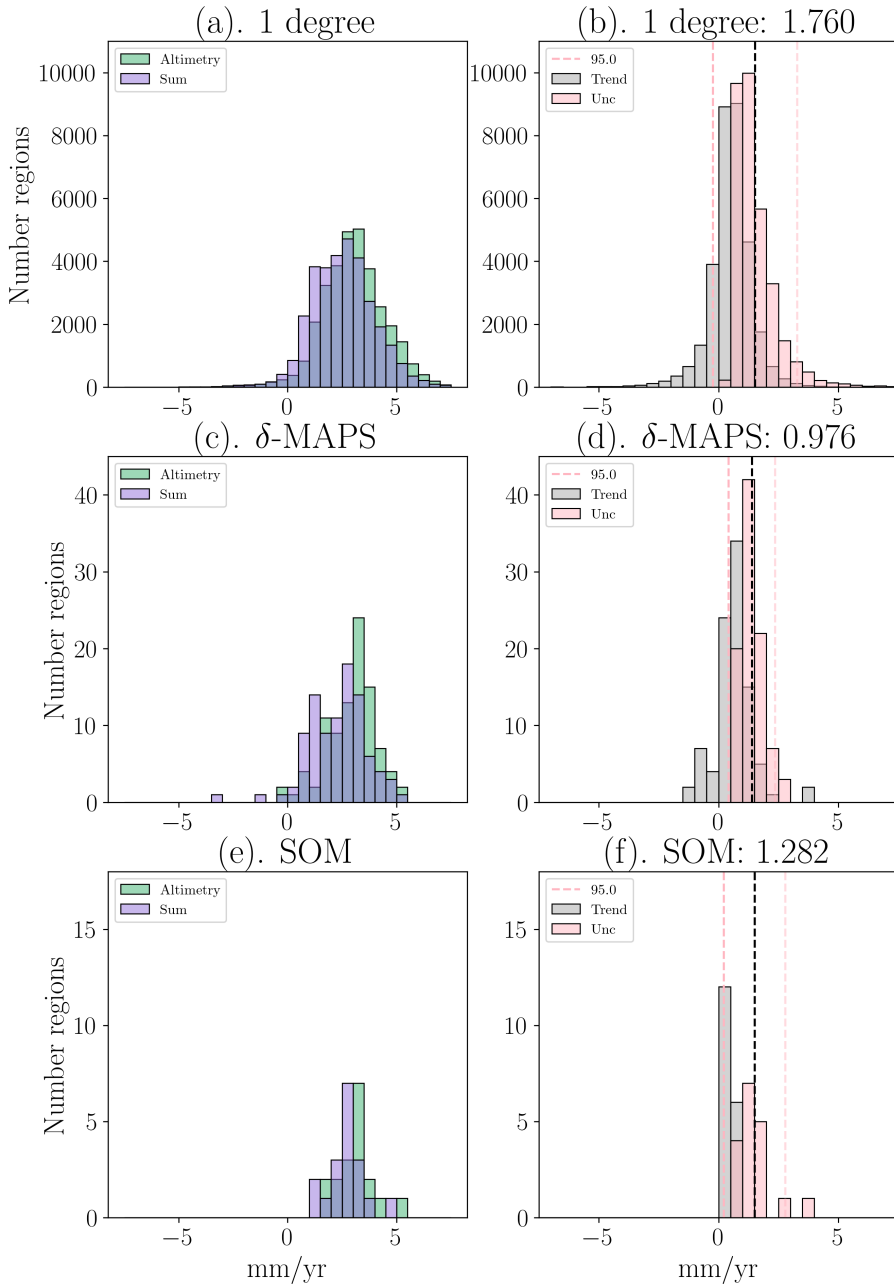


Figure S4.3: Distribution histograms of the altimetry (left column, green blocks), sum of the components (left column, purple blocks) and residuals trend (right column, gray) and uncertainty (right columns, pink), for the 1x1 degree budget (top row), δ -MAPS domains (middle) and SOM domains (bottom). The dashed pink lines indicate the 95% confidence interval of the residuals uncertainty, with the interval width reported in the subplots titles, and was used as a reference for the residuals scatters in Figure 3

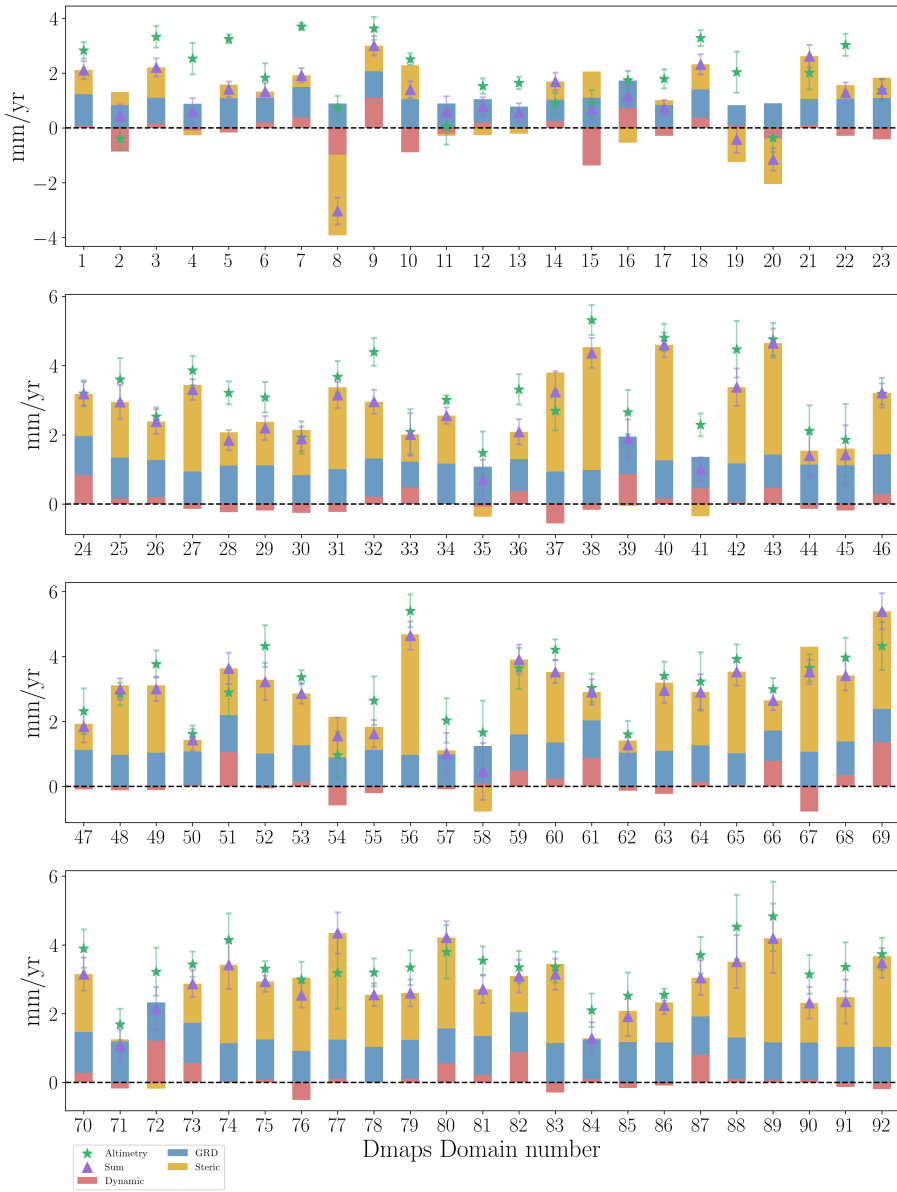


Figure S4.4: Extension of Figure 4.4, showing the trend contribution for each δ -MAPS domains. An interactive budget map is available at <https://carocamargo.github.io/resources/regional-SLB-domains/>

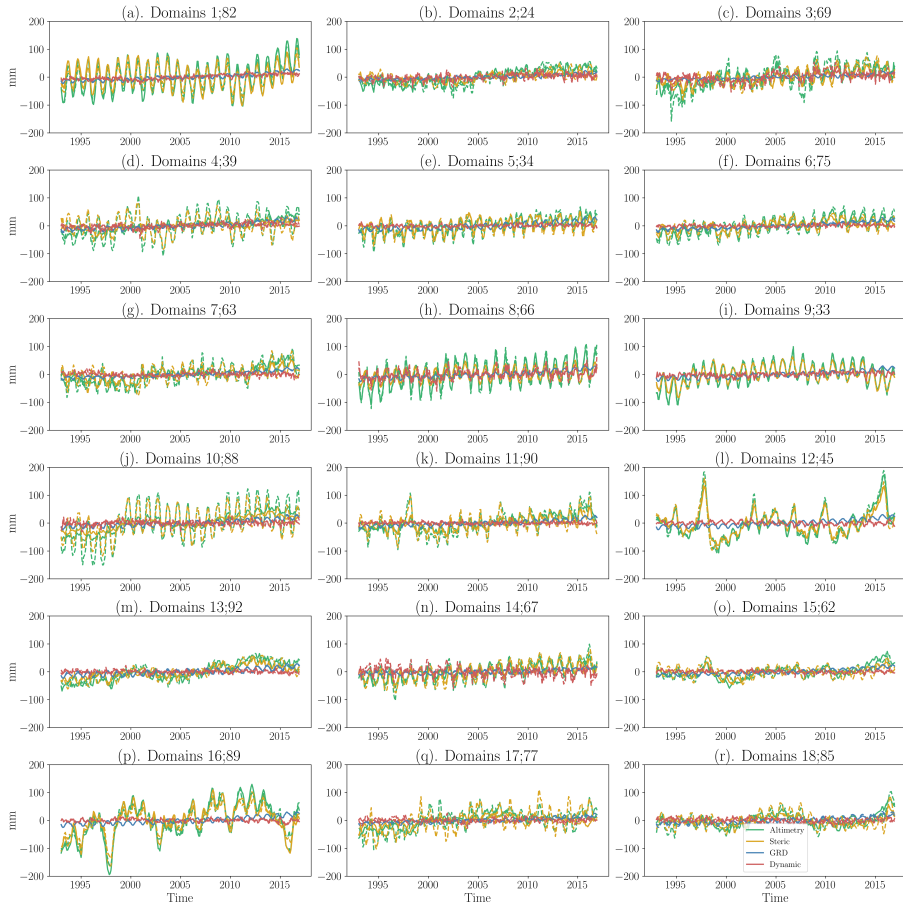


Figure S4.5: Extension of Figure 4.4, showing the time series for each of the SOM domains and corresponding δ -MAPS domains.

Table S4.1: Names of SOM and δ -MAPS domains

SOM	δ -MAPS	Domain name
1	82	Gulf Stream
2	24	Southeast Atlantic
3	69	Malvinas Current
4	39	Central North Atlantic Gyre
5	34	East Africa Atlantic coast
6	75	East Equatorial Atlantic
7	63	Brazil Current
8	66	Northwest European Shelf
9	33	South of Greenland
10	88	Kuroshio Extension
11	90	Northwest Indian Ocean
12	45	ENSO-tongue'
13	92	Southwest Australia, Freemantle region
14	67	Southeast Indian Ocean
15	62	Southwest Tropical Indian Ocean
16	89	West Tropical Pacific Ocean, Australasian Seas
17	77	Agulhas Current
18	85	Central North Pacific Ocean

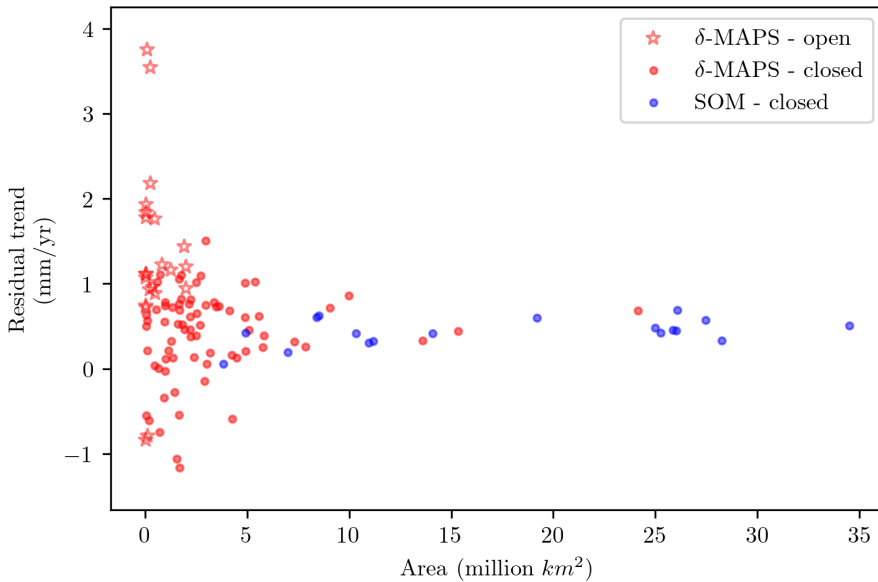


Figure S4.6: Scatter plot of the budget residuals (i.e., altimetry minus sum of components) against the area of each domain for δ -maps (red) and SOM (blue). Stars and circles indicate domains in which the sea-level budget is open and closed, respectively. As the domain area increases, the residuals converge towards 0. Not only all the SOM residuals are within $\pm 1 \text{ mm yr}^{-1}$, but also 74.2% of the δ -MAPS domains.

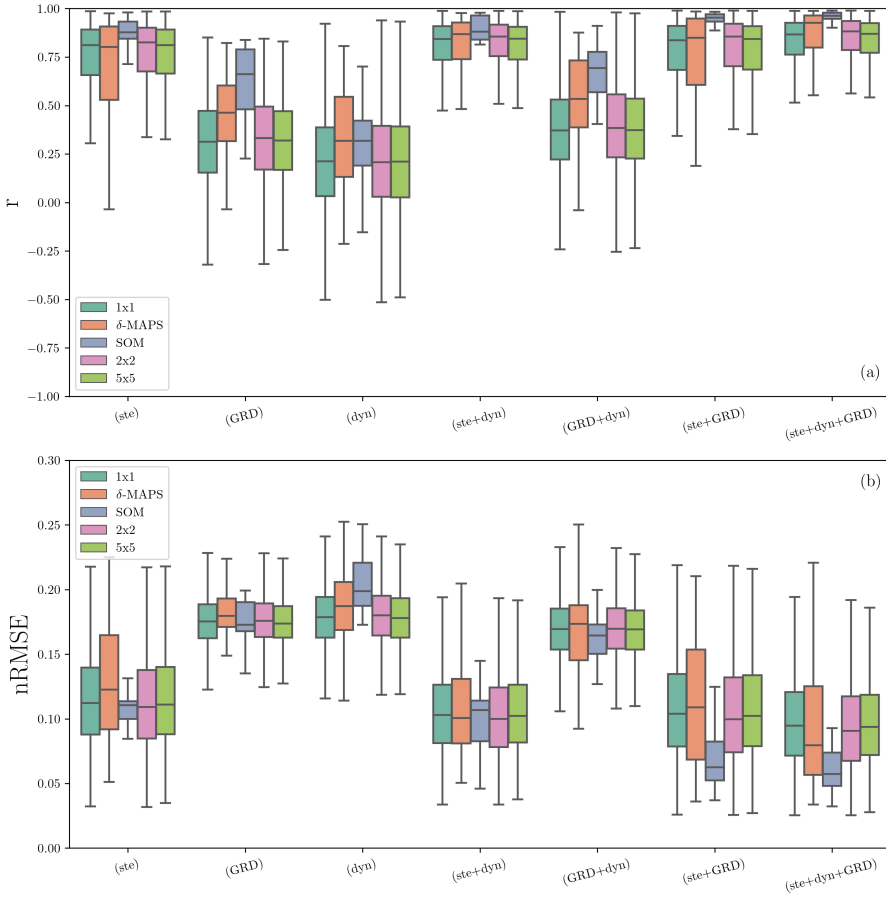


Figure S4.7: Same as Figure 4.5, but including sea-level budget considering blocks of 2x2 and 5x5 degrees. There is no clear improvement from the 1x1 degree budget to the 2x2 and 5x5, showing the added value of using the δ -MAPS and SOM domains.

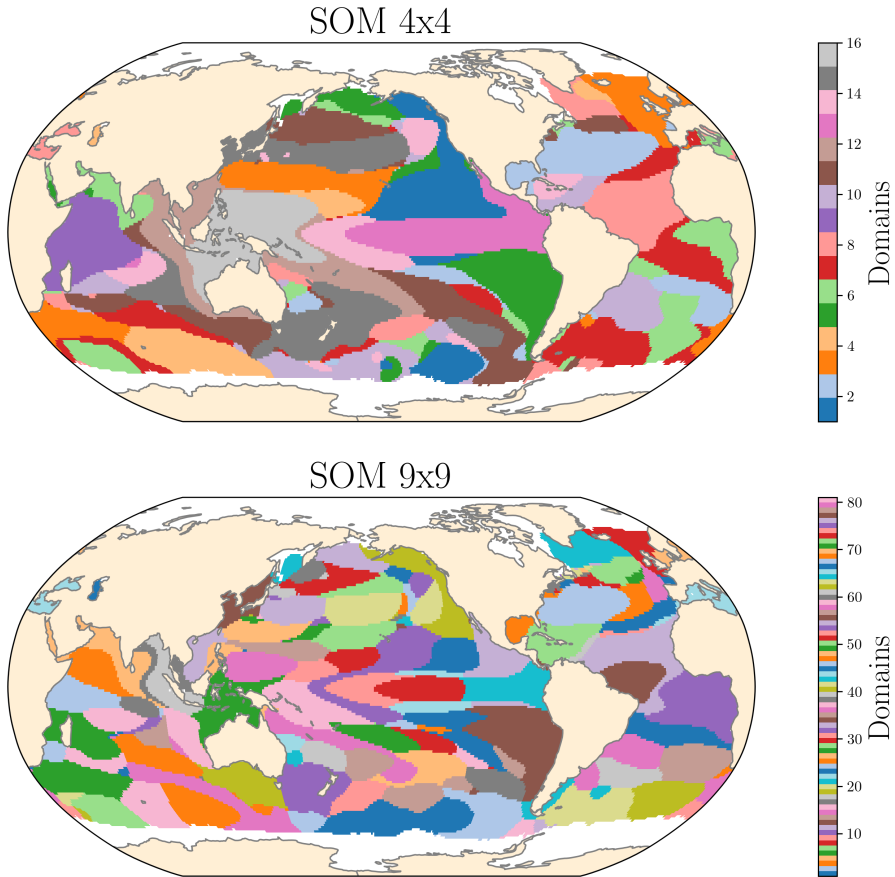


Figure S4.8: SOM domains for a neural map of (a) 4x4 (a) and of (b) 9x9, using the entire ocean as input for the clustering. Note that, even with a larger neural map, the SOM patterns are still different than the δ -MAPS domains (Figure 2), proving that the difference between the extracted patterns are not just a function of the number of SOM neurons, but due to differences between the two methods. It does, however, leads to fewer regions that are geographically distant being clustered in the same domain.

5

CONCLUSIONS & PERSPECTIVES

This thesis revolves around the regional drivers of sea-level change, and how they come together in the sea-level budget. In this final chapter, I revisit the questions posed in Chapter 1, highlighting the main findings of this thesis. I then discuss a list of recommendations of how the findings of this thesis can be applied in further research. I end this chapter with a reflection on the importance of communicating uncertainties in sea-level science and a perspective on how sea-level change studies can benefit from future satellite missions.

5.1. MAIN FINDINGS

The overarching question in this thesis is: **"Can we close the regional sea-level budget in the satellite altimetry era on a sub-basin scale consistently for the entire world?"** In order to answer this question, a suite of other research questions (RQ) had to be answered beforehand. I first focused on the drivers of regional sea-level change (RQ 1 and 2), and then on the regional sea-level budget itself (RQ 3 and 4). I now address these questions, synthesizing the main findings of this thesis. Note that all questions regard sea-level change in the satellite altimetry era, that is, since 1993.

RQ 1. How much have density variations contributed to sea-level change? (Chpt. 2)

In Chapter 2, I explored how the value of the steric (i.e., density-driven) sea-level change varies depending on the dataset and the noise model used to compute the rate of change. The noise model is related to the choice of how to represent the temporal correlation of the observations. That is, in a monthly time series, one month is not independent of the next. This dependence between observations can be described using different noise models, and influences mainly the value of the uncertainty of the trend.

On the other hand, the dataset choice influences mainly the value of the trend. In chapter 2, I showed that the best way to remove the influence of the dataset choice is to use an ensemble of datasets. By combining fifteen different ocean temperature and salinity datasets, most of the individual dataset dependence is removed from the ensemble mean trend. By varying both the datasets and the noise models, the global mean steric sea-level trend varied from 0.69 to 2.40 mm yr^{-1} , with uncertainty values ranging from 0.02 to 1.56 mm yr^{-1} , for the period of 1993–2017. Regionally, however, trend values can vary up to 30 mm yr^{-1} , with uncertainties ranging up to 10 mm yr^{-1} . **These results show that both regional and global mean steric sea-level trends can vary significantly as a result of different datasets and methods used.**

For the global mean steric contribution the best noise model is an autoregressive of order 1 (AR(1)), while regionally, a combination of different noise models is the best descriptor of the steric sea-level change and its uncertainty. Using the ensemble mean and the AR(1) noise model, global mean steric sea-level changed with a rate of 1.36 ± 0.10 mm yr^{-1} for 1993–2017 and of 1.08 ± 0.07 mm yr^{-1} for 2005–2015. Regionally, the steric trends are dominated by short-time-scale dynamics, such as the El Niño Southern Oscillation (ENSO), and by the strong signal trends of the western boundary currents. For example, in the region of the Gulf Stream Current, steric trends reach about 7 mm yr^{-1} for the period 2005–2015. The regional preference of the noise models displays a spatially coherent pattern based on the temporal and spatial variability of ocean processes. For instance, highly dynamic regions are better explained by more complex noise models. These findings show that the noise models should always be carefully chosen for each region, so that the rate of change is accurately estimated.

RQ 2. How much have mass variations contributed to sea-level change? (Chpt. 3)

Mass variations such as melting of continental ice from glaciers and ice sheets, and variations in land water storage cause sea-level change. In Chapter 3, I looked into this process, known as mass driven sea-level change, focusing on the regional sea-level patterns resulting from contemporary ice and water mass redistribution and the uncertainties within

these estimates. Specifically, I focused on the intrinsic uncertainties, related to the observation itself; spatial-structural uncertainties, related to the use of different datasets and to the spatial distribution of the mass change sources; and temporal uncertainties, related to the temporal correlation of the observations. For each of the contributions, I compared four different datasets, which led to large variations both in the global mean and the regional changes.

Based on the ice sheet mass balance inter-comparison exercise (IMBIE) datasets, the Antarctic ice sheet has contributed $0.19 \pm 0.15 \text{ mm yr}^{-1}$ to the global mean since 1993, and causing sea-level rise mainly in the Northern hemisphere. Ice mass loss from Greenland has contributed $0.36 \pm 0.12 \text{ mm yr}^{-1}$ to the global mean, causing sea-level rise mainly in the South Atlantic. Based on the WaterGAP dataset, mass loss from glaciers all over the world has contributed $0.51 \pm 0.16 \text{ mm yr}^{-1}$ to the global mean, causing a smooth sea-level rise in most part of the world, with exception of the Arctic ocean. The last contribution to ocean mass is the land water storage variation, which has contributed $0.21 \pm 0.07 \text{ mm yr}^{-1}$ to global mean sea-level rise, also based on the WaterGAP dataset. The sum of all mass components added $1.27 \pm 0.26 \text{ mm yr}^{-1}$ to global mean sea-level rise for the period 1993-2016. Regionally, negative sea-level trends are found close to West Antarctica and to the Greenland Ice Sheet, with a positive and increasing trend towards lower latitudes. This pattern is a reflection of the Gravitational-Rotational-Deformation (GRD) effect, which is marked by a sea-level rise in the far-field and negative sea-level change close to the mass change source. **The main sources of uncertainty are the temporal correlation of the land water storage observations, and the dataset used for Antarctica and land water storage components.** These findings reinforce the importance of clearly quantifying the uncertainties of mass-driven sea-level change trends.

RQ 3. Which regions should we use to analyse the sea-level budget? (Chpt. 4)

When talking about regional sea-level change, a key question is what spatial scale we are talking about. Ideally, we are interested in understanding the drivers of sea-level change at the highest possible spatial resolution. However, the spatial resolution of the observations is a limiting factor of regional to local studies. Additionally, it is important to take into account the spatial scale of the process itself: that is, sea level does not change according to artificial grid cells or political borders, but it has its own physical scale.

In Chapter 4, I applied, for the first time in sea-level research, two machine learning techniques (δ -MAPS and Self-organizing maps (SOM)) to identify smaller, sub-basin regions which have a similar sea-level variability. The identified patterns have an average spatial scale of $5 \cdot 10^6 \text{ km}^2$, and show how different ocean regions are connected, and how large-

scale circulation controls regional sea level. **These physically coherent regions improve our ability to close the regional sea-level budget**, as the selected regions have a common variability. Additionally, the spatial averaging reduces the uncertainties otherwise present when using the gridded data alone.

RQ 4. What are the drivers of regional sea-level change?(Chpt. 4)

In Section 1.2, the components of the regional sea-level budget were introduced. Regionally, steric sea-level change is not only a function of temperature variations, but salinity changes also need to be incorporated. Accounting for how ocean mass is redistributed as glaciers and ice sheets melt and due to ocean dynamic processes (e.g., ocean currents and wind) is also an integral piece of the regional sea-level budget. Thus, when the sea-level budget is analysed at a finer spatial scale, steric, mass and dynamic changes need to be considered (Figure 1.6). On average, we find that the steric, mass and dynamic changes are responsible for 50, 41 and 9% of the total global mean trend, respectively. Each of the identified regions (RQ 3), however, has its own relative ratio between the sea-level drivers (Figure 5.1).

The steric component is the dominant driver in 54% of the regions determined using the δ -MAPS technique (Figure 5.1a), while the mass and dynamic components dominate in 36% and 4%, respectively. For the regions determined using the self-organizing maps technique (SOM, Figure 5.1e), the steric and mass components are the dominant drivers in 72% and 28% of the regions, while the dynamic component is not dominant in any region. **Although it is clear that the regional changes are dominated by steric and ocean mass contributions, the dynamic component is required to close the regional sea-level budget** in 11% and 4% of the δ -MAPS and SOM regions, respectively. We find the highest rates of dynamic sea-level change in the Atlantic ocean (Figure 5.1d and h), especially in the region of the Gulf Stream current. Most of the regions in the Indian and West Pacific oceans have at least 50% of their trend explained by the steric component (Figure 5.1b and f), while the East Pacific is dominated by the mass component (Figure 5.1c and g). Interestingly, the domains in the Central Equatorial Pacific, highly influenced by ENSO dynamics, are dominated by the mass component, suggesting that the period analyzed is long enough to remove the interannual variability of ENSO from the trends. In the Atlantic, however, there is no clear dominant driver, as the dominant driver explains less than 50% of the total trend (indicated by stipples in Figure 5.1a and e). Thus, especially for those regions, sea-level projections of the three components should be considered for decision making.

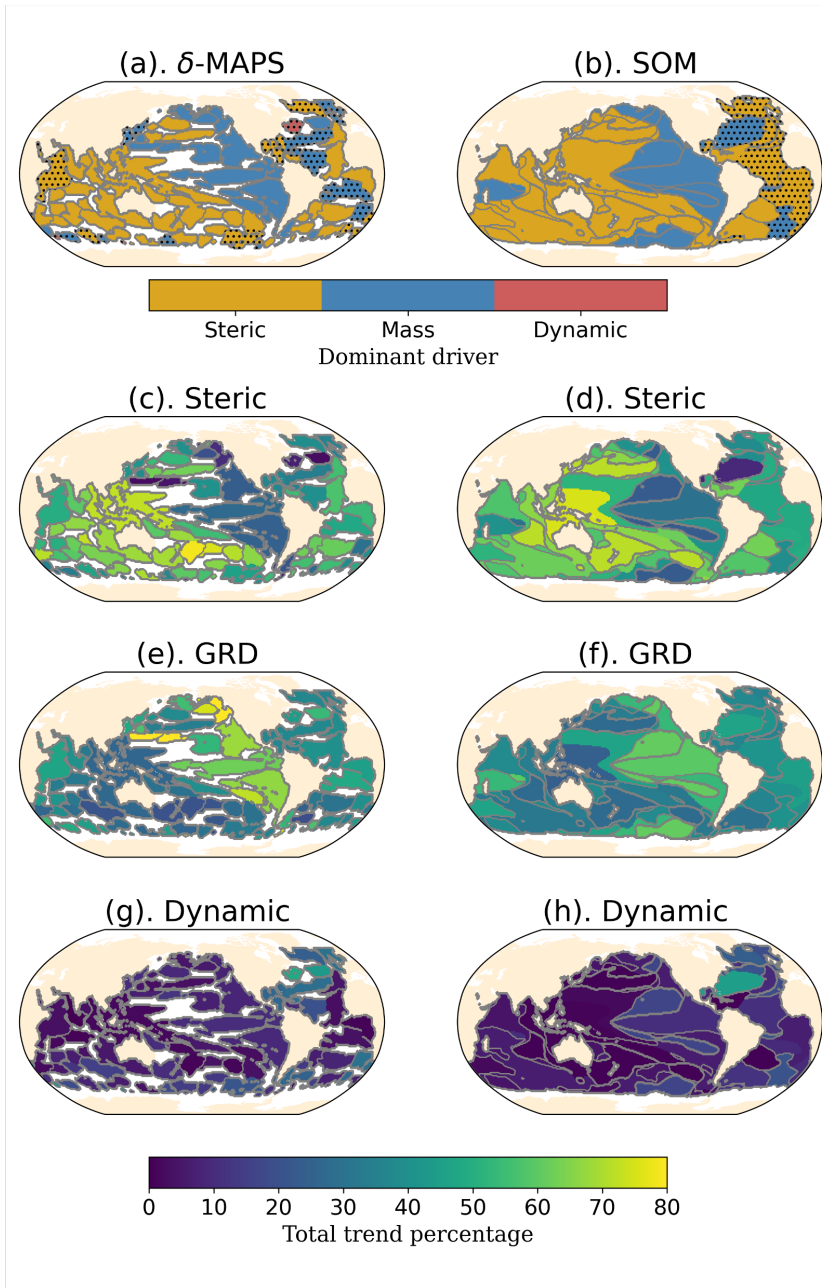


Figure 5.1: Dominant drivers of the budget in each (a) δ -MAPS and (b) SOM region. Stipples indicate where the dominant component is less than 50%. Percentage, in relation to the number of regions, of the (c,d) steric, (e,d) GRD and (g,h) dynamic components in relation to the total sum, (left column) δ -MAPS and (right column) SOM regions.

RQ 5. Can we close the regional sea-level budget in the satellite altimetry era on a sub-basin scale consistently for the entire world? (Chapter 4)

The answer to this question is still scale dependent. In all of the 18 SOM domains, which vary from 3.84 to 34.51 million km², and have an average size of 17.61 million km², we can close the sea-level budget over 1993-2016 within 1-sigma uncertainty for the entire world. On the other hand, for the 94 δ -MAPS domains, which vary from 0.03 to 24.15 million km², with an average size of 2.53 million km², we can close the budget in 72 domains, which account for 94% of the ocean area. The 20 δ -MAPS domains where total change and the sum of the contributions do not match have an individual area smaller than 2 million km². Thus, we can say that **we can close the regional sea-level budget in the satellite altimetry area on a sub-basin scale consistently for the entire world**, provided that the sub-basins are larger than 2 million km². This is a refinement from previous regional sea-level budget studies (e.g., Frederikse et al., 2020; Royston et al., 2020), which closed the budget on a basin scale, considering regions that varied from 7.3 to 91.4 million km².

5

5.2. POTENTIAL APPLICATIONS

5.2.1. MISSING OR MISREPRESENTED CONTRIBUTIONS

The sea-level budget can be used to identify missing or misrepresented contributions to the budget (Dieng et al., 2015c). For example, if we assume that all the contributions accounted for in the budget are correct, then the budget residual can inform us on contributions that have not been included in the analysis. The sea-level budget approach has already been applied to infer the deep ocean contributions to steric sea-level change (e.g., Llovel et al., 2014; Dieng et al., 2015a,c; Yang et al., 2021), and to estimate the contribution of ocean mass (e.g., Purkey et al., 2014; Horwath et al., 2022; Barnoud et al., 2022) and land water storage to sea-level change (e.g., Dieng et al., 2015b). The main challenge lies in identifying the missing or misrepresented contributions when the budget residual is highly contaminated by measurement errors and uncertainties (Dieng et al., 2015c). In this section, I discuss a number of uncertain contributions to sea-level change, and how these can be better constrained using the sea-level budget approach.

DEEP OCEAN STERIC CHANGE

In my sea-level budget analysis (Chapter 4), we complemented the upper ocean steric changes (Chapter 2) with the updated estimate of deep ocean steric sea-level change from Purkey and Johnson (2010), which has a global mean value of 0.1 mm yr⁻¹. This estimate,

however, is based on sparse ocean observations (both spatially and temporally), which likely misrepresent the true variability of the deep ocean (Garry et al., 2019). Estimates based on multiple reanalyses show a range of possible steric trends for the deep ocean, varying from -0.4 to 1.1 mm yr^{-1} for the period 1993-2017 (Appendix 2.8). While the deep steric estimates from ocean reanalyses have a large range of values and uncertainties (see Appendix 2.8, Storto et al., 2019), they indicate how the residual of the budget could be at least partially explained by the large uncertainties in the deep ocean steric contribution.

With a sea-level budget analysis using only upper ocean steric changes (Chapter 2), and assuming all the other components are well represented, I infer patterns of deep ocean steric contribution (Figure 5.2a). For the period 1993-2016, this leads to a global mean deep ocean steric contribution of 0.10 ± 0.10 mm yr^{-1} (Figure 5.2a). This is in line with observation-based estimates, which point to a global mean deep ocean steric contribution of 0.12 ± 0.03 mm yr^{-1} for the period 2005-2015 (Chang et al., 2019). My estimate also falls within the uncertainty range of Yang et al. (2021) and Llovel et al. (2010), who via a sea-level budget approach estimated a deep ocean contribution of 0.07 ± 0.18 mm yr^{-1} and -0.13 ± 0.72 mm yr^{-1} for 2005-2015 and 2005-2013, respectively. As the contribution of the deep ocean to the global trends is not expected to exhibit significant decadal and interannual variability (Desbruyères et al., 2016), rates for the period 1993-2016 can be compared with those from 2005 until 2013 or 2015.

Qualitatively, my regional patterns resemble the ones from Purkey and Johnson (2010, Figure 5.2a vs. d). However, my budget-based uncertainties are regionally very large (Figure 5.2b), and trends in most of the deep ocean are not statistically significant (Figure 5.2c). On the other hand, the inferred contribution to the global mean match published rates (e.g., Llovel et al., 2010; Purkey and Johnson, 2010; Desbruyères et al., 2016; Chang et al., 2019; Yang et al., 2021). Thus, this analysis demonstrates **the potential of the sea-level budget to constrain the deep ocean contribution to global mean sea-level change**. Further studies focusing on reducing the uncertainties, by for example including data from deep-profiling Argo floats (Desbruyères et al., 2016; Johnson et al., 2015), are necessary to improve estimates of the contribution of the deep ocean to regional sea-level change.

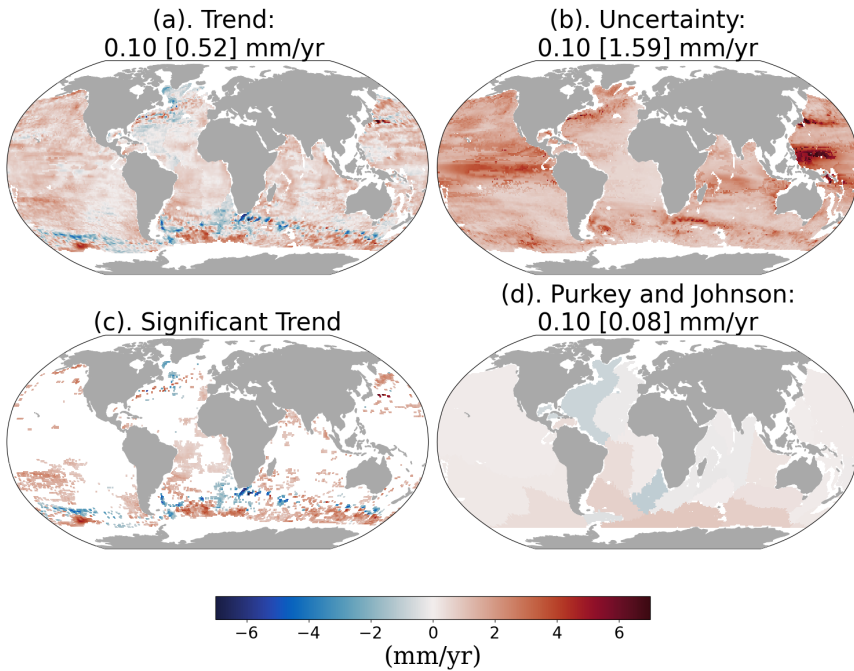


Figure 5.2: Inferred deep ocean steric sea-level (a) trends and (b) uncertainty from the sea-level budget residual. (c) Same as (a), but only areas where the trend is statistically significant, that is, where the trend is higher than the uncertainty. Number on the titles refer to the global mean trend and uncertainty, computed from the global mean time series and an autoregressive of order 1 (AR(1)), and the spatial average of the regional trends (value between square brackets). Ocean areas shallower than 2000m have been omitted from the analysis.

DYNAMIC SEA-LEVEL CHANGE

My estimates of dynamic sea-level change in the sea-level budget were based on sea surface height information from ocean reanalyses (Chapter 4, Appendix 4.6.1; Figure 5.3a and b). However, this method introduced some circularity in the budget, since most ocean reanalyses also assimilate satellite altimetry, which we also use to estimate the total sea-level change. Additionally, in comparison with the dynamic contribution derived from GRACE, there are local changes that are not captured by the reanalyses. Thus, it is possible that the budget residual contains signals of dynamic processes that were misrepresented in the budget.

By not including the dynamic term in the budget equation, and assuming all the other components are accurate, the budget residual can be used to infer the dynamic contribution to sea-level change (Figure 5.3c,d). Both the inferred and reanalyses based dynamic sea-level change have a similar and negligible contribution to the global mean. Regionally, however, the inferred values are much larger than the reanalyses based ones, with a spatial

average of $0.50 \pm 1.55 \text{ mm yr}^{-1}$ compared to $0.03 \pm 0.25 \text{ mm yr}^{-1}$. This means that, **using ocean reanalyses to compute the dynamic component may lead to an underestimation of the real regional dynamic sea-level change**. Thus, a large part of the residuals of our sea-level budget analysis (Chapter 4) might be related to the dynamic component. On the other hand, the inferred values have large local uncertainties, mostly not statistically significant. Thus, the use of the regional budget to constrain the regional dynamic sea-level change is currently limited by the magnitude of the uncertainties with respect to the magnitude of the signal.

Alternative methods to estimate the dynamic contribution could be (i) using ocean reanalyses that do not incorporate satellite altimetry; (ii) using ocean models; or (iii) using satellite gravimetry (i.e., GRACE). The latter is only available since 2002, hence it is not an option for longer periods. Options (i) and (ii) are also limited since there are only a few reanalyses that do not incorporate altimetry, and only a few ocean models available at a global scale.

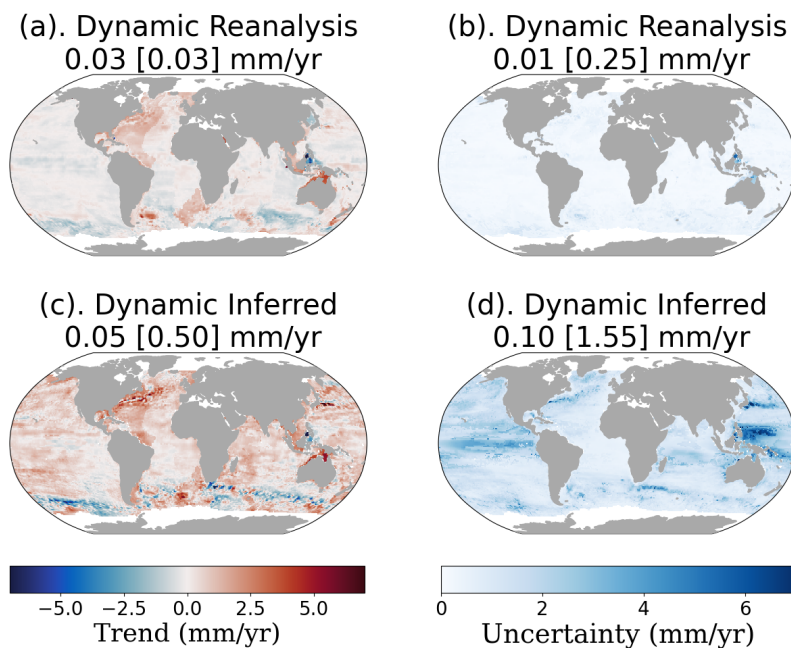


Figure 5.3: Dynamic sea-level change (a,c) trend and (b,d) uncertainty, estimated from (a,b) ocean reanalysis and (c,d) inferred from the sea-level budget residual. Numbers in the titles refer to the global mean trend and uncertainty, computed from the global mean time series and an autoregressive of order 1 (AR(1)), and the spatial average of the regional trends (value between square brackets).

GLACIAL ISOSTATIC ADJUSTMENT (GIA)

GIA is present in the sea-level budget in different ways. First, GIA changes the shape of the geoid. Geoid changes affect gravimetry (i.e., GRACE) and satellite altimetry measurements (Chen et al., 2013; Uebbing et al., 2019). Second, GIA affects the height of the Earth's surface with relation to the reference ellipsoid. This is relevant to determine the total sea-level change, that is the actual height of the water column, both from satellite altimetry and tide gauges. Finally, GIA also changes the total capacity of the oceans. The latter is relevant for estimates of global mean sea-level change from satellite altimetry. Consequently, the GIA effect needs to be removed both from total sea-level change and from mass-driven sea-level change. Usually, global mean sea-level change studies based on satellite altimetry apply a GIA correction of -0.3 mm yr^{-1} to the trend (e.g., Cazenave et al., 2018). For regional studies, however, it is important to apply a spatially varying GIA correction, instead of a uniform global mean average.

5

In our budget (Chapter 4), we used the ICE-6G (VM5a) model from Argus et al. (2014) and (Peltier et al., 2015) to remove the GIA effects from the altimetry trends. The GRACE data used in Chapter 3 also had the GIA signal removed based on the same model. However, depending on the version and/or parameters applied in the GIA model (Figure 5.4), the local values used for the geoid correction can vary, on average, by 0.3 mm yr^{-1} . Thus, some of the residuals present in the budget could be due to uncertainties in the GIA correction. Depending on the model used for the GIA correction, the total sea-level change could be closer to the sum of the components (for instance, the Tamisiea (2011) and ICE-5G), or even further from it (e.g., Caron et al. (2018)).

This model dependence of the GIA correction suggests that a systematic GIA error, of for example 0.22 mm yr^{-1} based on the average standard deviation of these four models, should be added to the uncertainties of the sea-level budget. Alternatively, instead of applying the GIA correction to the altimetry data, we could move the GIA component to the right hand-side of the sea-level budget equation (Equation 1.9). Then the GIA contribution to present-day sea-level change would become an independent element of the budget analysis, instead of a correction applied to the altimetry. By considering different GIA models, one could quantify the error introduced in the budget from the GIA component (as in e.g., Chen et al., 2013), and propagate the error due to GIA correction into the budget (as in e.g., Frederikse et al., 2020).

In comparison to the other contributions discussed in this section, the GIA global mean sea-level uncertainty is on the same scale as the deep ocean and dynamic contributions. Regionally, however, the dynamic and deep ocean values are much larger than the GIA

ones (note how the color scale of Figures 5.2 and 5.3 range from -7 to 7 mm yr^{-1} , and the one from Figure 5.4 ranges from -1 to 1 mm yr^{-1}). **Therefore, we can say that currently, the dynamic and the deep ocean changes are the main uncertain contributions of the regional sea-level budget.**

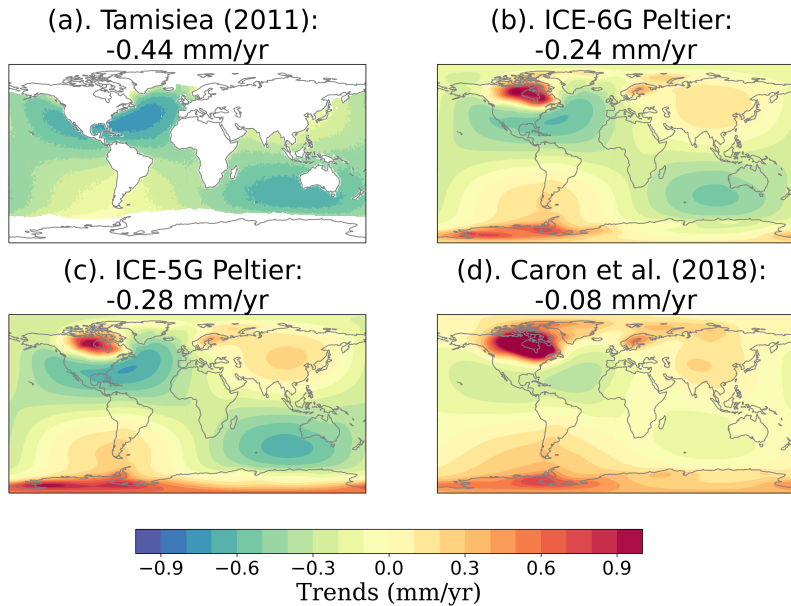


Figure 5.4: Geoid rate changes due to present-day GIA from different models: (a) GIA model from Tamisiea (2011) provided with altimetry dataset of CSIRO (2022), (b) ICE-6G from Argus et al. (2014); Peltier et al. (2015), (c) ICE-5G from Peltier (2009) and (d) GIA model from Caron et al. (2018). Number on the titles refer to the ocean averages, using the same land mask as in (a).

5.2.2. EVALUATING SEA-LEVEL PROJECTIONS

Sea-level projections provide highly relevant information for stakeholders. However, validating projections is not possible yet, as we cannot measure future sea-level changes. Thus, we rely on validating the ability of the climate models, used for the projections, by comparing observed changes to the simulated ones in the historical period (Slangen et al., 2017b; Meyssignac et al., 2017). Alternatively, we can compare older projections with recent observations. For example, the sea-level projections from the Fifth Assessment Report (AR5) of the Intergovernmental Panel on Climate Change (IPCC, Church et al., 2013), published in 2013, range from 2007 to 2100. Using the datasets from this thesis, which span from 1993 to 2017, I compare the first 10 years of AR5 projections with the observations.

Recently, Wang et al. (2021a) published a critical evaluation of AR5 sea-level projections with observations for global mean regional sea-level change at tide gauges locations. However, one of the challenges of validating regional projections with tide gauges observations is the influence of local factors on tide gauge records, such as vertical land motion (VLM) and storm surges (Wang et al., 2021a). Here, I demonstrate how the regional sub-basin sea-level budget from this thesis can complement the evaluation of Wang et al. (2021a).

The AR5 projections are based on Representative Concentration Pathways (RCPs), which are identified by the total increase in radiative forcing from 1750 to 2100. Here I use three scenarios: RCP 2.6, a mitigation scenario with low radiative forcing (2.6 W m^{-2}); RCP 4.5, the "business as usual" scenario with a stabilization of radiative forcing at 4.5 W m^{-2} ; and RCP 8.5, in which gas emissions increase leading to a radiative forcing of 8.5 W m^{-2} . Since the sea-level projections represent relative sea-level change, an ocean bottom deformation correction needs to be applied to the satellite altimetry data (Frederikse et al., 2017a). Additionally, I compute relative fingerprints of the ocean mass components, different from the spatial patterns used in Chapter 4, which were geocentric sea-level fingerprints.

Figure 5.5, shows that projected trends are spatially smoother than the observational trends. The observations are strongly affected by interannual processes, such as the ENSO signal, while this effect is less strong in the projections. A more in-depth evaluation could use climate indices to remove interannual processes from the observational trends (e.g., Royston et al., 2018). However, here I remove some of the short-term variability by comparing the observations and projections in the SOM domains (Figure 5.5c,e). This leads to a better match between the projected and observed trends for some of the SOM domains. For instance, domain 7, which covers the Brazil and Malvinas Currents Confluence Zone, has a good match between the projected and observed trends. The same is seen for domain 11 in the North Indian Ocean and domain 15 in the Southwest Tropical Pacific Ocean, indicating the spatial averaging can be used to remove some of the dynamic variability. On the other hand, some domains have considerable differences. For example, domain 9, south of Greenland, has opposite projected and observed trend signals. This region is influenced by the North Atlantic Subpolar Gyre, which has a characteristic decadal oscillation (Chafik et al., 2019). Other domains with striking differences are domain 12 and 16, located in the Tropical Central-East and West Pacific Ocean, respectively. These regions are influenced by ENSO, which also has a decadal temporal oscillation. The period used for the trend analysis, 10 years ranging from 2007 to 2016, is not long enough to

solve all interannual to decadal variability. Using the domains for spatially averaging and considering a longer trend period might bring the projected and observed trends closer together.

Future analysis could look at each region in more detail, to understand why some regions have an improved match while others are different. As the main difference between the projections and the observations seems to be due to sterodynamic effects, an evaluation looking at each component of the budget individually (instead of the sum of the drivers) can also give show which processes are well represented in the projections. Finally, this first comparison was made without accounting for the uncertainties, which should be incorporated for an in-depth evaluation.

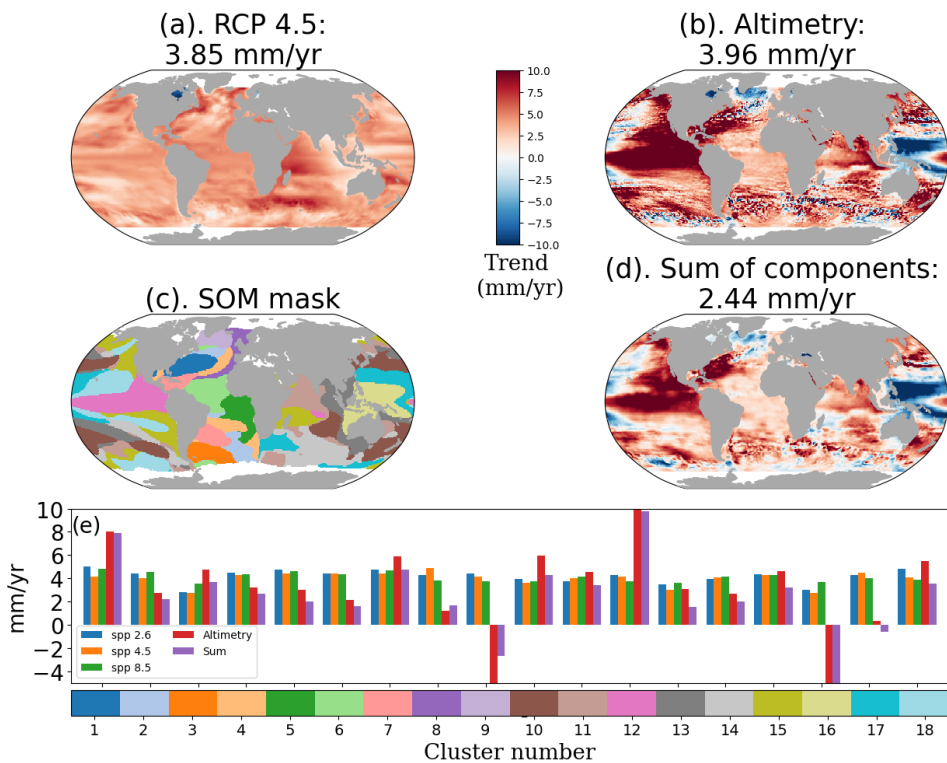


Figure 5.5: Sea-level trends (mm yr^{-1}) for the period 2007-2016 for (a) the RCP 4.5 scenario, (b) altimetry (d) and sum of the sea-level budget components. (c) SOM clusters used for (f) trend comparison.

5.2.3. LOCAL BUDGET ASSESSMENTS

Local sea-level studies can information targeted to local governments and stakeholders. In this section, I show a brief sub-basin sea-level budget analysis along the Brazilian coastline.

Compared to the number of tide gauges measuring in-situ sea-level change along the Northern Hemisphere coastlines, the Southern Hemisphere has a poor spatial distribution of stations (e.g., Frederikse et al., 2021; Woodworth, 2006). For example, along the South American Atlantic coastline, only 12 tide gauges are registered at the Permanent Service for Mean Sea-level (PSMSL, Holgate et al., 2013; Woodworth, 2006), of which only two have been updated in the last three years. While satellite altimetry can be used to provide data in locations where there is no in-situ data, estimating coastal sea-level change using altimetry data is also challenging due to the distortion of the satellite signal close to the land (Benveniste et al., 2020). Consequently, sea-level change along the coast of Brazil is still understudied.

Recently, significant effort has been put towards developing algorithms that improve the accuracy of standard radar altimetry in coastal regions (Passaro et al., 2014; Birol et al., 2017). Such dedicated coastal altimetry products and new satellite altimetry missions should provide better estimates at the coast than the standard altimetry product used in Chapter 4. Thus, for this case-study I use a new altimetry-derived coastal sea-level product (Cazenave et al., 2022), from which I can estimate rates of sea-level change over the period 2002-2016 along the coast of Brazil (Fig 5.6a).

Previous studies have shown that, for some regions, coastal sea level is driven by open ocean sea-level change (Dangendorf et al., 2021). Following this approach, I use the domains derived in Chapter 4, and select those δ -MAPS regions which border the South American Atlantic coast, as proxies of the drivers of sea-level change along the coastline (Figure 5.6b). Domain 1, the most northern of the study region, which covers the Amazon Plateau, has a good match between the coastal altimetry-observed sea-level change and the sum of the drivers. The sum of the drivers and coastal altimetry trends also match, considering the uncertainty bars, for the most southern domain, covering the Patagonian Shelf. For the other regions, there is a large difference between the coastal altimetry-observed sea-level change and the sum of the drivers. Thus, it is possible that these regions cover large-scale features which are not strongly correlated with coastal sea level.

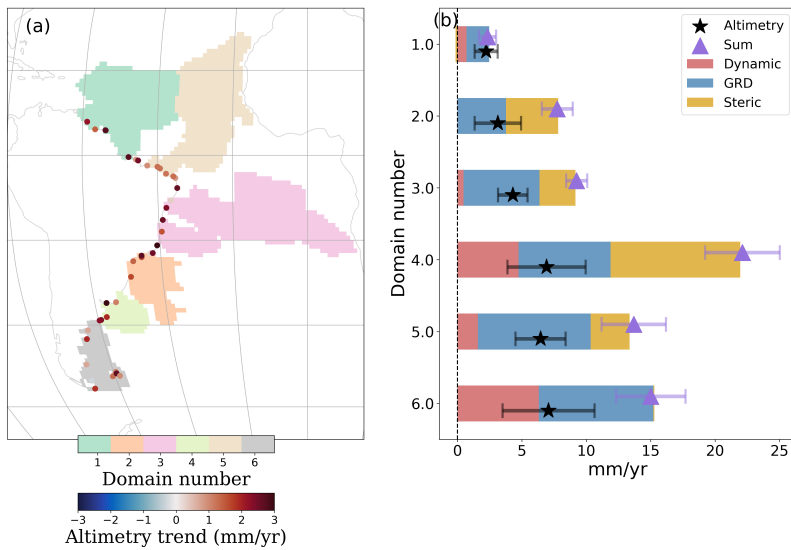


Figure 5.6: (a): Altimetry sea-level trends from 2002-2016, and δ -MAPS domains used as proxies for the local sea-level budget on (b). Trends and uncertainties were computed with an autoregressive of order 1 (AR(1)).

Future studies could: (i) validate the coastal altimetry rates with local tide gauges, using, for example, the new network of tide gauges deployed along the coast of Brazil (by the SIMCosta project); (ii) check if a better match would be obtained if using altimetry rates along the entire coastal zone, and not only the bordering the coast; (iii) compare the coastal altimetry rates with other altimetry datasets; (iv) perform the budget analysis using other regions as proxies for the coastal locations; and (v) test the budget with other datasets.

5.3. SOCIETAL IMPLICATIONS

As sea-level rise increasingly becomes an issue that governments around the world need to deal with, it is important to indicate how the knowledge of this thesis can be used not only for science, but also for society. Often, the main use of sea-level change in a societal framework is regarding sea-level projections (e.g., Fox-Kemper et al., 2021). While understanding present-day sea-level change can be used to force, improve and validate sea-level projections, there are other ways that observations can be used.

EARLY WARNING SIGNALS

In the concept of adaptive policy pathways for sea-level rise (Haasnoot et al., 2013), present-day processes can be used as signals to assist the choice of a policy pathway (e.g., Stephens et al., 2018). Stephens et al. (2018) presented a framework in which the monitoring of flooding frequency can be used as an early warning signal, indicating when new flood defense and adaptation mechanisms need to be incorporated about 20 years before an adaptation threshold is reached. Monitoring the drivers of sea-level change (i.e., the sea-level budget) could also be used in such a framework. As illustrated in Figure 5.1, ocean mass change is the main contributor to present-day sea-level change along most of the West American coastline. Thus, if an acceleration is detected in one of the components causing ocean mass change, both at the coast of interest and at the source, then adaptation policies in this region might need to be adjusted.

5

COHERENT REGIONS

Usually, local sea-level assessments are carried out for a specific coastal region of a country or state. However, sea level does not change according to geographic and political borders. This means that if, for example, the Dutch government decides to perform a local assessment, and they consider only the Dutch coastal zone in their sea-level budget analysis, they might not be able to fully explain what is driving sea-level change at their coast. Alternatively, if they used the entire Northwest European Shelf instead, then their budget analysis would likely have a better performance, as the clustering analysis indicates that sea-level change in this region is physically coherent. Hence, local assessments should use coherent sea-level regions, such as the ones presented in this thesis, as a proxy for sea-level change in their region of interest.

5.4. COMMUNICATING UNCERTAINTIES, A REFLECTION

The topic of uncertainties associated to sea-level change was discussed in all chapters of this thesis. But why are uncertainties in sea-level change so important?

While uncertainties are pertinent to any realm of science, they become an issue when scientists meet decision makers, and the uncertainties are used as a pretext for inaction regarding climate change (Lemos and Rood, 2010). Particularly when it comes to mitigation and adaptation strategies to sea-level rise, decisions are obscured by the uncertainties of sea-level observations and projections, and how the uncertainties are interpreted by non-scientists (Kettle, 2012; Bakker et al., 2017). Note that adaptation frameworks are set up to deal with uncertainties, to a certain level, as long as they are well defined.

Both scientists and policy-makers need to be aware of the **uncertainty fallacy**, that is, "a belief that the systematic reduction of uncertainty in climate projections is required in order for the projections to be used by decision makers" (Lemos and Rood, 2010). The fallacy lies in the need of reducing the uncertainties to make use of the projections, because as previously stated, no measurements will ever be completely certain. Uncertainties are inherent to measurements and projections and necessary to give a valuable estimate. Additionally, sea-level projections are known to have deep uncertainties, which arise from disagreement between experts of which model and method should be used (Bakker et al., 2017), besides also being subject to uncertainties in human behaviour. It is necessary that scientists focus on understanding the causes of the uncertainties (and hence, how to reduce them as much as possible), and learn how to communicate the uncertainties. This will support informed decisions by policy-makers and contribute to debunking misinformation by climate change deniers.

Uncertainties should not be seen as a reason to distrust sea-level assessments and scientists. We know that sea level is rising and that it will continue to rise in the coming centuries, regardless of the actions taken to reduce greenhouse gases emissions (Wigley, 2005; Oppenheimer et al., 2019; Fox-Kemper et al., 2021). There is enough certainty and knowledge to justify decision makers to take action. When communicating with general public, scientists should therefore focus on what is known about the uncertainties, such as the knowledge that sea-level will rise by a certain amount, but that the uncertainty affects when exactly this will happen (Slangen et al., 2022). In this way, uncertainty becomes a source of information instead of a reason for undermining scientific knowledge.

5.5. NEW SATELLITES, NEW POSSIBILITIES

Since 1993, satellite altimeters have been measuring sea-level change across the world, providing valuable information on the spatial and temporal variations in sea level. This now almost 30-years long time series complements the longer local tide gauge measurements, improving the understanding of sea-level change trends, variability and acceleration along the coasts and all over the oceans. However, the traditional altimetry products have a reduced quality close to the coast, owing to the land contamination that the reference altimetry missions (Topex-Poseidon and Jason series) suffer. Recent and future altimetry missions, such as the Sentinel-6/Michael Freilich and SWOT satellites, have allowed better measurements in coastal waters, improving our capabilities of measuring sea surface height in coastal regions. These new missions also have the potential to improve reconstructions of sea-level anomalies in the open ocean (Lopez-Radencio et al., 2018), by constraining the data-driven interpolation models, and to enlighten the relationship between ocean dynamics and coastal sea level, for instance by measuring ocean currents in unprecedented detail (Morrow et al., 2019). These new missions might reduce the observational uncertainty at a finer scale, improving the sea-level budget analysis at a local scale.

5



Figure 5.7: Example of new and upcoming satellite missions that will benefit sea-level science. (a) Sentinel-6 Michael Freilich spacecraft in orbit above Earth, launched in November 2020 and planned for 5.5 years of operation. Image source: NASA; (b) Artist impression of SWOT satellite, launched in December 2022, with 3 years of nominal operation. Image source: CNES; (c) Artist impression of NISAR satellite, planned launch in 2024 with 3 years of nominal operation. Image source: NASA/JPL-Caltech.

Impact of Currents on Coastal Sea-level Change

Ocean currents, in particular the strong western boundary currents, can impact coastal sea level in the adjacent regions (Diabaté et al., 2021; Little et al., 2019). The impact of the Gulf Stream, for example, on trends and variability of sea-level along the east coast of the U.S. has been highlighted in several works, based on tide gauge data, current altimetry observations and ocean models (e.g., Diabaté et al., 2021; Ezer, 2019). With a 120-km-wide swath, SWOT will for the first time provide two-dimensional sea-level observations, resolving spatial scales down to 15 to 30 km (Morrow et al., 2019). SWOT will fill the

knowledge gap on meso- and submesoscale ocean dynamics, providing information of ocean currents, eddies and fronts. Hence, with this data it will be possible to investigate connections between coastal sea-level change and smaller scale eddies released by ocean currents, such as the Gulf Stream. Additionally, these observations will give insights in the dynamic term of the sea-level budget, currently one of the most uncertain terms in the budget (see Section 5.2.1).

Coastal Sea-level Vulnerability

As we improve our understanding of coastal sea-level change, we need to translate this knowledge into relevant information for coastal communities. An example is to develop maps of coastal vulnerability. Coastal vulnerability mapping requires not only the rates at which sea level is changing, and knowledge of the processes underlying the changes (i.e., via sea-level budget analysis), but also of the predisposition of a place to be impacted (e.g., low-lying areas and cities close to rivers are more prone to flooding than high lands) and the frequency and magnitude of extreme events. The fact that not only sea level is rising, but also, in some places, the land is sinking (i.e., land subsidence), makes coastal regions even more vulnerable to the impacts of sea-level change. The NASA–ISRO Synthetic Aperture Radar (NISAR) mission, planned for 2023, will measure small-scale changes on the Earth's surface, providing a wide range of information, including rates of land subsidence. This mission will complement existing SAR missions, by filling the community needs in terms of resolution (6 to 12-m, in comparison to the Sentinel 1a/b resolution of 20 m), coverage (global coverage with 12 day revisit period) and accuracy (NISAR, 2018). The land subsidence rates can then be integrated with the sea-level rise trends based on tide gauges and satellite altimetry to produce maps of coastal vulnerability to relative sea-level change.

A promising future

In the last years, it has become clear not only to scientists, but also to the public, that sea-level change is a real problem that currently is, and will continue to, affecting societies all over the world. It is our role as scientists to gather as much knowledge as we can about sea-level change: what are the driving processes; at which scale, both temporal and spatial, are the processes happening; how much will sea-level change in the future and at what rate; and so on. Currently, we have a good level of understanding of the processes driving sea-level change at a global, basin, and now also sub-basin scales. However, the quantification of the physical processes at a higher spatial scale are still hampered by the uncertainties in our measurements. New observations, such as from SWOT and from the Deep Argo array, alongside new ocean and climate models, are essential to bridge this gap

and improve of our current knowledge. It is also important that the current observational systems, such as the reference altimetry missions, the core Argo program, gravimetry missions and tide gauge stations, be maintained and continued (Cazenave et al., 2019). The future of sea-level science is promising.

BIBLIOGRAPHY

- Abdalla, S., Kolahchi, A. A., Ablain, M., and International Altimetry Team, A. Altimetry for the future: Building on 25 years of progress. *Advances in Space Research*, 68(2):319–363, 2021. 10.1016/j.asr.2021.01.022.
- Ablain, M., Cazenave, A., Valladeau, G., and Guinehut, S. A new assessment of the error budget of global Mean Sea Level rate estimated by satellite altimetry over 1993-2008. *Ocean Science*, 5(2):193–201, 2009. 10.5194/os-5-193-2009.
- Ablain, M., Legeais, J. F., Prandi, P., Marcos, M., Fenoglio-Marc, L., Dieng, H. B., Benveniste, J., and Cazenave, A. Satellite Altimetry-Based Sea Level at Global and Regional Scales. *Surveys in Geophysics*, 38(1):7–31, 2017. 10.1007/s10712-016-9389-8.
- Ablain, M., Meyssignac, B., Zawadzki, L., Jugier, R., Ribes, A., Cazenave, A., and Picot, N. Uncertainty in Satellite estimate of Global Mean Sea Level changes, trend and acceleration. *Earth System Science Data Discussions*, 58344(January):1–26, 2019. 10.5194/essd-2019-10.
- Abram, N., Gattuso, J. P., Prakash, A., Cheng, L., Chidichimo, M. P., Crate, S., Enomoto, H., Garschagen, M., Gruber, N., Harper, S., Holland, E., Kudela, R. M., Rice, J., Steffen, K., and von Schuckmann, K. Framing and Context of the Report. In Portner, H.-O., Roberts, D. C., Masson-Delmotte, V., Zhai, P., Tignor, M., Poloczanska, E., Mintenbeck, K., Alegria, A., Nicolai, M., Okem, A., Petezold, J., Rama, B., and Weyer, N. M., editors, *IPCC Special Report on the Ocean and Cryosphere in a Changing Climate*, pages 73–129. Cambridge University Press, Cambridge, UK and New York, NY, USA, 2019. 10.1017/9781009157964.003.
- Adhikari, S., Ivins, E. R., Frederikse, T., Landerer, F. W., and Caron, L. Sea-level fingerprints emergent from GRACE mission data. *Earth System Science Data Discussions*, 11(January):629–646, 2019. 10.5194/essd-11-629-2019.
- Akaike, H. A New Look at the Statistical Model Identification. *IEEE Transactions on Automatic Control*, 19(6): 716–723, 1974. 10.1109/TAC.1974.1100705.
- Amante, C. and Eakins, B. W. ETOPO1 1 Arc-Minute Global Relief Model: Procedures, Data Sources and Analysis. *NOAA Technical Memorandum NESDIS NGDC*, 24(October):19, 2009. 10.7289/V5C8276M.
- Amin, H., Bagherbandi, M., and Sjöberg, L. E. Quantifying barystatic sea-level change from satellite altimetry, GRACE and Argo observations over 2005–2016. *Advances in Space Research*, 65(8):1922–1940, 2020. 10.1016/j.asr.2020.01.029.
- Andersen, O. B. and Scharroo, R. Range and Geophysical Corrections in Coastal Regions: And Implications for Mean Sea Surface Determination. In Vignudelli, S., Kostianoy, A. G., Cipollini, P., and Benveniste, J., editors, *Coastal Altimetry*, chapter 5, pages 103–145. Springer-Verlag Berlin, 2011. ISBN 9783642127953. 10.1007/978-3-642-12796-0.
- Angermann, D., Pail, R., Seitz, F., and Hugentobler, U. *Mission Earth : geodynamics and climate change observed through satellite geodesy*. Springer, Berlin, 1 edition, 2022. ISBN 9783662641057. 10.1007/978-3-662-64106-4.

- Argus, D. F., Peltier, W. R., Drummond, R., and Moore, A. W. The Antarctica component of postglacial rebound model ICE-6G_C (VM5a) based on GPS positioning, exposure age dating of ice thicknesses, and relative sea level histories. *Geophysical Journal International*, 198(1):537–563, 2014. 10.1093/gji/ggu140.
- Bakker, A. M. R., Louchard, D., and Keller, K. Sources and implications of deep uncertainties surrounding sea-level projections. *Climatic Change*, 140(3-4):339–347, 2017. 10.1007/s10584-016-1864-1.
- Bamber, J. L. and Riva, R. E. M. The sea level fingerprint of recent ice mass fluxes. *The Cryosphere*, 4:621–627, 2010. 10.5194/tc-4-621-2010.
- Barnoud, A., Pfeffer, J., Guérou, A., Frery, M. L., Siméon, M., Cazenave, A., Chen, J., Llovel, W., Thierry, V., Legeais, J. E., and Ablain, M. Contributions of Altimetry and Argo to Non-Closure of the Global Mean Sea Level Budget Since 2016. *Geophysical Research Letters*, 48(14):1–10, 2021. 10.1029/2021GL092824.
- Barnoud, A., Pfeffer, J., Cazenave, A., and Ablain, M. Revisiting the global mean ocean mass budget over 2005-2020. *EGUsphere*, [preprint]:1–21, 2022. 10.5194/egusphere-2022-716.
- Benveniste, J., Birol, F., Calafat, F., Cazenave, A., Dieng, H., Gouzenes, Y., Legeais, J. F., Léger, F., Niño, F., Passaro, M., Schwatke, C., Shaw, A., and Team, T. C. C. I. C. S. L. Coastal sea level anomalies and associated trends from Jason satellite altimetry over 2002–2018. *Scientific Data*, 7(1):357, 2020. 10.1038/s41597-020-00694-w.
- Bilbao, R. A. E., Gregory, J. M., and Bouttes, N. Analysis of the regional pattern of sea level change due to ocean dynamics and density change for 1993–2099 in observations and CMIP5 AOGCMs. *Climate Dynamics*, 45(9-10):2647–2666, 2015. 10.1007/s00382-015-2499-z.
- Bindoff, N. L., Willebrand, J., Artale, V., Cazenave, A., Gregory, J. M., Gulev, S., Hanawa, K., Quéré, C. L., Levitus, S., Nojiri, Y., Shum, C.-K., Talley, L. D., and Unnikrishnan, A. S. Observations: oceanic climate change and sea level. In [Solomon, S., Qin, D., Manning, M., Chen, Z., Marquis, M., Averyt, K., Tignor, M., and Mille, H., editors, *Climate Change 2007: The Physical Science Basis. Contribution of Working Group I to the Fourth Assessment Report of the Intergovernmental Panel on Climate Change*, chapter 5, pages 385–432. Cambridge University Press, Cambridge, UK and New York, NY, USA, 2007. ISBN 9780521880091.
- Birol, F., Fuller, N., Lyard, F., Cancet, M., Niño, F., Delebecque, C., Fleury, S., Toublanc, F., Melet, A., Saraceno, M., and Léger, F. Coastal applications from nadir altimetry: Example of the X-TRACK regional products. *Advances in Space Research*, 59(4):936–953, 2017. 10.1016/j.asr.2016.11.005.
- Blazquez, A., Meyssignac, B., Lemoine, J. M., Berthier, E., Ribes, A., and Cazenave, A. Exploring the uncertainty in GRACE estimates of the mass redistributions at the Earth surface: Implications for the global water and sea level budgets. *Geophysical Journal International*, 215(1):415–430, 2018. 10.1093/gji/ggy293.
- Blockley, E. W., Martin, M. J., McLaren, A. J., Ryan, A. G., Waters, J., Lea, D. J., Mirouze, I., Peterson, K. A., Sellar, A., and Storkey, D. Recent development of the Met Office operational ocean forecasting system: An overview and assessment of the new Global FOAM forecasts. *Geoscientific Model Development*, 7(6):2613–2638, 2014. 10.5194/gmd-7-2613-2014.
- Bos, M. S., Fernandes, R. M. S., Williams, S. D. P., and Bastos, L. Fast error analysis of continuous GNSS observations with missing data. *Journal of Geodesy*, 87(4):351–360, 2013. 10.1007/s00190-012-0605-0.
- Bos, M. S., Fernandes, R. M. S., Vethamony, P., and Mehra, P. Estimating absolute sea level variations by combining GNSS and tide gauge data. *Indian Journal of Geo-Marine Sciences*, 43(7):1327–1331, 2014a.

- Bos, M. S., Williams, S. D. P., Araújo, I. B., and Bastos, L. The effect of temporal correlated noise on the sea level rate and acceleration uncertainty. *Geophysical Journal International*, 196(3):1423–1430, 2014b. 10.1093/gji/ggt481.
- Bos, M. and Fernandes, R. Hector user manual, 2013.
- Bracco, A., Falasca, E., Nenes, A., Fountalis, I., and Dovrolis, C. Advancing climate science with knowledge-discovery through data mining. *npj Climate and Atmospheric Science*, 1(1):1–6, 2018. 10.1038/s41612-017-0006-4.
- Bradshaw, E., Rickards, L., and Aarup, T. Sea level data archaeology and the Global Sea Level Observing System (GLOSS). *GeoResJ*, 6:9–16, 2015. 10.1016/j.grj.2015.02.005.
- Broecker, W. S. Thermohaline circulation, the Achilles heel of our climate system: will man-made CO₂ upset the current balance? *Science*, 278(28):1582–1588, 1997.
- Broecker, W. S. Does the trigger for abrupt climate change reside in the ocean or in the atmosphere? *Science*, 300(5625):1519–1522, 2003. 10.1126/science.1083797.
- Broersen, P. M. T. Finite sample criteria for autoregressive model order selection. *IEEE Transactions on Signal Processing*, 48(12):3550–3558, 2000. 10.1109/78.887047.
- Broersen, P. M. T. Automatic Spectraal Analysis With Time Series Models. *IEEE Transactions on Instrumentation and Measurements*, 51(2):211–216, 2002. 10.1109/19.997814.
- Broersen, P. M. T. ARMASA (<https://www.mathworks.com/matlabcentral/fileexchange/1330-armasa>). *MATLAB Central File Exchange.*, 2022.
- Burnham, K. P. and Anderson, D. R. *Multimodel inference: A Practical Information-Theoretic Approach*. Springer, New York, 2 edition, 2002. ISBN 978-0-387-22456-5. 10.1007/b97636.
- Burnham, K. P., Anderson, D. R., and Huyvaert, K. P. AIC model selection and multimodel inference in behavioral ecology : some background , observations , and comparisons. *Behavioral Ecology and Sociobiology*, 65(1): 23–35, 2011. 10.1007/s00265-010-1029-6.
- Cabanes, C., Grouazel, A., Von Schuckmann, K., Hamon, M., Turpin, V., Coatanoan, C., Paris, F., Guinehut, S., Boone, C., Ferry, N., De Boyer Montégut, C., Carval, T., Reverdin, G., Pouliquen, S., and Le Traon, P. Y. The CORA dataset: Validation and diagnostics of in-situ ocean temperature and salinity measurements. *Ocean Science*, 9(1):1–18, 2013. 10.5194/os-9-1-2013.
- Cáceres, D., Marzeion, B., Malles, J. H., Gutknecht, B., Müller Schmied, H., and Döll, P. Assessing global water mass transfers from continents to oceans over the period 1948–2016. *Hydrology and Earth System Sciences Discussions*, pages 1–37, 2020. 10.5194/hess-2019-664.
- Calafat, F. M., Chambers, D. P., and Tsimplis, M. N. Mechanisms of decadal sea level variability in the eastern North Atlantic and the Mediterranean Sea. *Journal of Geophysical Research: Oceans*, 117(9):1–14, 2012. 10.1029/2012JC008285.
- Calafat, F. M., Chambers, D. P., and Tsimplis, M. N. Inter-annual to decadal sea-level variability in the coastal zones of the Norwegian and Siberian Seas: The role of atmospheric forcing. *Journal of Geophysical Research: Oceans*, 118(3):1287–1301, 2013. 10.1002/jgrc.20106.

- Camargo, C. M. L., Riva, R. E. M., Hermans, T. H. J., and Slangen, A. B. A. Exploring Sources of Uncertainty in Steric Sea-Level Change Estimates. *Journal of Geophysical Research: Oceans*, pages 1–18, 2020. 10.1029/2020jc016551.
- Camargo, C. M. L., Riva, R. E. M., Hermans, T. H. J., and Slangen, A. B. A. Trends and uncertainties of mass-driven sea-level change in the satellite altimetry era. *Earth System Dynamics*, 13:1351–1375, 2022. 10.5194/esd-13-1351-2022.
- Caron, L., Ivins, E. R., Larour, E., Adhikari, S., Nilsson, J., and Blewitt, G. GIA Model Statistics for GRACE Hydrology, Cryosphere, and Ocean Science. *Geophysical Research Letters*, 45(5):2203–2212, 2018. 10.1002/2017GL076644.
- Carse, F., Martin, M. J., Sellar, A., and Blockley, E. W. Impact of assimilating temperature and salinity measurements by animal-borne sensors on FOAM ocean model fields. *Quarterly Journal of the Royal Meteorological Society*, 141(693):2934–2943, 2015. 10.1002/qj.2613.
- Carton, J. A., Chepurin, G. A., and Cheng, L. SODA3: a new ocean climate reanalysis. *Journal of Climate*, 31(17): 6967–6983, 2018. 10.1175/JCLI-D-18-0149.s1.
- Carvalho, K. S. and Wang, S. Characterizing the Indian Ocean sea level changes and potential coastal flooding impacts under global warming. *Journal of Hydrology*, 569(October 2018):373–386, 2019. 10.1016/j.jhydrol.2018.11.072.
- Cazenave, A. and Llovel, W. Contemporary Sea Level Rise. *Annual Review of Marine Science*, 2:145–173, 2010. 10.1146/annurev-marine-120308-081105.
- Cazenave, A., Dominh, K., Guinehut, S., Berthier, E., Llovel, W., Ramilien, G., Ablain, M., and Larnicol, G. Sea level budget over 2003-2008. A reevaluation from GRACE space gravimetry, satellite altimetry and ARGO. *Global Planet Change*, 65:83–88, 2009. 10.1016/j.gloplacha.2008.10.004.
- Cazenave, A. and Moreira, L. Contemporary sea-level changes from global to local scales: a review. *Proceedings of the Royal Society A: Mathematical, Physical and Engineering Sciences*, 478(20220049):1–30, 2022. 10.1098/rspa.2022.0049.
- Cazenave, A., Meyssignac, B., Ablain, M., Balmaseda, M., Bamber, J., Barletta, V., Beckley, B., Benveniste, J., Berthier, E., Blazquez, A., Boyer, T., Caceres, D., Chambers, D., Champollion, N., Chao, B., Chen, J., Cheng, L., Church, J. A., Chuter, S., Cogley, J. G., Dangendorf, S., Desbruyères, D., Döll, P., Domingues, C., Falk, U., Famiglietti, J., Fenoglio-Marc, L., Forsberg, R., Galassi, G., Gardner, A., Groh, A., Hamlington, B., Hogg, A., Horwath, M., Humphrey, V., Husson, L., Ishii, M., Jaeggi, A., Jevrejeva, S., Johnson, G., Kolodziejczyk, N., Kusche, J., Lambeck, K., Landerer, F., Leclercq, P., Legresy, B., Leuliette, E., Llovel, W., Longuevergne, L., Loomis, B. D., Luthcke, S. B., Marcos, M., Marzeion, B., Merchant, C., Merrifield, M., Milne, G., Mitchum, G., Mohajerani, Y., Monier, M., Monselesan, D., Nerem, S., Palanisamy, H., Paul, F., Perez, B., Piecuch, C. G., Ponte, R. M., Purkey, S. G., Reager, J. T., Rietbroek, R., Rignot, E., Riva, R., Roemmich, D. H., Sørensen, L. S., Sasgen, I., Schrama, E. J., Seneviratne, S. I., Shum, C. K., Spada, G., Stammer, D., van de Wal, R., Velicogna, I., von Schuckmann, K., Wada, Y., Wang, Y., Watson, C., Wiese, D., Wijffels, S., Westaway, R., Woppelmann, G., and Wouters, B. Global sea-level budget 1993-present. *Earth System Science Data*, 10(3):1551–1590, 2018. 10.5194/essd-10-1551-2018.

- Cazenave, A., Hamlington, B., Horwath, M., Barletta, V. R., Benveniste, J., Chambers, D., Döll, P., Hogg, A. E., Legeais, J. F., Merrifield, M., Meysignac, B., Mitchum, G., Nerem, S., Pail, R., Palanisamy, H., Paul, F., von Schuckmann, K., and Thompson, P. Observational requirements for long-term monitoring of the global mean sea level and its components over the altimetry era. *Frontiers in Marine Science*, 6(SEP):1–14, 2019. 10.3389/fmars.2019.00582.
- Cazenave, A., Gouzenes, Y., Birol, F., Leger, E., Passaro, M., Calafat, F. M., Shaw, A., Nino, F., Legeais, J. F., Oelmann, J., Restano, M., and Benveniste, J. New network of virtual altimetry stations for measuring sea level along the world coastlines. *SEANOE*, 2022. 10.17882/74354.
- Cha, H., Moon, J.-H., Kim, T., and Song, Y. T. Underlying drivers of decade-long fluctuation in the global mean sea-level rise. *Environmental Research Letters*, 16(12):124064, 2021. 10.1088/1748-9326/ac3d58.
- Chafik, L., Nilsen, J. E. Ø., Dangendorf, S., Reverdin, G., and Frederikse, T. North Atlantic Ocean Circulation and Decadal Sea Level Change During the Altimetry Era. *Scientific Reports*, 9(1):1–9, 2019. 10.1038/s41598-018-37603-6.
- Chambers, D. P., Wahr, J., and Nerem, R. S. Preliminary observations of global ocean mass variations with GRACE. *Geophysical Research Letters*, 31(13):1–4, 2004. 10.1029/2004GL020461.
- Chambers, D. P., Tamisiea, M. E., Nerem, R. S., and Ries, J. C. Effects of ice melting on GRACE observations of ocean mass trends. *Geophysical Research Letters*, 34(5):1–5, 2007. 10.1029/2006GL029171.
- Chambers, D. P., Cazenave, A., Champollion, N., Dieng, H., Llovel, W., Forsberg, R., von Schuckmann, K., and Wada, Y. Evaluation of the Global Mean Sea Level Budget between 1993 and 2014. *Surveys in Geophysics*, 38(1):309–327, 2017. 10.1007/s10712-016-9381-3.
- Chang, L., Tang, H., Wang, Q., and Sun, W. Global thermosteric sea level change contributed by the deep ocean below 2000 m estimated by Argo and CTD data. *Earth and Planetary Science Letters*, 524, 2019. 10.1016/j.epsl.2019.115727.
- Chen, J. L., Wilson, C. R., Tapley, B. D., and Grand, S. GRACE detects coseismic and postseismic deformation from the Sumatra-Andaman earthquake. *Geophysical Research Letters*, 34(13):1–5, 2007. 10.1029/2007GL030356.
- Chen, J. L., Wilson, C. R., and Tapley, B. D. Contribution of ice sheet and mountain glacier melt to recent sea level rise. *Nature Geoscience*, 6(7):549–552, 2013. 10.1038/ngeo1829.
- Chen, J., Tapley, B., Seo, K. W., Wilson, C., and Ries, J. Improved Quantification of Global Mean Ocean Mass Change Using GRACE Satellite Gravimetry Measurements. *Geophysical Research Letters*, 46(23):13984–13991, 2019. 10.1029/2019GL085519.
- Chen, J., Tapley, B., Wilson, C., Cazenave, A., Seo, K. W., and Kim, J. S. Global Ocean Mass Change From GRACE and GRACE Follow-On and Altimeter and Argo Measurements. *Geophysical Research Letters*, 47(22):1–9, 2020. 10.1029/2020GL090656.
- Chen, X., Feng, Y., and Huang, N. E. Global sea level trend during 1993-2012. *Global and Planetary Change*, 112: 26–32, 2014. 10.1016/j.gloplacha.2013.11.001.
- Chen, X., Zhang, X., Church, J. A., Watson, C. S., King, M. A., Monselesan, D., Legresy, B., and Harig, C. The increasing rate of global mean sea-level rise during 1993-2014. *Nature Climate Change*, 7(7):492–495, 2017. 10.1038/nclimate3325.

- Cheng, L., Abraham, J., Goni, G., Boyer, T., Wijffels, S., Cowley, R., Gouretski, V., Reseghetti, F., Kizu, S., Dong, S., Bringas, E., Goes, M., Houpert, L., Sprintall, J., and Zhu, J. XBT science: Assessment of instrumental biases and errors. *Bulletin of the American Meteorological Society*, 97(6):923–933, 2016. 10.1175/BAMS-D-15-00031.1.
- Cheng, L., Trenberth, K. E., Fasullo, J., Boyer, T., Abraham, J., and Zhu, J. Improved estimates of ocean heat content from 1960 to 2015. *Science Advances*, 3(3):1–11, 2017. 10.1126/sciadv.1601545.
- Cheng, L., Abraham, J., Hausfather, Z., and Trenberth, K. E. How fast are the oceans warming? *Science Climate Change*, 128(January):1–8, 2019. 10.1126/science.aav7619.
- Church, J. A. and White, N. J. A 20th century acceleration in global sea-level rise. *Geophysical Research Letters*, 33:L01602, 2006. 10.1029/2005GL024826.
- Church, J. A., White, N. J., Konikow, L. F., Domingues, C. M., Cogley, J. G., Rignot, E., Gregory, J. M., van den Broeke, M. R., Monaghan, A. J., and Velicogna, I. Revisiting the Earth's sea-level and energy budgets from 1961 to 2008. *Geophysical Research Letters*, 38(L18601), 2011. 10.1029/2011GL048794.
- Church, J. A., Clark, P. U., Cazenave, A., Gregory, J. M., Jevrejeva, S., Levermann, A., Merrifield, M. A., Milne, G. A., Nerem, R. S., Nunn, P. D., Payne, A. J., Pfeffer, W. T., Stammer, D., and Unnikrishnan, A. S. Sea Level Change. In Stocker, T., Qin, D., Plattner, G.-K., Tignor, M., Allen, S., Boschung, J., Nauels, A., Xia, Y., Bex, V., and Midgley, P., editors, *Climate Change 2013: The Physical Science Basis. Contribution of Working Group I to the Fifth Assessment Report of the Intergovernmental Panel on Climate Change*, chapter 13, pages pp. 1137–1216. Cambridge University Press, Cambridge, U. K., and New York, 2013.
- CMEMS. Global ocean gridded L4 sea surface heights and derived variables reprocessed (1993-ongoing) SEALEVEL_GLO_PHY_L4_MY_008_047. *E.U. Copernicus Marine Service*, [data set]:39, 2022. 10.48670/moi-00148.
- Couldrey, M. P., Gregory, J. M., Boeira Dias, F., Dobrohotoff, P., Domingues, C. M., Garuba, O., Griffies, S. M., Haak, H., Hu, A., Ishii, M., Jungclaus, J., Köhl, A., Marsland, S. J., Ojha, S., Saenko, O. A., Savita, A., Shao, A., Stammer, D., Suzuki, T., Todd, A., and Zanna, L. What causes the spread of model projections of ocean dynamic sea-level change in response to greenhouse gas forcing? *Climate Dynamics*, 56(1-2):155–187, 2021. 10.1007/s00382-020-05471-4.
- CSIRO. Combined TOPEX Poseidon, Jason-1, Jason-2 OSTM, Jason-3 near-global gridded monthly-average sea level product. *CSIRO*, [data set]:1–5, 2022. <http://www.cmar.csiro.au/sealevel/>.
- Dangendorf, S., Calafat, F. M., Arns, A., Wahl, T., Haigh, I. D., and Jensen, J. Mean sea level variability in the North Sea: processes and implications. *Journal of Geophysical Research: Oceans*, 119:6820–6841, 2014. 10.1002/2014JC009901.
- Dangendorf, S., Frederikse, T., Chafik, L., Klinck, J. M., Ezer, T., and Hamlington, B. D. Data-driven reconstruction reveals large-scale ocean circulation control on coastal sea level. *Nature Climate Change*, 11(6):514–520, 2021. 10.1038/s41558-021-01046-1.
- Desbruyères, D. G., Purkey, S. G., McDonagh, E. L., Johnson, G. C., and King, B. A. Deep and abyssal ocean warming from 35 years of repeat hydrography. *Geophysical Research Letters*, 43(19):10,356–10,365, 2016. 10.1002/2016GL070413.

- Desportes, C. C., Garric, G., Régnier, C., Drévilion, M., Parent, L., Garric, G., Drillet, Y., Masina, S., Storto, A., Mirouze, I., Cipollone, A., Zuo, H., Balmaseda, M., Peterson, D., Wood, R., Jackson, L., Mulet, S., Greiner, E., and Gounou, A. For Global Ocean Reanalysis Multi-model Ensemble Products GREP. Technical Report 1, Copernicus, 2019.
- Diabaté, S. T., Swingedouw, D., Hirschi, J. J. M., Duchez, A., Leadbitter, P. J., Haigh, I. D., and McCarthy, G. D. Western boundary circulation and coastal sea-level variability in Northern Hemisphere oceans. *Ocean Science*, 17(5):1449–1471, 2021. 10.5194/os-17-1449-2021.
- Dieng, H. B., Cazenave, A., Von Schuckmann, K., Ablain, M., and Meyssignac, B. Sea level budget over 2005-2013: Missing contributions and data errors. *Ocean Science*, 11(5):789–802, 2015a. 10.5194/os-11-789-2015.
- Dieng, H. B., Champollion, N., Cazenave, A., Wada, Y., Schrama, E., and Meyssignac, B. Total land water storage change over 2003-2013 estimated from a global mass budget approach. *Environmental Research Letters*, 10(12), 2015b. 10.1088/1748-9326/10/12/124010.
- Dieng, H. B., Cazenave, A., Meyssignac, B., and Ablain, M. New estimate of the current rate of sea level rise from a sea level budget approach. *Geophysical Research Letters*, 44(8):3744–3751, apr 2017. 10.1002/2017GL073308.
- Dieng, H. B., Palanisamy, H., Cazenave, A., Meyssignac, B., and von Schuckmann, K. The Sea Level Budget Since 2003: Inference on the Deep Ocean Heat Content. *Surveys in Geophysics*, 36(2):209–229, 2015c. 10.1007/s10712-015-9314-6.
- Doll, P., Kaspar, F., and Lehner, B. A global hydrological model for deriving water availability indicators: Model tuning and validation. *Journal of Hydrology*, 270(1-2):105–134, 2003. 10.1016/S0022-1694(02)00283-4.
- Donlon, C. J., Cullen, R., Giulicchi, L., Vuilleumier, P., Francis, C. R., Kuschnerus, M., Simpson, W., Bouridah, A., Caleno, M., Bertoni, R., Ranaño, J., Pourier, E., Hyslop, A., Mulcahy, J., Knockaert, R., Hunter, C., Webb, A., Fornari, M., Vaze, P., Brown, S., Willis, J., Desai, S., Desjonqueres, J. D., Scharroo, R., Martin-Puig, C., Leuliette, E., Egido, A., Smith, W. H., Bonnefond, P., Le Gac, S., Picot, N., and Tavenrier, G. The Copernicus Sentinel-6 mission: Enhanced continuity of satellite sea level measurements from space. *Remote Sensing of Environment*, 258(October 2020), 2021. 10.1016/j.rse.2021.112395.
- Dziewonski, A. M. and Anderson, D. L. Preliminary reference Earth model. *Physics of the Earth and Planetary Interiors*, 25(4):297–356, 1981. 10.1016/0031-9201(81)90046-7.
- Epanechnikov, V. A. Non-Parametric Estimation of a Multivariate Probability Density. *Theory of Probability & Its Applications*, 14(1):153–158, 1969. 10.1137/1114019.
- Ezer, T. Regional Differences in Sea Level Rise Between the Mid-Atlantic Bight and the South Atlantic Bight: Is the Gulf Stream to Blame? *Earth's Future*, 7:771–783, 2019. 10.1029/2019EF001174.
- Falasca, F., Bracco, A., Nenes, A., and Fountalis, I. Dimensionality Reduction and Network Inference for Climate Data Using δ -MAPS: Application to the CESM Large Ensemble Sea Surface Temperature. *Journal of Advances in Modeling Earth Systems*, 11(6):1479–1515, 2019. 10.1029/2019MS001654.
- Falasca, F., Crétat, J., Braconnot, P., and Bracco, A. Spatiotemporal complexity and time-dependent networks in sea surface temperature from mid- to late Holocene. *European Physical Journal Plus*, 135(5):1–21, 2020. 10.1140/epjp/s13360-020-00403-x.

- Farrell, W. E. and Clark, J. A. On Postglacial Sea Level. *Geophysical Journal of the Royal Astronomical Society*, 46: 647–667, 1976. 10.1111/j.1365-246X.1976.tb01252.x.
- Feng, M., Li, Y., and Meyers, G. Multidecadal variations of Fremantle sea level: Footprint of climate variability in the tropical Pacific. *Geophysical Research Letters*, 31(16):2–5, 2004. 10.1029/2004GL019947.
- Feng, W., Lemoine, J. M., Zhong, M., and Hsu, H. T. Mass-induced sea level variations in the Red Sea from GRACE, steric-corrected altimetry, in situ bottom pressure records, and hydrographic observations. *Journal of Geodynamics*, 78:1–7, 2014. 10.1016/j.jog.2014.04.008.
- Feng, W., Zhong, M., and Xu, H. Z. Sea level variations in the South China Sea inferred from satellite gravity, altimetry, and oceanographic data. *Science China Earth Sciences*, 55(10):1696–1701, 2012. 10.1007/s11430-012-4394-3.
- Fountalis, I., Dovrolis, C., Bracco, A., Dilkina, B., and Keilholz, S. δ -MAPS: from spatio-temporal data to a weighted and lagged network between functional domains. *Applied Network Science*, 3(1):3–21, 2018. 10.1007/s41109-018-0078-z.
- Fox-Kemper, B., Hewitt, H. T., Xiao, C., Aðalgeirsdóttir, G., Drijfhout, S. S., Edwards, T. L., Hemer, M., Kopp, R. E., Krinner, G., Mix, A., Notz, D., Nowicki, S., Nurhati, I. S., Ruiz, L., Sallée, J. B., Slangen, A. B. A., and Yu, Y. Ocean, Cryosphere and Sea Level Change. In Masson-Delmotte, V., Zhai, P., Pirani, A., Connors, S. L., Péan, C., Berger, S., Caud, N., Chen, Y., Goldfarb, L., Gomis, M. I., Huang, M., Leitzell, K., Lonnoy, E., Matthews, J. B. R., Maaycock, T. K., Waterfield, T., Yeleçi, O., Yu, R., and Zhou, B., editors, *The Physical Science Basis. Contribution of Working Group I to the Sixth Assessment Report of the Intergovernmental Panel on Climate Change*, chapter 9, pages 1211–1362. Cambridge University Press, Cambridge, 2021. ISBN 9781009157896. 10.1017/9781009157896.011.
- Frankcombe, L. M., Spence, P., Hogg, A. M., England, M. H., and Griffies, S. M. Sea level changes forced by Southern Ocean winds. *Geophysical Research Letters*, 40(21):5710–5715, 2013. 10.1002/2013GL058104.
- Frederikse, T., Riva, R., Kleinherenbrink, M., Wada, Y., van den Broeke, M., and Marzeion, B. Closing the sea level budget on a regional scale: Trends and variability on the Northwestern European continental shelf. *Geophysical Research Letters*, 43(20):10,810–864,872, 2016. 10.1002/2016GL070750.
- Frederikse, T., Riva, R. E. M., and King, M. A. Ocean Bottom Deformation Due To Present-Day Mass Redistribution and Its Impact on Sea Level Observations. *Geophysical Research Letters*, 44(24):12,306–12,314, 2017a. 10.1002/2017GL075419.
- Frederikse, T., Simon, K., Katsman, C. A., and Riva, R. E. M. The sea-level budget along the Northwest Atlantic coast: GIA, mass changes, and large-scale ocean dynamics. *Journal of Geophysical Research : Oceans*, 122: 5486–5501, 2017b. 10.1002/2016JC012335.
- Frederikse, T., Jevrejeva, S., Riva, R. E. M., and Dangendorf, S. A consistent sea-level reconstruction and its budget on basin and global scales over 1958–2014. *Journal of Climate*, 31(3):1267–1280, 2018. 10.1175/JCLI-D-17-0502.1.
- Frederikse, T., Landerer, E., and Caron, L. The imprints of contemporary mass redistribution on local sea level and vertical land motion observations. *Solid Earth*, 10(6):1971–1987, 2019. 10.5194/se-10-1971-2019.

- Frederikse, T., Landerer, F., Caron, L., Adhikari, S., Parkes, D., Humphrey, V. W., Dangendorf, S., Hogarth, P., Zanna, L., and Cheng, L. The causes of sea-level rise since 1900. *Nature*, 584(August):393–397, 2020. 10.1038/s41586-020-2591-3.
- Frederikse, T., Adhikari, S., Daley, T. J., Dangendorf, S., Gehrels, R., Landerer, F., Marcos, M., Newton, T. L., Rush, G., Slangen, A. B. A., and Wöppelmann, G. Constraining 20th-Century Sea-Level Rise in the South Atlantic Ocean. *Journal of Geophysical Research: Oceans*, 126(3), 2021. 10.1029/2020JC016970.
- Gaillard, E., Reynaud, T., Thierry, V., Kolodziejczyk, N., and Von Schuckmann, K. In situ-based reanalysis of the global ocean temperature and salinity with ISAS: Variability of the heat content and steric height. *Journal of Climate*, 29(4):1305–1323, 2016. 10.1175/JCLI-D-15-0028.1.
- García, D., Chao, B. F., Del Río, J., Vigo, I., and García-Lafuente, J. On the steric and mass-induced contributions to the annual sea level variations in the Mediterranean Sea. *Journal of Geophysical Research: Oceans*, 111(9): 1–8, 2006. 10.1029/2005JC002956.
- Garric, G. and Parent, L. Quality Information Document For products GLOBAL-REANALYSIS-PHY-001-025. Technical report, Copernicus Marine Environment Monitoring Service, 2017.
- Garry, F. K., McDonagh, E. L., Blaker, A. T., Roberts, C. D., Desbruyères, D. G., Frajka-Williams, E., and King, B. A. Model-Derived Uncertainties in Deep Ocean Temperature Trends Between 1990 and 2010. *Journal of Geophysical Research: Oceans*, 124(2):1155–1169, 2019. 10.1029/2018JC014225.
- Gasparin, F., Hamon, M., Rémy, E., and Le Traon, P. Y. How deep argo will improve the deep ocean in an ocean reanalysis. *Journal of Climate*, 33(1):77–94, 2020. 10.1175/JCLI-D-19-0208.1.
- Ghobadi-Far, K., Han, S. C., Allgeyer, S., Tregoning, P., Sauber, J., Behzadpour, S., Mayer-Gürr, T., Sneeuw, N., and Okal, E. GRACE gravitational measurements of tsunamis after the 2004, 2010, and 2011 great earthquakes. *Journal of Geodesy*, 94(7):1–9, 2020. 10.1007/s00190-020-01395-3.
- Gill, A. E. and Niller, P. P. The theory of the seasonal variability in the ocean. *Deep Sea Research and Oceanographic Abstracts*, 20(2):141–177, 1973. 10.1016/0011-7471(73)90049-1.
- Gomez, N., Mitrovica, J. X., Tamisiea, M. E., and Clark, P. U. A new projection of sea level change in response to collapse of marine sectors of the Antarctic Ice Sheet. *Geophysical Journal International*, 180(2):623–634, 2010. 10.1111/j.1365-246X.2009.04419.x.
- Good, S. A., Martin, M. J., and Rayner, N. A. EN4: Quality controlled ocean temperature and salinity profiles and monthly objective analyses with uncertainty estimates. *Journal of Geophysical Research: Oceans*, 118(12): 6704–6716, 2013. 10.1002/2013JC009067.
- Gouretski, V. and Reseghetti, F. On depth and temperature biases in bathythermograph data: Development of a new correction scheme based on analysis of a global ocean database. *Deep-Sea Research Part I: Oceanographic Research Papers*, 57(6):812–833, 2010. 10.1016/j.dsr.2010.03.011.
- Gregory, J. M., White, N. J., Church, J. A., Bierkens, M. F., Box, J. E., Van Den Broeke, M. R., Cogley, J. G., Fettweis, X., Hanna, E., Huybrechts, P., Konikow, L. F., Leclercq, P. W., Marzeion, B., Oerlemans, J., Tamisiea, M. E., Wada, Y., Wake, L. M., and Van De Wal, R. S. W. Twentieth-century global-mean sea level rise: Is the whole greater than the sum of the parts? *Journal of Climate*, 26(13):4476–4499, 2013. 10.1175/JCLI-D-12-00319.1.

- Gregory, J. M., Griffies, S. M., Hughes, C. W., Lowe, J. A., Church, J. A., Fukimori, I., Gomez, N., Kopp, R. E., Landerer, E., Cozannet, G. L., Ponte, R. M., Stammer, D., Tamisiea, M. E., and van de Wal, R. S. W. Concepts and Terminology for Sea Level: Mean, Variability and Change, Both Local and Global. *Surveys in Geophysics*, 40(6):1251–1289, 2019. 10.1007/s10712-019-09525-z.
- Griffies, S. M. and Greatbatch, R. J. Physical processes that impact the evolution of global mean sea level in ocean climate models. *Ocean Modelling*, 51:37–72, 2012. 10.1016/j.ocemod.2012.04.003.
- Guinehut, S., Dhomps, A. L., Larnicol, G., and Le Traon, P. Y. High resolution 3-D temperature and salinity fields derived from in situ and satellite observations. *Ocean Science*, 8(5):845–857, 2012. 10.5194/os-8-845-2012.
- Haasnoot, M., Kwakkel, J. H., and Walker, W. E. Dynamic adaptive policy pathways : A method for crafting robust decisions for a deeply uncertain world. *Global Environmental Change*, 23(2):485–498, 2013. 10.1016/j.gloenvcha.2012.12.006.
- Hamlington, B. D., Reager, J. T., Lo, M. H., Karnauskas, K. B., and Leben, R. R. Separating decadal global water cycle variability from sea level rise. *Scientific Reports*, 7(1):1–7, 2017. 10.1038/s41598-017-00875-5.
- Hamlington, B. D., Gardner, A. S., Ivins, E., Lenaerts, J. T., Reager, J. T., Trossman, D. S., Zaron, E. D., Adhikari, S., Arendt, A., Aschwanden, A., Beckley, B. D., Bekaert, D. P., Blewitt, G., Caron, L., Chambers, D. P., Chandanpurkar, H. A., Christianson, K., Csatho, B., Cullather, R. I., DeConto, R. M., Fasullo, J. T., Frederikse, T., Freymueller, J. T., Gilford, D. M., Giroto, M., Hammond, W. C., Hock, R., Holschuh, N., Kopp, R. E., Landerer, F., Larour, E., Menemenlis, D., Merrifield, M., Mitrovica, J. X., Nerem, R. S., Nias, I. J., Nieves, V., Nowicki, S., Pangaluru, K., Piecuch, C. G., Ray, R. D., Rounce, D. R., Schlegel, N. J., Seroussi, H., Shirzaei, M., Sweet, W. V., Velicogna, I., Vinogradova, N., Wahl, T., Wiese, D. N., and Willis, M. J. Understanding of Contemporary Regional Sea-Level Change and the Implications for the Future. *Reviews of Geophysics*, 58(3):1–39, 2020. 10.1029/2019RG000672.
- Han, G., Ma, Z., Chen, N., Thomson, R., and Slangen, A. Changes in Mean Relative Sea Level around Canada in the Twentieth and Twenty-First Centuries. *Atmosphere - Ocean*, 53(5):452–463, 2015. 10.1080/07055900.2015.1057100.
- Han, W., Meehl, G. A., Stammer, D., Hu, A., Hamlington, B., Kenigson, J., Palanisamy, H., and Thompson, P. Spatial Patterns of Sea Level Variability Associated with Natural Internal Climate Modes. *Surveys in Geophysics*, 38(1):217–250, 2017. 10.1007/s10712-016-9386-y.
- Hardman-Mountford, N. J., Richardson, A. J., Boyer, D. C., Kreiner, A., and Boyer, H. J. Relating sardine recruitment in the Northern Benguela to satellite-derived sea surface height using a neural network pattern recognition approach. *Progress in Oceanography*, 59(2-3):241–255, 2003. 10.1016/j.pocean.2003.07.005.
- Hauer, M. E., Fussell, E., Mueller, V., Burkett, M., Call, M., Abel, K., McLeman, R., and Wrathall, D. Sea-level rise and human migration. *Nature Reviews Earth and Environment*, 1(1):28–39, 2019. 10.1038/s43017-019-0002-9.
- He, X., Bos, M. S., Montillet, J. P., and Fernandes, R. M. Investigation of the noise properties at low frequencies in long GNSS time series. *Journal of Geodesy*, 93(9):1271–1282, 2019. 10.1007/s00190-019-01244-y.
- Hermans, T. H. J., Le Bars, D., Katsman, C. A., Camargo, C. M. L., Gerkema, T., Calafat, F. M., Tinker, J., and Slangen, A. B. A. Drivers of Interannual Sea Level Variability on the Northwestern European Shelf. *Journal of Geophysical Research: Oceans*, 125(10):1–18, 2020. 10.1029/2020JC016325.

- Hernández-Carrasco, I. and Orfila, A. The Role of an Intense Front on the Connectivity of the Western Mediterranean Sea: The Cartagena-Tenes Front. *Journal of Geophysical Research: Oceans*, 123(6):4398–4422, 2018. 10.1029/2017JC013613.
- Hinkel, J., Church, J. A., Gregory, J. M., Lambert, E., Le Cozannet, G., Lowe, J., McInnes, K. L., Nicholls, R. J., van der Pol, T. D., and van de Wal, R. Meeting User Needs for Sea Level Rise Information: A Decision Analysis Perspective. *Earth's Future*, 7(3):320–337, 2019. 10.1029/2018EF001071.
- Holgate, S. J., Matthews, A., Woodworth, P. L., Rickards, L. J., Tamisiea, M. E., Bradshaw, E., Foden, P. R., Gordon, K. M., Jevrejeva, S., and Pugh, J. New Data Systems and Products at the Permanent Service for Mean Sea Level. *Journal of Coastal Research*, 29(3):493–504, 12 2013. 10.2112/JCOASTRES-D-12-00175.1.
- Horwath, M., Gutknecht, B. D., Cazenave, A., Palanisamy, H. K., Marti, E., Marzeion, B., Paul, F., Le Bris, R., Hogg, A. E., Otsuka, I., Shepherd, A., Döll, P., Cáceres, D., Müller Schmied, H., Johannessen, J. A., Nilsen, J. E. Ø., Raj, R. P., Forsberg, R., Sandberg Sørensen, L., Barletta, V. R., Simonsen, S. B., Knudsen, P., Andersen, O. B., Ranndal, H., Rose, S. K., Merchant, C. J., Macintosh, C. R., Von Schuckmann, K., Novotny, K., Groh, A., Restano, M., and Benveniste, J. Global sea-level budget and ocean-mass budget, with a focus on advanced data products and uncertainty characterisation. *Earth System Science Data*, 14(2):411–447, 2022. 10.5194/essd-14-411-2022.
- Hsu, C. W. and Velicogna, I. Detection of sea level fingerprints derived from GRACE gravity data. *Geophysical Research Letters*, 44(17):8953–8961, 2017. 10.1002/2017GL074070.
- Hughes, C. W. and Williams, S. D. P. The color of sea level: Importance of spatial variations in spectral shape for assessing the significance of trends. *Journal of Geophysical Research: Oceans*, 115(10):1–18, 2010. 10.1029/2010JC006102.
- Hughes, C. W., Fukumori, I., Griffies, S. M., Huthnance, J. M., Minobe, S., Spence, P., Thompson, K. R., and Wise, A. Sea Level and the Role of Coastal Trapped Waves in Mediating the Influence of the Open Ocean on the Coast. *Surveys in Geophysics*, 40(6):1467–1492, 2019. 10.1007/s10712-019-09535-x.
- Hugonnet, R., McNabb, R., Berthier, E., Menounos, B., Nuth, C., Girod, L., Farinotti, D., Huss, M., Dussailant, L., Brun, F., and Kääh, A. Accelerated global glacier mass loss in the early twenty-first century. *Nature*, 592(7856):726–731, 2021. 10.1038/s41586-021-03436-z.
- Humphrey, V., Gudmundsson, L., and Seneviratne, S. I. A global reconstruction of climate-driven subdecadal water storage variability. *Geophysical Research Letters*, 44(5):2300–2309, 2017. 10.1002/2017GL072564.
- Humphrey, V. and Gudmundsson, L. GRACE-REC: a reconstruction of climate-driven water storage changes over the last century. *Earth System Science Data*, 11(3):1153–1170, 2019. 10.5194/essd-11-1153-2019.
- Ishii, M. and Kimoto, M. Reevaluation of historical ocean heat content variations with time-varying XBT and MBT depth bias corrections. *Journal of Oceanography*, 65(3):287–299, 2009. 10.1007/s10872-009-0027-7.
- Ishii, M., Yasui, S., Fukuda, Y., Sato, K., Hirahara, S., and Suzuki, T. Accuracy of Global Upper Ocean Heat Content Estimation Expected from Present Observational Data Sets. *Sola*, 13(0):163–167, 2017. 10.2151/sola.2017-030.
- Iskandar, I. Variability of Satellite-Observed Sea Surface Height in the Tropical Indian Ocean: Comparison of Eof and Som Analysis. *MAKARA of Science Series*, 13(2):173–179, 2009. 10.7454/mss.v13i2.421.
- Jeon, T., Seo, K. W., Kim, B. H., Kim, J. S., Chen, J., and Wilson, C. R. Sea level fingerprints and regional sea level change. *Earth and Planetary Science Letters*, 567:116985, 2021. 10.1016/j.epsl.2021.116985.

- Jevrejeva, S., Frederikse, T., Kopp, R. E., Le Cozannet, G., Jackson, L. P., and van de Wal, R. S. W. Probabilistic Sea Level Projections at the Coast by 2100. *Surveys in Geophysics*, 40(6):1673–1696, 2019. 10.1007/s10712-019-09550-y.
- Johnson, G. C., Lyman, J. M., and Purkey, S. G. Informing deep argo array design using argo and full-depth hydrographic section data. *Journal of Atmospheric and Oceanic Technology*, 32(11):2187–2198, 2015. 10.1175/JTECH-D-15-0139.1.
- Kettle, N. P. Exposing compounding uncertainties in sea level rise assessments. *Journal of Coastal Research*, 28(1):161–173, 2012. 10.2112/JCOASTRES-D-10-00011.1.
- Klees, R. and Broersen, P. *How to handle colored noise in large least-squares problems: Building the optimal filter*. Delft University Press (DUP) Science, Delft, The Netherlands, 2002.
- Kleinherenbrink, M., Riva, R., Frederikse, T., Merrifield, M., and Wada, Y. Trends and interannual variability of mass and steric sea level in the Tropical Asian Seas. *Journal of Geophysical Research: Oceans*, 122(8): 6254–6276, 2017. 10.1002/2017JC012792.
- Kohonen, T. Self-organized formation of topologically correct feature maps. *Biological Cybernetics*, 43(1):59–69, 1982. 10.1007/BF00337288.
- Kopp, R., Oppenheimer, M., O'Reilly, J. L., Drijfhout, S. S., Edwards, T. L., Fox-Kemper, B., Garner, G. G., Golledge, N. R., Hermans, T. H. J., Hewitt, H. T., and et al. Communicating projection uncertainty and ambiguity in sea-level assessment. *Earth and Space Science Open Archive*, page 31, 2022. 10.1002/essoar.10511663.1.
- Kopp, R. E., Kemp, A. C., Bittermann, K., Horton, B. P., Donnelly, J. P., Cehrels, W. R., Hay, C. C., Mitrovica, J. X., Murrow, E. D., and Rahmstorf, S. Temperature-driven global sea-level variability in the Common Era. *Proceedings of the National Academy of Sciences*, 113(38), 2016. 10.1073/pnas.1517056113.
- Kouketsu, S., Doi, T., Kawano, T., Masuda, S., Sugiura, N., Sasaki, Y., Toyoda, T., Igarashi, H., Kawai, Y., Katsumata, K., Uchida, H., Fukasawa, M., and Awaji, T. Deep ocean heat content changes estimated from observation and reanalysis product and their influence on sea level change. *Journal of Geophysical Research: Oceans*, 116(3):1–16, 2011. 10.1029/2010JC006464.
- Kulp, S. A. and Strauss, B. H. New elevation data triple estimates of global vulnerability to sea-level rise and coastal flooding. *Nature Communications*, 10(1), 2019. 10.1038/s41467-019-12808-z.
- Landerer, F. W., Jungclaus, J. H., and Marotzke, J. Ocean bottom pressure changes lead to a decreasing length-of-day in a warming climate. *Geophysical Research Letters*, 34(L06307):1–5, 2007.
- Landerer, F. W., Flechtner, F. M., Save, H., Webb, F. H., Bandikova, T., Bertiger, W. I., Bettadpur, S. V., Byun, S. H., Dahle, C., Dobslaw, H., Fahnestock, E., Harvey, N., Kang, Z., Kruizinga, G. L., Loomis, B. D., McCullough, C., Murböck, M., Nagel, P., Paik, M., Pie, N., Poole, S., Strelakov, D., Tamisiea, M. E., Wang, F., Watkins, M. M., Wen, H. Y., Wiese, D. N., and Yuan, D. N. Extending the Global Mass Change Data Record: GRACE Follow-On Instrument and Science Data Performance. *Geophysical Research Letters*, 47(12):1–10, 2020. 10.1029/2020GL088306.
- Lange, S. WFDE5 over land merged with ERA5 over the ocean (W5E5). *GFZ Data Services*, [data set](V.1.0): 7505–7514, 2019. 10.5880/pik.2019.023.

- Larour, E., Ivins, E. R., and Adhikari, S. Should coastal planners have concern over where land ice is melting? *Science Advances*, 3(11):1–9, 2017. 10.1126/sciadv.1700537.
- Larour, E., Caron, L., Morlighem, M., Adhikari, S., Frederikse, T., Schlegel, N. J., Ivins, E., Hamlington, B., Kopp, R., and Nowicki, S. ISSM-SLPS: Geodetically compliant Sea-Level Projection System for the Ice-sheet and Sea-level System Model v4.17. *Geoscientific Model Development*, 13(10):4925–4941, 2020. 10.5194/gmd-13-4925-2020.
- Lehner, B., Liermann, C. R., Revenga, C., Vörösmarty, C., Fekete, B., Crouzet, P., Döll, P., Endejan, M., Frenken, K., Magome, J., Nilsson, C., Robertson, J. C., Rödel, R., Sindorf, N., and Wisser, D. High-resolution mapping of the world's reservoirs and dams for sustainable river-flow management. *Frontiers in Ecology and the Environment*, 9(9):494–502, 2011. 10.1890/100125.
- Lemos, M. C. and Rood, R. B. Climate projections and their impact on policy and practice. *Wiley Interdisciplinary Reviews: Climate Change*, 1(5):670–682, 2010. 10.1002/wcc.71.
- Leuliette, E. W. and Miller, L. Closing the sea level rise budget with altimetry, Argo and GRACE. *Geophysical Research Letters*, 36:5, 2009. 10.1029/2008GL036010,.
- Leuliette, E. The Budget of Recent Global Sea Level Rise. *Star.Nesdis.Noaa.Gov*, pages 1–10, 2014.
- Leuliette, E. and Willis, J. K. Balancing the sea level budget. *Oceanography*, 24(2):122–129, 2011. 10.5670/oceanog.2011.32.
- Leuliette, E. W. The Balancing of the Sea-Level Budget. *Current Climate Change Reports*, 1(3):185–191, 2015. 10.1007/s40641-015-0012-8.
- Levermann, A., Griesel, A., Hofmann, M., Montoya, M., and Rahmstorf, S. Dynamic sea level changes following changes in the thermohaline circulation. *Climate Dynamics*, 24(4):347–354, 2005. 10.1007/s00382-004-0505-y.
- Li, H., Xu, F., Zhou, W., Wang, D., Wright, J. S., Liu, Z., and Lin, Y. Development of a global gridded Argo data set with Barnes successive corrections. *Journal of Geophysical Research: Oceans*, 122(5423):866–889, 2017. 10.1002/2016JC012285.
- Liddle, A. R. How many cosmological parameters? *Monthly Notices of the Royal Astronomical Society*, 351(3), 2004. 10.1111/j.1365-2966.2004.08033.x.
- Liddle, A. R. Information criteria for astrophysical model selection. *Monthly Notices of the Royal Astronomical Society*, 377:74–78, 2007. 10.1111/j.1745.3933.00306.x.
- Lin, Y., Hibbert, F. D., Whitehouse, P. L., Woodroffe, S. A., Purcell, A., Shennan, I., and Bradley, S. L. A reconciled solution of Meltwater Pulse 1A sources using sea-level fingerprinting. *Nature Communications*, 12(1), 2021. 10.1038/s41467-021-21990-y.
- Little, C. M., Hu, A., Hughes, C. W., McCarthy, G. D., Piecuch, C. G., Ponte, R. M., and Thomas, M. D. The Relationship Between U.S. East Coast Sea Level and the Atlantic Meridional Overturning Circulation: A Review. *Journal of Geophysical Research: Oceans*, 124(9):6435–6458, 2019. 10.1029/2019JC015152.
- Liu, Y. and Weisberg, R. H. Patterns of ocean current variability on the West Florida Shelf using the self-organizing map. *Journal of Geophysical Research: Oceans*, 110(6):1–12, 2005. 10.1029/2004JC002786.

- Liu, Y. and Weisberg, R. H. Ocean currents and sea surface heights estimated across the west Florida shelf. *Journal of Physical Oceanography*, 37(6):1697–1713, 2007. 10.1175/JPO3083.1.
- Liu, Y., Weisberg, R. H., and Mooers, C. N. K. Performance evaluation of the self-organizing map for feature extraction. *Journal of Geophysical Research: Oceans*, 111(5):1–14, 2006. 10.1029/2005JC003117.
- Liu, Y., Weisberg, R. H., Vignudelli, S., and Mitchum, G. T. Patterns of the loop current system and regions of sea surface height variability in the eastern Gulf of Mexico revealed by the self-organizing maps. *Journal of Geophysical Research: Oceans*, 121(5):2347–2366, 2016. 10.1002/2015JC011493.
- Llovel, W., Willis, J. K., Landerer, F. W., and Fukumori, I. Deep-ocean contribution to sea level and energy budget not detectable over the past decade. *Nature Climate Change*, 4(11):1031–1035, 2014. 10.1038/nclimate2387.
- Llovel, W., Guinehut, S., and Cazenave, A. Regional and interannual variability in sea level over 2002–2009 based on satellite altimetry, Argo float data and GRACE ocean mass. *Ocean Dynamics*, 60(5):1193–1204, 2010. 10.1007/s10236-010-0324-0.
- Lopez-Radenceno, M., Pascual, A., Gomez-Navarro, L., Aissa-El-Bey, A., and Fablet, R. Analog Data Assimilation for Along-Track Nadir and Swot Altimetry Data in the Western Mediterranean Sea. In *IGARSS 2018 - 2018 IEEE International Geoscience and Remote Sensing Symposium*, pages 7684–7687, 2018. 10.1109/IGARSS.2018.8519089.
- Lu, S., Liu, Z., Li, H., Li, Z., Wu, X., and Sun, C. Manual of Global Ocean Argo gridded data set (BOA_Argo) (Version 2019). Technical report, Second Institute of oceanography SOA, 2019.
- MA, F., DIAO, Y. N., and LUO, D. H. Spatiotemporal characteristics of the sea level anomaly in the Kuroshio Extension using a self-organizing map. *Atmospheric and Oceanic Science Letters*, 9(6):471–478, 2016. 10.1080/16742834.2016.1235462.
- MacIntosh, C. R., Merchant, C. J., and von Schuckmann, K. Uncertainties in Steric Sea Level Change Estimation During the Satellite Altimeter Era: Concepts and Practices. *Surveys in Geophysics*, 38(1):59–87, 2017. 10.1007/s10712-016-9387-x.
- Maclachlan, C., Arribas, A., Peterson, K. A., Maidens, A., Fereday, D., Scaife, A. A., Gordon, M., Vellinga, M., Williams, A., Comer, R. E., Camp, J., Xavier, P., Madec, G., and National, F. Global Seasonal forecast system version 5 (GloSea5): a high-resolution seasonal forecast system. *Quarterly Journal of the Royal Meteorological Society*, 5(April):1072–1084, 2015. 10.1002/qj.2396.
- Marcos, M. and Amores, A. Quantifying anthropogenic and natural contributions to thermosteric sea level rise. *Geophysical Research Letters*, 41(April):2502–2507, 2014. 10.1002/2014GL059766.
- Marzeion, B., Jarosch, A. H., and Hofer, M. Past and future sea-level change from the surface mass balance of glaciers. *Cryosphere*, 6(6):1295–1322, 2012. 10.5194/tc-6-1295-2012.
- Maul, G. A. and Duedall, I. W. Demography of Coastal Populations. In Finkl, C. W. and Makowski, C., editors, *Encyclopedia of Earth Sciences Series*, volume 14, pages 692–700. Springer International Publishing, 2019.
- McDougall, T. J. and Barker, P. M. *Getting started with TEO-10 and the Gibbs Seawarer Oceanographic Toolbox*. SCOR/IAPSO WG127, 2011. ISBN 9780646556215.

- McGranahan, G., Balk, D., and Anderson, B. The rising tide: assessing the risks of climate change and human settlements in low elevation coastal zones. *Environment and Urbanization*, 19(1):17–37, 2007. 10.1177/0956247807076960.
- Meyssignac, B., Slangen, A. B. A., Melet, A., Church, J. A., Fettweis, X., Marzeion, B., Agosta, C., Ligtenberg, S. R. M., Spada, G., Richter, K., Palmer, M. D., Roberts, C. D., and Champollion, N. Evaluating model simulations of twentieth-century sea-level rise. Part II: Regional sea-level changes. *Journal of Climate*, 30(21):8565–8593, 2017. 10.1175/JCLI-D-17-0112.1.
- Milne, G. A. and Mitrovia, J. X. Postglacial sea-level change on a rotating Earth. *Geophysical Journal International*, 133:1–19, 1998. 10.1046/j.1365-246X.1998.1331455.x.
- Mitchum, G. T. An improved calibration of satellite altimetric heights using tide gauge sea levels with adjustment for land motion. *Marine Geodesy*, 23(3):145–166, 2000. 10.1080/01490410050128591.
- Mitrovia, J. X. and Peltier, W. R. On Postglacial Geoid Subsidence Over the Equatorial Oceans. *Journal of Geophysical Research*, 96(B12):20053–20071, 1991. doi:10.1029/91JB01284.
- Mitrovia, J. X., Tamisiea, M. E., Davis, J. L., and Milne, G. A. Recent mass balance of polar ice sheets inferred from patterns of global sea-level change. *Nature*, 409:1026–1029, 2001. 10.1038/35059054.
- Mitrovia, J. X., Gomez, N., Morrow, E., Hay, C., Latychev, K., and Tamisiea, M. E. On the robustness of predictions of sea level fingerprints. *Geophysical Journal International*, 187(2):729–742, 2011. 10.1111/j.1365-246X.2011.05090.x.
- Morrow, R., Fu, L.-L., Arduin, F., Benkiran, M., Chapron, B., Cosme, E., d’Ovidio, F., Farrar, J. T., Gille, S. T., Lapeyre, G., Le Traon, P.-Y., Pascual, A., Ponte, A., Qiu, B., Rasche, N., Ubelmann, C., Wang, J., and Zaron, E. D. Global Observations of Fine-Scale Ocean Surface Topography With the Surface Water and Ocean Topography (SWOT) Mission. *Frontiers in Marine Science*, 6, 2019. 10.3389/fmars.2019.00232.
- Mouginot, J. and Rignot, E. Glacier catchments / basins for the Greenland Ice Sheet. *Dryad*, [data set], 2019. 10.7280/D1WT11.
- Mouginot, J., Rignot, E., Bjørk, A. A., van den Broeke, M., Millan, R., Morlighem, M., Noël, B., Scheuchl, B., and Wood, M. Forty-six years of Greenland Ice Sheet mass balance from 1972 to 2018. *Proceedings of the National Academy of Sciences of the United States of America*, 116(19):9239–9244, 2019. 10.1073/pnas.1904242116.
- Mu, D., Xu, T., and Guan, M. Sea level instantaneous budget for 2003–2015. *Geophysical Journal International*, 229(2):828–837, 2022. 10.1093/gji/ggab506.
- Nerem, R. S., Chambers, D. P., Leuliette, E. W., Mitchum, G. T., and Giese, B. S. Variations in global mean sea level associated with the 1997-1998 ENSO event: Implications for measuring long term sea level change. *Geophysical Research Letters*, 26(19):3005–3008, 1999. 10.1029/1999GL002311.
- Nerem, R. S., Beckley, B. D., Fasullo, J. T., Hamlington, B. D., Masters, D., and Mitchum, G. T. Climate-change-driven accelerated sea-level rise detected in the altimeter era. *Proceedings of the National Academy of Sciences of the United States of America*, 115(9):2022–2025, 2018. 10.1073/pnas.1717312115.
- Neumann, B., Vafeidis, A. T., Zimmermann, J., and Nicholls, R. J. Future coastal population growth and exposure to sea-level rise and coastal flooding - A global assessment. *PLoS ONE*, 10(3), 2015. 10.1371/journal.pone.0118571.

- Nicholls, R. J., Wong, P. P., Burkett, V. R., Codignotto, J., Hay, J. E., McLean, R. F., Ragoonaden, S., and Woodroffe, C. D. Coastal systems and low-lying areas. In *Climate Change 2007: Impacts, Adaptation and Vulnerability*, pages 315–356. Cambridge University Press, 2007. ISBN 00472425.
- Nicholls, R. J., Lincke, D., Hinkel, J., Brown, S., Vafeidis, A. T., Meyssignac, B., Hanson, S. E., Merkens, J. L., and Fang, J. A global analysis of subsidence, relative sea-level change and coastal flood exposure. *Nature Climate Change*, 11(4):338–342, 2021. 10.1038/s41558-021-00993-z.
- Nickerson, A. K., Weisberg, R. H., and Liu, Y. On the Evolution of the Gulf of Mexico Loop Current Through Its Penetrative, Ring Shedding and Retracted States. *Advances in Space Research*, 69(11):4058–4077, 2022. 10.1016/j.asr.2022.03.039.
- NISAR. *NASA-ISRO SAR (NISAR) Mission Science Users' Handbook*. NASA Jet Propulsion Laboratory, 2018.
- Noerdlinger, P. D. and Brower, K. R. The melting of floating ice raises the ocean level. *Geophysical Journal International*, 170(1):145–150, 2007. 10.1111/j.1365-246X.2007.03472.x.
- Novi, L., Bracco, A., and Falasca, F. Uncovering marine connectivity through sea surface temperature. *Scientific Reports*, 11(1):1–9, 2021. 10.1038/s41598-021-87711-z.
- Oppenheimer, M., Abdelgawad, A., Hay, J., Glavovic, B., Cai, R., Marzeion, B., Hinkel, J., Cifuentes-Jara, M., Meyssignac, B., Van De Wal, R., DeConto, R., Sebesvari, Z., Magnan, A., and Ghosh, T. Sea Level Rise and Implications for Low-Lying Islands, Coasts and Communities. In Pörtner, H.-O., Roberts, D., Masson-Delmotte, V., Zhai, P., Tignor, M., Poloczanska, E., Mintenbeck, K., Alegria, A., Nicolai, M., Okem, A., Petzold, J., Rama, B., and Weyer, N., editors, *IPCC Special Report on the Ocean and Cryosphere in a Changing Climate*, pages 76–95. Cambridge University Press, Cambridge, U. K., and New York., 2019.
- Palmer, M. D., Domingues, C. M., Slangen, A. B. A., and Boeira Dias, F. An ensemble approach to quantify global mean sea-level rise over the 20th century from tide gauge reconstructions. *Environmental Research Letters*, 16(4):044043, 2021. 10.1088/1748-9326/abdaec.
- Passaro, M., Cipollini, P., Vignudelli, S., Quartly, G. D., and Snaith, H. M. ALES: A multi-mission adaptive subwaveform retracker for coastal and open ocean altimetry. *Remote Sensing of Environment*, 145:173–189, 2014. 10.1016/j.rse.2014.02.008.
- Passaro, M., Nadzir, Z. A., and Quartly, G. D. Improving the precision of sea level data from satellite altimetry with high-frequency and regional sea state bias corrections. *Remote Sensing of Environment*, 218(June): 245–254, 2018. 10.1016/j.rse.2018.09.007.
- Pattiaratchi, C. and Siji, P. Variability in ocean currents around Australia. In Richardson, A., Eriksen, R., Moltmann, T., Hodgson-Johnston, I., and Wallis, J., editors, *State and Trends of Australia's Ocean Report*, chapter 1.4 Variability, pages 1–6. Integrated Marine Observing System (IMOS), 2020. 10.26198/5e16a2ae49e76.
- Peck, R., Olsen, C., and Devore, J. L. *Introduction to statistics and data analysis*. Cengage Learning, 3 edition, 2008. ISBN 978-1-337-79361-2 1-337-79361-2 978-1-337-79432-9 1-337-79432-5 978-1-337-79415-2 1-337-79415-5.
- Peltier, W. R. Closure of the budget of global sea level rise over the GRACE era: the importance and magnitudes of the required corrections for global glacial isostatic adjustment. *Quaternary Science Reviews*, 28(17-18): 1658–1674, 2009. 10.1016/j.quascirev.2009.04.004.

- Peltier, W. R., Argus, D. F., and Drummond, R. Space geodesy constrains ice age terminal deglaciation: The global ICE-6G_C (VM5a) model. *Journal of Geophysical Research: Solid Earth*, 2015(120):450–487, 2015. 10.1002/2014JB011176.
- Peltier, W., Argus, D. F., and Drummond, R. Comment on “An Assessment of the ICE-6G_C (VM5a) Glacial Isostatic Adjustment Model” by Purcell et al. *Journal of Geophysical Research: Solid Earth*, 123(2):2019–2028, 2018. 10.1002/2016JB013844.
- Pfeffer, W. T., Arendt, A. A., Bliss, A., Bolch, T., Cogley, J. G., Gardner, A. S., Hagen, J. O., Hock, R., Kaser, G., Kienholz, C., Miles, E. S., Moholdt, G., Mölg, N., Paul, F., Radić, V., Rastner, P., Raup, B. H., Rich, J., Sharp, M. J., Andreassen, L. M., Bajracharya, S., Barrand, N. E., Beedle, M. J., Berthier, E., Bhambri, R., Brown, I., Burgess, D. O., Burgess, E. W., Cawkwell, F., Chinn, T., Copland, L., Cullen, N. J., Davies, B., De Angelis, H., Fountain, A. G., Frey, H., Giffen, B. A., Glasser, N. F., Gurney, S. D., Hagg, W., Hall, D. K., Haritashya, U. K., Hartmann, G., Herreid, S., Howat, I., Jiskoot, H., Khromova, T. E., Klein, A., Kohler, J., König, M., Kriegel, D., Kutuzov, S., Lavrentiev, I., Le Bris, R., Li, X., Manley, W. F., Mayer, C., Menounos, B., Mercer, A., Mool, P., Negrete, A., Nosenko, G., Nuth, C., Osmonov, A., Pettersson, R., Racoviteanu, A., Ranzi, R., Sarikaya, M. A., Schneider, C., Sigurdsson, O., Sirguey, P., Stokes, C. R., Wheate, R., Wolken, G. J., Wu, L. Z., and Wyatt, F. R. The randolph glacier inventory: A globally complete inventory of glaciers. *Journal of Glaciology*, 60(221):537–552, 2014. 10.3189/2014JoG13J176.
- Piecuch, C. G. and Quinn, K. J. El Niño, La Niña, and the global sea level budget. *Ocean Science*, 12(6):1165–1177, 2016. 10.5194/os-12-1165-2016.
- Ponte, R. M. An assessment of deep steric height variability over the global ocean. *Geophysical Research Letters*, 39(4):1–5, 2012. 10.1029/2011GL050681.
- Ponte, R. M., Carson, M., Cirano, M., Domingues, C. M., Jevrejeva, S., Marcos, M., Mitchum, G., van de Wal, R. S., Woodworth, P. L., Ablain, M., Arduhin, F., Ballu, V., Becker, M., Benveniste, J., Birol, F., Bradshaw, E., Cazenave, A., De Mey-Frémaux, P., Durand, E., Ezer, T., Fu, L. L., Fukumori, I., Gordon, K., Gravelle, M., Griffies, S. M., Han, W., Hibbert, A., Hughes, C. W., Idier, D., Kourafalou, V. H., Little, C. M., Matthews, A., Melet, A., Merrifield, M., Meyssignac, B., Minobe, S., Penduff, T., Picot, N., Piecuch, C., Ray, R. D., Rickards, L., Santamaría-Gómez, A., Stammer, D., Staneva, J., Testut, L., Thompson, K., Thompson, P., Vignudelli, S., Williams, J., Simon, S. D., Wöppelmann, G., Zanna, L., and Zhang, X. Towards comprehensive observing and modeling systems for monitoring and predicting regional to coastal sea level. *Frontiers in Marine Science*, 6 (JUL), 2019. 10.3389/fmars.2019.00437.
- Prandi, P., Meyssignac, B., Ablain, M., Spada, G., Ribes, A., and Benveniste, J. Local sea level trends, accelerations and uncertainties over 1993–2019. *Scientific Data*, 8(1):1–12, 2021. 10.1038/s41597-020-00786-7.
- Purkey, S. G. and Johnson, G. C. Warming of Global Abyssal and Deep Southern Ocean Waters between the 1990s and 2000s: Contributions to Global Heat and Sea Level Rise Budgets. *Journal of Climate*, 23:6336–6351, 2010. 10.1175/2010JCLI3682.1.
- Purkey, S. G., Johnson, G. C., and Chambers, D. P. Relative contributions of ocean mass and deep steric changes to sea level rise between 1993 and 2013. *Journal of Geophysical Research, Oceans*, 119:7509–7522, 2014. 10.1002/2013JC009622.
- Purkey, S. G., Johnson, G. C., Talley, L. D., Sloyan, B. M., Wijffels, S. E., Smethie, W., Mecking, S., and Katsumata, K. Unabated Bottom Water Warming and Freshening in the South Pacific Ocean. *Journal of Geophysical Research: Oceans*, 124(3):1778–1794, 2019. 10.1029/2018JC014775.

- Reager, J. T., Gardner, A. S., Famiglietti, J. S., Wiese, D. N., Eicker, A., and Lo, M. H. A decade of sea level rise slowed by climate-driven hydrology. *Science*, 351(6274):699–703, 2016. 10.1126/science.aad8386.
- RGI Consortium. Randolph Glacier Inventory - A Dataset of Global Glacier Outlines, Version 6.0. *NSIDC: National Snow and Ice Data Center*, [data set]:-, 2017. 10.7265/4m1f-gd79.
- Richardson, A. J., Risi En, C., and Shillington, F. A. Using self-organizing maps to identify patterns in satellite imagery. *Progress in Oceanography*, 59(2-3):223–239, 2003. 10.1016/j.pocean.2003.07.006.
- Rietbroek, R., Brunnabend, S.-E., Kusche, J., Schröter, J., and Dahle, C. Revisiting the contemporary sea-level budget on global and regional scales. *Proceedings of the National Academy of Sciences*, 113(6):1504–1509, 2016. 10.1073/pnas.1519132113.
- Rignot, E., Velicogna, I., van den Broeke, M. R., Monaghan, A., and Lenaerts, J. Acceleration of the contribution of the Greenland and Antarctic ice sheets to sea level rise. *Geophysical Research Letters*, 38(L05503), 2011. 10.1029/2011GL046583.
- Rignot, E., Mouginot, J., Scheuchl, B., Van Den Broeke, M., Van Wessem, M. J., and Morlighem, M. Four decades of Antarctic ice sheet mass balance from 1979–2017. *Proceedings of the National Academy of Sciences of the United States of America*, 116(4):1095–1103, 2019. 10.1073/pnas.1812883116.
- Riva, R. E. M., Bamber, J. L., Lavallée, D. A., and Wouters, B. Sea-level fingerprint of continental water and ice mass change from GRACE. *Geophysical Research Letters*, 37(19):1–6, 2010. 10.1029/2010GL044770.
- Roemmich, D. and Gilson, J. The 2004 – 2008 mean and annual cycle of temperature , salinity , and steric height in the global ocean from the Argo Program. *Progress in Oceanography*, 82(2):81–100, 2009. 10.1016/j.pocean.2009.03.004.
- Roemmich, D., Johnson, G. C., Riser, S., Davis, R., Gilson, J., Owens, W. B., Garzoli, S. L., Schmid, C., and Ignaszewski, M. The Argo Program: Observing the global ocean with profiling floats. *Oceanography*, 22(2): 34–43, 2009. doi:10.5670/oceanog.2009.36.
- Rougier, J. Ensemble averaging and mean squared error. *Journal of Climate*, 29(24):8865–8870, 2016. 10.1175/JCLI-D-16-0012.1.
- Royston, S., Watson, C. S., Legresy, B., King, M. A., Church, J. A., and Bos, M. S. Sea-Level Trend Uncertainty With Pacific Climatic Variability and Temporally-Correlated Noise. *Journal of Geophysical Research : Oceans*, 123(3):1–16, 2018. 10.1002/2017JC013655.
- Royston, S., Vishwakarma, B. D., Westaway, R., Rougier, J., and Sha, Z. Can We Resolve the Basin-Scale Sea Level Trend Budget From GRACE Ocean Mass ? *Journal of Geophysical Research : Oceans*, 125:1–16, 2020. 10.1029/2019JC015535.
- Save, H. CSR GRACE and GRACE-FO RL06 Mascon Solutions v02. *CSR*, 2 [dataset](last access 2020-10-28), 2020. 10.15781/cgq9-nh24.
- Save, H., Bettadpur, S., and Tapley, B. D. High-resolution CSR GRACE RL05 mascons. *Journal of Geophysical Research : Solid Earth*, 121:7547–7569, 2016. 10.1002/2017JB015312.

- Scanlon, B. R., Zhang, Z., Save, H., Sun, A. Y., Schmied, H. M., Van Beek, L. P. H., Wiese, D. N., Wada, Y., Long, D., Reedy, R. C., Longuevergne, L., Döll, P., and Bierkens, M. F. P. Global models underestimate large decadal declining and rising water storage trends relative to GRACE satellite data. *Proceedings of the National Academy of Sciences of the United States of America*, 115(6):E1080–E1089, 2018. 10.1073/pnas.1704665115.
- Scharroo, R., Smith, W., Leuliette, E., and Lillibridge, J. The performance of cryosat-2 as an ocean altimeter. Technical Report 2, RADS, 2012.
- Schneider, U., Becker, A., Finger, P., Meyer-Christoffer, A., Rudolf, B., and Ziese, M. GPCP Full Data Monthly Product Version 7.0 at 0.5°: Monthly Land-Surface Precipitation from Rain-Gauges built on GTS-based and Historic Data. *Global Precipitation Climatology Centre (GPCP)*, 7.0 [dataset], 2015. 10.5676/DWD-GPCP/FD-M-V7-050.
- von Schuckmann, K., Palmer, M. D., Trenberth, K. E., Cazenave, A., Chambers, D., Champollion, N., Hansen, J., Josey, S. A., Loeb, N., Mathieu, P. P., Meyssignac, B., and Wild, M. An imperative to monitor Earth's energy imbalance. *Nature Climate Change*, 6(2):138–144, 2016. 10.1038/nclimate2876.
- von Schuckmann, K., Sallé, J.-B., Chambers, D., Le Traon, P.-Y., Cabanes, C., Gaillard, E., Speich, S., and Hamon, M. Monitoring ocean heat content from the current generation of global ocean observing systems. *Ocean Science Discussions, European Geosciences Union*, 10(3):923–949, 2013. 10.5194/osd-10-923-2013.
- Schwarz, G. Estimating the dimension of a model. *Annals of Statistics*, 6(2):461–464, 1978. 10.1214/aos/1176344136.
- Shepherd, A., Ivins, E., Rignot, E., Smith, B., Van Den Broeke, M., Velicogna, I., Whitehouse, P., Briggs, K., Joughin, I., Krinner, G., Nowicki, S., Payne, T., Scambos, T., Schlegel, N., Geruo, A., Agosta, C., Ahlström, A., Babonis, G., Barletta, V., Blazquez, A., Bonin, J., Csatho, B., Cullather, R., Felikson, D., Fettweis, X., Forsberg, R., Gallee, H., Gardner, A., Gilbert, L., Groh, A., Gunter, B., Hanna, E., Harig, C., Helm, V., Horvath, A., Horwath, M., Khan, S., Kjeldsen, K. K., Konrad, H., Langen, P., Lecavalier, B., Loomis, B., Luthcke, S., McMillan, M., Melini, D., Mernild, S., Mohajerani, Y., Moore, P., Mouginit, J., Moyano, G., Muir, A., Nagler, T., Nield, G., Nilsson, J., Noel, B., Otosaka, I., Pattle, M. E., Peltier, W. R., Pie, N., Rietbroek, R., Rott, H., Sandberg-Sørensen, L., Sasgen, I., Save, H., Scheuchl, B., Schrama, E., Schröder, L., Seo, K. W., Simonsen, S., Slater, T., Spada, G., Sutterley, T., Talpe, M., Tarasov, L., Van De Berg, W. J., Van Der Wal, W., Van Wessel, M., Vishwakarma, B. D., Wiese, D., and Wouters, B. Mass balance of the Antarctic Ice Sheet from 1992 to 2017. *Nature*, 558(7709):219–222, 2018. 10.1038/s41586-018-0179-y.
- Shepherd, A., Ivins, E., Rignot, E., Smith, B., van den Broeke, M., Velicogna, I., Whitehouse, P., Briggs, K., Joughin, I., Krinner, G., Nowicki, S., Payne, T., Scambos, T., Schlegel, N., A. G., Agosta, C., Ahlström, A., Babonis, G., Barletta, V. R., Bjørk, A. A., Blazquez, A., Bonin, J., Colgan, W., Csatho, B., Cullather, R., Engdahl, M. E., Felikson, D., Fettweis, X., Forsberg, R., Hogg, A. E., Gallee, H., Gardner, A., Gilbert, L., Gourmelen, N., Groh, A., Gunter, B., Hanna, E., Harig, C., Helm, V., Horvath, A., Horwath, M., Khan, S., Kjeldsen, K. K., Konrad, H., Langen, P. L., Lecavalier, B., Loomis, B., Luthcke, S., McMillan, M., Melini, D., Mernild, S., Mohajerani, Y., Moore, P., Mottram, R., Mouginit, J., Moyano, G., Muir, A., Nagler, T., Nield, G., Nilsson, J., Noël, B., Otosaka, I., Pattle, M. E., Peltier, W. R., Pie, N., Rietbroek, R., Rott, H., Sandberg Sørensen, L., Sasgen, I., Save, H., Scheuchl, B., Schrama, E., Schröder, L., Seo, K. W., Simonsen, S. B., Slater, T., Spada, G., Sutterley, T., Talpe, M., Tarasov, L., van de Berg, W. J., van der Wal, W., van Wessel, M., Vishwakarma, B. D., Wiese, D., Wilton, D., Wagner, T., Wouters, B., and Wuite, J. Mass balance of the Greenland Ice Sheet from 1992 to 2018. *Nature*, 579(7798):233–239, 2020. 10.1038/s41586-019-1855-2.

- Siedler, G., Griffies, S. M., Gould, J., and Church, J. A. Part I: The Ocean's Role in the Climate System. In Siedler, G., Griffies, S. M., Gould, J., and Church, J. A., editors, *Ocean Circulation and Climate*, volume 103, chapter Part I, page 1. Academic Press, 2013. 10.1016/B978-0-12-391851-2.09995-5.
- Simon, K. M. and Riva, R. E. M. Uncertainty Estimation in Regional Models of Long-Term GIA Uplift and Sea Level Change: An Overview. *Journal of Geophysical Research: Solid Earth*, 125(8), 2020. 10.1029/2019JB018983.
- Slangen, A. B. A., Katsman, C. A., van de Wal, R. S. W., Vermeersen, L. L. A., and Riva, R. E. M. Towards regional projections of twenty-first century sea-level change based on IPCC SRES scenarios. *Climate Dynamics*, 38(5-6):1191–1209, 2012. 10.1007/s00382-011-1057-6.
- Slangen, A. B. A., Van De Wal, R. S. W., Wada, Y., and Vermeersen, L. L. A. Comparing tide gauge observations to regional patterns of sea-level change (1961-2003). *Earth System Dynamics*, 5(1):243–255, 2014. 10.5194/esd-5-243-2014.
- Slangen, A. B. A., Adloff, F., Jevrejeva, S., Leclercq, P. W., Marzeion, B., Wada, Y., and Winkelmann, R. A Review of Recent Updates of Sea-Level Projections at Global and Regional Scales. *Surveys in Geophysics*, 38(1):385–406, 2017a. 10.1007/s10712-016-9374-2.
- Slangen, A. B. A., Church, J. A., Zhang, X., and Monselesan, D. P. The sea level response to external forcings in historical simulations of CMIP5 climate models. *Journal of Climate*, 28(21):8521–8539, 2015. 10.1175/JCLI-D-15-0376.1.
- Slangen, A. B. A., Church, J. A., Agosta, C., Fettweis, X., Marzeion, B., and Richter, K. Anthropogenic forcing dominates global mean sea-level rise since 1970. *Nature Climate Change*, 6(7):701–705, 2016. 10.1038/nclimate2991.
- Slangen, A. B. A., Meyssignac, B., Agosta, C., Champollion, N., Church, J. A., Fettweis, X., Ligtenberg, S. R. M., Marzeion, B., Melet, A., Palmer, M. D., Richter, K., Roberts, C. D., and Spada, G. Evaluating model simulations of twentieth-century sea level rise. Part I: Global mean sea level change. *Journal of Climate*, 30(21):8539–8563, 2017b. 10.1175/JCLI-D-17-0110.1.
- Slangen, A. B. A., Palmer, M. D., Camargo, C. M. L., Church, J. A., Edwards, T. L., Hermans, T. H. J., Hewitt, H., Garner, G. G., Gregory, J. M., Kopp, R. E., Santos, V. M., and van de Wal, R. S. W. The evolution of 21st century sea-level projections from IPCC AR5 to AR6 and beyond. *Cambridge Prisms: Coastal Futures*, pages 1–33, 2022. 10.1017/cft.2022.8.
- SLcci. Time series of gridded sea level anomalies. *ESA*, [dataset]:1–2, 2022. 10.5270/esa-sea.
- Sonniewald, M., Wunsch, C., and Heimbach, P. Linear predictability: A sea surface height case study. *Journal of Climate*, 31(7):2599–2611, 2018. 10.1175/JCLI-D-17-0142.1.
- Sonniewald, M., Wunsch, C., and Heimbach, P. Unsupervised Learning Reveals Geography of Global Ocean Dynamical Regions. *Earth and Space Science*, 6(5):784–794, 2019. 10.1029/2018EA000519.
- Spada, G. Glacial Isostatic Adjustment and Contemporary Sea Level Rise: An Overview. *Surveys in Geophysics*, 38(1):153–185, 2017. 10.1007/s10712-016-9379-x.
- Stammer, D., Cazenave, A., Ponte, R. M., and Tamisiea, M. E. Causes for Contemporary Regional Sea Level Changes. *Annual Review of Marine Science*, 5, 2013. 10.1146/annurev-marine-121211-172406.

- Stephens, S. A., Bell, R. G., and Lawrence, J. Developing signals to trigger adaptation to sea-level rise. *Environmental Research Letters*, 13(10), 2018. 10.1088/1748-9326/aadf96.
- Stewart, R. H. *Introduction To Physical Oceanography*. Open textbook Library, september edition, 2008.
- Storto, A. and Masina, S. C-GLORSv5: An improved multipurpose global ocean eddy-permitting physical reanalysis. *Earth System Science Data*, 8(2):679–696, 2016. 10.5194/essd-8-679-2016.
- Storto, A., Masina, S., Balmaseda, M., Guinehut, S., Xue, Y., Szekely, T., Fukumori, I., Forget, G., Chang, Y. S., Good, S. A., Köhl, A., Vernieres, G., Ferry, N., Peterson, K. A., Behringer, D., Ishii, M., Masuda, S., Fujii, Y., Toyoda, T., Yin, Y., Valdivieso, M., Barnier, B., Boyer, T., Lee, T., Gourrion, J., Wang, O., Heimback, P., Rosati, A., Kovach, R., Hernandez, F., Martin, M. J., Kamachi, M., Kuragano, T., Mogensen, K., Alves, O., Haines, K., and Wang, X. Steric sea level variability (1993–2010) in an ensemble of ocean reanalyses and objective analyses. *Climate Dynamics*, 49(3):709–729, 2017. 10.1007/s00382-015-2554-9.
- Storto, A., Bonaduce, A., Feng, X., and Yang, C. Steric Sea Level Changes from Ocean Reanalyses at Global and Regional Scales. *Water*, 11:1–31, 2019. 10.3390/w11101987.
- Sutanudjaja, E. H., Van Beek, R., Wanders, N., Wada, Y., Bosmans, J. H. C., Drost, N., Van Der Ent, R. J., De Graaf, I. E. M., Hoch, J. M., De Jong, K., Karssenber, D., López López, P., Peßenteiner, S., Schmitz, O., Straatsma, M. W., Vannamete, E., Wisser, D., and Bierkens, M. F. P. PCR-GLOBWB 2: A 5 arcmin global hydrological and water resources model. *Geoscientific Model Development*, 11(6):2429–2453, 2018. 10.5194/gmd-11-2429-2018.
- Szekely, T., Gourrion, J., Pouliquen, S., and Reverdin, G. The CORA 5.2 dataset for global in situ temperature and salinity measurements: Data description and validation. *Ocean Science*, 15(6):1601–1614, 2019. 10.5194/os-15-1601-2019.
- Talley, L. D., Pickard, G. L., Emery, W. J., and Swift, J. H. *Descriptive Physical Oceanography: An Introduction*. Academic press, sixth edition, 2011.
- Tamisiea, M. E. Ongoing glacial isostatic contributions to observations of sea level change. *Geophysical Journal International*, 186(3):1036–1044, sep 2011. 10.1111/j.1365-246X.2011.05116.x.
- Tapley, B. D., Bettadpur, S., Watkins, M., and Reigber, C. The Gravity Recovery and Climate Experiment: Mission Overview and Early Results. *Geophysical Research Letters*, 31(L09607):1–4, 2004. 10.1029/2004GL019920.
- Taylor, J. R. *An introduction to error analysis: the study of uncertainties in physical measurements*. University Science Books, Sausalito, California, 1997.
- Thompson, P. R. and Merrifield, M. A. A unique asymmetry in the pattern of recent sea level change. *Geophysical Research Letters*, 41(21):7675–7683, 2014. 10.1002/2014GL061263.
- Thorne, P. W., Parkes, D. E., Christy, J. R., and Mears, C. A. Lessons from Upper-Air Temperature Records. *American Meteorological Society*, 86(10):1437–1442, 2005. 10.1175/BAMS-86-10-1437.
- Thorne, P. Global surface temperatures. In *Climate Change*, pages 95–109. Elsevier B.V., 2021. ISBN 9780128215753. 10.1016/b978-0-12-821575-3.00005-0.
- Tomczak, M. and Godfrey, J. S. Temperature, salinity, density, and the oceanic pressure field. In *Regional Oceanography: An Introduction*, volume 2, chapter 2, pages 15–28. Delhi: Daya Publishing House, 2003.

- Uebbing, B., Kusche, J., Rietbroek, R., and Landerer, F. W. Processing Choices Affect Ocean Mass Estimates From GRACE. *Journal of Geophysical Research: Oceans*, 124(2):1029–1044, 2019. 10.1029/2018JC014341.
- van de Wal, R. S. W., Zhang, X., Minobe, S., Jevrejeva, S., Riva, R. E. M., Little, C., Richter, K., and Palmer, M. D. Uncertainties in Long-Term Twenty-First Century Process-Based Coastal Sea-Level Projections. *Surveys in Geophysics*, 40(6):1655–1671, 2019. 10.1007/s10712-019-09575-3.
- Vermeersen, L. L. A. and Sabadini, R. Polar wander, sea-level variations and ice age cycles. *Surveys in Geophysics*, 20:415–440, 1999. 10.1023/A:1006691724099.
- Vesanto, J., HlMBERG, J., Alhoniemi, E., and Parhankangaas, J. SOM Toolbox for Matlab 5. Technical report, Helsinki University of Technology, 2000.
- Vishwakarma, B. D., Royston, S., Riva, R. E. M., Westaway, R. M., and Bamber, J. L. Sea Level Budgets Should Account for Ocean Bottom Deformation. *Geophysical Research Letters*, 47(3), 2020. 10.1029/2019GL086492.
- Vishwakarma, B. D., Bates, P., Sneeuw, N., Westaway, R. M., and Bamber, J. L. Re-assessing global water storage trends from GRACE time series. *Environmental Research Letters*, 16(3), 2021. 10.1088/1748-9326/abd4a9.
- Wagner, P. and Böning, C. W. Decadal sea-level variability in the Australasian Mediterranean Sea. *Ocean Science*, 17(5):1473–1487, 2021. 10.5194/os-17-1473-2021.
- Wahr, J., Swenson, S., and Velicogna, I. Accuracy of GRACE mass estimates. *Geophysical Research Letters*, 33 (L06401):1–5, 2006. 10.1029/2005GL025305.
- Wang, C. and Picaut, J. Understanding ENSO physics—a review. In Wang, C., Xie, S. P., and Carton, J. A., editors, *Earth's Climate: The Ocean-Atmosphere Interaction*, volume 147, pages 21–48. American Geophysical Union, 2004. ISBN 9781118665947. 10.1029/147GM02.
- Wang, J., Church, J. A., Zhang, X., and Chen, X. Reconciling global mean and regional sea level change in projections and observations. *Nature Communications*, 2021a. 10.1038/s41467-021-21265-6.
- Wang, J., Church, J. A., Zhang, X., Gregory, J. M., Zanna, L., and Chen, X. Evaluation of the Local Sea-Level Budget at Tide Gauges Since 1958. *Geophysical Research Letters*, 48(20):1–12, 2021b. 10.1029/2021GL094502.
- Watkins, M. M., Wiese, D. N., Yuan, D.-N., Boening, C., and Landerer, F. W. Improved methods for observing Earth's time variable mass distribution with GRACE using spherical cap mascons Michael. *Journal of Geophysical Research: Solid Earth*, 120:2648–2671, 2015. 10.1002/2014JB011547.
- Watson, C. S., White, N. J., Church, J. A., King, M. A., Burgette, R. J., and Legresy, B. Unabated global mean sea-level rise over the satellite altimeter era. *Nature Climate Change*, 5(6):565–568, 2015. 10.1038/nclimate2635.
- Webb, E. J. and Magi, B. I. The Ensemble Oceanic Niño Index. *International Journal of Climatology*, 42(10): 5321–5341, 2022. 10.1002/joc.7535.
- Weedon, G. P., Balsamo, G., Bellouin, N., Gomes, S., Best, M. J., and Viterbo, P. Data methodology applied to ERA-Interim reanalysis data. *Water Resources Research*, 50(9):7505–7514, 2014. 10.1002/2014WR015638.
- Weisberg, R. H. and Liu, Y. On the Loop Current Penetration into the Gulf of Mexico. *Journal of Geophysical Research: Oceans*, 122(12):9679–9694, 2017. 10.1002/2017JC013330.

- WGMS. Fluctuations of Glaciers Database. *World Glacier Monitoring Service (WGMS)*, [dataset], 2022. 10.5904/wgms-fog-2022-09.
- Whitehouse, P. L. Glacial isostatic adjustment modelling: Historical perspectives, recent advances, and future directions. *Earth Surface Dynamics*, 6(2):401–429, 2018. 10.5194/esurf-6-401-2018.
- Wiese, D. N., Yuan, D.-N., Boening, C., Landerer, F. W., and Watkins, M. M. JPL GRACE and GRACE-FO Mascon Ocean, Ice, and Hydrology Equivalent Water Height Coastal Resolution Improvement (CRI) Filtered Release 06 Version 02. *JPL*, 2 [dataset] (last access 2020-10-28), 2019. 10.5067/TEMSC-3JC62.
- Wiese, D. N., Landerer, F. W., and Watkins, M. M. Quantifying and reducing leakage errors in the JPL RL05M GRACE mascon solution. *Water Resources Research*, 52, 2016. 10.1002/2014WR016259.
- Wigley, T. M. L. The Climate Change Commitment. *Science*, 307(18 March):1766–1769, 2005. 10.1126/science.1103934.
- Willis, J. K., Chambers, D. P., and Nerem, R. S. Assessing the globally averaged sea level budget on seasonal to interannual timescales. *Journal of Geophysical Research: Oceans*, 113(6):1–9, 2008. 10.1029/2007JC004517.
- Woodworth, P. L. Some important issues to do with long-term sea level change. *Philosophical Transactions of the Royal Society A: Mathematical, Physical and Engineering Sciences*, 364(1841):787–803, 2006. 10.1098/rsta.2006.1737.
- Woodworth, P. L., Gehrels, W. R., and Nerem, R. S. Nineteenth and Twentieth Century Changes in Sea Level. *Oceanography*, 24(2):80–93, 2011. 10.1080/03031853.1992.9524702.
- Wöppelmann, G. and Marcos, M. Vertical land motion as a key to understanding sea level change and variability. *Reviews of Geophysics*, 54(1):64–92, 2015. 10.1002/2015RG000502.
- Wouters, B., Gardner, A. S., and Moholdt, G. Global Glacier Mass Loss During the GRACE Satellite Mission (2002-2016). *Frontiers in Earth Science*, 7(May):1–11, 2019. 10.3389/feart.2019.00096.
- Wunsch, C. and Heimbach, P. Bidecadal thermal changes in the Abyssal Ocean. *Journal of Physical Oceanography*, 44(8):2013–2030, 2014. 10.1175/JPO-D-13-096.1.
- Yang, Y., Zhong, M., Feng, W., and Mu, D. Detecting Regional Deep Ocean Warming below 2000 meter Based on Altimetry, GRACE, Argo, and CTD Data. *Advances in Atmospheric Sciences*, 38(10):1778–1790, 2021. 10.1007/s00376-021-1049-3.
- Yang, Y., Feng, W., Zhong, M., Mu, D., and Yao, Y. Basin-Scale Sea Level Budget from Satellite Altimetry, Satellite Gravimetry, and Argo Data over 2005 to 2019. *Remote Sensing*, 14(4637):1–12, 2022. 10.3390/rs14184637.
- Yi, S., Sun, W., Heki, K., and Qian, A. An increase in the rate of global mean sea level rise since 2010. *Geophysical Research Letters*, 42(10):3998–4006, 2015. 10.1002/2015GL063902.
- Zemp, M., Huss, M., Thibert, E., Eckert, N., McNabb, R., Huber, J., Barandun, M., Machguth, H., Nussbaumer, S. U., Gärtner-Roer, I., Thomson, L., Paul, F., Maussion, F., Kutuzov, S., and Cogley, J. G. Global glacier mass changes and their contributions to sea-level rise from 1961 to 2016 (Author Correction). *Nature*, 568(7752):382–386, 2019. 10.1038/s41586-019-1071-0.
- Zlotnicki, V., Qu, Z., Willis, J. K., Ray, R., and Hausman, J. JPL MEASURES Gridded Sea Surface Height Anomalies Version JPL1812. Technical report, PO.DAAC, CA, USA, 2019.

Zuo, H., Balmaseda, M. A., Tietsche, S., Mogensen, K., and Mayer, M. The ECMWF operational ensemble reanalysis-analysis system for ocean and sea ice: A description of the system and assessment. *Ocean Science*, 15(3):779–808, 2019. [10.5194/os-15-779-2019](https://doi.org/10.5194/os-15-779-2019).

DATA STATEMENTS

All data supporting this dissertation is available at the 4TU.Research Data repository <https://doi.org/10.4121/22117046>. Additionally, for each of the published chapters the underlying data and code are available at individual repositories, as described below.

Chapter 2

The steric fields and trends produced in this research, as well as supporting scripts, are available at the 4TU.Research Data repository <https://doi.org/10.4121/12764933>.

Chapter 3

The regional mass-driven sea-level fields and uncertainties the figures of this chapter are available from the 4TU.ResearchData repository: <https://doi.org/10.4121/16778794>. The code for generating the figures is available at the GitHub repository <https://github.com/carocamargo/barystaticSLC>.

Chapter 4

All the contributions to the regional sea-level budget as well as the sub-basins polygons are available from Zenodo repository: <http://dx.doi.org/10.5281/zenodo.7007330>. Interactive maps of the sea-level budget are available at <https://carocamargo.github.io/resources/regional-SLB-domains/>

ACKNOWLEDGEMENTS

Where to begin? Somehow this seems to be the most difficult part of the thesis. And that's because a lot of people helped to get here, both professionally and personally, directly and indirectly, and it is not easy to put feelings of gratitude into words. I also have a terrible memory, so don't be offended if I don't mention your name below. If you helped me to get here, thank you!

I would like to start by thanking my supervising team, Aimée, Riccardo and Bert, first for giving me the chance of doing this PhD, and then for guiding me until the end of it. Thanks Bert for being my promotor, revising my thesis and guiding me through the administrative process of the PhD. Aimée and Riccardo, thank you for introducing me to the sea-level topic in depth, teaching me how to be an independent researcher, helping me believe in myself as a researcher (and continuously assuring me that 3 papers was enough), answering all of my (sometimes quite silly) questions, and all the career and life advises. I've always felt very comfortable in discussing with both of you any topic, both research and personal wise, and I do not take this relationship for granted. Thank you very much. Aimée, since the beginning you made sure I was settling in well in the Netherlands, always making time to talk about personal life in addition to work, and I really appreciate it.

I would also like to thank Marta for receiving me in Mallorca and supervising me while I was there. Thanks also to Ismael also for introducing me and helping with the Self-organizing maps. Thanks to all my co-authors for reading and revising the manuscripts, and helping me to get our papers published.

During a PhD we need to learn how to be independent researchers, and depending on the PhD topic and project, the research can be quite lonely. In this sense, I would like to say a special thanks to Tim, for making my research less isolated. Thanks for being my PhD mentor, helping me with all the forms and requirements of the graduate school, for all the brainstorm and discussions sessions, and for being my friend. I would also like to thank the NIOZ Sea Level team for the nice meetings and discussions. Victor and Jeemijn, I'm looking forward to see where our collaboration project goes. Matteo, was very nice to

collaborate with you, thanks for involving me in your research. Thanks Yochi and Eike for being my students and thrusting me with your supervision. Thanks to all my NIOZ colleagues, for the nice coffee and lunch breaks, inspiring talks and discussion. And a special thanks to Victor and Lauren, for helping me handle all my emotional (and crying) crisis, you were the seat belts in my emotional roller coaster. Thanks to Alexander Ebbing and Tim Grandjean, for being great office mates, even if for a short while. Rosanna, Marte and Celine, I had a great time writing our kids paper, thanks for letting me tag along in this project. Thanks also to the writing buddies. *En bedankt Tim en Roel voor het vertalen van de samenvatting.*

A significant part of my success today goes to my family and friends, who have supported me and allowed me to get here with a sane mind. À minha família, especialmente meus pais, que sempre acreditaram em mim, e me impulsionaram a seguir meus sonhos, mesmo eles me levando para o outro lado do oceano. Ciça, obrigada por ser minha irmã e melhor amiga, aguentar minhas mensagens e desabafos da vida acadêmica, mesmo não fazendo sentido nenhum, e por sempre estar presente mesmo estando longe. Às minhas amigas de infância, Kate, Mari, Gé, Maíra, Manda, Sofia, Rafa e Fe, saber que nossa amizade não muda mesmo com tanto tempo (e distância) passando é um conforto que não tem igual. Thanks to my Oceans & Lakes, especially to Leo, Pedro, Kumari, Heleen, Jana and Jolien for visiting me in Bergen op Zoom.

Living abroad means having to find your home all over again. So I would like to thank Adina and the "BoZ Groupies" for making Bergen op Zoom feel like home. Adina, many thanks for welcoming me to Bergen op Zoom, making it feel like a nice and fun place to live, and taking care of Napo. Thanks Dunia and Victor for being my flatmates. A especial thanks to Greg, Puck, Lauren, Colin, Marte, Tori, Tim, Vic, Chiu and Roel, for all the fun times with game nights, pub quiz, going to the movies, getting drinks, playing frisbee and others. Obrigada também Gra e Fe, por trazerem um pouco do Brasil pra perto de mim, por me incentivarem a adotar o Napo, e por toda as cervejas e bons momentos.

Thanks Napo for always brightening up my day, making me go out of the house (even when I don't want to) and for your unconditional love.

Last but not least, thanks Roel for everything. For being there for me, supporting me through all the ups and downs of the last years, for making me laugh, for understanding me and for making silly Napo voices. You are the one certain thing amidst all the unknowns that surround the end of a PhD and the academic life. You are my home, and look forward to our future together.

LIST OF PUBLICATIONS

Camargo, C.M.L., Riva, R.E.M., Hermans, T.H.J., & Slangen, A.B.A.: Exploring Sources of Uncertainty in Steric Sea-Level Change Estimates, *Journal of Geophysical Research: Oceans*, 125, e2020JC016551, doi: 10.1029/2020JC016551, 2020.

Hermans, T.H.J., Le Bars, D., Katsman, C.A., **Camargo, C.M.L.**, Gerkema, T., Calafat, F.M., Tinker, J., & Slangen, A.B.A.: Drivers of Interannual Sea Level Variability on the Northwestern European Shelf, *Journal of Geophysical Research: Oceans*, 125, e2020JC016325, doi: 10.1029/2020JC016325, 2020

Azevedo, C.C., **Camargo, C.M.L.**, Alves, J., & Caldeira, R.M.A.: Convection and heat transfer in island (Warm) wakes, *Journal of Physical Oceanography*, 51(4), 1187–1203. doi: 10.1175/JPO-D-20-0103.1, 2021.

Hermans, T.H.J., Katsman, C.A., **Camargo, C.M.L.**, Garner, G.G., Kopp, R.E., & Slangen, A.B.A.: The Effect Of Wind Stress On Seasonal Sea-Level Change On the Northwestern European Shelf, *Journal of Climate*, 1-31. doi: 10.1175/JCLI-D-21-0636.1, 2022.

Camargo, C.M.L., Riva, R.E.M., Hermans, T.H.J., & Slangen, A.B.A.: Trends and uncertainties of mass-driven sea-level change in the satellite altimetry era, *Earth System Dynamics*, 13, 1351–1375, doi: 10.5194/esd-13-1351-2022, 2022.

Slangen, A.B.A., Palmer, M.D., **Camargo, C.M.L.**, Church, J.A., Edwards, T.L., Hermans, T.H.J., Hewitt, H., Garner, G.G., Gregory, J.M., Kopp, R.E., Santos, V.M., & van de Wal, R.S.W.: The evolution of 21st century sea-level projections from IPCC AR5 to AR6 and beyond, *Cambridge Prisms: Coastal Futures*, 1-33, doi: 10.1017/cft.2022.8, 2022.

Camargo, C.M.L., Riva, R.E.M., Hermans, T.H.J., Marcos, M., Schütt, E.M., Hernandez-Carrasco, I., & Slangen, A.B.A.: Regionalizing the Sea-level Budget With Machine Learning Techniques, *Ocean Science*, 19, 17–41, doi: 10.5194/os-19-17-2023, 2023.

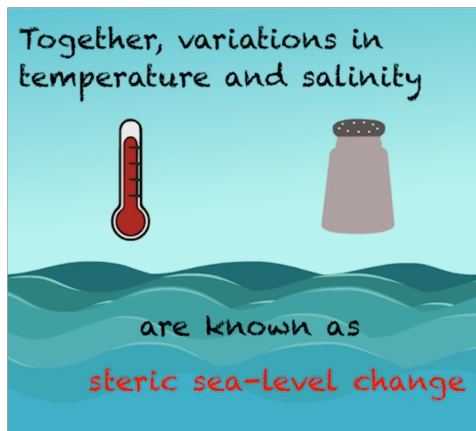
van Hesperen, R., van Bijsterveldt, C.E.J., **Camargo, C.M.L.**, Stoorvogel, M.M., & Bouma, T.J.: How Can Nature Protect People Against Sea-Level Rise?, *Frontiers for Young Minds*, 11:910803. doi: 10.3389/frym.2023.910803, 2023.

Meli, M., **Camargo, C.M.L.**, Olivieri, M., Slangen, A.B.A., Romagnoli, C.: Sea-level trend variability in the Mediterranean during the 1993-2019 period, *Frontiers in Marine Science*, 10. doi: doi: 10.3389/fmars.2023.1150488, 2023.

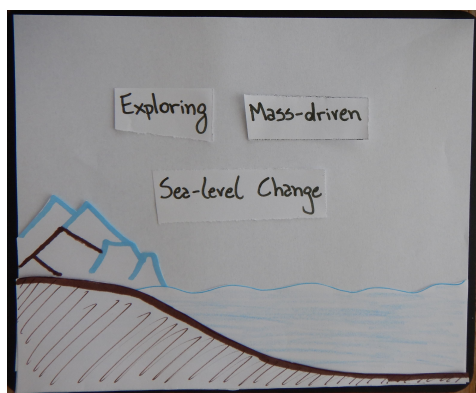
OUTREACH VIDEOS

To promote the research published in this thesis, I made video abstracts for Chapter 2 and 3:

Exploring steric sea-level change: <https://youtu.be/Uh-GN9QznFI>



Mass-driven sea-level change: <https://youtu.be/I6HpLwchfWQ>



CURRICULUM VITÆ

Carolina M.L. de Camargo was born in São Paulo, Brazil, on the 21st of December, 1991. Carolina obtained a BSc degree in Oceanography at the Universidade Federal do Rio Grande in 2015. During this program, she spent one year (2013-2014) at the University of British Columbia, Canada, in the Earth and Ocean Sciences BSc Program as a Science Without Borders scholar. She then moved to Belgium to pursue a MSc degree in Marine and Lacustrine Science and Management in the inter-university program between the Free University of Brussel (VUB), Antwerp University (UAntwerpen) and Ghent University (UGent), graduating (Great Distinction) in 2018. Her MSc studies was funded by ISA/GSR Training Programme Fellowship. In 2019 Carolina started her PhD project on the regional sea-level budget at NIOZ and Delft University of Technology.

